Dissertation
submitted to the
Combined Faculties for the Natural Sciences
and for Mathematics
of the Ruperto-Carola University of Heidelberg,
Germany
for the degree of
Doctor of Natural Sciences

Put forward by
Diplom-Physiker Sebastian Westermann
born in Freiburg i.Br.
Oral examination: 14 October 2010

Sensitivity of permafrost

Referees: Prof. Dr. Kurt Roth
Prof. Dr. Ulrich Platt

Zusammenfassung

Permafrostböden in der Arktis unterliegen im Zuge des Klimawandels einer Reihe von Veränderungen, was den Aufbau eines weltweiten Monitoring-Programms zwingend notwendig macht. In dieser Arbeit wird ein Energiebilanz-Modell für einen Permafrost-Standort auf Svalbard in Norwegen entwickelt, das in Analogie zu Klimamodellen die einzelnen Komponenten der Energiebilanz an der Oberfläche und die Bodentemperaturen berechnet. Dazu wurde die Oberflächenenergiebilanz, bestehend aus den Strahlungskomponenten, dem fühlbaren und latenten Wärmestrom sowie dem Bodenwärmestrom, für die Dauer eines Jahres gemessen, was bisher für arktische Landgebiete noch nicht durchgeführt wurde. Messungen der Oberflächentemperatur mit einer Thermalkamera zeigen eine deutliche räumliche Variabilität dieser wichtigen Variablen, die sich im Rahmen des Energiebilanz-Modells reproduzieren lässt. Auch die Auswirkung der in Messungen dokumentierten starken Heterogenität der Schneehöhen auf die Bodentemperaturen kann mit dem entwickelten Energiebilanzmodell simuliert werden. Des weiteren werden Bodenmessungen der Oberflächentemperatur mit Satellitendaten verglichen, wobei sich insbesondere während des Winters deutlich zu kalte Temperaturen in der Satellitenmessung ergeben. Abschließend werden verschiedene Möglichkeiten diskutiert, wie die entwickelten Konzepte für ein Permafrost-Monitoring-Programm genutzt werden könnten. Hierbei zeichnen sich Energiebilanzmodelle vor allem durch ihre enge Anlehnung an vorhandene Klimamodelle sowie die Flexibilität aus, verschiedene Satellitendaten als Trainingsdatensätze zur Parameterschätzung einbeziehen zu können.

Abstract

Arctic permafrost may be adversely affected by climate change in a number of ways, so that establishing a world-wide monitoring program seems imperative. This thesis evaluates possibilities for permafrost monitoring at the example of a permafrost site on Svalbard, Norway. An energy balance model for permafrost temperatures is developed that evaluates the different components of the surface energy budget in analogy to climate models. The surface energy budget, consisting of radiation components, sensible and latent heat fluxes as well as the ground heat flux, is measured over the course of one year, which has not been accomplished for arctic land areas so far. A considerable small-scale heterogeneity of the summer surface temperature is observed in long-term measurements with a thermal imaging system, which can be reproduced in the energy balance model. The model can also simulate the impact of different snow depths on the soil temperature, that has been documented in field measurements. Furthermore, time series of terrestrial surface temperature measurements are compared to satellite-borne measurements, for which a significant cold-bias is observed during winter. Finally, different possibilities for a world-wide monitoring scheme are assessed. Energy budget models can incorporate different satellite data sets as training data sets for parameter estimation, so that they may constitute an alternative to purely satellite-based schemes.

Contents

List of Tables

List of Figures

Definitions, constants and employed values

S_{in}: incoming short-wave radiation [$\mathrm{W\,m^{-2}}$]
S_{out}: outgoing short-wave radiation [$\mathrm{W\,m^{-2}}$]
ΔS: net short-wave radiation [$\mathrm{W\,m^{-2}}$]
α: surface albedo [-]
L_{in}: incoming long-wave radiation [$\mathrm{W\,m^{-2}}$]
L_{out}: outgoing long-wave radiation [$\mathrm{W\,m^{-2}}$]
ΔL: net long-wave radiation [$\mathrm{W\,m^{-2}}$]
Q_{net}: net radiation [$\mathrm{W\,m^{-2}}$]
ε: Kirchhoff emissivity [-]
σ_{sb}: Stefan-Boltzmann constant [$\mathrm{W\,m^{-2}K^{-4}}$]
Q_h: sensible heat flux [$\mathrm{W\,m^{-2}}$]
Q_e: latent heat flux [$\mathrm{W\,m^{-2}}$]
Q_g: ground or snow heat flux [$\mathrm{W\,m^{-2}}$]
Q_{melt}: energy flux consumed by melt of snow [$\mathrm{W\,m^{-2}}$]
C: residual of the energy balance [$\mathrm{W\,m^{-2}}$]

$\vec{x} = (x, y, z)$: coordinate of space
x, y: horizontal coordinate [m]
z: vertical coordinate [m]
$\vec{u} = (u, v, w)$: velocity
u, v: horizontal velocity components [$\mathrm{m\,s^{-1}}$]
w: vertical velocity [$\mathrm{m\,s^{-1}}$]
T: temperature [°C, K]
ρ: density [$\mathrm{kg\,m^{-3}}$]

d_h: thermal diffusivity [$\mathrm{m^2 s^{-1}}$]
K_h: thermal conductivity [$\mathrm{W\,m^{-1}K^{-1}}$]
c_h: specific volumetric heat capacity [$\mathrm{J\,m^{-3}K^{-1}}$]
c_{eff}: effective volumetric heat capacity [$\mathrm{J\,m^{-3}K^{-1}}$]
θ_w: volumetric water content [-]
θ_i: volumetric ice content [-]
θ_a: volumetric air content [-]
θ_m: volumetric mineral content [-]
θ_o: volumetric organic content [-]
E: energy [J]
e: energy per unit volume [$\mathrm{J\,m^{-3}}$]
j_e: energy flux [$\mathrm{W\,m^{-2}}$]
j_g: conductive ground or snow heat flux [$\mathrm{W\,m^{-2}}$]
j_w: flow rate of water per cross-sectional unit area [$\mathrm{ms^{-1}}$]
j_a: flow rate of air per cross-sectional unit area [$\mathrm{ms^{-1}}$]
$j_{h,w}$: energy flux due to water flow [$\mathrm{W\,m^{-2}}$]
$j_{h,a}$: energy flux due to air flow [$\mathrm{W\,m^{-2}}$]
$F(T)$: freezing characteristic of soil [-]
T_f: freezing temperature of free water [K]
T_{surf}: surface temperature [°C, K]

T_{air}: air temperature [°C, K]
T_s: sonic air temperature [K]
T_v: virtual temperature [K]
Θ: potential temperature [K]
Θ_v: virtual potential temperature [K]
q: specific humidity [$\mathrm{kg\,kg^{-1}}$]
RH: relative humidity [%]
μ: dynamic viscosity [$\mathrm{Pa\,s}$]
s: entropy [$\mathrm{J\,K^{-1}}$]
c_p: specific heat capacity of air at constant pressure [$\mathrm{J\,kg^{-1}K^{-1}}$]
ρ_a: density of air [$\mathrm{kg\,m^{-3}}$]
κ: von Kármán-constant [-]
u_*: friction velocity [$\mathrm{m\,s^{-1}}$]
z_0: aerodynamic roughness length [m]
L_*: Obukhov length [m]
R_f: flux Richardson number [-]
$\zeta = z/L_*$: stability parameter (z: measurement height) [-]
$\varphi_{M,H,W}(\zeta)$: stability functions for momentum, heat and water vapor [-]
$\Psi_{M,H,W}(\zeta_1, \zeta_2)$: integrated stability functions for momentum, heat and water vapor [-]
p: pressure [Pa]
R_d: specific gas constant of dry air [$\mathrm{J\,kg^{-1}K^{-1}}$]
R_w: specific gas constant of moist air [$\mathrm{J\,kg^{-1}K^{-1}}$]
$\vec{f}$: Coriolis parameter [$\mathrm{s^{-1}}$]
g: gravitational constant [$\mathrm{m\,s^{-2}}$]
r_s: surface resistance against evapotranspiration [$\mathrm{s\,m^{-1}}$]
γ: adiabatic constant [-]
c_s: speed of sound in air [$\mathrm{m\,s^{-1}}$]
f: frequency [Hz]

I: spectral intensity [$\mathrm{W\,m^{-3}nm^{-1}}$]
λ: wavelength [m]
c: speed of light [$\mathrm{m\,s^{-1}}$]
h: Planck constant [$\mathrm{J\,s}$]
k_B: Boltzmann constant [$\mathrm{J\,K^{-1}}$]
T_b: brightness temperature [K]

δ_{ij}: Kronecker symbol
ε_{ijk}: Levi-Civita symbol
$\delta(x)$: Dirac delta function
$\vec{n}$: unit vector

$c_{h,\mathrm{water}} = 4.2\,\mathrm{MJ\,m^{-3}K^{-1}}$
$K_{h,\mathrm{water}} = 0.45\,\mathrm{W\,m^{-1}K^{-1}}$
$c_{h,\mathrm{ice}} = 1.9\,\mathrm{MJ\,m^{-3}K^{-1}}$
$K_{h,\mathrm{ice}} = 2.2\,\mathrm{W\,m^{-1}K^{-1}}$
$c_{h,\mathrm{mineral}} = 2.0\,\mathrm{MJ\,m^{-3}K^{-1}}$
$K_{h,\mathrm{mineral}} = 2.9\,\mathrm{W\,m^{-1}K^{-1}}$

$c_{h,\text{organic}} \approx c_{h,\text{mineral}}$
$K_{h,\text{organic}} = 0.25\,\text{W}\,\text{m}^{-1}\text{K}^{-1}$
$c_{h,\text{air}} \approx 0.001\,\text{MJ}\,\text{m}^{-3}\text{K}^{-1}$
$K_{h,\text{air}} \approx 0.025\,\text{W}\,\text{m}^{-1}\text{K}^{-1}$
$\rho_w = 1000\,\text{kg}\,\text{m}^{-3}$: density of water
$\rho_i = 910\,\text{kg}\,\text{m}^{-3}$: density of ice
$L_{\text{sl}} = 0.33\,\text{MJ}\,\text{kg}^{-1}$: specific latent heat of fusion of water
$L_{\text{lg}} = 2.5\,\text{MJ}\,\text{kg}^{-1}$: specific latent heat of vaporization of water
$L_{\text{sg}} = 2.8\,\text{MJ}\,\text{kg}^{-1}$: specific latent heat of sublimation of ice
Values according to Hillel (1982).
$\kappa = 0.4$: von Kármán-constant (e.g. Foken, 2008a)

Chapter 1

Introduction

1.1 Permafrost – an essential climate variable in the "Global Climate Observing System"

Permafrost is defined as sub-surface earth materials that remain continuously at or below the freezing temperature of water for at least two consecutive years (Harris et al., 1988). A distinction is made between the continuously frozen permafrost and the so-called "active layer" on top of the permafrost, which is subject to annual thawing and freezing (Harris et al., 1988). The active layer is of outstanding importance as all biological processes, including the formation and decomposition of organic material, are restricted to this zone. Permafrost occurs mainly in arctic regions, but also in high mountain areas, such as the Tibet plateau (Fig. 1.1). Due to the distribution of the land masses on the earth, permafrost is strongly concentrated on the Northern Hemisphere, where approximately a quarter of the land area is occupied by permafrost. The largest extent of permafrost is found in Siberia, followed by arctic Canada and Alaska. In Europe, permafrost exists in the Alps, in mountainous regions of Scandinavia and in the non-glaciated areas of Greenland and Svalbard. This thesis investigates permafrost on Svalbard.

Permafrost is a temperature phenomenon on the local scale, as the temperature distribution in the ground at each point is largely determined by the temperature conditions at the surface and not by neighboring areas. As the local surface temperature is influenced by a range of factors, such as exposition, vegetation or soil moisture, areas with and without permafrost can coexist in a region, which gives rise to the classification of permafrost areas in continuous (more than 90% of the area underlain by permafrost), discontinuous (50 to 90% of the area), sporadic (less than 50% of the area) and isolated (only small patches). The permafrost on Svalbard is in the zone of continuous permafrost (Fig. 1.1).

In the past decade, a large number of studies has gathered convincing observational and modeling evidence for a sustained warming of the Arctic (e.g. Serreze et al., 2000; Hansen et al., 2001; Comiso and Parkinson, 2004; Hinzman et al., 2005; Turner et al., 2007; Comiso et al., 2008; Overland et al., 2008). On Svalbard, a significant warming of air temperatures since 1960 has been detected,

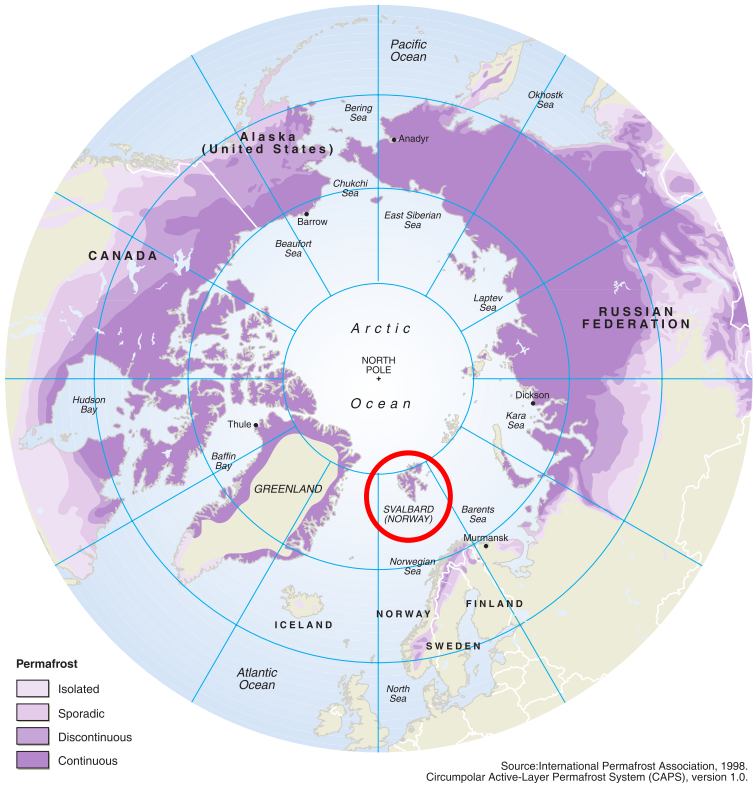

Figure 1.1: Circum-polar permafrost distribution with classification in continuous, discontinuous, sporadic and isolated permafrost from Brown et al. (1997). Svalbard, where the field measurements for this study have been performed, is circled in red.

which is mainly attributed to changes in circulation patterns (Hanssen-Bauer and Førland, 1998). The ongoing warming trend naturally has an impact on the permafrost, and increasing permafrost temperatures have been reported for many regions (e.g. Hinzman et al., 2005; Osterkamp, 2005), including Svalbard (Isaksen et al., 2001, 2007).
General circulation models (GCMs) predict an accelerated future warming trend for the Arctic, with increases of the mean air temperature exceeding 10 K until the end of the century (Fig. 1.2). Accordingly, a sizable reduction of the permafrost area is projected until 2100 (Delisle, 2007; Lawrence et al., 2008), which is likely to have strong impacts on the ecology (e.g. Jorgenson et al., 2001), infrastructure (Parker, 2001) and economy (Prowse et al., 2009) of these regions. However, even more drastic scenarios are conceivable: The total carbon stored in the uppermost three meters of soil in permafrost areas is estimated to be about half of the world-wide soil carbon stock, or more than twice the atmospheric carbon pool (Schuur et al., 2008). Zimov et al. (2006) suggest that degradation of permafrost and an increase in average active layer thickness will make large amounts of previously frozen organic material, that has been ac-

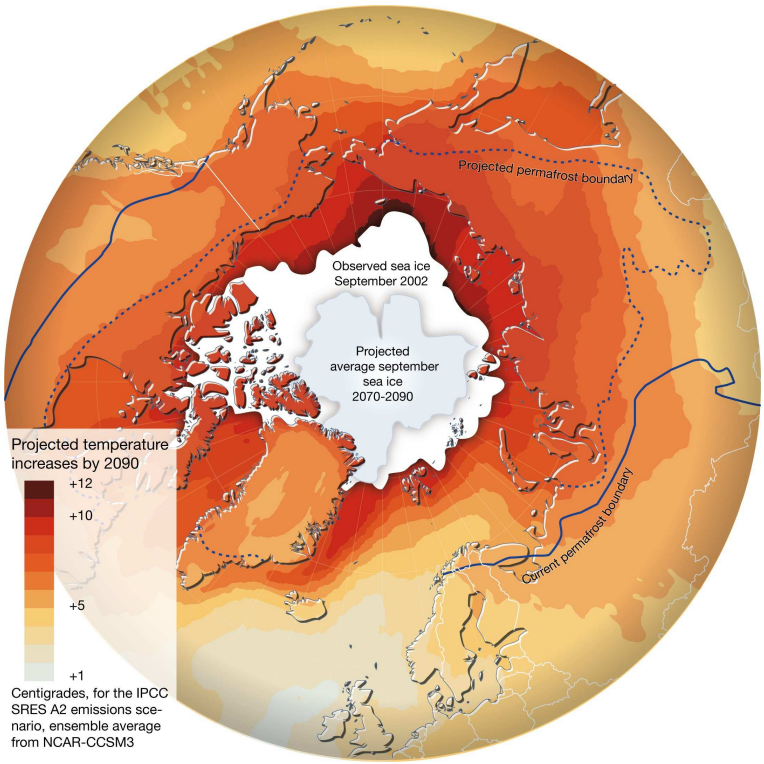

Figure 1.2: Projected changes of the Arctic climate until 2090, as given by the average of the scenarios included in the Arctic Climate Impact Assessment (ACIA, 2005). Shown is the near-surface air temperature, the September sea ice extent and the current and projected outer limits of the permafrost area (UNEP/GRID-Arendal, 2010).

cumulated over millenia, available for microbial decomposition. As anaerobic decomposition is dominant in the extensive wetland areas in Siberia, Canada and Alaska, this may lead to a massive release of methane from permafrost regions. The activation of this carbon stock would convert northern permafrost regions from net sinks to net sources of greenhouse gases (Walter et al., 2006; Schuur et al., 2008), resulting in an amplification of the global warming trend. Based on such drastic projections, permafrost has been included in the "Global Climate Observing System" (GCOS) as an "Essential Climate Variable" for terrestrial systems (gcos.wmo.int, 2010). The ambition of GCOS is "to provide continuous, reliable, comprehensive data and information on the state and behavior" (gcos.wmo.int, 2010) of the earth systems to compile a common data basis for national and international agencies, e.g. for the reports of the "Intergovernmental Panel on Climate Change" (IPCC). The GCOS framework constitutes the obligation to establish long-term monitoring programs for environmental variables, that can characterize the state of the permafrost.

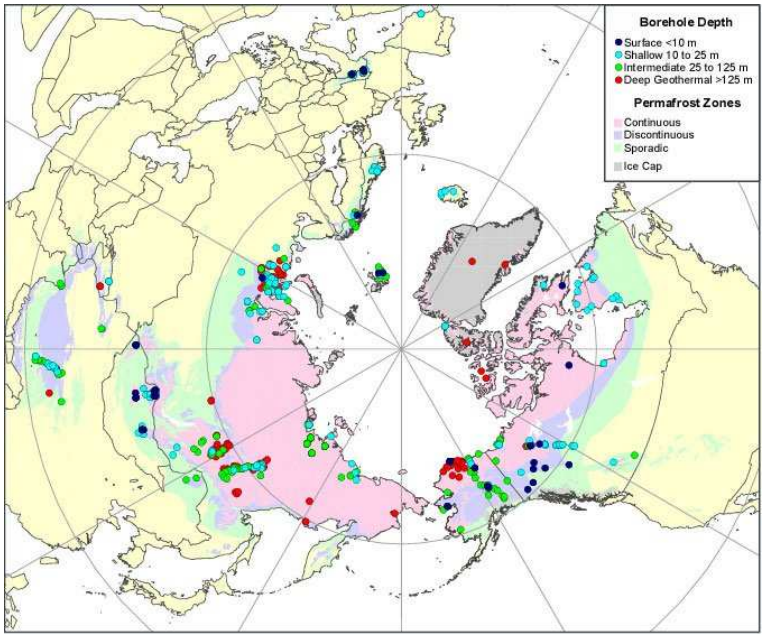

Figure 1.3: Location of the boreholes of the TSP program (www.gtnp.org, 2010).

1.2 State of the art in permafrost monitoring

Considering the extent of the permafrost area and the potential impacts of a large-scale degradation, it seems imperative to continuously map and monitor the thermal state of the permafrost world-wide in order to assess its vulnerability to climate change. Two terrestrial monitoring programs are currently operational, the "Circumpolar Active Layer Monitoring" (CALM) program and the "Thermal State of Permafrost" (TSP) program, which both form the backbone of the permafrost monitoring required for GCOS. The degradation of permafrost usually is preceded by an increase in the thickness of the active layer, followed by the formation of a talik and the subsequent thawing of the remaining permafrost body from top and bottom. An ongoing monitoring of the active layer thickness might therefore serve as an "early-warning system" to detect the onset of permafrost degradation. The CALM program coordinates measurements of the active layer thickness at more than 150 sites (Nelson et al., 2008; Shiklomanov et al., 2008). The main disadvantage of the CALM approach is that the active layer thickness mainly reflects the summer conditions. At sites in Alaska, Osterkamp (2007) observes stable active layer thicknesses despite of a warming of the permafrost temperatures, which is caused by a warming trend during the much longer winter season.
Therefore, the TSP program (Burgess et al., 2000; www.gtnp.org, 2010) targets the thermal state, i.e. the temperature distribution, of the permafrost underlying the active layer, which reflects the temperature conditions of the entire year. Another advantage of temperature monitoring in deep boreholes is that inter-

annual variations, which can be of considerable magnitude, are not reflected in deeper soil layers, as they decay close to the surface. Therefore, the temperature at a certain depth gives the integrated temperature signal for a certain period, which is the longer the deeper the temperature is measured. The TSP program currently comprises more than 500 boreholes of depths between less than 10 m to several 100 m, in which the temperature distribution is either measured manually at regular intervals or automatically recorded using dataloggers. As the majority of the boreholes has been drilled in the course of prospecting operations for mineral resources or infrastructure projects, the boreholes are strongly concentrated in the resource-rich regions of West Siberia, Yakutia and Alaska, while vast regions are not covered at all (Fig. 1.3). Despite of the accurate temperature information at the borehole site, the considerable heterogeneity of the surface and snow cover to a certain extent questions the representativeness of the borehole data for the larger surrounding area. To gain a better understanding of this problem, it is necessary to investigate the controlling factors, which give rise to the formations of spatial heterogeneity of subsurface temperatures under different conditions.

Although the CALM and TSP programs have been expanded rapidly in the past five years, it is evident that the vast and remote permafrost areas cannot be sufficiently covered by such a labor-intensive scheme alone. It is thus desirable to better exploit the potential of remotely sensed data sets to complement terrestrially-based monitoring. However, as permafrost is a ground temperature phenomenon, none of the potential measures used to characterize permafrost, such as the thaw depth or the temperature distribution in the ground, is directly accessible through remote sensing techniques. Some studies have evaluated the performance of proxies for the state of the permafrost, such as the occurrence of certain vegetation types (Walker et al., 2003) or the increase or shrinkage of lakes (Smith et al., 2005; Stow et al., 2004), which can be detected in high-resolution multi-spectral satellite images. However, such indicators are usually only meaningful for limited areas, so that it seems questionable that they can be employed for a larger-scale monitoring.

Remotely sensed land surface temperatures (LST) are a more universal proxy, although the relationship between surface and subsurface temperatures is complex. While a warming trend over the arctic land masses has been observed in long-term records of satellite-derived LST (Comiso and Parkinson, 2004; Comiso, 2006), the implications for the thermal state of the permafrost remain debatable. Marchenko et al. (2009) propose to use the existing time series of remotely sensed LST as upper boundary condition for a conductive heat transfer model (e.g Sazonova and Romanovsky, 2003), which delivers the full temperature distribution in the ground. Despite of the large number of required additional input parameters, such as information on the snow cover and the composition of the soil, this concept may possess the flexibility to incorporate the full range of different climatic, geological and ecological conditions found in permafrost areas. The application of such an LST-based scheme for Northern Quebec and Labrador, Canada, (Hachem et al., 2009) highlights the prospects for large-scale permafrost monitoring.

The land surface temperature is currently accessible by a number of remote sensing platforms, some of which provide a high overpass frequency at the expense of spatial resolution (e.g. Terra MODIS, Aqua MODIS, ERS-AATSR, NOAA-AVHRR), while others follow the opposite concept (e.g. Landsat TM,

ASTER). For the purpose of permafrost monitoring, daily to monthly LST averages are required, as high-frequency fluctuations of the surface temperature, such as the daily cycle, decay close to the surface and do not affect the temperature evolution of deeper soil layers. However, accurate temporal averages of LST can only be obtained, if a sufficient overpass frequency is provided. In this point, satellite platforms such as Terra/Aqua MODIS, which under ideal conditions are even capable to resolve the daily cycle, are superior to high-resolution sensors such as Landsat TM, which can only provide a few measurements per averaging period. On the other hand, as strong variations of the surface cover and the soil moisture conditions occur on scales of meters in permafrost regions, pronounced subpixel differences of the surface temperature are conceivable for a medium-resolution sensor such as MODIS, which has a footprint area on the order of one square kilometer. A strong subpixel variability of LST would add additional complexity to a permafrost monitoring scheme, as the employed heat transfer models are highly non-linear due to the phase change of water.
To gain a better insight in the performance and limitations of an LST-based permafrost monitoring scheme, case studies at different permafrost sites are required, where remotely sensed LST and other input parameters are validated. Furthermore, the performance of different heat transfer models to reproduce the thermal regime of the ground should be evaluated. In addition to potential improvements of the employed techniques and models, such case studies are key to building (or destroying) confidence in the reliability of satellite-based permafrost monitoring.

1.3 Modeling the future state of permafrost

In permafrost regions, the partitioning of energy at the surface is a crucial process, which strongly influences the heat flux into the ground and thus ultimately the thermal conditions of the permafrost. The basic terms in this surface energy budget are the short- and long-wave radiation, the sensible and latent heat fluxes and the ground heat flux. The surface energy budget is influenced by a number of factors, such as synoptic weather conditions, surface characteristics and surface soil moisture. The correct representation of the surface energy budget is one of the challenges in global coupled Atmosphere-Ocean General Circulation Models (AOGCMs) in the Arctic. The scientific report from the "Arctic Climate Impact Assessment" (ACIA, 2005) concludes:

"The Arctic is a region characterized by complex and insufficiently understood climate processes and feedbacks, contributing to the challenge that the Arctic poses from the view of climate modeling. Several weaknesses of the models related to descriptions of high-latitude surface processes have been identified, and these are among the most serious shortcomings of present-day arctic climate modeling. [...] The atmospheric boundary layer in the Arctic is poorly represented in current AOGCMs. It is unlikely that the representation can be improved just by increasing model vertical resolution. Insufficient understanding of the physics of the atmospheric boundary layer in the Arctic and the inappropriate parameterizations used in the current generation of AOGCMs call for further research in this field."

The models make use of mostly semi-empirical parameterizations of the different fluxes of the surface energy budget, which have usually been developed and validated for non-arctic regions (e.g. Viterbo and Beljaars, 1995). In the Arctic, the perennial snow cover and the annual snowmelt, which greatly modify the surface processes for a large part of the year, constitute additional challenges for modeling, which have not been fully resolved (Douville et al., 1995; Slater et al., 1998). Another unresolved problem is the parameterization of the sensible and latent heat fluxes during stable atmospheric stratification conditions which frequently occur in the arctic winter (Zilitinkevich et al., 2002; Lüers and Bareiss, 2009a).
Therefore, direct measurements of the surface energy budget in arctic regions are indispensable to evaluate the performance of the employed flux parameterizations and surface parameter sets, especially if the study can provide the entire annual cycle and thus a complete picture including snow-associated processes. The scarcity of such data sets in the Arctic is yet intriguing. Eugster et al. (2000) have compiled a data basis of the surface energy budget of different landcover types for the summer months, but a similar survey for the winter does not exist. For sea ice on the arctic ocean, the extensive SHEBA study has provided a record of the entire annual cycle of the surface energy budget (Persson et al., 2002; Uttal et al., 2002). For arctic land areas occupied by permafrost, where the logistical effort is much smaller, such a comprehensive long-term study has not been initiated so far.
Permafrost is currently not represented in an adequate way in General Circulation Models (GCMs). The "European Centre/Hamburg Model" (ECHAM) from the Max-Planck Institute for Meteorology, Hamburg, (Roeckner et al., 2003), for instance, contains a total of five soil layers to a depth of 10 m, but does not include the freezing of soil water at all. Thus, a considerable fraction of the energy exchange between the soil and the atmosphere is not accounted for, and the dynamics of freeze and thaw processes cannot be properly represented. Therefore, two questions must be raised with respect to permafrost:

1. Would an adequate representation of permafrost in GCMs lead to an improved accuracy in the model predictions of the target variables, such as air temperatures or precipitation, both for permafrost areas and on the global scale?

2. Can atmospheric variables derived from current climate models (e.g. air temperature or precipitation, obtained with an inadequate representation of permafrost-related processes) be used to drive stand-alone permafrost models, which do include a proper representation of permafrost dynamics?

The first question would have to be answered with "yes", if strong feedbacks between permafrost processes and the climate system existed. A prime example for such a feedback process would be the massive emission of methane from degrading permafrost (see Sect. 1.1), which is not accounted for in current climate models. To include this permafrost-atmosphere feedback, the addition of a suitable soil model which can reproduce the annual freezing and thawing of the active layer would only be a first step, which needs to be complemented by a biogeochemical model for methane production and release. A second conceivable, yet less spectacular link between permafrost and the climate system is the

modification of the surface energy budget due to the seasonality of energy storage and release from permafrost-dominated ground. This is particularly true for times when the soil close to the surface freezes or thaws, which has been found to directly impact the near-surface air temperature in model simulations (Viterbo et al., 1999). Furthermore, it is conceivable that changes in the vegetation due to thawing permafrost could modify the surface energy budget over large areas within the Arctic. Some studies have suggested a feedback of such processes on the climate system at least on the regional scale (Chapin et al., 2005).
The second question can be answered with "yes", if the impact of ground processes on atmospheric variable is small, i.e. the ground heat flux is small compared to the other terms in the surface energy budget. It is interesting to note that this is implicitly assumed in all global simulations of future permafrost extent (e.g. Delisle, 2007; Lawrence et al., 2008). To investigate this issue, measurements of the annual surface energy budget of permafrost areas across climatic and ecological gradients are needed.
To obtain permafrost temperatures from atmospheric variables, process-oriented permafrost models have been developed (Hoelzle et al., 2001). In principle, they make use of the same parameterizations of the surface energy budget as GCMs to evaluate the ground heat flux and the thermal conditions of the subjacent permafrost (Hinzman et al., 1995; Ling and Zhang, 2004). Accordingly, they are subject to the same shortcomings of the flux parameterizations, which can lead to biased results. To build or destroy confidence in simulations based on process-oriented permafrost and climate models, case studies are required which investigate the performance of various measured and modeled input data sets and permafrost models to reproduce a measured temperature distribution in the ground.

1.4 Outline

This thesis investigates the sensitivity of the ground thermal regime at a permafrost site on Svalbard towards a variety of environmental factors. It is designed to connect three different disciplines in permafrost research - field measurements, remote sensing and modeling. A major challenge of this work is to resolve the inherent scale conflict between the three fields. While this study is ultimately focused on the ground thermal regime, land-atmosphere interactions are investigated to obtain a detailed understanding of the determining physical processes.
The surface temperature is the key parameter in monitoring and modeling efforts for the thermal regime of the ground, as it reflects the combined effects of surface-atmosphere interactions as well as surface-ground processes. This thesis explores the relevant processes that give rise to the formation of the surface temperature and the spatial and temporal scales, over which they vary.

- The surface temperature forms as the result of the surface energy budget, i.e. the partitioning of energy at the earth surface. Therefore, the different components of the surface energy budget are evaluated in independent measurements over the course of one year. The detailed understanding of

the surface energy budget is key to an adequate representation in models.

- During summer, the surface temperature displays a considerable spatial heterogeneity. Spatially resolved monitoring of the surface temperature has been conducted during two summer seasons with a thermal imaging system. The determining factors for the formation of spatially different surface temperatures are interpreted within the framework of the surface energy budget. Conversely, the surface temperature measurements allow insight in the spatial variability of the surface energy budget, which is a challenge in modeling schemes.

- During winter, the snow cover plays a crucial role for the thermal regime of the ground, as it insulates the soil and prevents propagation of the low winter temperatures into the ground. In extensive field measurements, the impact of the spatial variability of the snow cover on the ground thermal regime is investigated.

- The performance of remotely sensed land surface temperatures from the Moderate Resolution Imaging Spectroradiometer (MODIS), which are proposed as key input parameter for satellite-based permafrost monitoring, is evaluated for the study area. A detailed assessment of subpixel variability is given, and the prospects of satellite-based LST measurements for permafrost monitoring are assessed.

- The process understanding gathered in the various field measurements is implemented in a process-oriented permafrost model based on the surface energy budget, that is optimized to deliver the ground thermal regime. First model runs forced by global reanalysis data for the past 50 years are presented.

Finally, a critical appraisal of the eligibility of process-oriented schemes for permafrost monitoring is given. The superior performance compared to schemes that are entirely forced by remotely sensed data is highlighted. With the assessment of a data fusion strategy, this thesis aims to make a distinct contribution to the current discussion towards operational permafrost monitoring on the pan-arctic scale.

Chapter 2

Theory

2.1 The surface energy budget

The partitioning and redistribution of energy at the surface is the driving process for the energy and water budget of the earth. The earth surface is the lower boundary of the atmosphere, where energy and water are transported by radiative and convective processes, as well as the upper boundary for the lithosphere, where conductive transfer of energy dominates. The surface energy budget (SEB) equation connects atmospheric and lithospheric processes and reflects the conservation of energy,

$$0 = S_{\text{in}} + S_{\text{out}} + L_{\text{in}} + L_{\text{out}} + Q_h + Q_e + Q_g \, . \tag{2.1}$$

All quantities represent energy fluxes (unit Wm^{-2}) and the equation is satisfied at each point in space and time. We use the convention that fluxes directed away from the surface, are denoted positive, while fluxes directed towards the surface are denoted negative. The atmospheric part consists for one of the incoming and outgoing short-wave and long-wave radiation terms S_{in}, S_{out}, L_{in} and L_{out} and of the sensible heat flux Q_h and the latent heat flux Q_e, which are turbulent land-atmosphere exchange fluxes. The ground heat flux (denoted snow heat flux, when the ground is snow-covered) is the only considered flux term of the lithosphere. In the surface energy budget equation, we assume the surface to be an infinitely thin layer, where all energy reallocation processes occur. While this is certainly not true for surfaces covered with a dense canopy, e.g. for forests, it appears adequate for barren tundra surfaces with little vegetation or snow, which this thesis will deal with. A few exceptions to this rule must be made, which are discussed later. For a full description of the surface processes, the energy budget equation must be complemented by a water budget equation, which includes evapotranspiration, rain and water (and in principle water vapor) transport in the soil. The two budget equations are coupled by the latent heat flux. In this thesis, we focus on the energy budget and only strive the water budget occasionally.

The radiative terms consist of a "short-wave" part, which originates as black-body radiation from the sun, and a "long-wave" part, which originates from black-body radiation of the earth surface as well as radiation emitted by the

atmosphere. The distinction is feasible, as the two spectral ranges are well separated. The short-wave radiation is typically defined as the spectral range from approximately 300 to 2800 nm, while the long-wave radiation comprises the range from 5 to 50 μm.
The incoming and outgoing short-wave radiation are related through the surface albedo $\alpha = S_{\text{out}}/S_{\text{in}}$, which typically is in the range of 0.1 to 0.2 for snow-free surfaces and 0.6 to 0.8 for snow. The outgoing long-wave radiation mainly originates from the blackbody radiation of the surface, which according to Stefan-Boltzmann Law is $\sigma_{\text{sb}} T_{\text{surf}}^4$. However, the emission and absorption characteristics of natural surfaces are generally different from a black body, which is accounted for by the emissivity ε in Kirchhoff's law

$$L_{\text{out}} = \varepsilon \sigma_{\text{sb}} T_{\text{surf}}^4 - (1 - \varepsilon) L_{\text{in}} \, . \tag{2.2}$$

The surface emissivity in principle depends on the wavelength, but for our application, a bulk formulation with a spectrally averaged emissivity is sufficient. Therefore, we will refer to the spectrally averaged emissivity only as emissivity, unless stated otherwise. The emissivity is a property of the surface material and can thus vary. Typical surface emissivities are between 0.96 (dry grass) and 0.99 (snow). Therefore, the surface energy budget equation can be written as

$$0 = (1 - \alpha) S_{\text{in}} + \varepsilon L_{\text{in}} + \varepsilon \sigma_{\text{sb}} T_{\text{surf}}^4 + Q_h + Q_e + Q_g \, . \tag{2.3}$$

When the ground is snow-covered, the governing surface energy budget equation is essentially the same, with three notable exceptions:

1. Short-wave radiation is known to penetrate a snow cover to a depth of more than 0.5 m (e.g. Brandt and Warren, 1993), so that the energy is distributed over a whole slab. Although most of the energy is delivered in the first centimeters, the concept of an infinitely small surface layer, in which the redistribution of energy occurs, is clearly violated in this case. If the snow pack is shallow, the short-wave radiation can even penetrate to the ground surface, which has a much smaller albedo than the snow, and melt the snow pack from the bottom.

2. When the perennial snow pack melts, the melt water from the upper layers percolates into the snow pack and may refreeze at the bottom, thus distributing the energy throughout the snow pack. Hence, a redistribution of energy occurs over the entire snow pack (in combination with the above mentioned penetration of short-wave radiation).

3. A similar situation occurs, when rain falls on the snow pack in winter, percolates down and refreezes at a certain depth. To some degree, these rain-on-snow events can be included in the definition of the snow heat flux (see Sect. 4.1.3)

While it is principally possible to model these situations, the solution would be highly dependent on a number of generally unknown and spatially variable properties, such as the stratification of the snow pack, the grain size, internal ice layers and layers with high contamination of soot. Therefore, we introduce the

energy consumption of the snow pack as a storage term, which can be formally expressed as a flux term. In the snow melt period, the additional term Q_{melt} is added to the surface energy budget equation (see Sect. 4.6).

2.2 Ground thermal regime

In this section, the governing equations for heat transfer into the soil are derived, loosely following Jury and Horton (2004). The focus is put on the representation of soil freezing processes, which are crucial to understand and model the heat transfer in permafrost soils.

2.2.1 Conductive heat transfer

We consider a slab of soil of volume V. Its internal energy $E(t)$ is given by

$$E(t) = \int_V e(\vec{x}, t) \, , \tag{2.4}$$

where the volume integration must be understood as integration over elementary volumes in which local thermodynamic equilibrium is assumed, so that the definition of a local temperature $T(\vec{x}, t)$ and associated internal energy per unit volume $e(\vec{x}, t)$ is meaningful. From conservation of energy, it follows that the change of the internal energy of the slab over time is equal to the energy flux $\vec{j_e}(\vec{x}, t)$ through the surface S of the slab.

$$\frac{d}{dt} E(t) = \int_V \frac{d}{dt} e(\vec{x}, t) = - \oint_S \vec{j_e}(\vec{x}, t) \cdot \vec{n} = - \int_V \vec{\nabla} \cdot \vec{j_e}(\vec{x}, t) \, . \tag{2.5}$$

Hereby, $\vec{n}$ denotes the unit vector normal to the surface of S and we have used Gauss's theorem in the final step. The equation must be satisfied at any point in V, so that one obtains

$$\frac{d}{dt} e(\vec{x}, t) + \vec{\nabla} \cdot \vec{j_e}(\vec{x}, t) = 0 \, . \tag{2.6}$$

In case of permafrost soil, the internal energy e depends on the temperature T and the volumetric fractions $\theta_{w,i,a,m}$ of water, ice, air and of the solid matrix. Here, the solid matrix is assumed to consist of minerals, which is a good assumption for the soil in the study area (Roth and Boike, 2001), but it may also contain an organic fraction. In case of constant volumetric fractions, the equation becomes

$$\frac{de}{dt} = \frac{\partial e}{\partial T} \frac{\partial T}{\partial t} = c_h \frac{\partial T}{\partial t} \, . \tag{2.7}$$

The specific volumetric heat capacity c_h can be expressed by the specific volumetric heat capacities $c_{w,i,a,m}$ of the soil constituents as

$$c_h = \theta_w c_w + \theta_i c_i + \theta_a c_a + \theta_m c_m \, . \tag{2.8}$$

However, the volumetric fractions $\theta_{w,i,a,m}$ are usually not constant in the soil, but change e.g due to infiltration of water as well as phase change of soil water. In the following, the phase transition from the liquid to the gaseous phase is not

considered, so that only freezing of water and melting of ice in the soil must be accounted for. We first omit infiltration and allow only for freezing processes, so that θ_a, θ_m and the sum of θ_w and θ_i are constant. In soil, the freezing of water does not occur at the freezing temperature T_f of free water, but the interfacial energy between water and the solid matrix (the matric potential, i.e. the energy per unit volume of liquid water required to bring it in the porous medium) facilitates the existence of unfrozen water at temperatures well below T_f. If the temperature is decreased below T_f, the water in the largest voids will freeze first, while the water in smaller voids remains unfrozen due to the higher matric potential. This leads to a functional dependence between unfrozen water content θ_w and temperature, the so-called soil freezing characteristic, which depends on the soil texture. In fine-textured material, such as clay, the unfrozen water content at a specific temperature is higher compared to coarse-textured soils, such as sand or gravel. In the following, we assume $T_f = 0°\mathrm{C}$ and define $e = 0$ at $T = 0°\mathrm{C}$ and all water in the liquid phase. We can now rewrite Eq. 2.6 to

$$\begin{aligned} \frac{de}{dt} &= \frac{\partial e}{\partial T}\frac{\partial T}{\partial t} + \frac{\partial e}{\partial \theta_w}\frac{\partial \theta_w}{\partial T}\frac{\partial T}{\partial t} + \frac{\partial e}{\partial \theta_i}\frac{\partial \theta_i}{\partial T}\frac{\partial T}{\partial t} \\ &= c_h(T)\frac{\partial T}{\partial t} + c_w T\frac{\partial \theta_w}{\partial T}\frac{\partial T}{\partial t} + (-\rho_w L_{\mathrm{sl}} + c_i T)(-1)\frac{\partial \theta_w}{\partial T}\frac{\partial T}{\partial t}\,, \end{aligned} \tag{2.9}$$

where c_h is now a function of temperature due to the changing ice and water contents. Furthermore, we have used the relation $\partial\theta_w/\partial T + \partial\theta_i/\partial T = 0$, which is obtained by differentiating $\theta_w + \theta_i = \text{const}$. As the volumetric latent heat of fusion $\rho_w L_{\mathrm{sl}}$ is much greater than $(c_w - c_i)\,T$ at reasonable temperatures, we can omit this term and define an effective volumetric heat capacity

$$c_{\mathrm{eff}}(T) = c_h(T) + \rho_w L_{\mathrm{sl}}\frac{\partial \theta_w}{\partial T}\,, \tag{2.10}$$

which accounts for the phase change in terms of an increased heat capacity at temperatures below 0°C.
If the volumetric fractions are constant and mass fluxes of liquid water do not occur, the energy flux $\vec{j}_e$ is a purely conductive heat flux. The conductive ground heat flux, which we denote $\vec{j}_g$, is given by Fourier's law of heat conduction as

$$\vec{j}_g = -K_h(T)\,\vec{\nabla}T\,, \tag{2.11}$$

where K_h is the isotropic thermal conductivity of the soil. In soil, K_h is an effective value accounting both for the "true" conductivity and the diffusion of water vapor and thus latent heat, which enhances the heat flux particularly at higher temperatures. As the heat capacity, it has a functional dependence on the volumetric fractions of the constituents and thus on the temperature T (see Sect. 2.2.4).
The heat conduction in soil is approximated as a one-dimensional problem with a temperature gradient only in z-direction. From Eqs. 2.6, 2.9 and 2.11, we obtain the governing equation for the heat transfer in soil including freezing of soil water

$$c_{\mathrm{eff}}(z,T)\frac{\partial T}{\partial t} - \frac{\partial}{\partial z}\left(K_h(z,T)\frac{\partial T}{\partial z}\right) = 0\,. \tag{2.12}$$

If the conductivity K_h is constant with depth, an effective thermal diffusivity d_h can be defined as

$$d_h(z,t) = \frac{K_h(z,T)}{c_{\text{eff}}(z,T)}\,, \tag{2.13}$$

so that a diffusion equation for temperature is obtained

$$\frac{\partial T}{\partial t} - d_h(z,T)\frac{\partial^2 T}{\partial z^2} = 0\,. \tag{2.14}$$

However, the thermal conductivity is not necessarily constant in the region of a freeze front, where steep gradients of the soil water and ice content exist, so that Eq. 2.12 must be solved for accurate permafrost modeling.

From Eq. 2.9, we can calculate the change in the internal energy between two points in time, t_1 and t_0, as

$$e(t_1) - e(t_0) = \rho_w\, L_{\text{sl}}\, [\theta_w(T(t_1)) - \theta_w(T(t_0))] + \int_{T(t_0)}^{T(t_1)} c_h(T)\, dT\,. \tag{2.15}$$

Note that this relation only holds if the sum of water and ice content is constant, not in case of changing water content through infiltration. Furthermore, as stated above, a potential change of the water vapor concentration between t_0 and t_1 is not accounted for. Eq. 2.15 can be integrated over a volume with a temperature and soil water content distribution to yield the total internal energy content of the soil (see Sect. 2.3.1).

2.2.2 Extension to variable soil water content

In the previous paragraph, the basic equations have been derived, that are employed in this thesis for determining ground heat fluxes and modeling the soil thermal regime (Eqs. 2.12, 2.15). However, infiltration of water in the soil can occur and thus violate the assumption of purely conductive heat transfer. To understand the limitations of conductive heat transfer, it is instructive to derive the governing equation for the soil thermal budget, if infiltration of water is allowed. In this case, only θ_m is constant, and we use the following relations between water, ice and air content:

$$\theta_w = (1 - \theta_m - \theta_a)\, F(T) \tag{2.16}$$
$$\theta_i = (1 - \theta_m - \theta_a)\, [1 - F(T)] \tag{2.17}$$
$$1 = \theta_w + \theta_i + \theta_a + \theta_m \tag{2.18}$$

Assuming thermodynamic equilibrium at the scale of the formulation, the function $F(T)$ determines the freezing characteristic and hence $F(T) = 1$ for $T \geq 0°\text{C}$ and $0 \leq F(T) < 1$ for $T < 0°\text{C}$. Furthermore, the energy flux $\vec{j}_e$ is now

the sum of the conductive heat flux and energy fluxes due to the flow of air and water, $\vec{j}_{h,a}$ and $\vec{j}_{h,w}$,

$$\begin{aligned}
\vec{j}_e &= \vec{j}_g + \vec{j}_{h,w} + \vec{j}_{h,a} && (2.19)\\
\vec{j}_g &= -K_h(T)\,\vec{\nabla}T && (2.20)\\
\vec{j}_{h,w} &= c_w T\,\vec{j}_w && (2.21)\\
\vec{j}_{h,a} &= c_a T\,\vec{j}_a\,, && (2.22)
\end{aligned}$$

where $\vec{j}_w$ and $\vec{j}_a$ denote the flow rates of water and air per unit cross-sectional area and unit time. In the following, only flow in z-direction is considered, with the flow rates denoted j_w and j_a, respectively. Furthermore, incompressibility is assumed so that the following continuity equations for air and water are fulfilled:

$$\begin{aligned}
0 &= \frac{\partial\theta_a}{\partial t} + \frac{\partial}{\partial z}j_a && (2.23)\\
0 &= \frac{\partial\theta_w}{\partial t} + \frac{\partial\theta_i}{\partial t} + \frac{\partial}{\partial z}j_w && (2.24)
\end{aligned}$$

Subtracting Eq. 2.18 differentiated with respect to z, one obtains

$$0 = \frac{\partial}{\partial z}j_w + \frac{\partial}{\partial z}j_a\,. \qquad (2.25)$$

Starting from Eq. 2.6, we basically follow the same procedure as above and expand the term as de/dt as

$$\begin{aligned}
\frac{de}{dt} &= \frac{\partial e}{\partial T}\frac{\partial T}{\partial t} + \frac{\partial e}{\partial\theta_w}\frac{\partial\theta_w}{\partial T}\frac{\partial T}{\partial t} + \frac{\partial e}{\partial\theta_w}\frac{\partial\theta_w}{\partial\theta_a}\frac{\partial\theta_a}{\partial t} && (2.26)\\
&+ \frac{\partial e}{\partial\theta_i}\frac{\partial\theta_i}{\partial T}\frac{\partial T}{\partial t} + \frac{\partial e}{\partial\theta_i}\frac{\partial\theta_i}{\partial\theta_a}\frac{\partial\theta_a}{\partial t} + \frac{\partial e}{\partial\theta_a}\frac{\partial\theta_a}{\partial t}\\
&= \left(c_h(T) + (1-\theta_m-\theta_a)[\rho_w\,L_{\rm sl} - (c_w - c_i)\,T]\frac{\partial F(T)}{\partial T}\right)\frac{\partial T}{\partial t}\\
&+ \rho_w\,L_{\rm sl}\,[1-F(T)]\frac{\partial\theta_a}{\partial t} + (c_a - F(T)c_w - [1-F(T)]\,c_i)\;T\frac{\partial\theta_a}{\partial t}\,,
\end{aligned}$$

where the first term is equal to $c_{\rm eff}(T)\,\partial T/\partial t$ for $(c_w - c_i)T \ll \rho_w\,L_{\rm sl}$. The term $\vec{\nabla}\cdot\vec{j_e}(\vec{x},t)$ in Eq. 2.6 (assuming fluxes only in z direction) can be expanded as

$$\begin{aligned}
\frac{\partial}{\partial z}j_e &= \frac{\partial}{\partial z}j_g + \frac{\partial}{\partial z}j_{h,w} + \frac{\partial}{\partial z}j_{h,a} && (2.27)\\
&= -\frac{\partial}{\partial z}\left(K_h\frac{\partial T}{\partial z}\right) + c_w T\frac{\partial}{\partial z}j_w + c_a T\frac{\partial}{\partial z}j_a\\
&+ (c_w j_w + c_a j_a)\frac{\partial T}{\partial z}\\
&= -\frac{\partial}{\partial z}\left(K_h\frac{\partial T}{\partial z}\right) + (c_w - c_a)T\frac{\partial\theta_a}{\partial t}\\
&+ (c_w j_w + c_a j_a)\frac{\partial T}{\partial z}\,,
\end{aligned}$$

where Eqs. 2.23 and 2.25 have been used in the final step. Adding the two equations yields

$$\begin{aligned} 0 &= c_{\text{eff}} \frac{\partial T}{\partial t} - \frac{\partial}{\partial z}\left(K_h \frac{\partial T}{\partial z}\right) \\ &+ (\rho_w L_{\text{sl}} + (c_w - c_i)\, T)[1 - F(T)] \frac{\partial \theta_a}{\partial t} + (c_w j_w + c_a j_a) \frac{\partial T}{\partial z} \,. \end{aligned} \tag{2.28}$$

For positive temperatures, when the soil is unfrozen (i.e. $F(T) = 1$), the equation simplifies to

$$0 = c_{\text{eff}} \frac{\partial T}{\partial t} - \frac{\partial}{\partial z}\left(K_h \frac{\partial T}{\partial z}\right) + c_w j_w \frac{\partial T}{\partial z} \,, \tag{2.29}$$

where the term $c_a j_a \, \partial T / \partial z$ due to advection of air has been neglected. We notice that the diffusion equation is complemented by an advection or infiltration term, so that the heat transfer is no longer purely conductive. This term depends on the flow rate of water, which hence determines the degree of violation of the assumption of conductive heat transfer. Note that an effective 1D-process is assumed, where all phases are well mixed, so that the equation does not hold for infiltration through coarse block material, which can occur in permafrost regions. Eq. 2.29 does not make any statement about the nature of the water flow in the soil. For a fully coupled model of heat and water transfer, the governing equations for water flow in porous media must be included, e.g. Buckingham-Darcy law for flow in unsaturated soil or Darcy's law for flow in saturated soil (e.g. Jury and Horton, 2004).
In case of infiltration of water at subzero temperatures, where $0 \leq F(T) < 1$, the equation (using $(c_w - c_i)\, T \ll \rho_w \, L_{\text{sl}}$) can be approximated by

$$0 = c_{\text{eff}} \frac{\partial T}{\partial t} - \frac{\partial}{\partial z}\left(K_h \frac{\partial T}{\partial z}\right) + c_w j_w \frac{\partial T}{\partial z} + \rho_w L_{\text{sl}} [1 - F(T)] \frac{\partial \theta_a}{\partial t} \,, \tag{2.30}$$

which is approximately equal to

$$0 = c_{\text{eff}} \frac{\partial T}{\partial t} + \rho_w \, L_{\text{sl}} \, [1 - F(T)] \frac{\partial \theta_a}{\partial t} \tag{2.31}$$

in case of strong infiltration. Hereby, the last term describes the release of latent heat through partial refreezing of infiltrating water. In case of increasing water content, the air content θ_a decreases with time, so that the last term is negative, which is compensated by the first term and increasing temperature T. Due to the magnitude of L_{sl}, the infiltration of water at subzero temperatures can invoke a rapid step-like increase of the soil temperatures, which has frequently been recorded in permafrost areas during the snowmelt period, when water pools up in the snow pack and leads to a pressure head (Kane et al., 2001). While the qualitative effect is described by Eq. 2.31, the true nature of infiltration is more complex, as it preferentially occurs at localized spots such as cracks, thus leading to a strong spatial heterogeneity of the infiltration process.

2.2.3 Special cases

In the following, two simplified cases of heat transfer are outlined. Although the stringent assumptions are violated in real situations, they provide qualitative insight into important aspects of heat transfer in permafrost regions.

Heat transfer with periodic forcing

We consider the soil as a semi-infinite half-space with uniform thermal properties (i.e. heat capacity, thermal conductivity and thermal diffusivity). The phase change of water is excluded, so that the heat conduction can be described in terms of a simple diffusion equation for temperature

$$\frac{\partial T}{\partial t} - d_h \frac{\partial^2 T}{\partial z^2} = 0 \,. \tag{2.32}$$

We now assume $T(z,0) = T_0 = \text{const}$ as initial condition and periodic steady-state conditions $T(0,t) = T_0 + T_m \sin(2\pi f t)$ as upper boundary. Hereby, $1/f$ denotes the oscillation period, which could be one day to capture the diurnal cycle or one year for the seasonal cycle. The lower boundary is set to a constant temperature T_0, i.e. $\lim_{z \to -\infty} T(z,t) = T_0$.
The diffusion equation can then be solved by the approach

$$T(z,t) = T_0 + D(z)\, T_m \sin(2\pi f t + \delta(z)) \,, \tag{2.33}$$

where $D(z)$ represents a damping factor for the amplitude of the oscillation and $\delta(z)$ a phase shift. One obtains

$$\delta(z) = z\sqrt{\frac{\pi f}{d_h}} \tag{2.34}$$

$$D(z) = \exp\left(z\sqrt{\frac{\pi f}{d_h}}\right) \,. \tag{2.35}$$

We notice that the temperature oscillation at depth $-z$ is a sine wave damped proportional to $\exp(z)$ and features a phase shift proportional to z. The proportionality constant depends on $(f/d_h)^{1/2}$, so that a high-frequency signal decays more rapidly and experiences a stronger phase shift with depth. For a thermal diffusivity $d_h = 10^{-6}\,\mathrm{m^2 s^{-1}}$, which is in the range of typical values for soil, the daily temperature cycle would hence be damped to $1/e$ of the surface amplitude at a depth of approximately 0.2 m, while the annual cycle would experience the same amount of damping at a depth of roughly 3 m.
Although the situation is more complex in permafrost soils due to the phase change of water, the statements remain widely valid: if the thaw depth is sufficiently large, the diurnal temperature cycle decays close to the surface and only long-term average temperatures determine the temperature evolution in deeper soil layers.
In case of variable upper boundary conditions, e.g. determined by measurements of the surface temperature, a Fourier decomposition can be applied, so that the heat transfer problem can be solved as superposition of periodic solutions 2.33.

This method has been successfully applied to describe the temperature dynamics in the study area when the ground is frozen (Roth and Boike, 2001).
There exist analytical solutions for conductive heat transfer including phase change of water under periodic forcing (Kudryavtsev et al., 1974), but they still cannot incorporate the freezing characteristic of water in soil, nor can they account for soil properties varying with depth. Therefore, simulations of permafrost temperatures for real situations are best performed by numerical solving schemes for Eq. 2.12.

The Stefan solution - a "bathtub" model for the seasonal thawing of permafrost

While the last paragraph has dealt with heat conduction without freezing of soil water, the Stefan equation describes the freezing or thawing of water or soil without including the actual temperature change of the soil. Furthermore, the freezing characteristic of the soil water is not accounted for. The rate of energy consumption or release at the freeze-thaw interface, which is related to the advance rate of the thawing or freezing front, is set to be equal to the conductive ground heat flux, approximated by a linear interpolation between the surface temperature T_{surf} and freezing temperature of water T_f at the freeze-thaw interface:

$$-\rho_w L_{\mathrm{sl}} \theta_w \frac{\partial d(t)}{\partial t} = -K_h \frac{T_{\mathrm{surf}}(t) - T_f}{d(t)} \text{ for thawing} \tag{2.36}$$

$$\rho_w L_{\mathrm{sl}} \theta_w \frac{\partial d(t)}{\partial t} = -K_h \frac{T_{\mathrm{surf}}(t) - T_f}{d(t)} \text{ for freezing} \tag{2.37}$$

$d(t)$ hereby denotes the depth of the freezing or thawing front (taken to be positive) below the surface, and θ_w the water content in the unfrozen part of the soil, or the ice content in the frozen soil, respectively. The analytical solution for d is

$$d(t) = \sqrt{\frac{K_h |J(t)|}{\rho_w L_{\mathrm{sl}} \theta_w}} \tag{2.38}$$

with

$$J(t) = \int_{t_0}^{t} (T_{\mathrm{surf}}(t) - T_f)\, dt\,, \tag{2.39}$$

which can be verified by inserting in Eq. 2.36. t_0 is the time when the thawing of the frozen soil or the freezing of the unfrozen soil has begun. With $T_f = 0°C$, J is denoted the thawing index J_t (integrated from the start of thawing) and $-J$ the freezing index J_f (integrated from the start of freezing), which are typically given in terms of "degree days". The freezing and thawing index has been used in early assessments of permafrost distribution (e.g. Carlson, 1952), with permafrost present, when the depth of the seasonal freezing exceeds the depth of the seasonal thawing, i.e.

$$K_{\mathrm{h,frozen}} J_f > K_{\mathrm{h,thawed}} J_t\,. \tag{2.40}$$

Apart from the practical problem to obtain suitable records for the surface temperature for the soil domain (which in winter is strongly determined by the properties of the seasonal snow cover on top of the soil), particularly the description of refreezing with the Stefan model features a major shortcoming: in this case, two freezing fronts exist, one spreading down from the surface and one spreading up from the permanently frozen permafrost body below. While the advance of the lower freezing front could again be estimated by a Stefan approach, the temperature at a certain depth in the permafrost body must be known, which in most cases is not available.
Despite of the simplicity of the Stefan model, it illustrates two important effects of the surface temperature on the seasonal thawing and freezing process:

1. To factor out the impact of the surface temperature on the freezing and thawing of permafrost soil, the integral over the surface temperature from the beginning of the thawing/ freezing process is the relevant quantity. It allows to compare sites with different seasonal characteristics of the surface temperature and different times when the thawing and freezing begin.

2. The thaw depth is proportional to the square root of the integrated surface temperatures. While this is an extreme simplification, it is important to note, that the impact of a change in J on the thaw depth is not linear. It decreases with increasing value of J, which reflects the diminishing temperature gradient between the surface and the freeze-thaw interface with increasing depth of thaw.

2.2.4 The de Vries model for the thermal conductivity

In this section, we briefly present a modeling approach to obtain the thermal conductivity of soil from the volumetric fractions of the soil constituents water, ice, air and solid matrix, which is composed of a mineral and an organic fraction. The problem is not trivial, as the thermal conductivity of a porous medium does not only depend on its composition, but also the distribution of the phases and the geometry of the pores space. For simplicity, the soil particles are assumed to be spherical.
The thermal conductivity of a porous medium can be approximated by the following empirical formulation (de Vries, 1952)

$$K_h = \frac{\sum_n f_n \theta_n K_{\mathrm{h\,n}}}{\sum_n f_n \theta_n} \,, \tag{2.41}$$

where the summations run over the five constituents of the soil presented above. While the $K_{\mathrm{h\,n}}$ denote the thermal conductivities of pure water, ice, etc., for which literature values are available, the f_n are weighting factors that enhance or dampen the influence of a component. If all f_n were unity, the situation would be analogous to electrical resistors connected in parallel, through which flow of heat/current occurs unaffected by the neighboring phase/resistor. de Vries (1952) and Campbell et al. (1994) introduce the concept, that only one of the constituents occurs as interconnected "continuous phase" with thermal conductivity K_c, while the other constituents are conceptualized as discontinuous

phases, i.e. small domains intercepted by the continuous phase. We can now postulate the following properties for the weighting factors f_n, where K_d denotes the thermal conductivity of a discontinuous phase.

- The weighting factor f_c for the continuous phase is unity.
- For $K_d > K_c$, the heat flux through the discontinuous phase is limited by the sections, where the heat flux must pass the "eye of the needle" of the continuous phase with lower thermal conductivity. This limits the ability of the discontinuous phase to conduct heat, so that the weighting factor f_d of the discontinuous phase must be smaller than unity.
- In the limit $K_d \gg K_c$, the resulting thermal conductivity must be independent of K_d, as the heat flow is entirely limited by the sections, where it passes through the continuous phase. This requires an asymptotic form $f_d \propto (K_d)^{-1}$ (compare to Eq. 2.41).
- For $K_d < K_c$, the heat flux is concentrated through the continuous phase. Now, the discontinuous phase creates an "eye of the needle" for heat flow through the continuous phase. The weighting factor f_d must hence be greater than unity.
- In the limit $K_d \ll K_c$, the entire heat flux passes through the continuous phase, so that changing the thermal conductivity of the discontinuous phase has no effect on the resulting thermal conductivity. Hence, the condition $\lim_{K_d \to 0} f_d \, K_d = 0$ must be satisfied, e.g. by $f_d = \text{const}$.

These constraints are satisfied by the functional form for the weighting factors

$$f_n = \left[1 + \frac{1}{3} \left(\frac{K_{\mathrm{h\,n}}}{K_c} - 1 \right) \right]^{-1} , \tag{2.42}$$

which reduces the problem to determining the continuous phase. As the mineral and organic components are conceptualized as particles, only water, ice or air can constitute the continuous phase. For unfrozen soil with fixed mineral and organic, but varying water and air contents, Campbell et al. (1994) suggest a smooth transition from an air-dominated regime ($K_c = K_{\mathrm{h\,a}}$) to a water-dominated regime ($K_c = K_{\mathrm{h\,w}}$) by defining

$$K_c \; = \; K_{h\,a} + \beta_{\mathrm{aw}} (K_{h\,w} - K_{h\,a}) \tag{2.43}$$

with

$$\beta_{\mathrm{aw}} \; = \; \left[1 + \left(\frac{\theta_w}{\theta_{w0}} \right)^{-\epsilon_s} \right]^{-1} . \tag{2.44}$$

The transition between air and water as continuous phase occurs at the "liquid recirculation cutoff" θ_{w0}, and the range, over which this transition takes place, is determined by the smoothing parameter ϵ_s. Campbell et al. (1994) give values for both parameters for a range of soils that have been determined in laboratory experiments. For this thesis, we employ values of $\theta_{w0} = 0.15$ and $\epsilon_s = 4$, which

is in the range of the values given by Campbell et al. (1994) for silty and clayey soils (as predominantly found in the study area).
The concept of Eq. 2.43 can be applied to air-ice systems (i.e. zero water content) and water-ice systems (i.e. zero air content). As measurements are not available, we assume the same parameters $\theta_{i0} = \theta_{w0}$ and ϵ_s for the air-ice system as for the air-water system. For the water-ice system, the choice of β_{wi} is uncritical, as the thermal conductivities of pure water and ice are not strongly different, as it is the case for air-water and air-ice systems. We assume a linear interpolation between $K_{\mathrm{h\,w}}$ and $K_{\mathrm{h\,i}}$ according to the water and ice contents. Finally, the thermal conductivity of a soil with non-zero fractions of all constituents is obtained by interpolating between the three confining systems air-water, air-ice and water-ice, which span a three-dimensional space.
Despite this rather involved derivation, it must be emphasized that the choice of the parameterization is only one factor contributing to a considerable uncertainty in the obtained thermal conductivity. Even more severe weighs the uncertainty in determining the volumetric fractions of the constituents, particularly if average values over a larger area and/or a deep soil column are required. Furthermore, a strong uncertainty exists in case of the required thermal conductivity of a pure "organic" material (e.g Farouki, 1981).

2.3 Measurements of ground heat flux

For measuring the ground heat flux, heat flux plates are employed in most studies. Here, a plate made of a material with known thermal conductivity is inserted horizontally in the ground. The temperatures at the top and the bottom of the plate are measured, so that the ground heat flux can be evaluated from the temperature gradient. The method is satisfactory if the thermal conductivity of the heat flux plate is equal or at least close to the thermal conductivity of the soil. If this is not the case, the assumption of 1D-heat flow inherent in the idea of the heat flux plates breaks down. This problem is particularly severe in permafrost-dominated soil, where the temperature gradients can be extreme. An additional problem is the accumulation of ice in the voids around the heat flux plates, which can alter the heat flux. Furthermore, it is highly difficult to achieve an adequate quality assessment for ground heat fluxes obtained with heat flux plates. For this thesis, we therefore do not make use of heat flux plates, but employ two alternative methods.

2.3.1 Calorimetric method

If one is interested in average ground heat fluxes over longer periods of a few weeks or months, it is feasible to make use of the difference over time in the total internal energy $E(t)$ of the soil. For this, Eq. 2.15 is integrated over the soil column between the surface $z = 0$ and $z = z_b$, below which the internal energy does not change between times t_1 and t_2:

$$E(t_2) - E(t_1) = \rho_w L_{\mathrm{sl}} \int_{z_b}^{0} [\theta_w(T(t_2, z)) - \theta_w(T(t_1, z))]\, dz + \int_{z_b}^{0} \int_{T(t_1)}^{T(t_2)} c_h(T, z)\, dT\, dz \tag{2.45}$$

For the applicability of Eq. 2.45, it is important that only changes in the water content due to freezing or thawing of are considered, not due to infiltration. Therefore, the evaluation of the first term must be restricted to temperatures below 0°C. Complications arise in case of infiltration in frozen soil, when the formula is no longer applicable in a strict sense, as it is not possible to differentiate between infiltrated water and water from thawed ice. However, infiltration is normally restricted to the uppermost soil layer, so that the error is bearable. The average ground heat flux through the surface can then be calculated as

$$j_{g,av} = \frac{E(t_2) - E(t_1)}{t_2 - t_1}\,, \tag{2.46}$$

if one assumes the flux through the lower boundary at $z = z_b$ to be zero. This is fulfilled to a very good approximation, if z_b is chosen sufficiently deep. In this case, the ground heat flux is close to the geothermal heat flux, which is on the order of 10^{-2} to $10^{-1}\,\mathrm{Wm}^{-2}$ and thus negligible compared to normal average values of the ground heat flux. For this thesis, only rather shallow temperature and soil moisture profiles within the active layer to a depth of $z_b \approx 1.5\,\mathrm{m}$ are available, so that the non-zero flux through the lower boundary constitutes a major source of error.
For the evaluation of the soil water content, a profile of Time-Domain-Reflectometry (TDR) measurements is employed. The technique used to evaluate the soil water and ice contents during the winter is described in Boike et al. (2003b). The specific heat capacity $c_h(T)$ is then evaluated as

$$c_h(T) = \theta_w(T)\, c_w + \theta_i(T)\, c_i + \theta_m\, c_m + \theta_a\, c_a\,. \tag{2.47}$$

If the freeze curve $\theta_w(T)$ is known, the integral in Eq. 2.45 can be evaluated. In practice, most of the energy is consumed by the phase transition of the soil water, so that the impact of changing heat capacities on the evaluation of the ground heat flux is rather limited.

2.3.2 Conductive method

The second method makes use of times series of soil temperature measurements. A profile of three temperature sensors at depths z_1, z_2 and z_3, $z_1 > z_2 > z_3$ beneath each other yields the time series $T_{\mathrm{meas}}(z_1, t)$, $T_{\mathrm{meas}}(z_2, t)$ and $T_{\mathrm{meas}}(z_3, t)$.

To calculate the ground heat flux

$$j_g(z, t) \;=\; -K_h(z, t)\, \frac{\partial}{\partial z} T(z, t)\,, \tag{2.48}$$

the first step is to evaluate the thermal conductivity K_h of the soil or snow. We assume a conductive 1D-heat transport and constant thermal conductivity and heat capacity between z_1 and z_3 and over the considered period. Furthermore, periods are excluded when a phase change of water occurs between z_1 and z_3. We then numerically solve Eq. 2.14 with $T_{\mathrm{meas}}(z_1, t)$ and $T_{\mathrm{meas}}(z_3, t)$ as Dirichlet boundary conditions. The initial condition is chosen as a linear interpolation between the first two data points of the boundary conditions. In this case, the exact choice of the initial condition is not critical, since the solution converges to a value independent of the initial condition after few time steps. The numerical solution of Eq. 2.14 is performed with the partial differential equation solver of MATLAB (Skeel and Berzins, 1990), yielding the modeled times series of temperatures for a given d_h, $T_{d_h}(z_2, t)$, for all values of z_2 with $z_1 > z_2 > z_3$.
With $T_{\mathrm{meas}}(z_2, t)$, we can perform a least-square fit for d_h by minimizing the RMS error between $T_{\mathrm{meas}}(z_2, t)$ and $T_{d_h}(z_2, t)$. This method relies on rapid temperature changes which induce a time lag of the surface temperature signal in deeper soil layers characteristic for a certain d_h (see Sect. 2.2.3). In the summer period, when a strong diurnal temperature signal exists, the method generally works at the study site for depths of $z_1 \approx -0.01\,\mathrm{m}$, $z_2 \approx -0.15\,\mathrm{m}$ and $z_3 \approx -0.30\,\mathrm{m}$. The same procedure is used by Putkonen (1998), and the basic idea of obtaining soil properties from a time series of temperature measurements is extended by Nicolsky et al. (2007) and Nicolsky et al. (2009).
With the heat capacity c_h of the soil determined from the volumetric fractions θ_w and θ_m in soil samples (or θ_i in snow samples), the thermal conductivity K_h can be evaluated as $K_h = c_h d_h$. The heat flux $j_g(z_1, t)$ through the upper boundary is then calculated by

$$j_g(z_1, t) \;=\; -K_h(z_1, t)\, \frac{\partial}{\partial z} T(z, t)|_{z=z_1}\,. \tag{2.49}$$

Note that the required derivative of the temperature can be easily evaluated from the numerical solution of Eq. 2.14 which delivers the full temperature field between z_1 and z_3.
Although convective heat transport, e.g. through infiltrating rain water, is not accounted for in the conductive method, the inherent assumption of a purely conductive heat transfer has been shown to be adequate for the study area during winter (Roth and Boike, 2001), a site approximately 10 km from the study area (Putkonen, 1998) and for other permafrost areas (e.g. Romanovsky and Osterkamp, 1997).

2.4 Boundary Layer Physics

Unlike the energy transfer in the soil, which is mainly determined by heat conduction, the energy transfer in the lowest part of the troposphere, the so-called atmospheric boundary layer, is largely accomplished by turbulent motion of air parcels. The boundary layer is the part of the atmosphere, where the effects of surface friction and surface heating play a role. Above the boundary layer, in the free atmosphere, the flow is largely controlled by non-turbulent geostrophic conditions, while turbulence only occurs intermittently.
In the following, the basic framework for the description of turbulent land-atmosphere exchange processes is outlined (following Stull, 1988; Kraus, 2008). As this thesis is focused on surface processes in permafrost regions, we restrict ourselves to the lowest part of the boundary layer, the so-called Prandtl layer, which typically comprises a few tens of meters above the surface.

2.4.1 Basic equations

The set of equations governing the transport of heat and mass (both air and water vapor) in the boundary layer is:

1. The continuity equation for mass

$$\frac{\partial \rho_a}{\partial t} + \sum_k \frac{\partial}{\partial x_k}(\rho_a u_k) = 0\,, \tag{2.50}$$

   where ρ_a denotes the density and $\vec{u}$ the velocity of an air parcel.

2. The gas law:

$$p = R_w \rho_a T = R_d\,(1 + 0.61q)\,\rho_a T = R_d \rho_a T_v \tag{2.51}$$

   The gas constant R_w of moist air in the gas law depends on the concentration q of water vapor (in units of kg of water vapor per kg of dry air), as the molar mass of water vapor and the mean molar mass of dry air differ by a factor of 1.61. This leads to the definition of the virtual temperature $T_v = T\,(1 + 0.61q)$, which is the temperature a parcel of dry air must be heated to in order to have the same density as a parcel of moist air at pressure p.

3. The thermodynamic equation:
   To account for the changing pressure with height, it is convenient to define the potential temperature Θ, which follows from Poisson's equation as

$$\Theta = T\left(\frac{p_0}{p}\right)^{R_d/c_p}\,. \tag{2.52}$$

   The potential temperature is the temperature that a parcel of dry air at pressure p would have, if it were compressed or expanded adiabatically to

pressure p_0. The potential temperature is a conservative property for adiabatic processes, which simplifies the description of vertical transport. In a similar way, the virtual potential temperature Θ_v can be defined, which is the temperature that a parcel of moist air at pressure p would have, if it were compressed or expanded adiabatically to pressure p_0. The potential temperature is used to classify the stratification of the atmosphere in neutral ($\partial\Theta/\partial z = 0$), stable ($\partial\Theta/\partial z > 0$) and unstable conditions ($\partial\Theta/\partial z < 0$).
The first law of thermodynamics

$$Tds = c_p dT - \frac{1}{\rho_a} dp \tag{2.53}$$

can hence be written as

$$c_p \, d\Theta = \frac{\Theta}{T} T \, ds \, , \tag{2.54}$$

where the left side is equal to the differential of the enthalpy, the so-called sensible heat. The term $T\,ds$ on the left side represents the generation or dissipation of heat, which is accounted for by a bulk source term χ_H, to which four terms can contribute: the divergence of the radiative flux, corresponding to radiative warming or cooling of the air; the divergence of the heat transport through molecular diffusion; the dissipation of kinetic energy in heat through viscous friction, which is strictly positive (i.e. it always generates heat); the release or generation of latent heat through phase changes of water.
We can now formulate the budget equation for the sensible heat content of air as

$$\rho_a c_p \frac{d\Theta}{dt} = \rho_a c_p \frac{\partial \Theta}{\partial t} + \sum_k \rho_a c_p u_k \frac{\partial \Theta}{\partial x_k} = \chi_H \, , \tag{2.55}$$

where the left side represents the change of the sensible heat content, divided in the local change and advection of sensible heat.

4. The humidity equation:

$$\frac{dq}{dt} = \frac{\partial q}{\partial t} + \sum_k u_k \frac{\partial q}{\partial x_k} = \chi_W \tag{2.56}$$

The total change of the concentration of water vapor can again be divided in the local change and an advection term, while a bulk source term χ_W is introduced in analogy to χ_H. It accounts for both molecular diffusion of water vapor and for condensation or evaporation.

5. The Navier-Stokes equations:
The equations of motion for an air parcel are given by

$$\begin{aligned} \rho_a \frac{du_i}{dt} &= \rho_a \frac{\partial u_i}{\partial t} + \sum_k \rho_a u_k \frac{\partial u_i}{\partial x_k} \\ &= -\frac{\partial p}{\partial x_i} - \delta_{i3} \rho_a g - \sum_{j,k} \varepsilon_{ijk} f_j \rho_a u_k + \mu \frac{\partial^2 u_i}{\partial x_k^2} \, . \end{aligned} \tag{2.57}$$

As in the two previous equations, the change of the velocity vector can be separated in the local change and an advection term. The right side describes the acceleration due to pressure gradients, gravity, the Coriolis force (using the Coriolis parameter $\vec{f}$) and the force due to viscous molecular friction (using the dynamic viscosity μ). The latter dissipates kinetic energy into heat, which contributes to the bulk source term χ_H in the the thermodynamic equation 2.55.
Adding the continuity equation (Eq. 2.50) multiplied by u_i yields the budget equation for the momentum per unit volume:

$$\begin{aligned} &\frac{\partial(\rho_a u_i)}{\partial t} + \sum_k \frac{\partial(\rho_a u_k u_i)}{\partial x_k} \\ =& -\frac{\partial p}{\partial x_i} - \delta_{i3}\rho_a g - \sum_{j,k} \varepsilon_{ijk} f_j \rho_a u_k + \mu \frac{\partial^2 u_i}{\partial x_k^2} \end{aligned} \tag{2.58}$$

2.4.2 Reynolds decomposition

The study of turbulent flows is focused on statistical properties, as a full description of the phase space is neither feasible nor desirable. Following Reynolds (1895), we assume that a property s can be decomposed in a mean flow component $\overline{s}$ and a rapidly varying turbulent component s' as

$$s = \overline{s} + s' \,, \tag{2.59}$$

which satisfies the following relations:

$$\overline{s'} = 0 \tag{2.60}$$
$$\overline{sw} = \overline{s}\,\overline{w} + \overline{s'w'} \tag{2.61}$$
$$\overline{s+w} = \overline{s} + \overline{w} \tag{2.62}$$
$$\overline{\overline{s}} = \overline{s} \tag{2.63}$$
$$\overline{bs} = b\,\overline{s} \quad \text{for } b = \text{const} \tag{2.64}$$
$$\overline{\frac{\partial s}{\partial \alpha}} = \frac{\partial \overline{s}}{\partial \alpha} \tag{2.65}$$

We consider three types of averaging procedures:

1. The statistical ensemble average, i.e. the average over all possible states of the system:

$$\overline{s} = \overline{s(\vec{x},t)} = \lim_{N\to\infty} N^{-1} \sum_{i=1}^{N} s_i(\vec{x},t) \tag{2.66}$$

The ideal ensemble average cannot be realized in measurements. Therefore, ergodicity must be invoked to replace the ensemble average by time-averaging or spatial averaging.

2. The time average:

$$\overline{s_T(\vec{x})} = T^{-1} \int_0^T s(\vec{x}, t) dt \tag{2.67}$$

In a strict sense, the time average is only equal to the ensemble average in the infinity limit of the averaging period, where the process is assumed ergodic. In measurements, the time average is always a compromise between an acceptable averaging time and the at least partial violation of ergodicity.

3. The spatial line average:

$$\overline{s_x(y, z, t)} = l^{-1} \int_0^l s(\vec{x}, t)\, dx \tag{2.68}$$

The same restrictions as for the time average apply.

The different averaging procedures will play a role in the discussion of turbulence measurements with the eddy covariance method and other techniques (see Sects. 2.5.2, 4.2.8, 5.1.2).

2.4.3 The simplified mean equations for the Prandtl layer

Thermodynamic equation

We apply a Reynolds decomposition with $\Theta = \overline{\Theta} + \Theta'$ and $u_i = \overline{u_i} + u_i'$, using Eqs. 2.60 ff:

$$\begin{aligned} \overline{\chi_H} = & \quad \overline{\frac{\partial \Theta}{\partial t} + \sum_k u_k \frac{\partial \Theta}{\partial x_k}} = \frac{\partial \overline{\Theta}}{\partial t} + \sum_k \overline{u_k} \frac{\partial \overline{\Theta}}{\partial x_k} + \overline{u_k' \frac{\partial \Theta'}{\partial x_k}} \\ = & \quad \frac{\partial \overline{\Theta}}{\partial t} + \sum_k \overline{u_k} \frac{\partial \overline{\Theta}}{\partial x_k} + \frac{\partial}{\partial x_k}(\overline{u_k' \Theta'}) - \overline{\Theta' \frac{\partial u_k'}{\partial x_k}} \end{aligned} \tag{2.69}$$

The fluctuations of the bulk source term χ_H in Eq. 2.55 have been assumed small, so that covariances of fluctuations of the terms represented by χ_H are negligible. The last term is zero, as the air can be assumed an incompressible fluid, so that the divergence of the velocity (and hence of the velocity fluctuations) vanishes. The covariance term $\overline{w'\Theta'}$ is proportional to the turbulent vertical flux of sensible heat $Q_h = c_p \rho_a \overline{w'\Theta'}$, which can thus be inferred from high-frequency measurements of the vertical wind speed and the potential

temperature with an eddy covariance system, if time averaging is employed to calculate the covariances.
Assuming spatial homogeneity of all variables (i.e. $\partial/\partial x = 0$, $\partial/\partial y = 0$) and $\overline{v} = \overline{w} = 0$, the equation simplifies to

$$\frac{\partial \overline{\Theta}}{\partial t} = -\frac{\partial}{\partial z}(\overline{w'\Theta'}) + \overline{\chi_H} \,. \tag{2.70}$$

It is not possible to solve this equation for the mean temperature even for $\chi_H = 0$, as this would require knowledge of the fluctuating terms Θ' and w'. One therefore has to find a parameterization of $\overline{w'\Theta'}$ in terms of the average quantities $\overline{\Theta}$ and $\overline{w}$, which is necessarily a "physically-based guess" and ultimately has to be confirmed by experiment. The problem that arises from averaging statistically dependent quantities, is referred to as the turbulence closure problem. The most commonly used parameterization is the K-approach

$$\overline{w'\Theta'} = -K_H \frac{\partial \overline{\Theta}}{\partial z} \,, \tag{2.71}$$

where the eddy thermal diffusivity K_H can depend on both height and time. It is clear, that Eq. 2.70 reduces to a diffusion-like problem, which in principle can be solved if the functional dependencies of K_H (and the bulk source term χ_H) are known.

Humidity equation

The same procedure can be applied to the humidity equation 2.56, where the fluctuations of the source term χ_W are again assumed negligible:

$$\overline{\chi_W} = \frac{\partial \overline{q}}{\partial t} + \sum_k \overline{u_k} \frac{\partial \overline{q}}{\partial u_k} + \frac{\partial}{\partial x_k}(\overline{u_k' q'}) \,, \tag{2.72}$$

with the covariance term $\overline{w'q'}$ being proportional to the turbulent vertical flux of latent heat $Q_e = \rho_a L_{lg} \overline{w'q'}$. In case of spatial homogeneity and $\overline{v} = \overline{w} = 0$, the equation simplifies to

$$\frac{\partial \overline{q}}{\partial t} = -\frac{\partial}{\partial z}(\overline{w'q'}) + \overline{\chi_W} \,, \tag{2.73}$$

for which the K-approach is

$$\overline{w'q'} = -K_W \frac{\partial \overline{q}}{\partial z} \,. \tag{2.74}$$

Navier-Stokes equations

We repeat the same steps for the Navier-Stokes equations 2.57, and apply the so-called Boussinesq approximation (e.g Stull, 1988): density fluctuations can be neglected ($\rho_a \approx \overline{\rho_a}$), unless they directly affect buoyancy, i.e. only terms containing density fluctuations and the gravitational constant g are retained.

The latter is not the case in the Navier-Stokes equations, which can hence be written in average form as

$$\overline{\rho}_a \frac{\partial \overline{u_i}}{\partial t} + \sum_k \overline{\rho}_a \, \overline{u_k} \frac{\partial \overline{u_i}}{\partial x_k} + \overline{\rho}_a \frac{\partial}{\partial x_k} (\overline{u_k' u_i'}) \tag{2.75}$$
$$= - \frac{\partial \overline{p}}{\partial x_i} - \delta_{i3} \overline{\rho}_a g - \sum_{j,k} \overline{\rho}_a \varepsilon_{ijk} f_j \, \overline{u_k} + \mu \overline{\frac{\partial^2 u_i}{\partial x_k^2}} \, .$$

The covariance term $\overline{u'w'}$ (mean wind in x direction) represents the effect of surface friction through turbulent motion and gives rise to the definition of the friction velocity u_* with $u_*^2 = -\overline{u'w'}$. The last term containing the effects of viscous friction is generally neglected, and the Coriolis terms $-\overline{\rho}_a \varepsilon_{ijk} \, f_j \, \overline{u_k}$ are negligible close to the surface in the Prandtl layer, where the surface-induced friction by turbulent motion dominates. However, the Coriolis force becomes important above the Prandtl layer, where it causes a rotation of the mean wind direction (the so-called Ekman-spiral), until geostrophic wind conditions are reached at the top of the atmospheric boundary layer. In this case, the friction velocity is essentially zero, so that the remaining Coriolis force and the force due to the horizontal pressure gradient balance each other in the steady-state case, which results in the geostrophic wind parallel to the isobars.
For the horizontally homogeneous Prandtl layer and $\overline{v} = \overline{w} = 0$, the equations again simplify to:

$$\frac{\partial \overline{u}}{\partial t} = - \frac{\partial}{\partial z} (\overline{w'u'}) \tag{2.76}$$
$$\frac{\partial \overline{v}}{\partial t} = 0 \tag{2.77}$$
$$0 = \frac{\partial \overline{w}}{\partial t} = - \overline{\rho}_a^{-1} \frac{\partial \overline{p}}{\partial z} - g \tag{2.78}$$

The vertical equation is the hydrostatic equation, which is a very good approximation for the vertical distribution of the mean pressure in the atmosphere. The K-approach for the horizontal equation is

$$\overline{w'u'} = -u_*^2 = -K_M \frac{\partial \overline{u}}{\partial z} \, . \tag{2.79}$$

The logarithmic wind profile for neutral atmospheric stratifications

The most simple parameterization for K_M has been formulated in the mixing length theory by Prandtl (1925), which is only applicable under neutral conditions, i.e. $\partial \Theta / \partial z = 0$, when the turbulence is not influenced by buoyancy effects. The eddy diffusivity K_M has the dimension of velocity times length. It is therefore plausible, that K_M is proportional to the friction velocity u_* and the height z above the surface. Adopting this ansatz, Eq. 2.79 yields

$$u_*^2 = \kappa u_* z \frac{\partial \overline{u}}{\partial z} \, . \tag{2.80}$$

The proportionality constant κ is the von Kármán-constant which is determined to be 0.4 from measurements (e.g. Foken, 2008a). Assuming zero mean horizontal wind speed at a height z_0, which is denoted the roughness length, as lower boundary condition, a logarithmic wind profile is obtained

$$\overline{u}(z) = \frac{u_*}{\kappa} \ln \frac{z}{z_0} \,. \tag{2.81}$$

While the logarithmic wind profile has not been strictly derived, it is well confirmed in measurements under neutral atmospheric stratification conditions (e.g. Foken, 2008a). The roughness length is a property of the surface material and structure. Typical literature values range from 10^{-5} m for smooth snow surfaces to a few meters in case of a forest. When eddy covariance measurements of the friction velocity u_* and of the mean horizontal wind speed $\overline{u}$ are available under neutral atmospheric stratifications, the roughness length z_0 can be calculated from Eq. 2.81.

Before the functional dependencies for the K-factors under non-neutral atmospheric stratifications can be approached, some basic considerations on turbulence are required.

2.4.4 Turbulent kinetic energy (TKE)

The average kinetic energy per unit volume of an air parcel moving in direction i, $\frac{1}{2}\overline{\rho_a u_i^2}$, can be expressed as

$$\frac{1}{2}\overline{\rho_a u_i^2} = \frac{1}{2}\overline{\rho_a}\,\overline{u_i}^2 + \frac{1}{2}\overline{\rho_a u_i'^2} + \overline{u_i}\,\overline{\rho_a' u_i'} \,, \tag{2.82}$$

where the first term on the right side represents the kinetic energy of the mean flow, the second term the kinetic energy of the turbulent flow (denoted TKE) and the third term can be neglected due to the Boussinesq approximation (see Sect. 2.4.3). In the following, the TKE term is discussed.
Multiplying Eq. 2.58 with u_i', averaging and applying some algebraic manipulations (e.g. Businger, 1982), we obtain the TKE equation which is fundamental for stability considerations in the boundary layer:

$$\begin{aligned}\frac{\partial}{\partial t}\left(\frac{1}{2}\overline{\rho_a u_i'^2}\right) = &- \underbrace{\delta_{i3}\, g\, \overline{\rho_a' u_i'}}_{(1)} + \sum_{j,k} \overline{\rho_a' u_i'}\left(\frac{\partial \overline{u_i}}{\partial t} + 2\varepsilon_{ijk}\omega_j \overline{u_k}\right) - \underbrace{\overline{(\rho_a u_k)' u_i'}\frac{\partial \overline{u_i}}{\partial x_k}}_{(2)} \\ &+ \mu \frac{\partial}{\partial x_k}\left(\overline{u_i' \frac{\partial u_i'}{\partial x_k}}\right) - \underbrace{\mu \overline{\left(\frac{\partial u_i'}{\partial x_k}\right)^2}}_{(3)} - \underbrace{\overline{u_k' \frac{\partial p'}{\partial x_k}}}_{(4)} - \underbrace{\frac{\partial}{\partial x_k}\left(\overline{\rho_a u_k \frac{1}{2} u_i'^2}\right)}_{(5)}\end{aligned} \tag{2.83}$$

Only the marked terms play a significant role as sources or sinks of TKE in the boundary layer and will be discussed in detail, while the other terms are generally neglected (e.g. Stull, 1988).

1. **Production or destruction of TKE through buoyancy**: This term is only effective in vertical direction and corresponds to the turbulent vertical mass flux density $\overline{\rho_a' w'}$ times the acceleration due to gravity g. Note that it is retained in the Boussinesq approximation (see Sect. 2.4.3). In case of an unstable atmospheric stratification ($\partial\Theta/\partial z < 0$), a negative $\overline{\rho_a' w'}$ stems from turbulence elements, which correspond to a combination of $\rho_a' < 0$ (the volume element is lighter than the elements in its environment) and $w' > 0$ (the volume element moves up), or $\rho_a' > 0$ (the volume element is heavier than the elements in its environment) and $w' < 0$ (the volume element moves down). Therefore, the volume elements are further accelerated by buoyancy forces, which leads to an increase in TKE. In stable atmospheric stratifications ($\partial\Theta/\partial z > 0$), the volume elements are decelerated by buoyancy forces accordingly for $\overline{\rho_a' w'} > 0$, so that TKE is dissipated. Using Eqs. 2.51 and 2.52 and the definitions of the virtual temperature, sensible heat flux $Q_h = \overline{\rho}_a c_p \overline{w'\Theta'}$ and latent heat flux $Q_e = \overline{\rho}_a L_{\mathrm{lg}} \overline{w'q'}$, the following relations are obtained

$$\frac{\rho_a'}{\overline{\rho}_a} = \frac{p'}{\overline{p}} - \frac{T_v'}{\overline{T_v}}\,,\ \frac{\Theta'}{\overline{\Theta}} = \frac{T'}{\overline{T}} - \frac{R_d}{c_p}\frac{p'}{\overline{p}}\,,\ T_v' = \left(\overline{T} + T'\right)(1 + 0.61(\overline{q} + q')) - \overline{T_v}\,, \tag{2.84}$$

which are used to simplify

$$\begin{aligned} g\overline{\rho_a' w'} &\approx -g\frac{\overline{\rho}_a}{\overline{T_v}}\overline{\left[\left(\overline{T} + T'\right)(1 + 0.61(\overline{q} + q')) - \overline{T_v}\right] w'} && (2.85)\\ &\approx -g\frac{\overline{\rho}_a}{\overline{T_v}}\left[\frac{\overline{T_v}}{\overline{\Theta}}\overline{\Theta' w'} + 0.61\overline{T}\,\overline{q' w'}\right] && (2.86)\\ &\approx -\frac{g}{c_p\overline{T}}\left(Q_h + \frac{0.61 c_p \overline{T}}{L_{\mathrm{lg}}} Q_e\right) = -\frac{g\overline{\rho}_a}{\overline{T}}\overline{w'\Theta_v'}\,. && (2.87) \end{aligned}$$

   Hereby, pressure fluctuations and third-order correlation terms are neglected, and $T \approx T_v \approx \Theta$ i set in the final line. As $0.61 c_p\overline{T}/L_{lg}$ is on the order of 0.1, the production or destruction of TKE is largely proportional to the sensible heat flux Q_h.

2. **Dynamical production of TKE through wind shear**: For the homogeneous case, where the mean wind $\overline{u}$ is spatially constant for each height z, only the term

$$\overline{(\rho_a w')u'}\frac{\partial\overline{u}}{\partial z} \tag{2.88}$$

   directed in the mean wind direction remains. The TKE production through shear stress is dominant close to the surface where the vertical gradient of the wind speed is largest.

3. **Viscous dissipation of TKE**: This term, which is strictly positive, represents the dissipation of kinetic energy in heat through molecular friction. Under unstable and neutral stratification conditions, it is the only sink for turbulent kinetic energy. While the viscous dissipation is important in the context of turbulence, the generated heat is negligible in terms of atmospheric warming. See Stull (1988) for a more detailed discussion.

4. **Pressure-velocity interaction**: Under the assumption of incompressibility, $\vec{\nabla} \cdot \vec{u} = 0$, so that the sum of the components x, y, z vanishes. However, the individual pressure-velocity correlation terms for each component are not necessarily zero, which distributes TKE generated by (1) and (2) over the three directions in space and facilitates transport of TKE.

5. **Divergence of average flux density of TKE**: These terms characterize the difference in in- and outflow of TKE in a considered elementary volume and thus represent advection of TKE.

2.4.5 Atmospheric stability parameters

In the following, we again assume $\overline{v} = \overline{w} = 0$, i.e. a mean wind in x-direction. The main sources of TKE are the buoyancy term $g\overline{\rho_a' w'}$ and the shear term $\overline{(\rho_a w')u'}\,\partial\overline{u}/\partial z$. Their ratio, which is denoted the flux Richardson number R_f, is used to characterize the local structure of the turbulence at a certain height above the surface:

$$R_f := \frac{g}{\overline{\Theta_v}} \cdot \frac{\overline{w'\Theta_v'}}{\overline{u'w'}\,\partial\overline{u}/\partial z} \tag{2.89}$$

Under neutral conditions, the buoyancy term is zero and so is the flux Richardson number, while unstable conditions are characterized by negative values of R_f, with high negative values indicating a dominant buoyancy term and thus a highly unstable atmospheric stratification. Stable atmospheric stratifications feature positive R_f, as the buoyancy term changes its sign. While the shear term usually dominates close to the surface, it decreases more rapidly than the buoyancy term with height, so that $R_f = 1$ or $R_f = -1$ at a certain height. This is exploited in the definition of the Obukhov length

$$L_* := \frac{\overline{\Theta_v}}{\kappa g} \frac{(\overline{u'w'})^{3/2}}{\overline{w'\Theta_v'}} = \frac{\overline{\rho}_a c_p \overline{T}}{\kappa g} \frac{u_*^3}{Q_h + 0.61 c_p L_{\mathrm{lg}}^{-1} \overline{T}\, Q_e} , \tag{2.90}$$

which is contained in the widely used dimensionless stability parameter

$$\zeta := \frac{z}{L_*} = R_f \varphi_M . \tag{2.91}$$

The stability function φ_M is a result of parameterizing the covariances and relates the gradient term $\partial\overline{u}/\partial z$ in the definition of R_f to the covariance terms, on which the Obukhov Length L_* is based. For near-neutral atmospheric stratification conditions, φ_M is approximately one (see next section), so that the absolute values of the buoyancy and the shear term are equal at a height $z \approx L_*$. For a fixed height z, $\zeta \approx 0$ for neutral or near-neutral atmospheric stratification conditions, while it becomes increasingly positive with increasing atmospheric stability and increasingly negative under unstable conditions. In the limit of free convection with a buoyancy term much greater than the shear term, ζ goes to minus infinity.
The stability parameter ζ can be derived from high-frequency measurements of

the wind field, the temperature and the concentration of water vapor with an eddy covariance system, which is a commonly employed method to continuously assess the atmospheric stratification from a ground-based point measurement.

2.4.6 Monin-Obukhov similarity theory for the Prandtl layer

In this section, the relationships for the mass, heat and water vapor fluxes in the Prandtl layer are derived. We assume stationary conditions, i.e. constant fluxes of momentum, sensible and latent heat with time. Furthermore, all fluxes are assumed constant with height in the Prandtl layer.

Non-neutral atmospheric stratifications

Monin and Obukhov (1954) hypothesized that the characteristics of the turbulence in the Prandtl layer can only depend on the quantities z, z_0, u_*, $g/\overline{\Theta_v}$ and $\overline{w'\Theta_v'}$, which can be realized by introducing a functional dependence of the proportionality constant in Eq. 2.80 on the stability parameter $\zeta = z/L_*$. We hence write

$$\frac{\kappa z}{u_*}\frac{\partial \overline{u}}{\partial z} = \varphi_M(\zeta)\,. \tag{2.92}$$

The universal stability function $\varphi_M(\zeta)$ is the proportionality constant between ζ and the flux Richardson number R_f (Eq. 2.91), which is easily verified by comparing the definitions of L_*, Eq. 2.90 and R_f, Eq. 2.89. Similar approaches can be made for the gradients of the potential temperature and humidity, namely

$$\frac{\kappa z u_*}{\overline{w'\Theta'}}\frac{\partial \overline{\Theta}}{\partial z} = \varphi_H(\zeta) \tag{2.93}$$

$$\frac{\kappa z u_*}{\overline{w'q'}}\frac{\partial \overline{q}}{\partial z} = \varphi_W(\zeta)\,. \tag{2.94}$$

The universal functions $\varphi_M(\zeta)$, $\varphi_H(\zeta)$ and $\varphi_W(\zeta)$ must be determined by measuring u_*, $\overline{w'\Theta'}$ and $\overline{w'q'}$ as well as profiles of $\partial\overline{u}/\partial z$, $\partial\overline{\Theta}/\partial z$ and $\partial\overline{q}/\partial z$ over a wide range of atmospheric stability conditions. The functions, which are commonly used today, are mainly based on a few comprehensive studies such as the Kansas-experiment in 1968 (overview by Kaimal and Wyngaard, 1990). Such studies are strongly complicated by the stringent assumptions of spatial homogeneity and especially stationarity, which in practice is violated at least to a certain degree by the diurnal temperature cycle. The commonly employed functions (Høgstrøm, 1988) are

$$\varphi_M(\zeta) = (1 - 19\zeta)^{-1/4} \tag{2.95}$$

$$\varphi_H(\zeta) = \varphi_W(\zeta) = 0.95\,(1 - 11.6\zeta)^{-1/2} \tag{2.96}$$

for neutral to unstable atmospheric stratifications and

$$\varphi_M(\zeta) = 1 + 6\zeta \tag{2.97}$$

$$\varphi_H(\zeta) = \varphi_W(\zeta) = 0.95 + 7.8\zeta \tag{2.98}$$

for neutral to stable atmospheric stratifications. The formulations are well established under unstable, neutral and weakly stable atmospheric stratification conditions (for ζ smaller than 0.5 to 1), but are challenged for strongly stable atmospheric stratifications as they occur under polar night conditions in the Arctic and Antarctic. The concept of "z-less scaling", which means constant universal functions $\varphi_{M,H,W}$ independent of the height z for strongly stable stratifications, is favored by some studies (e.g. Handorf et al., 1999). The improvement of the universal functions in the strongly stable limit, i.e $\zeta \gg 0$, under polar night conditions was one of the goals of the SHEBA campaign on arctic sea ice in 1997 and 1998 (Uttal et al., 2002). The study has compiled a set of functions for stable stratifications (Grachev et al., 2007)

$$\varphi_M(\zeta) = 1 + \frac{6.5\zeta(1+\zeta)^{1/3}}{1.3+\zeta} \tag{2.99}$$

$$\varphi_H(\zeta) = 1 + \frac{5\zeta(1+\zeta)}{1+3\zeta+\zeta^2}\,, \tag{2.100}$$

which in case of φ_H confirms z-less scaling, as the function becomes constant for large values of ζ and thus independent of the height z. However, φ_M becomes proportional to $\zeta^{1/3}$ for large ζ, which contradicts z-less scaling.

Integration of flux-gradient relationships

The flux-gradient equations 2.92, 2.93 and 2.94 can be integrated from the roughness length z_0 to the height z, which for the wind profile yields

$$\overline{u}(z) = \frac{u_*}{\kappa}\int_{z_0}^{z}\frac{\varphi_M(\frac{z'}{L_*})}{z'}dz' = \frac{u_*}{\kappa}\left[\ln\frac{z}{z_0} - \Psi_M\left(\frac{z}{L_*},\frac{z_0}{L_*}\right)\right] \tag{2.101}$$

with

$$\Psi_M\left(\frac{z}{L_*},\frac{z_0}{L_*}\right) = \int_{z_0}^{z}\frac{1-\varphi_M(\frac{z'}{L_*})}{z'}dz'\,. \tag{2.102}$$

For the temperature profile, one obtains

$$\overline{\Theta}(z) = \overline{\Theta}(z_{0_\Theta}) + \frac{\overline{w'\Theta'}}{\kappa u_*}\left[\ln\frac{z}{z_{0_\Theta}} - \Psi_H\left(\frac{z}{L_*},\frac{z_{0_\Theta}}{L_*}\right)\right] \tag{2.103}$$

with

$$\Psi_H\left(\frac{z}{L_*},\frac{z_{0_\Theta}}{L_*}\right) = \int_{z_{0_\Theta}}^{z}\frac{1-\varphi_H(\frac{z'}{L_*})}{z'}\,dz' \tag{2.104}$$

and for the humidity profile

$$\overline{q}(z) = \overline{q}(z_{0_q}) + \frac{\overline{w'q'}}{\kappa u_*}\left[\ln\frac{z}{z_{0_q}} - \Psi_W\left(\frac{z}{L_*}, \frac{z_{0_q}}{L_*}\right)\right] \tag{2.105}$$

with

$$\Psi_W\left(\frac{z}{L_*}, \frac{z_{0_q}}{L_*}\right) = \int_{z_{0_q}}^{z} \frac{1 - \varphi_W(\frac{z'}{L_*})}{z'}\, dz' \,. \tag{2.106}$$

The roughness lengths for the temperature z_{0_Θ} and humidity z_{0_q} have to be chosen so that the temperature is equal to the surface temperature, and the humidity equal to the humidity just above the surface. In practice, one usually assumes the same roughness length z_0 for both wind speed, temperature, and humidity.
At this point, it is worthwhile to go back to the basic thermodynamic and humidity equations, Eqs. 2.55 and 2.56. There, molecular diffusion terms for heat and water vapor have been included in the bulk source terms χ_H and χ_W, which have not been considered in the following description of turbulent flow. However, heating and evaporation occur directly at the surface (or the latter even within the soil), not at the heights z_{0_Θ} and z_{0_q}, respectively. In a thin layer just above the surface, which is referred to as the viscous sublayer, the flow is necessarily laminar so that transport of heat and water vapor indeed occurs through diffusion. There is considerable difficulty with this concept over natural, rough surfaces or even in a canopy, where a transition zone between the molecular sublayer and the turbulent layer must exist. Thus, one generally assumes Eqs. 2.103 and 2.105 to be only valid at heights well above the roughness length.

2.4.7 A coupled model for energy exchange at the surface

In conjunction with the surface energy budget equation (see Sect. 2.1), a set of equations can be compiled, which model the energy exchange processes at the surface and thus deliver the surface temperature T_{surf} and the unknown fluxes L_{out}, Q_h, Q_e and Q_g. The set of input parameters is:

- incoming solar radiation S_{in}
- albedo α
- incoming long-wave radiation L_{in}
- surface emissivity ε
- wind speed $\overline{u}$ at a height z
- mean temperature $\overline{T}$ at a height z
- mean relative humidity $\overline{RH}$ at a height z

- the roughness length z_0
- thermal conductivity K_h of the soil or snow
- soil temperature $T(d)$ at depth d

The full set of equations is (neglecting the snow melt term Q_{melt}):

$$\overline{q}(z_0) = \frac{0.622}{p} e^*(T_{\mathrm{surf}}) \tag{2.107}$$

$$\overline{q}(z) = \frac{0.622\,\overline{RH}}{p} e^*(\overline{T}(z)) \tag{2.108}$$

$$L_* = \frac{\overline{\rho}_a c_p \overline{T}(z)}{\kappa g} \frac{u_*^3}{Q_h + 0.61 c_p L_{\mathrm{lg}}^{-1} \overline{T}(z)\, Q_e} \tag{2.109}$$

$$u_* = \overline{u}(z)\kappa \left[\ln \frac{z}{z_0} - \psi_M \left(\frac{z}{L_*}, \frac{z_0}{L_*} \right) \right]^{-1} \tag{2.110}$$

$$Q_h = -\overline{\rho}_a c_p \kappa u_* \left(\overline{T}(z) - T_{\mathrm{surf}} \right) \left[\ln \frac{z}{z_0} - \psi_H \left(\frac{z}{L_*}, \frac{z_0}{L_*} \right) \right]^{-1} \tag{2.111}$$

$$Q_e = -\overline{\rho}_a L_{\mathrm{lg}} \kappa u_* \left(\overline{q}(z) - \overline{q}(z_0) \right) \left[\ln \frac{z}{z_0} - \psi_W \left(\frac{z}{L_*}, \frac{z_0}{L_*} \right) + \kappa u_* r_s \right]^{-1} \tag{2.112}$$

$$Q_g = K_h d \left(T_{\mathrm{surf}} - T(d) \right) \tag{2.113}$$

$$0 = (1-\alpha) S_{\mathrm{in}} + \varepsilon L_{\mathrm{in}} + \varepsilon \sigma_{\mathrm{sb}} T_{\mathrm{surf}}^4 + Q_h + Q_e + Q_g \tag{2.114}$$

The specific latent heat of evaporation, L_{lg}, must be replaced by the specific latent heat of sublimation, L_{sg}, in case of sublimation from snow surfaces.
In the equation for the latent heat flux Q_e (Eq. 2.112), a term containing the so-called surface resistance against evapotranspiration, r_s, has been added. It reflects the fact that evapotranspiration not only depends on the atmospheric exchange but also on the availability of water in the soil. The term

$$r_a := (\kappa u_*)^{-1} \left[\ln \frac{z}{z_0} - \psi_W \left(\frac{z}{L_*}, \frac{z_0}{L_*} \right) \right] \tag{2.115}$$

can be viewed as an aerodynamic resistance (units of sm^{-1}) towards evapotranspiration, so that the total resistance is described as the sum of aerodynamic resistance r_a and surface resistance r_s. The latent heat flux can therefore be written as

$$Q_e = -\frac{\overline{\rho}_a L_{\mathrm{lg}}}{r_a + r_s} \left(\overline{q}(z) - \overline{q}(z_0) \right) . \tag{2.116}$$

For the saturation vapor pressure $e^*(T)$, the empirically derived Magnus formula is used

$$e^*(T) = a_1 \exp \left(\frac{a_2 (T - 273.15\,K)}{T - 273.15\,K + a_3} \right) , \tag{2.117}$$

where the values $a_1 = 611\,\mathrm{Pa}$, $a_2 = 17.62$ and $a_3 = 243.12\,\mathrm{K}$ for saturation vapor pressure over water surfaces and $a_1 = 611\,\mathrm{Pa}$, $a_2 = 22.46$ and $a_3 = 272.62\,\mathrm{K}$

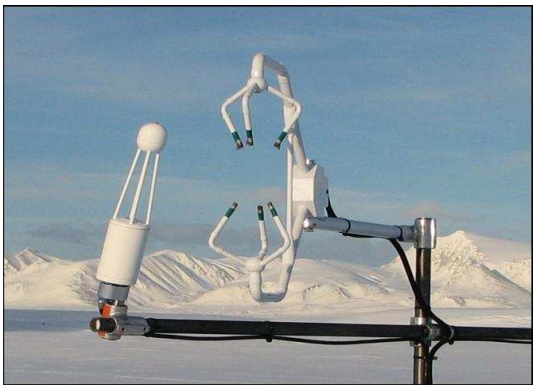

Figure 2.1: The eddy covariance system on Svalbard employed in this thesis, consisting of a Campbell CSAT 3D sonic anemometer (right) and a LiCor LI–7500 CO_2 and H_2O open-path gas analyzer (left).

for saturation vapor pressure over ice surfaces are used (Sonntag, 1990).
The set of equations can be solved numerically, so that the surface temperature can be computed based on observations of atmospheric parameters. With the surface temperature known, the dynamics of the subsurface temperature can be simulated using the equations of conductive heat transfer in the soil derived in the previous section. The ground heat flux term Q_g and the surface temperature induce a coupling between the soil and the atmospheric part. Instead of parameterizing the ground heat flux with a simple temperature gradient, one could also couple the set of equations to a numerical solving scheme for the heat transfer equation (Eq. 2.12).

2.5 Measuring turbulent fluxes with eddy covariance

2.5.1 Eddy covariance system

An eddy covariance system consists of a 3D-sonic anemometer and a gas analyzer, which can both be sampled at a frequency of 20 Hz (Fig 2.1). The system can resolve the dynamics of energy-carrying eddies, that can be conceptualized by an cycle of upwind with warm and moist air followed by downwind with cold and dry air (in case of positive sensible and latent heat fluxes). From the fluctuations of wind speed, air temperature and specific humidity, the turbulent fluxes of sensible heat and water vapor can be calculated.
The gas analyzer (Fig. 2.2) is based on absorption spectroscopy for water vapor and carbon dioxide. The LI–7500 uses the water absorption centered at a wavelength of 2.59 μm and the carbon dioxide absorption at 4.26 μm, while a non-absorbing region around 3.95 μm is used to correct for a varying intensity of the beam, e.g due to attenuation from dirt on the windows (www.licor.com, 2010). A rotating filter wheel continuously switches between the three wave-

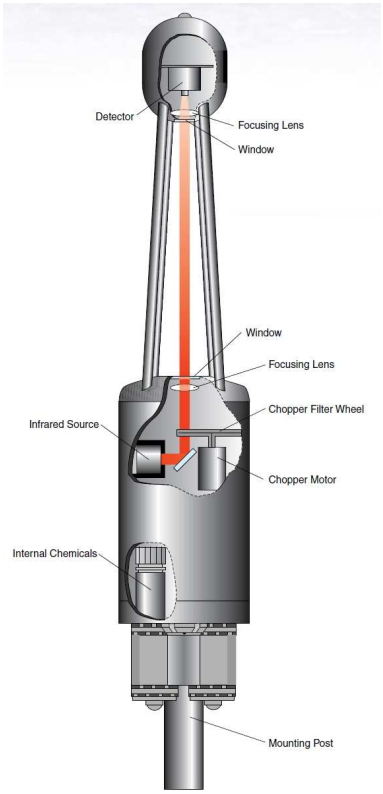

Figure 2.2: Schematic drawing of the functional elements of the LiCor LI–7500 gas analyzer (from www.licor.com, 2010).

length ranges (Fig. 2.2), and a lead selenide detector is used to measure the intensity. The carbon dioxide data are not part of this thesis.
The sonic anemometer (Campbell CSAT 3D sonic anemometer, Fig. 2.1) measures the wind field in the three directions in space and the so-called sonic temperature T_s of the air, which can be converted to the real air temperature with the additional humidity data derived from the gas analyzer (see above). Sound pulses are transmitted back and forth between transducers over a distance l and the travel time is recorded. The travel time of a sound pulse (speed of sound c_s) in case of wind speed $v_\parallel$ in the direction of l and $v_\perp$ perpendicular to l is given by

$$t_1 = \frac{l}{\sqrt{c_s^2 - v_\perp^2} + v_\parallel} \tag{2.118}$$

for sound propagation along with $v_\parallel$ and

$$t_2 = \frac{l}{\sqrt{c_s^2 - v_\perp^2} - v_\parallel} \tag{2.119}$$

in opposite direction. The speed of sound in air is related to the air temperature T and the specific humidity q by

$$c_s^2 = \gamma R_d T(1 + 0.51q) := \gamma R_d T_s \,, \tag{2.120}$$

which leads to the definition of the sonic temperature T_s. Hereby, γ denotes the adiabatic constant and R_d the gas constant of dry air. The specific humidity appears, as the gas constant is modified due to the different molar masses of dry air and water vapor and the adiabatic constants of dry air (predominantly diatomic molecules, $\gamma \approx 7/5$) and water vapor (triatomic molecule, $\gamma \approx 4/3$) are different. The factor 0.51 can be derived with a Taylor expansion around $q = 0$.
The four unknowns (three wind components and the sonic temperature) can be determined if at least four transmitter-receiver-combinations in a suitable geometry are available. The CSAT features a total of six, and by the chosen configuration (Fig. 2.1), an unobstructed wind path for the horizontal wind is achieved (which features much larger velocities than the vertical fluctuations of the wind speed).

With high-frequency measurements of the vertical wind speed w, T_s and q, the momentum flux u_*^2 and the sensible and latent heat fluxes Q_h and Q_e can be inferred as

$$u_*^2 = -\overline{u'w'} \tag{2.121}$$

$$Q_h = \rho_a \, c_p \left(\overline{T_s'w'} - 0.51 \, \overline{T} \, \overline{q'w'} \right) \tag{2.122}$$

$$Q_e = \rho_a \, L_{\mathrm{lg}} \, \overline{q'w'} \,, \tag{2.123}$$

where the covariances are calculated as time averages. Note that $T \approx \Theta$ is used for the sensible heat flux, which is unproblematic as the measurements are conducted at constant height and to a good approximation constant pressure. Furthermore, it is possible to employ the average sonic temperature $\overline{T}_s$ instead of the average temperature $\overline{T}$, as the difference in absolute temperatures is negligible. If sublimation over snow surfaces gives rise to the latent heat flux, L_{lg} must be replaced by L_{sg}, which increases the latent heat flux by about 10% in case of the same covariance $\overline{q'w'}$. It is yet important that high-frequency measurements of the fluctuations of the specific humidity are required to accurately determine the sensible heat flux (Schotanus et al., 1983).
The evaluation of the fluxes is performed with the software package 'TK2' (Mauder and Foken, 2004; Mauder et al., 2008), which is one of the most commonly employed flux software packages and used as a reference standard to evaluate the performance of other flux softwares (Mauder et al., 2007). The TK2 includes a quality assessment scheme for the flux data (Foken et al., 2004), that has been developed to discard strongly erroneous measurements. Before the quality assessment, the so-called steady-state test, can be discussed, we must take a closer look at the evaluation of the covariances using time averages.

2.5.2 Calculation of covariances

In this section, Reynold's averaging (Sect. 2.4.2) is revisited, as the covariances $\overline{u'w'}$, $\overline{T_s'w'}$ and $\overline{q'w'}$ must be calculated from time series of u, w, T_s and q

measured at a single point in space. Therefore, time averaging is employed to approximate the ensemble average.
We consider an infinitely long time series of two scalar variables, e.g $u(t)$ and $w(t)$, that is sampled between times $-\tau/2$ and $\tau/2$. With the definition of the boxcar function

$$P_\tau(t) = \begin{cases} 1 & \text{for} \quad t \in [-\tau/2, \tau/2] \\ 0 & \text{for} \quad t \notin [-\tau/2, \tau/2] \end{cases} \tag{2.124}$$

and the Fourier transformation of $u(t)$

$$\hat{u}(f) = \int_{-\infty}^{\infty} u(t) e^{-2\pi\imath f t}\, dt\,, \tag{2.125}$$

the covariance $\overline{uw}_\tau$ (or $\overline{u'w'}_\tau$ if fluctuations around the mean value are considered) for time averaging performed from $-\tau/2$ to $\tau/2$ is calculated as

$$\begin{aligned}
\overline{uw}_\tau &= \frac{1}{\tau} \int_{-\tau/2}^{\tau/2} dt\, u(t)\, w(t) = \frac{1}{\tau} \int_{-\infty}^{\infty} dt\, u(t)\, w(t)\, P_\tau(t) \qquad (2.126)\\
&= \frac{1}{\tau} \int_{-\infty}^{\infty} dt \int_{-\infty}^{\infty} df_1 \int_{-\infty}^{\infty} df_2 \int_{-\infty}^{\infty} df_3\, \hat{u}^*(f_1)\, \hat{w}(f_2)\, \hat{P}_\tau(f_3) e^{-2\pi\imath(f_1 - f_2 - f_3)t} \\
&= \frac{1}{\tau} \int_{-\infty}^{\infty} df_1 \int_{-\infty}^{\infty} df_2 \int_{-\infty}^{\infty} df_3\, \hat{u}^*(f_1)\, \hat{w}(f_2)\, \hat{P}_\tau(f_3)\, \delta(f_1 - f_2 - f_3) \\
&= \frac{1}{\tau} \int_{-\infty}^{\infty} df_1 \int_{-\infty}^{\infty} df_2\, \hat{u}^*(f_1)\, \hat{w}(f_2)\, \hat{P}_\tau(f_1 - f_2) \\
&= \frac{1}{\tau} \int_{-\infty}^{\infty} df_1 \int_{-\infty}^{\infty} df_2\, \hat{u}^*(f_1)\, \hat{w}(f_2)\, \frac{\sin(\pi(f_1 - f_2)\tau)}{\pi(f_1 - f_2)}\,.
\end{aligned}$$

In the limit of very long averaging times τ, the last term approaches the Dirac delta function and the equation becomes the integral over the cospectrum of u and w

$$\overline{uw}_\tau = \frac{1}{\tau} \int_{-\infty}^{\infty} df\, \hat{u}^*(f)\, \hat{w}(f)\,, \tag{2.127}$$

which is equal to the idealized ensemble average (Sect. 2.4.2) under the assumption of ergodicity. It is important that the spectra $\hat{u}(f)$ and $\hat{w}(f)$ are the

spectra of the ideal, infinitely long time series of $u(t)$ and $v(t)$, not the spectra that would be obtained from the sample between $-\tau/2$ and $\tau/2$.
The limit of an infinite averaging time cannot be realized in measurements, so that the last term in Eq. 2.126 acts as a highpass filter and induces mixing of frequencies. To a good approximation, the contribution of frequencies $f_1 - f_2$ is nullified if the absolute value of the argument of the sine function is greater than or equal to π which is fulfilled for

$$|f_1 - f_2| \geq \frac{1}{\tau} \,. \tag{2.128}$$

On the other hand, for each frequency f_1 contained in $\hat{u}$, a band of frequencies $f_2 \in (f_1 - 1/\tau, f_1 + 1/\tau)$ of $\hat{w}$ contributes to the covariance. Now let $f_{\min}$ denote the smallest frequency present in $\hat{u}$ and $\hat{w}$.

1. If $f_{\min} \gg 1/\tau$, the frequency band where mixing occurs is very narrow (relative to frequencies of $\hat{u}$ and $\hat{w}$), and the covariance calculated over the averaging time τ is a good approximation for the "true" covariance given by Eq. 2.127.

2. If $f_{\min} < 1/\tau$, time averaging with averaging time τ is not a suitable mean to determine the "true" covariance Eq. 2.127. The low frequencies of $\hat{u}$ and $\hat{w}$ will mix and create a false cospectrum.

From this reasoning, the averaging time τ should be chosen much longer than the longest period (i.e. the lowest frequency) in the data set. While an averaging time of $\tau = 30\,\mathrm{min}$ is much longer than the periods of typical eddies (Foken, 2008a), lower frequencies are also induced by factors other than energy-carrying eddies, such as the diurnal cycle that imposes a frequency of $(1\,\mathrm{day})^{-1}$ on the temperature and possibly humidity and wind speed. Changing synoptic conditions can have the same effect, that may affect temperature, wind speed and humidity. In all cases, contributions to the covariance arise due to frequency mixing, that do not represent "real" fluxes in the sense of Eq. 2.127.
It is a nearby thought to increase the averaging time, which naturally limits the time resolution of the flux measurements, but at the same time should increase the accuracy of the obtained fluxes. To remove effects of the daily cycle and changing synoptic conditions, the averaging period should at least comprise a few days. However, on such timescales, new "low" frequencies can arise e.g. from long-term temperature trends. Furthermore, measurement errors, e.g. due to instrument failure or due to strong precipitation affecting both the sonic anemometer and the open-path gas analyzer, are commonplace on timescales of a few days, so that the averaging period in reality cannot be strongly extended.
The issue is a direct consequence of the point measurement of turbulence with the eddy covariance system, that must necessarily rely on time averaging to approximate the ensemble average. We therefore adopt the standard procedure for flux measurements (Foken, 2008a) and select a fixed averaging time of 30 min for the eddy covariance measurements, knowing that some errors of the fluxes are unavoidable.
For the averaging interval of 30 min, the accuracy of the fluxes is qualitatively estimated by a steady-state or stationarity test implemented in the evaluation

software 'TK2'. Hereby, the covariance $\overline{u'w'}_{30\mathrm{min}}$ calculated for the standard averaging interval of 30 min is compared with the mean of the covariance $\overline{u'w'}_{5\mathrm{min,i}}$ of 5-min subintervals and a normalized deviation De is calculated:

$$De = \left| \frac{\overline{u'w'}_{30\mathrm{min}} - \sum_i \overline{u'w'}_{5\mathrm{min,i}}}{\overline{u'w'}_{30\mathrm{min}}} \right| \tag{2.129}$$

The deviation is zero, if the spectra of all 5 min averages and of the 30 min average are equal and Eq. 2.127 can be assumed to hold, i.e low frequencies do not occur that would lead to mixing on the 5 min and 30 min timescale. A graduation of the deviation is used to classify the quality of the fluxes (Foken and Wichura, 1996; Foken, 2008a): the flux measurements are of good quality if both results agree within 30%, while a system of quality flags reflects the increasingly poor quality of flux measurements with increasing value of De. In this thesis, half-hourly flux values are considered, if De is smaller than 2.5, corresponding to flux measurements with a quality flag of 6 or better, which can be considered "in long-term studies" (Foken and Wichura, 1996). While this may sound rather arbitrary, it is a standard practice in flux measurements with the eddy covariance method world-wide. Nevertheless, it remains unsatisfactory to the author of this thesis that the threshold values are justified "by long experiences" (Mauder and Foken, 2004), while they are not convincingly linked to the uncertainty in the fluxes or at least a meaningful physical quantity. Mauder et al. (2006) suggest relative uncertainties between 5% and 15% for quality flags of 6 or better, but these numbers are derived from few micrometeorological studies in Central Europe, so that it seems highly questionable to assign these error margins to the present study.

2.6 Radiative transfer in the atmosphere

Measurements of the surface temperature T_{surf} are conducted by measuring the outgoing long-wave radiation

$$L_{\mathrm{out}} = \varepsilon \sigma_{\mathrm{sb}} T_{\mathrm{surf}}^4 - (1-\varepsilon) L_{\mathrm{in}} \,. \tag{2.130}$$

Although the Kirchhoff emissivity ε is close to unity for natural surfaces, a dependence on the incoming thermal radiation L_{in} remains. Furthermore, the incoming thermal radiation is the dominant source term in the surface energy budget during polar night conditions. Thus, the understanding of the basic processes that determine the intensity and the spectral characteristics of the incoming thermal radiation is highly beneficial for interpreting the surface energy budget in arctic regions. In the following, the basic equations for radiative transfer in the atmosphere are presented.
A beam of radiation, that travels vertically downwards from the top of the atmosphere (in this section defined as $z = 0$) to the surface (defined as $z = z_s$), loses energy due to absorption, gains energy by means of emission and redistributes energy by scattering. We do not consider scattering in the following, so that the radiation can be conceptualized as a ray. The equation of radiative transfer relates the change in spectral irradiance $I(\lambda, z)$ at wavelength λ and position z along the ray path to local absorption $k_\lambda(z)$ and emission $j_\lambda(z)$ as

$$\frac{dI(\lambda, z)}{dz} = -k_\lambda(z) I(\lambda, z) + j_\lambda(z) \,. \tag{2.131}$$

A solution is given by Chandrasekhar (1960)

$$I(\lambda, z_s) = I(\lambda, 0) e^{-\tau_\lambda(0, z_s)} + \int_0^{z_s} j_\lambda(z') e^{-\tau_\lambda(z', z_s)} \, dz' \,, \tag{2.132}$$

which is verified by inserting in Eq. 2.131. $\tau(z_1, z_2)$ denotes the optical depth of the atmosphere between z_1 and z_2 given by

$$\tau_\lambda(z_1, z_2) = \int_{z_1}^{z_2} k_\lambda(z') \, dz' \,. \tag{2.133}$$

We now assume absorption and emission in a gas cloud in local thermodynamic equilibrium, where the gas molecules are in thermodynamic equilibrium at temperature T, while the radiation field is not. In this situation, emission and absorption are related by Kirchhoff's law as

$$j_\lambda = k_\lambda I_{\mathrm{bb}}(\lambda, T) \,, \tag{2.134}$$

where $I_{\mathrm{bb}}(\lambda, T)$ is the spectral irradiance emitted by a black body at kinetic temperature T, given by Planck's law

$$I_{\mathrm{bb}}(\lambda, T) = \frac{2hc^2}{\lambda^5} \frac{1}{e^{\frac{hc}{\lambda k_B T}} - 1} \,. \tag{2.135}$$

Eq. 2.132 can hence be written as

$$I(\lambda, z_s) = I(\lambda, 0)e^{-\tau_\lambda(0,z_s)} + \int_0^{z_s} k_\lambda(z')I_{\mathrm{bb}}(\lambda, T(z'))e^{-\tau_\lambda(z',z_s)}\,dz' \,. \quad (2.136)$$

From Eq. 2.136, the spectral irradiance at each height z can be evaluated, if the concentrations of the different molecule species and their absorption cross sections are known. The absorption cross sections are usually obtained from the HITRAN molecular spectral database (Rothman et al., 2009). While a published radiation transfer code is used for all quantitative evaluations of radiative fluxes in this thesis (see Sect. 2.7), we discuss a few aspects of the radiative transfer equation in the following, that are important for the surface energy budget in arctic regions.

If the spectral intensity at the top of the atmosphere is set to zero, i.e $I(\lambda, 0) = 0$, the spectral intensity incident at the surface is entirely determined by the optical depth and the temperature distribution in the air column of the atmosphere. The segment from which the radiation stems is hereby determined by the strength of molecular absorption at the respective wavelength: the radiation originates in the part which is not optically thick seen from the surface, so that only the temperature distribution in this part is relevant. With decreasing optical depth, the mean free path of thermal photons eventually exceeds the thickness of the atmosphere, so that the incident spectral radiance is less than the black-body irradiance at the temperatures in the atmosphere. Minimal molecular absorption at wavelengths between 7.5 and 14.0 μm gives rise to the so-called atmospheric window where the incident spectral irradiance features much lower values compared to the neighboring spectral regions in case of clear skies. Conversely, radiation emitted by the earth surface in the atmospheric window experiences little absorption in the atmosphere and the energy is largely emitted to space.

In general, clouds are optically thick for thermal radiation, so that the thermal radiation incident at the surface is almost entirely determined by the temperature at the cloud base, at least in case of low clouds, where the emitted radiation is not modified strongly by atmospheric emission and absorption between the cloud base and the earth surface. Clouds "close" the atmospheric window for thermal radiation, so that they are a determining factor for the budget of thermal radiation. If solar radiation is available, the increase of the incident thermal radiation is counterbalanced or even exceeded by the reduction of the incident solar radiation. Under polar night conditions, though, the increase of thermal radiation incident at the surface due to clouds can lead to a strong net warming (Curry et al., 1996).

The energy of the incident thermal radiation originates from the kinetic energy of the air molecules, so that the air temperature decreases due to radiative cooling. Conversely, the absorption of outgoing thermal radiation, which is largely black-body radiation from the earth surface, leads to radiative warming of the air. The two processes are in equilibrium if the surface temperature is equal to the temperature of the atmosphere. Under clear sky conditions during polar night, the surface is colder than the atmosphere due to the constant loss of radiation through the atmospheric window. This leads to radiative cooling of the atmosphere and represents an important energy reallocation chain, from the

atmosphere to the surface where the radiation is absorbed and partly reemitted in the atmospheric window, through which it is finally lost to space. Ultimately, the surface and associated atmospheric cooling is only limited by the availability of other energy sources, such as advection of warmer air (Curry et al., 1996). Another source of energy is the ground heat flux: it is significant in permafrost regions, as large amounts of energy are stored in the active layer during summer and released in winter.

2.7 Radiometric correction of surface temperature measurements

For this thesis, we evaluate spatially resolve measurements of the surface temperature conducted with a high-resolution thermal imaging system (VARIOCAM HR^{TM}, Infratec GmbH, Dresden, Germany), which features a resolution of of 384 x 288 pixel. The system is based on an uncooled microbolometer array that is thermally stabilized at ambient temperature (Dereniak and Boreman, 1996). The Noise Equivalent Temperature Difference (NETD) is specified to be smaller than 30 mK for the thermal imaging system used in this study. The thermal imaging is sensitive in the atmospheric window from 7.5 to 14 μm, where atmospheric absorption and emission are minimal, so that the outgoing long-wave radiation from a surface point is received at the thermal imaging system without strong modification in the traversed air column. Nevertheless, the measured surface temperatures require a radiometric correction, which is presented in the following.
The spectral irradiance at wavelength λ of a black body at kinetic temperature T (Norman and Becker, 1995) is given by Planck's law Eq. 2.135, so that the irradiance of a black body in the sensitivity range of the thermal imaging system from 7.5 to 14 μm is

$$R_{bb}(T) = \int_{7.5\mu m}^{14.0\mu m} I_{bb}(\lambda, T)\, d\lambda \approx a + b\, T^{\,c}\,, \tag{2.137}$$

where a, b and c are fitted coefficients. The thermal imaging system is internally calibrated to deliver the brightness temperatures T_b of a scene, which is defined as the temperature of a black body emitting the same irradiance as measured (Norman and Becker, 1995). The irradiance received at the sensor for a brightness temperature T_b is hence $R_{\mathrm{bb}}(T_b)$. The brightness temperature T_b provided by the thermal imaging system is equal to the kinetic temperature T of a surface area, if the black body assumption is fulfilled. However, the emission and absorption characteristics of natural surfaces are generally different from a black body, so that a correction must be applied to obtain the kinetic temperature. Kirchhoff's law gives the spectral irradiance $I_n(\lambda, T, \theta, \phi)$ of a gray body emitted in the direction given by angles θ and ϕ to the surface:

$$I_n(\lambda, T, \theta, \phi) = \varepsilon(\lambda, \theta, \phi)\, I_{\mathrm{bb}}(\lambda, T) + (1 - \varepsilon(\lambda, \theta, \phi))\; I^{\searrow}(\lambda, \theta', \phi') \tag{2.138}$$

Hereby, $\varepsilon(\lambda, \theta, \phi)$ denotes the directional spectral emissivity and $I^{\searrow}(\lambda, \theta', \phi')$ the incident spectral radiance at reciprocal angles θ' and ϕ'. The molecular absorption and emission of the thermal radiation in the air column between the point of origin and the thermal imaging system (which is weak in the atmospheric window, but still not negligible) is accounted for by a spectral transmissivity $\tau_a(\lambda, T, T_{\text{air}}, s, c_1, \ldots c_N)$, which is a function of kinetic surface temperature T, air temperature T_{air}, traversed path length s and concentrations c_i of molecule species $i = 1, \ldots N$. Note that τ_a can be smaller or greater than unity depending on the difference between air and kinetic surface temperature. Hence, the irradiance incident at the thermal imaging system, R_{ti}, can be evaluated as

$$R_{\text{ti}}(T, \theta, \phi, T_{\text{air}}, s, c_1, \ldots c_N) = \int_{7.5\mu m}^{14.0\mu m} \tau_a(\lambda, T, T_{air}, s, c_1, \ldots c_N) \times \left[\varepsilon(\lambda, \theta, \phi)\, I_{bb}(\lambda, T) + (1 - \varepsilon(\lambda, \theta, \phi))\, I^{\searrow}(\lambda, \theta', \phi')\right] d\lambda\,. \quad (2.139)$$

By equating Eq. 2.139 to $R_{\text{bb}}(T_b)$ (Eq. 2.137), the kinetic surface temperature T can in principle be evaluated. In practice, in particular the spectral and angular dependence of ε is not known, so that we restrain to spectrally averaged quantities for the emissivity and transmissivity. Therefore, the evaluation of the kinetic surface temperature is based on the following simplifications:

1. We make use of a spectrally averaged emissivity $\overline{\varepsilon}$ defined as

$$\overline{\varepsilon} = R_{\text{bb}}(0°C)^{-1} \int_{7.5\mu m}^{14.0\mu m} \varepsilon(\lambda) I_{\text{bb}}(\lambda, 0°C)\, d\lambda\,. \quad (2.140)$$

   Note that the temperature dependence of $\overline{\varepsilon}$ is negligible in the relevant temperature range. To estimate $\overline{\varepsilon}$, we use the MODIS UCSB emissivity library (Wan and Zhang, 1999), which provides spectral emissivities of basic landcover types. Using Eq. 2.140, we obtain 0.985 for free water and 0.965 for dry vegetation, which is in good agreement with other published surface emissivities from arctic landcovers (Rees, 1993; Bussières, 2002) or similar landcover types from other regions (Salisbury and D'Aria, 1992; Snyder and Wan, 1998). A problem arises with the potential angular dependence of the emissivity, which can be substantial under extreme off-nadir angles for some landcover types (Becker et al., 1985; Labed and Stoll, 1991; Norman and Becker, 1995; Snyder et al., 1997). A comprehensive study by Snyder and Wan (1998) suggests decreases in emissivities between 0.01 and 0.05 for land cover types characteristic for our study site (e.g bare soil, water) for off-nadir angles of 75°, which occur with the setup used in this study. As we cannot provide direct measurements of emissivities and their view-angle dependence, we assume a spatially constant emissivity and include the potential variability in the error calculation. We choose an emissivity value of $\overline{\varepsilon}$=0.96±0.04, which accounts for potential variations of the emissivities both due to the variability of the land cover and due to a potential view-angle dependence.

2. We assume the surface reflectance to be lambertian, so that the angular dependence of the incident spectral irradiance does not need to be taken into account. Therefore, we can employ the downwelling spectral irradiance $I^{\downarrow}$ (i.e. the spectral irradiance incident from the complete hemisphere of the sky) instead of $I^{\searrow}(\theta', \phi')$ (Norman and Becker, 1995). $I^{\downarrow}$ is evaluated using the radiative transfer model 'uvspec' with the software package 'libRadtran' (Mayer and Kylling, 2005). As we are finally interested in irradiances over a wide spectral range, a band parameterization approach (correlated–k approximation SBDART, Ricchiazzi et al., 1998) is sufficient. As an estimate for the atmospheric composition, we use the "subarctic summer atmosphere" standard profile and the temperature and relative humidity profiles from daily radiosoundings at the village of Ny-Ålesund. In the atmospheric window, the downwelling spectral irradiance is critically determined by the presence of a cloud cover. We evaluate the height of the cloud base from the radiosonde profiles using the scheme of Chernykh and Eskridge (1996), which assigns a cloud layer if the second derivative of temperature with respect to altitude is greater and the second derivative of relative humidity smaller than zero. If this criterion is not matched within a radiosonde profile, we assign the altitude with the highest measured relative humidity as the most likely cloud base altitude. We then conduct two separate evaluations for the downwelling spectral radiance, one assuming clear sky conditions, denoted $I^{\downarrow}_{\mathrm{cs}}(\lambda)$, and one assuming full cloud cover, denoted $I^{\downarrow}_{\mathrm{fc}}(\lambda)$. From measurements of the incoming long-wave radiation L_{in}, i.e. of the total downwelling long-wave irradiance, with a pyrgeometer (spectral range from 5 to 50 μm) in the village of Ny-Ålesund, we evaluate an estimated cloud fraction cf as

$$\mathrm{cf} = \begin{cases} 0 & \text{for} \quad L_{\mathrm{in}} < L^{\downarrow}_{\mathrm{cs}} \\ (L_{\mathrm{in}} - L^{\downarrow}_{\mathrm{cs}})/(L^{\downarrow}_{fc} - L^{\downarrow}_{cs}) & \text{for} \quad L^{\downarrow}_{\mathrm{cs}} \leq L_{\mathrm{in}} \leq L^{\downarrow}_{\mathrm{fc}} \\ 1 & \text{for} \quad L_{\mathrm{in}} > L^{\downarrow}_{\mathrm{fc}} \end{cases} , \quad (2.141)$$

where $L^{\downarrow}_{\mathrm{cs}}$ and $L^{\downarrow}_{\mathrm{fc}}$ are defined as

$$L^{\downarrow}_{\mathrm{cs/fc}} = \int_{5\mu m}^{50\mu m} I^{\downarrow}_{\mathrm{cs/fc}}(\lambda)\, d\lambda \,. \quad (2.142)$$

The downwelling irradiance $R^{\downarrow}$ in the 7.5 to 14 μm window is subsequently obtained as

$$R^{\downarrow} = \int_{7.5\mu m}^{14.0\mu m} \mathrm{cf} \times I^{\downarrow}_{\mathrm{fc}}(\lambda) + (1 - \mathrm{cf}) \times I^{\downarrow}_{\mathrm{cs}}(\lambda)\, d\lambda \,. \quad (2.143)$$

We create an hourly record for $R^{\downarrow}$ from the hourly record of L_{in} and the radiosonde profile, that is closest in time. This scheme is capable to

resolve changes in cloud cover, which give rise to fast jumps in L_{in} by more than $100\,\mathrm{Wm}^{-2}$. Since only a single radiosonde profile is available per day, the dynamics of the temperature and humidity profile, which causes more gradual changes in L_{in}, is not properly resolved, which can result in a bias of cf and $R^{\downarrow}$. The potential uncertainty is largest at the midpoint between two radiosoundings. By conducting the evaluation of $R^{\downarrow}$ for the two neighboring radiosoundings for these times, we estimate an error margin of approximately 20% on the hourly values of $R^{\downarrow}$.

3. A spectrally averaged transmissivity $\overline{\tau}_a$ is derived using the radiative transfer model 'uvspec' with the software package 'libRadtran' (Mayer and Kylling, 2005). The path lengths s are evaluated for each pixel of the thermal imaging system according to the georeferencing procedure (see Sect. 3.2.6). We assume constant concentrations of the standard molecules as given by the lowest level of the "subarctic summer atmosphere" profile in 'libRadtran', except for water vapor, for which we use hourly concentrations inferred from measurements of relative humidity and air temperature at 2 m height above ground in the village of Ny-Ålesund (see Sect. 3.2.5). Using a band parameterization (see above) for the radiation transfer, we evaluate the spectral irradiance I_{tr} at distance s from a black body with kinetic temperature T, when an air column with temperature T_{air} and relative humidity RH is traversed. As the kinetic temperature is the target of the evaluation and thus not known, we use the brightness temperature T_b as a first-order approximation for T, and account for the difference between the two in the error analysis of $\overline{\tau}_a$. The spectrally averaged transmissivity is then evaluated as

$$\overline{\tau}_a(T_b, T_{\mathrm{air}}, RH, s) \;=\; R_{\mathrm{bb}}(T_b)^{-1} \int_{7.5\mu m}^{14.0\mu m} I_{\mathrm{tr}}(\lambda, T_b, T_{\mathrm{air}}, RH, s)\, d\lambda\,. \quad (2.144)$$

We estimate a liberal error of 0.005 on the transmissivity, which corresponds to an error of about 5 K of the difference between T_{air} and T at 100% relative humidity and a path length of 100 m.

As a result of (1)-(3), we can simplify Eq. 2.139 and equate it to the irradiance received at the thermal imaging system, $R_{\mathrm{bb}}(T_b)$, as

$$R_{\mathrm{ti}} \;=\; \overline{\tau}_a \left[\overline{\varepsilon}\, R_{\mathrm{bb}}(T) + (1-\overline{\varepsilon}) R^{\downarrow}\right] = R_{\mathrm{bb}}(T_b)\,. \quad (2.145)$$

The kinetic temperature T can now be evaluated by numerically solving the equation for T. The obtained difference between the kinetic temperature T and the brightness temperature T_b is close to zero for overcast conditions, when incoming and outgoing long-wave radiation are approximately equal, but can exceed 2 K in case of clear skies. In the following, kinetic temperatures of the surface obtained with a radiometric correction are simply denoted as surface temperature.

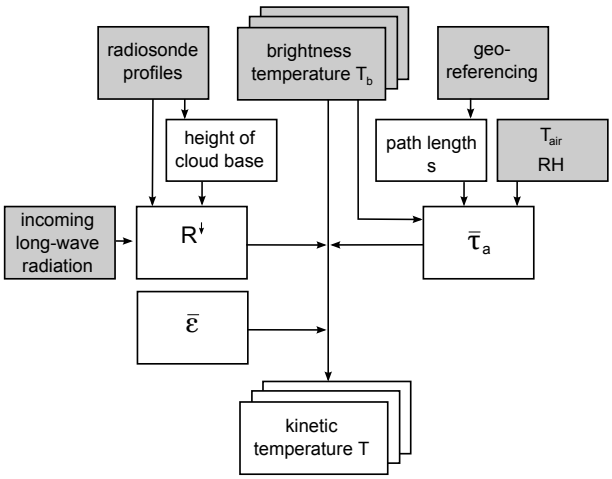

Figure 2.3: Schematic diagram of the different measured input data sets (shaded in gray) and the work flow employed for the processing of the kinetic surface temperatures T. Intermediate results and the estimated parameter $\overline{\varepsilon}$ in white. The measurements of the input data are described in Sect. 3.2.2, the georeferencing procedure yielding the path length s for each pixel is presented in Sect. 3.2.6.

We consider three sources of error: the emissivity $\overline{\varepsilon}$ with an uncertainty of 0.04, the downwelling irradiance $R^{\downarrow}$ with 20% of each value and the average transmissivity $\overline{\tau}_a$ with 0.005. Using Gaussian error propagation in Eq. 2.145 with the polynomial approximation for R_{bb} (Eq. 2.137), the uncertainty in T can be calculated for each pixel and each scene. The by far largest error stems from the emissivity: it is largest under clear-sky conditions (up to 2 K), when the downwelling irradiace is small, and becomes zero, when the ground is in thermal radiation balance with a cloud cover. For the calculation of uncertainties for temporal averages, we have to distinguish between the random errors on $R^{\downarrow}$ and $\overline{\tau}_a$ and the uncertainty on $\overline{\varepsilon}$, which is an offset from the "true" value and approximately constant over time. The two random errors are essentially negligible in temporal averages, and the resulting uncertainty for each pixel is the average of the uncertainties due to emissivity for the respective period.

Chapter 3

Field measurements on Svalbard

The field measurements for this thesis have been conducted close to the village of Ny-Ålesund (Figs. 3.1, 3.2), which is located on the Brøgger peninsula in NW Svalbard. Ny-Ålesund was founded as a coal mining settlement in 1916, but designated a support facility for polar research after coal mining was abandoned in the 1960s. As the world's northernmost port, it was the starting point for many polar expedition, such as the first successful North Pole flight by Roald Amundsen in 1926. Today, four nations (Norway, Germany, France and China) operate all-year research stations in Ny-Ålesund, which has become one of the most active locations for atmospheric, marine and terrestrial research in the Arctic. Since the early 1990s, a large number of measurement campaigns and long-term monitoring programs has created an outstanding data base on climatological and atmospheric variables (e.g. Yamanouchi and Ørbaek, 1995; Beine et al., 2001; Winther et al., 2002). Routine measurements of air temperature and precipitation are available for more than fourty years (www.eklima.no, 2010). As the ground temperature phenomenon permafrost is much more determined by long-term trends rather than by short-term variability of the climate, the long time series is an excellent starting point for permafrost research, even more as such data sets rarely exist for arctic locations.

3.1 Ny-Ålesund and the Bayelva study area

3.1.1 Climatic conditions in NW Svalbard

The NW part of Svalbard is strongly influenced by a branch of the Gulf Stream, which leads to a maritime climate with cool summers, while the winter temperatures are comparatively mild compared to locations at similar northern latitudes. The warmest month is July with an average air temperature of around +5 °C, while February is on average coldest with mean air temperatures of −14°C. Since the 1970s, the air temperatures in Ny-Ålesund have increased by about 2 K, which can be attributed to warmer winter temperatures (Fig. 3.3). The

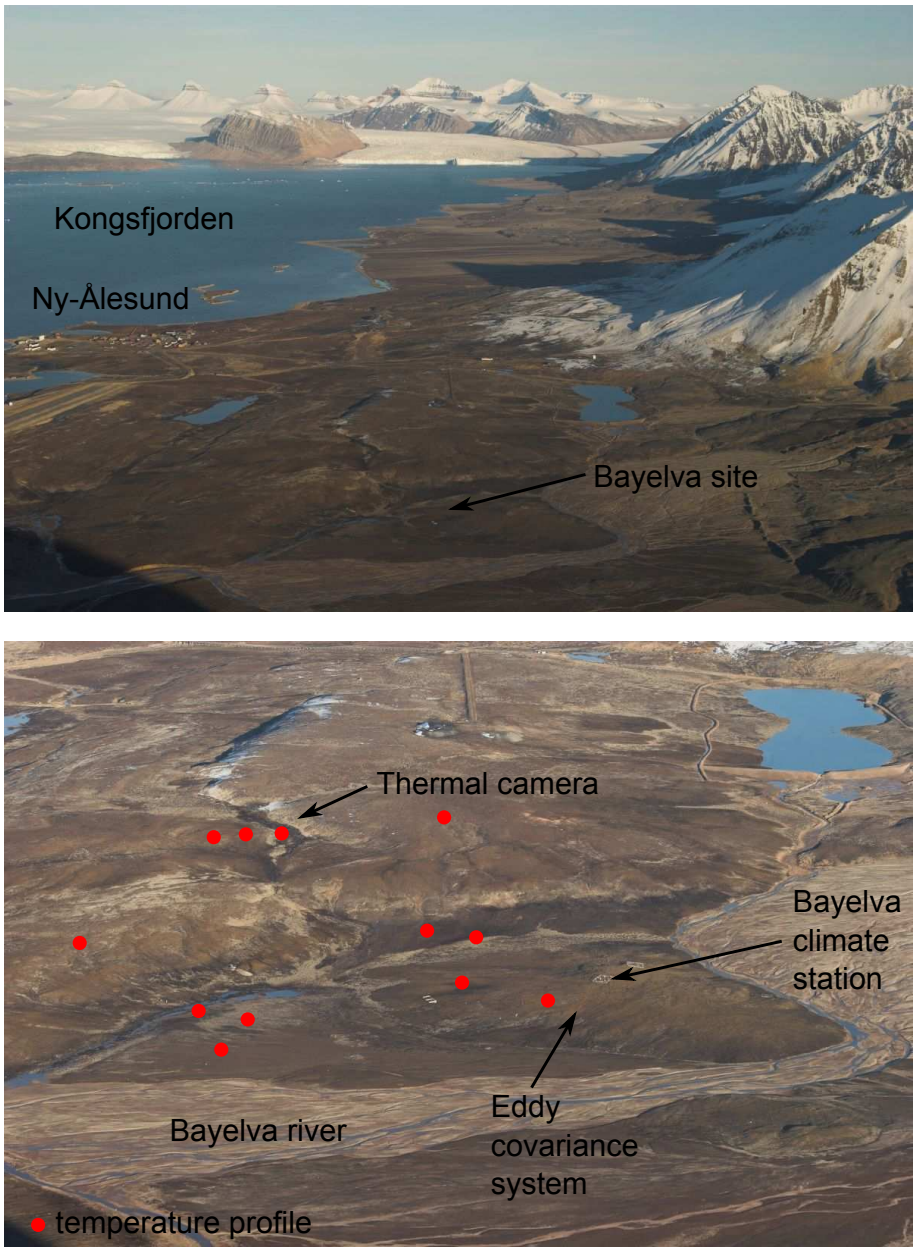

Figure 3.1: Photos of the Kongsfjorden area and the study area at the Bayelva river taken from Schetelig mountain (740 m a.s.l.) on 8 September 2007. As can be seen in the upper image, the "lowland" permafrost areas comprise a 2 to 4 km wide strip between the Kongsfjorden and the partly glaciated mountain chain of the Brøgger peninsula to the right. A closer view of the study area, which covers roughly 0.5 km^2, is shown in the lower image with the locations of all installations marked (see text).

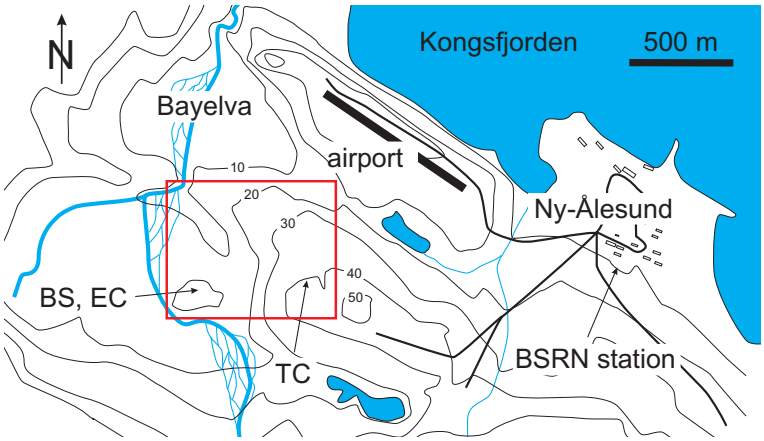

Figure 3.2: Location of the study area (red) and the BSRN site in the village of Ny-Ålesund, where routine meteorological measurements are conducted; BS: Bayelva station; EC: Eddy covariance system; TC: Thermal imaging system; thick black lines: roads; contour lines in meters above sea level.

increased winter temperatures can be largely explained by to changes in atmospheric circulation patterns, which lead to more frequent advection of warm maritime air masses to Svalbard (Hanssen-Bauer and Førland, 1998). In the long-term mean, the area around Ny-Ålesund receives an annual precipitation of around 400 mm (Førland et al., 1997), with on average 75% of the annual precipitation occurring during the "winter" months October to May (www.eklima.no, 2010). While the precipitation features a strong interannual variability, it has not increased significantly since the 1970s (Fig. 3.3).
Due to the influence of warm ocean currents, the NW part of Svalbard receives the least sea ice of all areas of the archipelago. During summer, the sea off Ny-Ålesund is generally ice-free, and a permanent ice cover on Kongsfjorden does not form before December (Gerland and Renner, 2007). While strong variations in the ice conditions on decadal timescales have been observed in the past, sea ice concentrations around NW Svalbard have gradually diminished since the mid of the 20th century. In the past five years, the Kongsfjorden has only been sporadically frozen even during winter, which has not been recorded previously (Gerland and Renner, 2007; Cottier et al., 2007).
The budget of solar radiation is naturally determined by the annual cycle of polar night and day, but is strongly modulated by albedo changes due to the seasonality of the snow cover. In Ny-Ålesund, the polar night lasts approximately from mid of October until mid of February, while the sun does not set below the horizon from mid April to mid August. The average duration of the snow-free period is three months, typically from July to September, but it can vary from 50 to 150 days (Winther et al., 2002). During summer, the west coast of Svalbard is predominantly influenced by moist Atlantic air masses, which leads to a high percentage of cloudy days and thus effectively reduces the available solar radiation.
In winter, the NW of Svalbard is under the influence of both moist Atlantic and

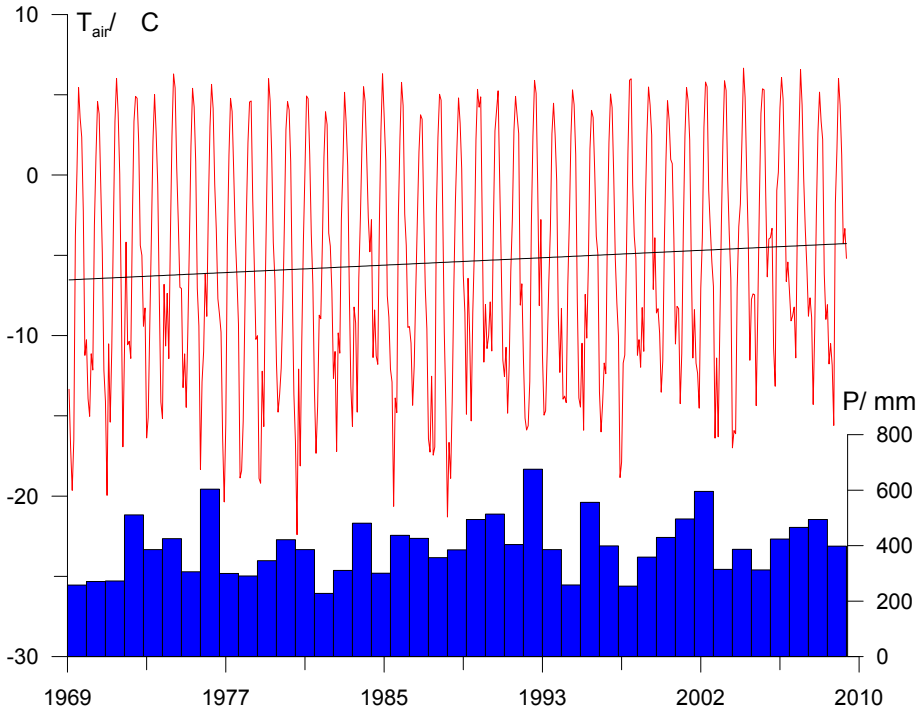

Figure 3.3: Average monthly air temperatures and total annual precipitation at Ny-Ålesund from 1969 to 2009 from the records of the Norwegian Meteorological service (www.eklima.no, 2010). The warming trend for the depicted period is on the order of 2 K.

dry polar air masses, which are typically associated with comparatively warm air temperatures with overcast skies and cold air temperatures with clear skies, respectively (e.g. Førland et al., 1997). As a result of the exchange of the air masses during winter, the incoming long-wave radiation is found to vary over a wide range, while its range is much smaller during summer (Yamanouchi and Ørbaek, 1995).

3.1.2 The study period

Daily means of air temperatures and monthly totals of precipitation are displayed in Fig. 3.4 for the period, when the field measurements for this thesis have been conducted. The period integrates well in the warming trend of the past 40 years (compare to Fig. 3.3), but does not represent exceptionally warm conditions, which have been recorded previously on Svalbard (e.g. Isaksen et al., 2007). The summer air temperatures are usually in the range between 0°C and 10°C, with the highest temperatures recorded in July in both 2008 and 2009. The winter periods are characterized by rapid changes between cold periods with air temperatures below -20°C and much warmer periods with temperatures partly above 0°C. This pattern is typical for the western parts of Svalbard, that

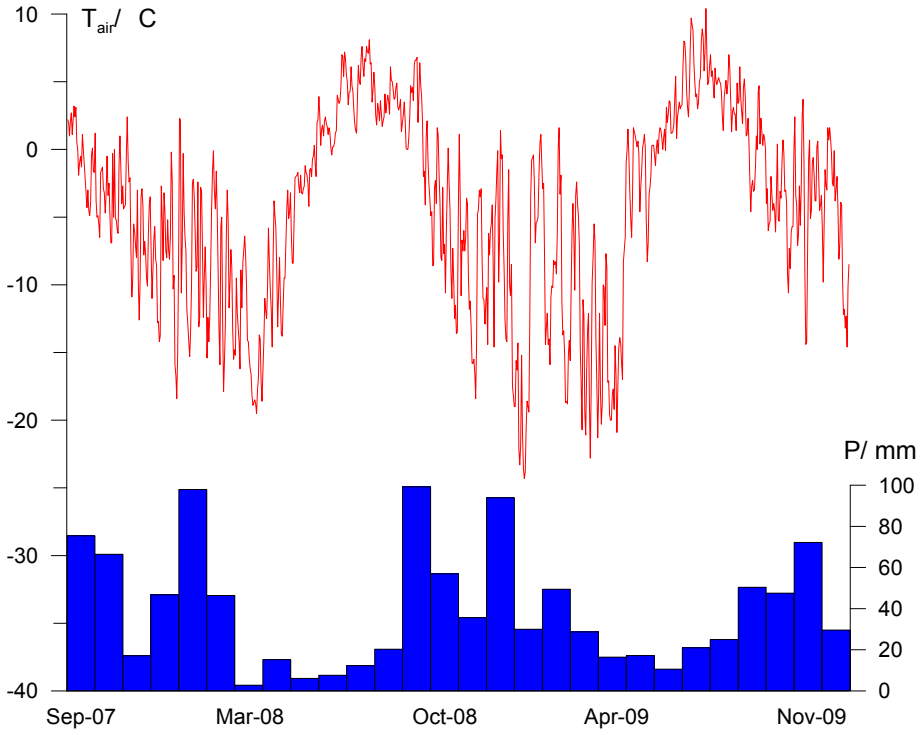

Figure 3.4: Daily average air temperatures and total monthly precipitation at Ny-Ålesund for the study period from the records of the Norwegian Meteorological service (www.eklima.no, 2010).

is situated at the boundary between polar air masses and warm maritime air masses during winter.
The monthly precipitation is highly variable during the presented period (Fig. 3.4). The highest precipitation rates are recorded in fall and early winter from September to February, which is the typical precipitation pattern for NW Svalbard (www.eklima.no, 2010). With almost 100 mm of precipitation each, the months of January, September and December 2008 stand out. Although these months feature more than twice the amount of precipitation of the long-term averages for these months, similar precipitation rates have been observed in a number of occasions in fall and early winter since 2000 (www.eklima.no, 2010). Therefore, the high precipitation rates rather reflect the strong variability of the precipitation in NW Svalbard than exceptional events. From March to August, only little precipitation is recorded compared to fall and early winter. The Kongsfjorden off Ny-Ålesund has been free or almost free of sea ice during the winter 2007/2008. In the consecutive winter 2008/2009, the Kongsfjorden has been covered with sea ice from March to May.

3.1.3 The Bayelva study area

In the area around Ny-Ålesund, "lowland" permafrost is restricted to an about 2 to 4 km wide strip along the coast of the Kongsfjorden, which is bordered by the inland glaciers and mountain chains of the Brøgger peninsula (Fig. 3.1). All field measurements have been conducted in a tundra area in the catchment of the Bayelva river at 78°, 55′N, 11°, 50′E (Fig. 3.1), which is located approximately 2 km SW of the village of Ny-Ålesund (Fig. 3.2). The study area is situated about half-way between the glacier Brøggerbreen, from which the Bayelva river originates, and the Kongsfjorden. The area roughly comprises the catchment of a small tundra stream (Fig. 3.1), while the gravel floodplain of the Bayelva river borders to the area to the W and S. It includes Leirhaugen hill in a bend of the Bayelva river, which is elevated by about 10 m above the floodplain of the Bayelva River.
The study area is characterized by hilly tundra at elevations between 10 m and 45 m above sea level. Sparse vegetation alternates with exposed soil and rock fields, and frost features, such as mud boils (Boike et al., 2008) and sorted circles, are found in many parts of the study area. The soil at the study site features a high mineral content, while the organic content is low, with volumetric fractions below 10%. The soil texture comprises a wide range, from gravel close to the Bayelva river to clayey sediments on the slopes of Leirhaugen hill (Boike et al., 2008). A wide variety of soil moisture conditions is found in the study area: close to the small tundra stream, the ground is permanently water-saturated, and in the streambed itself, areas with permanent standing water and even a small lake with a diameter of about 30 m exist. The ridge slopes adjacent to the stream and Leirhaugen hill feature intermediate soil moisture conditions, which strongly depend on the precipitation and the synoptic conditions. Very dry conditions can occur on the well-drained crests of the ridges, which dry out rapidly after rain events. However, these areas only comprise a very small fraction of the total area.

3.2 Installations and measurements

3.2.1 Orthofoto and Digital Elevation Model

An orthofoto and a Digital Elevation Model (DEM) have been created for some parts of the Bayelva study area by photogrammetric processing of aerial images, that have been obtained with a NIKON D200 digital camera from a remotely controlled drone (Thamm and Judex, 2006) on 29 August 2008. The ground control points necessary for orthorectification and georeferencing (Slama et al., 1980) have been marked on the ground and their location has subsequently been determined with a Differential GPS system. Examples of the resulting orthofoto and the DEM are displayed in Figs. 3.5, 3.6 and 4.1.

3.2.2 Bayelva station

Located on top of Leirhaugen hill, the Bayelva climate and soil monitoring station has provided a long-term record of climatological parameters and soil

temperatures since 1998 (Roth and Boike, 2001; Boike et al., 2010). At the station, air temperature, relative humidity, wind speed, precipitation, incoming short-wave radiation, outgoing long-wave radiation and snow depth are continuously recorded. Measurements of S_{in} are performed with a Skye Pyranometer SP1110 and of L_{out} with a Kipp & Zonen CG1 long-wave radiation sensor, while S_{out} and L_{in} are not measured. The precipitation is recorded with an unheated RM Young 52203 Tipping Bucket rain gauge, which can only measure precipitation in the form of rain and possibly slush. The snow depth is measured with an Campbell Scientific SR50 ultrasonic ranging sensor.
In the soil, profile measurements of active layer temperatures to depths of up to 1.5 m are performed. A profile of the volumetric soil water content is measured with Time-Domain-Reflectometry (TDR) to a depth of 1.13 m (Boike et al., 2003b). In March 2009, a borehole, that is now part of the TSP network (see Sect. 1.2), has been drilled about 20 m from the temperature profiles at the Bayelva station to a depth of 9 m and instrumented with a chain of temperature sensors, so that information about the temperature distribution in the permanently frozen ground is available since then.

3.2.3 Soil temperature profiles

In summer 2008, a total of 12 additional soil temperature profiles ranging to depths of up to 1.5 m have been installed (Fig. 3.1) to explore the spatial and temporal variability of active layer temperatures at the study area. The sites represent a cross-section through the wide range of surface covers and soil moisture conditions as well as different snow conditions during winter. They allow to assess the representativeness of the temperature profile at the Bayelva station for the study area. Each of the profiles features an array of three temperature sensors, one just below the surface and one at depths of 0.15 m and 0.3 m. Such temperature data are used to determine the ground heat flux with the conductive method (see Sec. 2.3). A similar array of three temperature sensors has been installed above the surface at heights of 0.0 m, 0.15 m and 0.4 m at eight of the stations, which is used for the evaluation of the snow heat flux, as soon as it is buried under snow during winter.

3.2.4 The eddy covariance system

In March 2007, an eddy covariance system (see Sect. 2.5.1) to measure fluxes of sensible and latent heat has been installed about 100 m NW of the Bayelva station on the slightly inclined slope ($< 5°$) of Leirhaugen hill. At the chosen location, the flow paths in the main wind directions to the S, E and NW are unobstructed by man-made artificial structures, so that an undisturbed footprint area can be assumed. As the eddy covariance system is operated far from the power grid of Ny-Ålesund, an autonomous power supply has been designed, which facilitates operation even under polar night conditions. The power supply is realized by a combination of solar panels and a wind generator in conjunction with a large battery capacity of 800 Ah at 12 V. To avoid disturbance of the wind flow especially by the wind generator, all installations are placed next to the existing Bayelva station approximately 100 m from the eddy covariance sys-

tem. After initial problems with the power supply, the eddy covariance system has been operational since March 2008.
The measurement height above ground of the eddy covariance system is adjusted to 2.1 m, when the ground is free of snow. To keep track of the changing height due to accumulation or melting of snow, the snow depth at the eddy covariance site is recorded using a Campbell Scientific SR50 ultrasonic ranging sensor.
Between October 2008 to March 2009, a gradient tower with measurements of the air temperature at 2 m and 10 m above ground, denoted $T_{\mathrm{air}}(2\,\mathrm{m})$ and $T_{\mathrm{air}}(10\,\mathrm{m})$ in the following, has been operated approximately 150 m from the location of the eddy covariance system to obtain additional data on the atmospheric stratification. With increasing snow height, the distances of the sensors to the snow surface decrease accordingly, with the 2 m-temperature sensor being approximately at the same height above the surface as the eddy covariance system (see Sect. 4.1.2).

3.2.5 Ancillary measurements in the village of Ny-Ålesund

In the village of Ny-Ålesund, a station of the Baseline Surface Radiation Network (BSRN) is located, which is maintained daily. Here, incoming and outgoing short- and longwave radiation are measured according to WMO accuracy standards (Ohmura et al., 1998), as well as air temperature, relative humidity and wind speed. Furthermore, the Norwegian Meteorological Institute provides a detailed long-term record of air temperature, relative humidity, precipitation, pressure and cloud fraction (according to visual observations) from Ny-Ålesund, that is available from www.eklima.no (2010). In Ny-Ålesund, radiosoundings are conducted daily at 1200 UTC, that provide the temperature and humidity profile of the atmosphere. These data, which are obtained from the "Integrated Global Radiosonde Archive" (Durre et al., 2006), are used for the radiometric correction of surface temperature measurements with the thermal imaging system (see Sect. 2.7).

3.2.6 Thermal imaging system

In the summer seasons of the years 2008 and 2009, a thermal imaging system has been installed about 400 m E of the Bayelva station (Figs. 3.1, 3.2) to continuously monitor the surface temperatures of a patch of tundra with highly variable surface cover and soil moisture conditions (Fig. 3.5). The location (78°55.296'N, 11°51.345'E) is chosen on top of an about 10 m high escarpment, which facilitates to cover a larger area by looking down on the region at the foot of the escarpment (Fig. 3.6). The thermal imaging system faces approximately North at an off-nadir angle of 65°, which results in a monitored area of 10,000 m^2. The monitored scene contains many features typical for the entire study area, with the surface characterized by a mixture of vegetation patches, exposed soil and fields of rocks and gravel. The lowest part of the monitored area at the foot of the escarpment gives way to a roughly S-facing slope with an inclination of approximately 5°. Accordingly, the area features a wide range of soil moisture conditions, from permanently water-saturated areas close to the escarpment to much drier conditions found at protruding knolls in the sloping

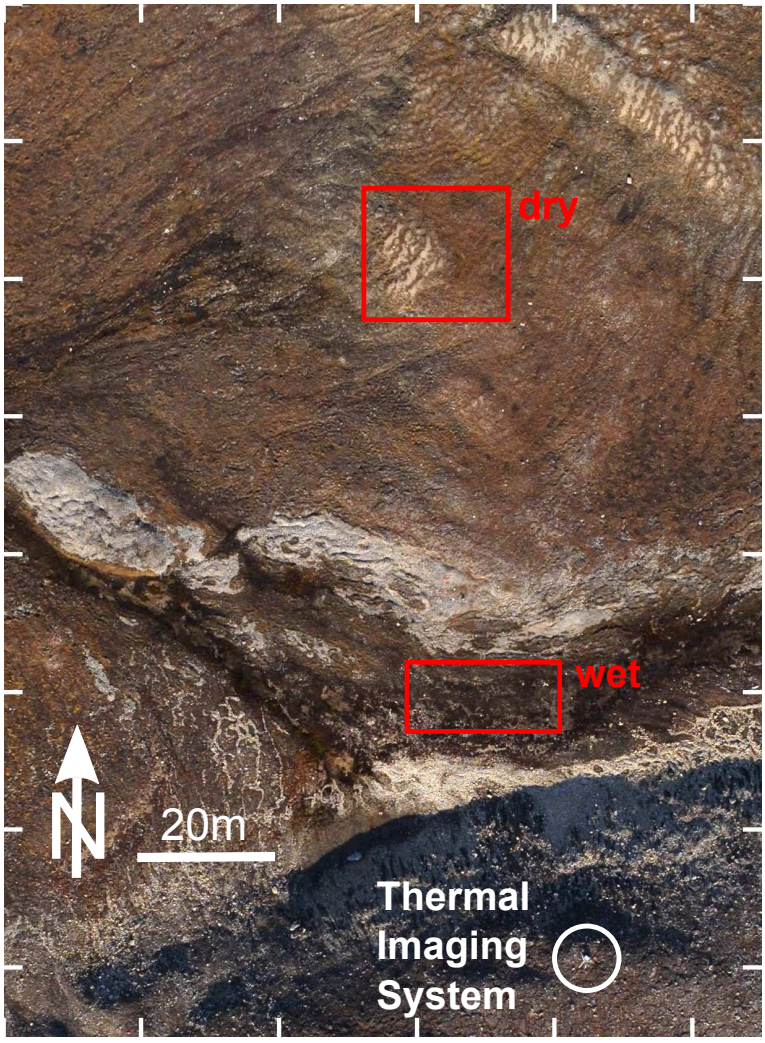

Figure 3.5: Orthorectified aerial photo of the area recorded by the thermal imaging system, acquired on 29 August 2008 from a remotely controlled drone (see Sect. 3.2.1). Reference areas for dry and wet surface conditions are indicated in red.

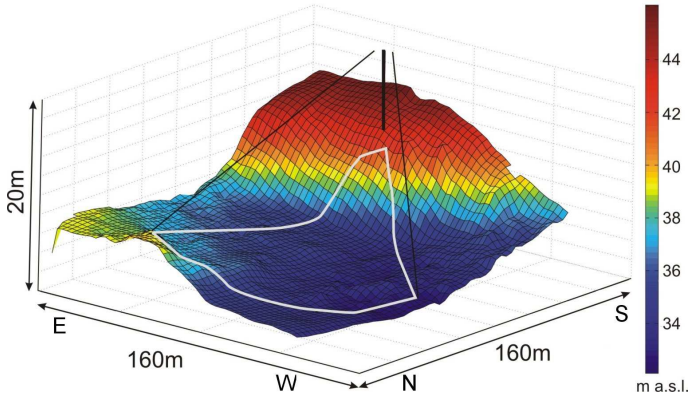

Figure 3.6: Digital elevation model compiled from aerial images acquired from a remotely controlled drone on 29 August 2008 (see Sect. 3.2.1). The thick black bar indicates the mast on which the thermal imaging system is placed (drawn to scale). The scene recorded in the study period of 2008 is depicted in white, the viewing direction is approximately opposite to that of Fig. 3.5 and 4.15.

area. Due to the formation of a snow drift at the escarpment in winter, a slowly melting snow field, from where a small tundra stream originates, remains at its foot throughout most of the summer. A coarse classification of the surface soil moisture conditions based on field observations is shown in Fig. 4.15, which is valid after the tundra has sufficiently dried up following snow melt.
The images delivered by the thermal imaging system under an oblique angle are reprojected to the UTM coordinate system to obtain georeferenced measurements of the surface temperature. For this purpose, we compile a transfer function which maps an image point (X, Y) in the thermal image to its UTM coordinate (x, y, z). The transfer function accounts for the geometric and optical parameters of the imaging system (focal length, sensor and pixel sizes, two radial lens distortion parameters), the external orientation (location, view angles) and the shape of the terrain in the footprint area of the thermal imaging system (Slama et al., 1980). While the focal length and sensor properties are provided by the manufacturer, the view angles and the lens distortion parameters are calculated from a set of image points and corresponding control points on the ground. The UTM coordinates of the ground control points and of the thermal imaging system itself have been measured with a Differential GPS system. The shape of the terrain is accounted for by the DEM created from the aerial images (see Sect. 3.2.1). The reprojected thermal images are then gridded with a spatial resolution of 0.5 m to yield georeferenced surface temperature measurements with equal pixel size.
We estimate a maximum horizontal displacement error between the georeferenced thermal images and the orthofoto, which ranges from 1 m in the the wet and moist areas in the foreground to up to 5 m in the dry areas in the background of the thermal images (Fig. 3.5). This spatial uncertainty is mainly due to the limited accuracy of the DEM and gitter-like movements of the thermal imaging system during periods with strong winds.

The thermal imaging system delivers brightness temperatures, that are radiometrically corrected to obtain the kinetic temperature of the surface, as has been outlined in Sect. 2.7. Fig. 2.3 gives and overview over the parameters employed in the radiometric correction: the path lengths s of the traversed air column are calculated individually for each point in the scene according to the DEM and the position of the thermal imaging system, while air temperature, relative humidity, incoming long-wave radiation and the radiosoundings are obtained from the village of Ny-Ålesund (see Sect. 3.2.5). The kinetic temperature of the surface is simply denoted as surface temperature in Sect. 4.3, where the results of this study are presented.

3.3 Satellite and reanalysis data

One goal of this thesis is to evaluate and benchmark the performance of possible schemes for permafrost monitoring and modeling for study area. Such schemes must necessarily rely on data sets that are available for large areas rather than point measurements on the ground. On the one hand, we consider measurements of the land surface temperature (LST) from the MODIS sensor on board of the satellites Terra and Aqua. These measurements are available at a spatial resolution of about one square kilometer, which makes it feasible to evaluate their performance for the study area. They are available for the past 10 years, which is a relatively long time series for satellite products.
On the other hand, reanalysis products, which are essentially results of atmospheric circulation models, can provide global datasets of a number of important input variables for permafrost monitoring. In this thesis, we use the reanalysis products ERA–40 (Uppala et al., 2006) and ERA–interim from the European Centre for Medium-Range Weather Forecast (ECMWF). While the main drawback of reanalysis products is the very coarse spatial resolution, they offer the invaluable advantage of a gapless time series at temporal resolutions of a few hours, that is available for more than 50 years in case of the ECMWF reanalysis products. The NCEP/NCAR reanalysis (Kalnay et al., 1996) issued by the "National Oceanic and Atmospheric Administration" (NOAA) goes back in time even further, which is an exciting prospect for modeling a long-term temperature phenomenon like permafrost.

3.3.1 MODIS LST data

As the vicinity of the study area is extremely heterogeneous with glaciers, mountains and the water surface of the Kongsfjorden, the control the footprint area of satellite-derived surface temperatures is a crucial prerequisite for a meaningful comparison to terrestrial surface temperature measurements. The version 5 MODIS L2 LST products (MOD11L2.5 and MYD11L2.5) obtained by the satellites Terra and Aqua provide radiometrically corrected surface temperature measurements using the generalized split window approach (Wan and Dozier, 1996), where each pixel can be assigned to a direct measurement of a certain footprint area. This footprint area can be derived from the unprojected swath data format of the L2 product (Wan, 2008), which also provides the exact time

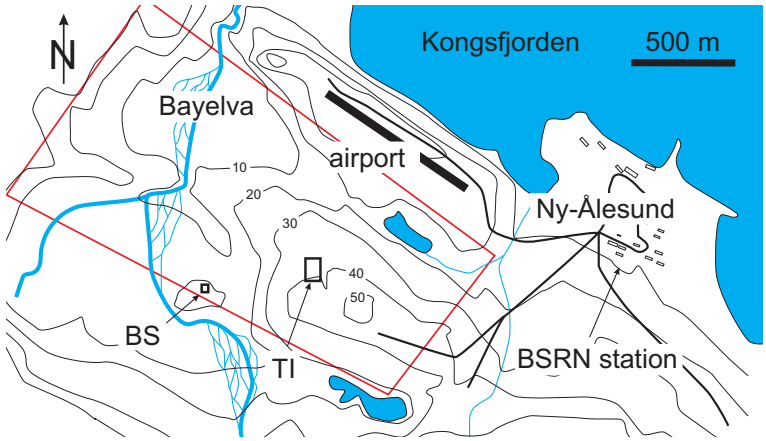

Figure 3.7: Location of the target area for MODIS LST (depicted in red), with which a 60% overlap is required to assign an LST measurement to the study area; TI: location of the thermal imaging system; BS: location of the Bayelva station; thick black lines: roads; contour lines in meters above sea level.

of acquisition. Due to the polar orbit of Terra and Aqua, more than 20 overpasses per day in principle facilitate an almost continuous coverage of the daily cycle with intervals of generally less than two hours. In practice, the frequent cloudiness leads to a drastic reduction of the data density with prolonged periods without measurements.
For the footprint analysis, the field of view of each pixel can be assumed circular (Nishihama et al., 1997). Using simple geometry, the circle is projected on the flat earth surface, based on the center position of the footprint area and the zenith angle given by the geolocation fields L1A V005 (Wolfe et al., 2002), the position of the satellite and internal instrument parameters such as the focal length and the pixel size. We then calculate the overlap of the resulting elliptically shaped footprint with a target area of approximately $4 \times 2\,\mathrm{km}^2$ (Fig. 3.7), which mainly features a surface cover that is reasonably similar to that the study area. Wolfe et al. (2002) estimate the accuracy of the center position on the earth surface to about 50 m for nadir angles, which suffices our requirements considering the size of the target area. However, as the footprint ellipse rapidly increases in size with increasing off-nadir angle of the measurement, the required overlap with the target area leads to a further reduction of the data density. In practice, an adequate data density can only be achieved, if we employ satellite measurements, where the footprint ellipse and the target area overlap by at least 60%. We emphasize, that major contributions of the Kongsfjorden and the glacier Brøggerbreen to the footprint area do not occur with the chosen overlap criterion.

3.3.2 ERA-40 and ERA-interim reanalysis

The ERA reanalysis products are results from a simplified version of the Numerical Weather Prediction (NWP) model operational at the ECMWF. As they cover a long period of time with a strongly inhomogeneous basis of forcing data, the performance of the reanalysis data can vary over time. While the early period is entirely based on weather observations from land- and sea-based stations and wind, temperature and humidity profiles from radiosoundings, satellite observations of atmospheric water vapor and wind fields are incorporated in the forcing data from the 1970s, so that the overall performance of the ERA data sets for reproducing ground observations appears to increase with time (Uppala et al., 2006). While ERA-interim offers some improvements over ERA–40, it is designated to be an "interim reanalysis of the period 1989-present in preparation for the next-generation extended reanalysis to replace ERA-40" (Simmons et al., 2007).
The ERA-40 and ERA-interim data sets are available for the period from 1958 to 2002 and from 1989 to 2009, respectively. For this thesis, the data for the surface level of air temperature (2 m height), relative humidity (2 m height), wind speed (10 m height) as well as total precipitation, snowfall, incoming short-wave radiation and incoming long-wave radiation at the surface are employed. The full temporal resolution of six hours is exploited. The ERA–40 data are available on a Gaussian grid with spatial resolution of $2.5° \times 2.5°$, while the resolution with $1.5° \times 1.5°$ is marginally better for ERA–interim. To obtain a data set for the study area, the reanalysis data are interpolated between the four closest-lying grid cells. It is important that the employed grid cells largely consist of ocean (ice-free or ice-covered), so that the data are generated using an entirely different surface forcing compared to the study site. Nevertheless, it seems promising to employ the above mentioned variables, which are more homogeneous over larger areas compared to parameters like the surface temperature, that strongly depends on the site-specific conditions.

Chapter 4

Results

The results section consists of six parts: In the first two sections, the annual cycle of the surface energy budget is presented from an almost continuous record of independent measurements. In Section three, the spatial variability of the summer surface temperature is discussed in the light of the surface energy budget. Section four is dedicated to the impact of the perennial snow cover on the soil temperatures. In Section five, the performance of remotely sensed surface temperatures, which are regarded a key component in future satellite-based permafrost monitoring, is evaluated for the study site. Finally, key findings from the field studies are conceptualized in a process-oriented permafrost model, that is forced by atmospheric parameters obtained from reanalysis products. The performance of the model is explored for the decadal soil temperature record of the Bayelva station.

4.1 The data set on the surface energy budget

In this thesis, an almost continuous time series of all componets of the surface energy budget (see Sect. 2.1) has been compiled over the course of one year from March 2008 to March 2009 (Westermann et al., 2009). It consists of independent measurements of radiation, sensible and latent heat fluxes, the ground heat flux and the energy consumed by the melting snow pack, which is unique for arctic land areas. In the following, the single data sets are described, while the surface energy budget is presented in the next section.

4.1.1 Radiation

The incoming short-wave radiation L_{in} and outgoing long-wave radiation L_{out} are derived from the records of the Bayelva station, while small data gaps have been filled with the corresponding data from the BSRN station. The incoming long-wave radiation L_{in} from the BSRN station is used for this study, since this quantity is mainly influenced by the cloud cover and the temperature distribution in the atmosphere (see Sect. 2.6), which should not differ considerably

between the study area and the village of Ny-Ålesund. The determination of the outgoing short-wave radiation S_{out} or the albedo α, respectively, is difficult, as a time series from the study area is not available due to instrument failure. Therefore, the average surface albedo is inferred from measurements at the BSRN site, except for the snow melt period. When the ground is covered by snow, systematic differences in the albedo of the undisturbed snow surfaces at the study area and the BSRN site are not to be expected. When the ground is snow-free, the albedo at the two sites may differ slightly, though. In August 2008, the surface albedo has been determined at 40 points within the study area from single measurements of incoming and outgoing short-wave radiation under clear-sky conditions using a pyranometer. The resulting average albedo of 0.18±0.05 compares well with the albedo of 0.15, which we infer from the time series of the BSRN station for the months of July and August. We use the latter value for our analysis, but assume an error of at least 5% on the net short-wave radiation, when the ground is snow-free. For the snow melt period, we assume an albedo estimate of 0.65, which is the average albedo at the BSRN station between 1 and 15 June 2008. In this period, the snow melt occurs at the BSRN site, associated with a decrease in albedo from the winter value 0.8 to 0.5, before it decreases within one day to the summer value.

4.1.2 Turbulent fluxes

The turbulent fluxes have been measured with the eddy covariance technique outlined in Sect. 2.5.1, while the set-up and the measurement location are presented in Sect. 3.2.4. Between March 2008 and March 2009, approximately 15% of the values of both for the sensible and the latent heat fluxes are excluded due to the quality assessment (see Sect. 2.5.1). Furthermore, all flux values from wind sectors are removed, where the tower structure, to which the eddy covariance system is mounted, is upwind, so that it could produce flow distortions affecting the sonic anemometer (wind directions 15°–55°). However, this applies only to about 1.5% of the flux values, as the tower structure is placed away from the prevailing wind directions. The half-hourly values are averaged to obtain a data set with hourly resolution.
From 2 October to 18 October 2008 and from 1 January to 6 February 2009, the raw data sampled at 20 Hz have not been recorded by the datalogger due to instrument failure. In these cases, fluxes based on 30 min covariances calculated by the standard datalogger software are used, where a subsequent quality assessment is not possible. However, the obtained flux values are considered in this study, because the standard datalogger software can reproduce the magnitude of the average fluxes for times when the quality assessment scheme is available. During the snow-free period, the measurement height above ground of the sonic anemometer was adjusted to 2.1 m. During both winter periods, heavy snowfall and accumulation of drifting snow occurred in the area around the eddy covariance system, which caused a considerable reduction of the measurement height above ground. From March to May 2008, the distance between the CSAT anemometer and the snow surface was recorded to around 1.1 m. From end of September 2008 onwards, the measurement height decreased with increasing snow depth, but remained above 1.0 m until end of January 2009. At the end of the study period, an even smaller measurement height of less of around

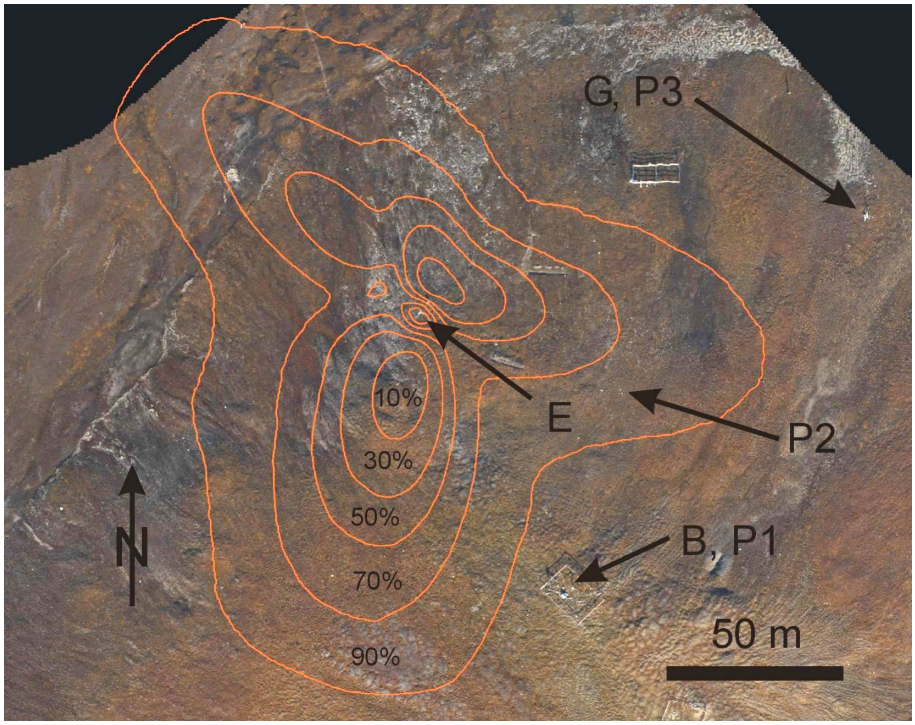

Figure 4.1: Orthorectified aerial photo with all installations (E: eddy covariance system; B: Bayelva climate station; G: gradient tower; P1, P2, P3: temperature profile measurements). The average footprint of the eddy covariance system from 1 July to 30 September 2008 is shown, with the percentages of the total flux originating within the respective contours (calculated according to Schmid, 1994).

0.6 m was recorded. Particularly flux data obtained at measurement heights below 1.0 m may bear a considerable uncertainty due to high-frequency losses (e.g. Moore, 1986) or drifting snow affecting the sonic anemometer (Lüers and Bareiss, 2009a).

For the snow-free period, the aerodynamic roughness length z_0 is estimated to be 7 mm from the measured values of u_* and the horizontal wind speed during neutral atmospheric stratification conditions (Eq. 2.81), which are recognized by a near-zero stability parameter $\zeta = z/L_*$. We then use the footprint model of Schmid (1994) to estimate the footprint area of the eddy covariance system, which is given in terms of a two-dimensional probability distribution of the flux source area for each half-hourly value. The calculation of the probability distribution is based on measured values of the horizontal wind speed, the wind direction, the stability parameter $\zeta = z/L_*$, the friction velocity u_* and the standard deviation of the horizontal wind speed perpendicular to the mean wind direction, as well as the roughness length and the measurement height (see Schmid, 1994). From the half-hourly probability densities, the average flux source area of longer periods can be calculated, which is displayed

in Fig. 4.1 for the snow-free period from July to September 2008. The main contributions originate from tundra areas in the prevailing wind directions from approximately 180° (wind from the glacier Austre Brøggerbreen), approximately 110° (wind from the inner Kongsfjorden) and from 310° to 350° (wind from the outer Kongsfjorden). Most importantly, areas with a strongly different surface cover, such as the gravel floodplain of the Bayelva River, which may constitute distinctly different flux source areas, are not contained in the footprint area.

4.1.3 Ground and snow heat fluxes

Calorimetric method

To calculate ground heat fluxes with the calorimetric method (see Sect. 2.3.1), a depth profile of the soil temperature, the volumetric soil water content and the volumetric heat capacity is required (Eq. 2.45). The volumetric soil water content is compiled from a profile of seven Time Domain Reflectometry (TDR) measurements located next to a profile of temperature measurements at the Bayelva station (P1 in Fig. 4.1), from which the content of sensible heat is derived. In soil samples collected in the vicinity of the temperature profile, the volumetric bulk (mineral and organic) content has been determined to 0.45 to 0.65. With the volumetric soil water content varying between 0.2 and 0.4 in TDR measurements, the volumetric heat capacity of the thawed soil can be estimated to $c_h = (2.3 \pm 0.5)\,\mathrm{MJ\,m^{-3}}$, while the corresponding volumetric heat capacity of the fully frozen soil is $c_h = (1.6 \pm 0.4)\,\mathrm{MJ\,m^{-3}}$ (Eq. 2.8). For the evaluation, a time series of the volumetric heat capacity is calculated for the soil layer around each TDR sensor according to the measured water and ice contents, which facilitates to evaluate the integral over the volumetric heat capacity in Eq. 2.45. Uncertainties arise from the bulk content and the absolute accuracy of the TDR method, which has been estimated to about 0.05 in measurements at the Bayelva station (Roth and Boike, 2001). In addition, the determination of the ground heat flux with the calorimetric method features a strong systematic bias, as the installations at the Bayelva station are not sufficient to capture the entire change of temperatures and soil water content to the depth of zero annual temperature amplitude. The maximum active layer thickness has been around 1.5 m during the study period, which is well below the deepest TDR sensor, located at 1.13 m. Therefore, the fluxes are biased, when the soil below the deepest TDR sensor thaws or freezes, which mainly affects the thaw period in August and September 2008 and the following refreezing period in October and November 2008. Another error source is the changing temperature in the permanently frozen soil below the deepest temperature sensor, that are not captured by our evaluation. The deep borehole next to the Bayelva station, which has not been available for the considered period, shows seasonal temperature variations on the order of 5 K at a depth of 1.5 m, 1 K at 2.5 m and less than 0.1 K at 5 m depth, which yields additional average fluxes of $\pm 0.5\,\mathrm{Wm^{-2}}$ for half-yearly periods for the used volumetric heat capacities of the soil.
When the ground is snow-covered, the average temperature of the snow pack is evaluated as the mean between the surface temperature (dermined from L_{out}, L_{in} and ε=0.99 for snow, using Eq. 2.130) and a temperature sensor at the

Table 4.1: Installations of the temperature profiles used to calculate the ground heat flux; z_{min}, z_{max}: minimum and maximum depths of the temperature sensors; Th: thermistor; TC: type T thermocouple; PT100: platinum resistance temperature sensor; TDR: measurement of soil water content using Time Domain Reflectometry.

profile	P1	P2	P3
z_{min}/ m	0.02	0.01	0.01
z_{max}/ m	1.55	0.25	0.30
soil	7 × PT100, 6 × TDR	1 × Th, 2 × TC	2 × Th, 1 × TC
snow	2 × PT100	3 × TC	3 × TC
installed	01/09/1998	07/07/2008	01/10/2008

snow-soil interface. The snow depth is recorded at the Bayelva station, while the average volumetric heat capacity of the snow has been determined in snow samples: in March 2009, snow density profiles have been determined gravimetrically in increments of 0.1 m at five sites in the eddy footprint area and in its vicinity. The average snow density is $\rho_{snow} = (0.37 \pm 0.05)\,\mathrm{g\,cm^{-3}}$, which results in a heat capacity $c_{h,snow} = (0.75 \pm 0.1)\,\mathrm{MJ\,m^{-3}K^{-1}}$ (using $c_{h,snow} = c_{h,ice} \times \rho_{snow}/\rho_i$). No measurements exist for a potential non-zero water and thus latent heat content of the snow pack. Therefore, the snow is completely excluded from the evaluation during the snow melt period (see Sect. 4.1.4). During winter, rain-on-snow events can occur in the study area (Putkonen and Roe, 2003; Boike et al., 2003b). The rain water percolates into the snow pack, and can constitute a significant energy input, as it finally refreezes within the snow pack or even at the snow-soil interface (see Sect. 4.4). The energy input from rain-on-snow events is estimated from the precipitation record of the Bayelva station, which only measures liquid precipitation. This is justified, since no run-off occurs during these events and the entire amount of water refreezes subsequently. Using the specific latent heat of fusion, L_{sl}, the total heat input through rain-on-snow events can be calculated, which is then converted to an average flux.
The calorimetric method is well suited to deliver average fluxes for longer periods, but has short-comings on the timescale of one hour due to the limited number of temperature and soil moisture sensors, which cannot resolve the temperature distribution in the uppermost soil column. Furthermore, a considerable uncertainty must be accepted for times, when the soil below the deepest TDR sensor thaws, so that the obtained ground and snow heat fluxes are verified with the conductive method.

Conductive method

The basic equations for determining ground and snow heat fluxes with the conductive method are outlined in Sect. 2.3.2. To evaluate the thermal diffusivity d_h, the heat capacity c_h and the thermal conductivity K_h of the soil during the snow-free period, we use the shallow temperature profile P2 (Fig. 4.1, Table 4.1).

The thermal diffusivity is fitted for different periods in July and August 2008, with values ranging from $d_h = 5.2 \times 10^{-7}\,\mathrm{m^2 s^{-1}}$ to $d_h = 6.5 \times 10^{-7}\,\mathrm{m^2\,s^{-1}}$. For the fit, we exclude periods with measurement errors or strong rain events, which may induce non-conductive transport of heat (see Eq. 2.29). The found variability of d_h may at least partly originate from natural processes, e.g. through changing soil water content. For the evaluation of the ground heat fluxes in the snow-free period, we apply a constant value $d_h = (5.5 \pm 1.0) \times 10^{-7}\,\mathrm{m^2 s^{-1}}$.
From soil samples and TDR measurements at the Bayelva station, the volumetric heat capacity of the soil is estimated to $c_h = (2.3 \pm 0.5)\,\mathrm{MJ\,m^{-3}}$ (see above), which results in a thermal conductivity of $K_h = (1.3 \pm 0.4)\,\mathrm{W m^{-1} K^{-1}}$. With K_h known, the ground heat flux can be evaluated (see Sect. 2.3). Note, that the considerable uncertainties on both d_h and c_h propagate to K_h, resulting in an uncertainty of more than 25% for the obtained ground heat flux.
During the winter 2008/2009, a profile of three temperature sensors in the snow pack located at P3 is used to fit the thermal diffusivity of the snow. This is possible from December 2008 onwards, as soon as the snow pack has reached the uppermost sensor. Initially, the array is contained in the young snow pack, but gets progressively buried with increasing snow depth. The obtained values range from $d_h = 4.5 \times 10^{-7}\,\mathrm{m^2 s^{-1}}$ to $d_h = 7.0 \times 10^{-7}\,\mathrm{m^2 s^{-1}}$, with a tendency towards higher values of d_h at the end of the considered period for the then older snow. As no measurements of the thermal diffusivity of the overlying, not instrumented snow pack are available, a constant value of $d_h = (5.5 \pm 1.5) \times 10^{-7}\,\mathrm{m^2 s^{-1}}$ is chosen for the evaluation of the snow heat flux, while the found variability of d_h is included as uncertainty. With the volumetric heat capacity $c_{h,\mathrm{snow}} = (0.75 \pm 0.1)\,\mathrm{MJ\,m^{-3} K^{-1}}$ determined in the snow samples (see above), the resulting snow conductivity is $K_h = (0.45 \pm 0.15)\,\mathrm{W\,m^{-1} K^{-1}}$. While the error in this determination is large, the thermal conductivity of snow is known to vary naturally in a large range depending on the structure of the snow. Sturm et al. (1997) presents a large data set, which displays a scatter of a more than a factor of two for thermal conductivities at similar snow densities. Since the temperature sensors are placed at fixed heights above the ground, it is only possible to infer the heat flux within the snow pack up to the height of the uppermost sensor, which is clearly different from the targeted heat flux through the snow surface. Therefore, the snow surface temperatures inferred from measurements of long-wave radiation (Eq. 2.130) at the Bayelva climate station, next to P1, are used as upper boundary condition, while temperatures at the snow-soil interface at P1 are used as lower boundary. The snow heat flux is then calculated (see Sect. 2.3) for periods defined by snow heights that fall within classes of 0.1 m increments, with the snow height being measured next to P1 with an ultrasonic ranging sensor. This method induces discontinuities in the flux at the boundary of each two periods, so the flux values have to be discarded at these boundaries. The obtained snow heat flux is associated with an error of approximately 30%, which mainly originates from the uncertainty in the thermal conductivity. It must be emphasized that the snow pack is treated as homogeneous in time and space, which does not reflect processes such as aging and densification of the snow.
When a rain-on-snow event occurs, the fluxes are discarded, until all measured temperatures in the snow decrease below -0.5°C and refreezing processes can be excluded. This leads to the exclusion of in total seven days during the winter 2008/2009. Particularly the strong rain-on-snow events provoke a pronounced

warming of the underlying soil column, which then slowly cools by means of conductive heat transport through the snow (see Sect. 4.4). Therefore, the conduction method accounts for at least some part of the heat input through rain-on-snow events, although the time directly after the rain-on-snow events is excluded.

4.1.4 Melt energy of the snow

During snow melt, the latent heat consumed by the melting snow Q_{melt} appears as an additional component in the surface energy budget. Between 25 May and 28 May 2008, before the onset of the snow melt, the snow water equivalent of the snow at the study site has been estimated by seven snow density measurements and systematic snow depth measurements on a $20\times20\,\mathrm{m}^2$ grid. With the specific latent heat of fusion, L_{sl}, the total energy required to melt the snow can be evaluated, which is then converted to an average flux for the snow melt period. A considerable uncertainty is induced by a basal ice layer underneath the snow with a thickness of more than 0.15 m at some points, which has not been spatially surveyed.

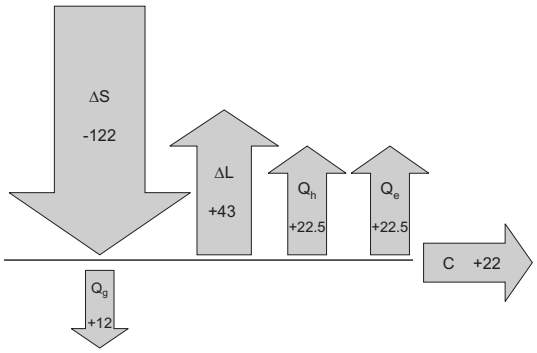

Figure 4.2: Schematic diagram of the contributions of the surface energy budget for the summer period. The area of the arrows is proportional to the relative importance in the energy budget. Arrows pointing away from the surface indicate positive fluxes. The flux values are given in Wm^{-2}.

4.2 The annual surface energy budget of the study area

The one year study period is divided into six segments, each of which feature distinct characteristics of the surface energy budget. The transition between different segments is mostly gradual, but the segmentation is closely orientated at "real" events, such as the onset or termination of the snow melt or the beginning of the polar night. The average fluxes for each of the segments are presented in Table 4.2 at the end of the section.

4.2.1 Summer (1 July 2008–31 August 2008)

The summer period is characterized by a strong forcing by short-wave radiation and the absence of the seasonal snow cover. The net short-wave radiation ΔS is compensated by the net long-wave radiation, the sensible and latent heat flux, and the ground heat flux, which leads to the seasonal thawing of the active layer (Fig. 4.2, Table 4.2). Cloudy conditions are typical for the summer season (Table 4.2), which effectively reduces the incoming solar radiation. The difference in the incoming short-wave radiation S_{in} between cloud-covered and clear skies can exceed $150\,\mathrm{Wm}^{-2}$ in the daily average. On the other hand, the incoming long-wave radiation L_{in} increases during cloudy periods, with daily average differences of around $80\,\mathrm{Wm}^{-2}$. However, this does not nearly compensate for the reduction of the short-wave radiation, so that a cloud cover considerably reduces the incoming radiation. The absolute values of L_{in} range from -230 Wm^{-2} to -340 Wm^{-2}, while the outgoing long-wave radiation L_{out} ranges from 300 Wm^{-2} to 400 Wm^{-2}, corresponding to surface temperatures between -5 °C and +17 °C (Eq. 2.130).

During the polar day season, approximately until mid of August, the atmospheric stratification is either unstable or neutral, characterized by negative values of $\zeta = z/L_*$. Later, neutral to weakly unstable atmospheric stratifica-

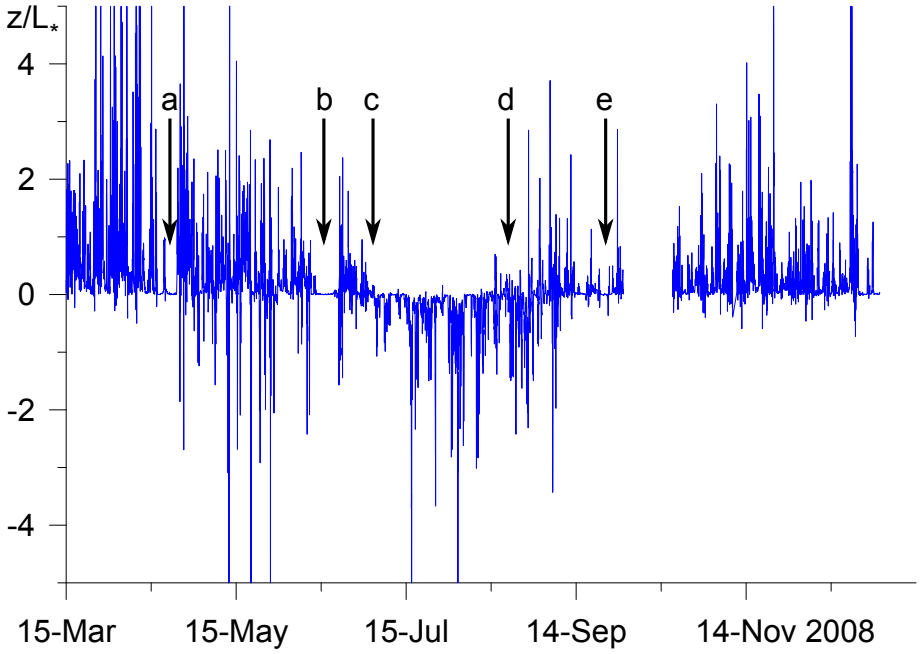

Figure 4.3: Atmospheric stability parameter $\zeta = z/L_*$ over the period from 15 March to 31 December 2008. The atmospheric stratification is predominantly stable before snow melt (c), although prolonged periods with neutral stratification (a and b) and sporadic unstable stratifications during midday can occur. During the snow-free time of the polar day season, the atmospheric stratification is predominantly unstable. With a day-and night cycle from end of August, the stratification follows a diurnal pattern (d) between unstable during the day and stable during the night, before returning to predominantly stable conditions (e) at the end of the fall season.

tions, $\zeta \leq 0$, prevail during the day, while stable atmospheric stratification are observed during the night, $\zeta \geq 0$ (Fig. 4.3). The sensible, latent and ground heat fluxes are shown in Fig. 4.4. The average Bowen ratio is approximately one, but it shows strong variations, which are closely related to the soil water content of the surface layer (Figs. 4.4, 4.5). For a wide range of intermediate soil moisture conditions, it remains around one, but extremely wet or dry conditions lead to Bowen ratios of around 0.25 or 2, respectively (Fig. 4.5). The sensible and the latent heat flux display a strong diurnal amplitude, with peak fluxes between 60 Wm^{-2} and 120 Wm^{-2} associated with maxima of net radiation around midday. At the lowest sun angles, around midnight, the absolute values of both fluxes decrease to close to zero, but usually remain positive. The latent heat flux observed in July and August 2008 corresponds to a total evaporation of 48 mm, which is significantly more than the precipitation of 32 mm recorded during the same period. This can be related to the drying of the water-saturated tundra after snow melt. The average ground heat fluxes peaks at the beginning of the summer period, when the thaw front is close to the soil surface and a strong temperature gradient exists in the soil. Peak values are around 60 Wm^{-2}, which

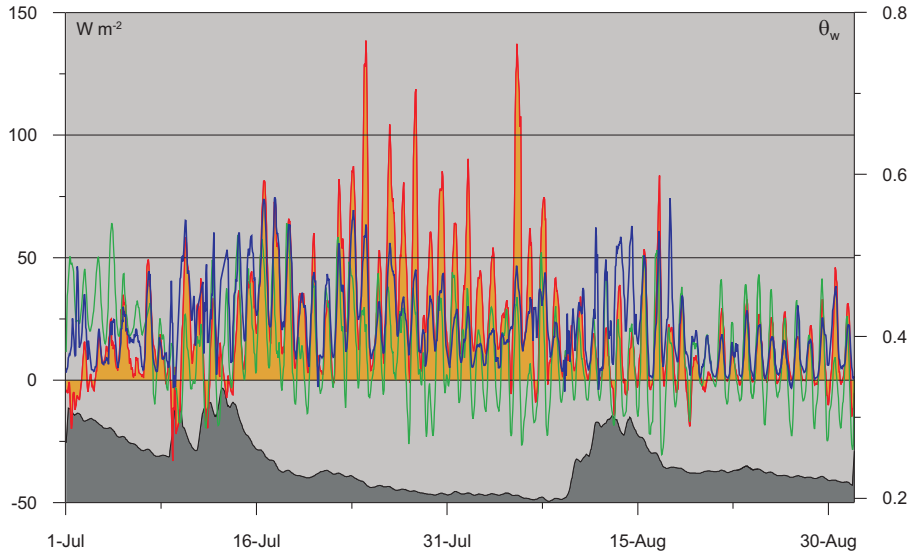

Figure 4.4: Sensible (red), latent (blue) and ground heat fluxes (green) for the summer period from 1 July to 31 August 2008 (left axis). The soil water content θ_w measured with Time Domain Reflectometry at a depth of 0.1 m at the Bayelva climate station is shown below (right axis).

is of comparable magnitude as the sensible and latent flux (Fig. 4.4). However, the storage effect of the soil is reflected in generally negative ground heat fluxes of up to -30 Wm^{-2} during night times (i.e. times with low solar angle during polar day), so that the average ground heat flux is considerably smaller than the average sensible and latent heat flux (Fig. 4.2, Table 4.2). An energy balance closure term of 22 Wm^{-2} remains, which is further discussed in Sect. 4.2.8.

4.2.2 Fall (1 September 2008–30 September 2008)

During fall, the net short-wave radiation strongly decreases due to the much lower sun angles, but a permanent snow cover has not yet formed and a sustained refreezing of the active layer has not started. September 2008 was characterized by a series of cyclones, which transported warm air masses from the south and led to strong precipitation. At Ny-Ålesund, 99 mm of precipitation were recorded, almost entirely as rain, which is more than twice of the usual September precipitation. The many rain events result in frequent data gaps and generally poor data quality regarding the eddy covariance measurements, but the general magnitude of the average fluxes should still be correctly reproduced. The observed latent heat flux (Fig. 4.6, Table 4.2) corresponds to an evaporation of 9 mm during the fall period, so that the precipitation is not even roughly balanced by the evaporation. As a consequence, the water content of the soil is increased compared to the summer season, just before the soil starts to freeze. Most likely, this process still occurs, when the precipitation during September is not unusually high. Other than during summer, the sensible heat flux is on

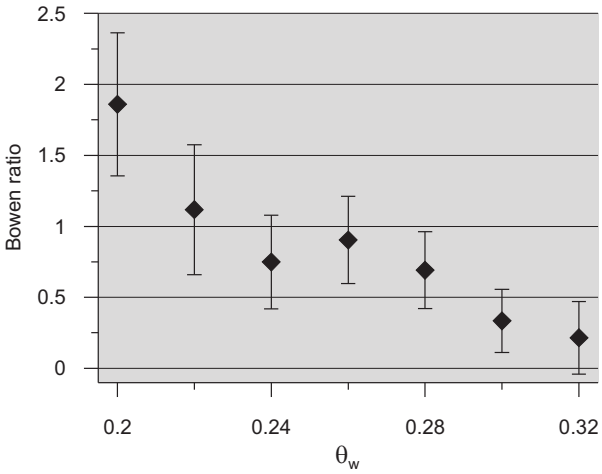

Figure 4.5: Average daily Bowen ratio vs. volumetric soil water content θ_w in soil water content classes of widths of 0.02 for the summer period from 1 July to 31 August 2008 (see Fig. 4.4). The points are drawn at the center of each class, and the error bars represent the standard deviation of the Bowen ratio values within one class. Three days with negative average Q_h are discarded.

average negative, i.e. the advection of relatively warm air results in a warming of the surface. The average ground heat flux is still positive, corresponding to a transport of energy in the ground, which results in a further increase of the active layer depth.
In 2008, the perennial snow cover has formed on 29 September, when the average incoming short-wave radiation at the Bayelva station is approximately -12 Wm^{-2} (average data from 25 September to 5 October 2008).

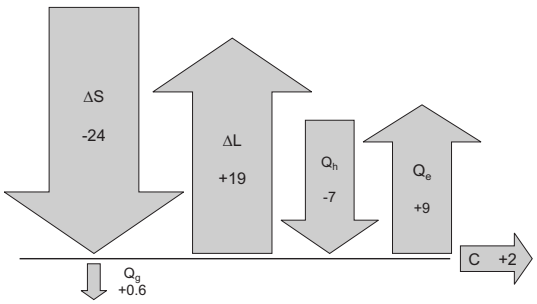

Figure 4.6: Schematic diagram of the contributions of the surface energy budget for the fall period. Notation as in Fig. 4.2.

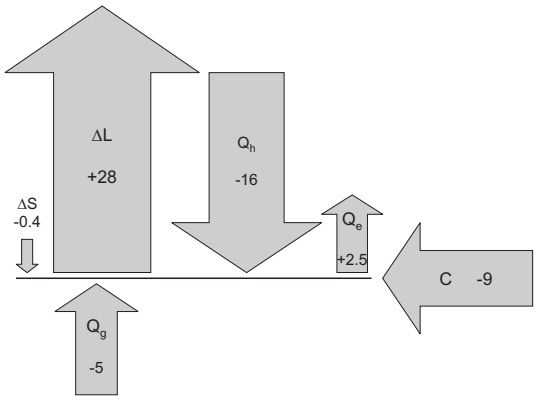

Figure 4.7: Schematic diagram of the contributions of the surface energy budget for the dark winter period. Notation as in Fig. 4.2.

4.2.3 Dark winter (1 October 2008–15 March 2009)

The short-wave radiation is essentially zero during this period (Fig. 4.7, Table 4.2), as it mostly falls within the polar night, which lasts from 25 October to 14 February in Ny-Ålesund. The peak values of ΔS during midday at the very beginning and end of the dark winter period are around -20 Wm^{-2}. In the absence of short-wave radiation, the long-wave radiation becomes the main forcing of the system. Between October 2008 and March 2009, L_{in} ranges from -140 Wm^{-2} to -320 Wm^{-2}, while L_{out} is between 190 Wm^{-2} and 320 Wm^{-2}. For the entire period, the absolute value of L_{in} is found to be equal or smaller than L_{out}. With an average value of 28 Wm^{-2}, the net long-wave radiation represents the dominant energy loss term during dark winter.
The net long-wave radiation is mainly compensated by a negative average sensible heat flux, corresponding to a warming of the surface and a cooling of the atmosphere. With an average of -16 Wm^{-2}, the sensible heat flux is a strong supply of energy to the snow surface. In addition, the snow heat flux compensates for about 20% of the energy loss by net long-wave radiation. The latent heat flux is found to be of minor importance in the overall surface energy budget during the dark winter period (Fig. 4.7, Table 4.2). A residual term of -9 Wm^{-2} remains.
During the dark winter period, we estimate about 80 mm of rain, which can be largely attributed to three rain-on-snow events in October 2008, January 2009 and February 2009 (see also Fig. 4.24). This corresponds to an average heat flux of -1.8 Wm^{-2} (see Sect. 4.1.3) and is thus significant compared to the heat flux supplied by the refreezing active layer, which is about -5 Wm^{-2} (calorimetric method for Q_g).

The incoming long-wave radiation is clearly the determining factor for the temperature of the snow surface and hence for the outgoing long-wave radiation (Fig. 4.8), but a significant influence of other factors, particularly of the wind speed, remains. At high wind speeds, atmospheric turbulence is mechanically induced. This facilitates the exchange of energy between the surface and the warmer atmosphere, so that the surface temperature is sustained at higher val-

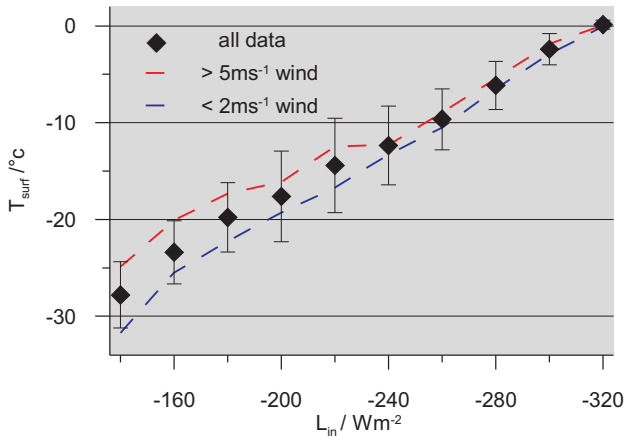

Figure 4.8: Surface temperature T_{surf} vs. incoming long-wave radiation L_{in} during the dark winter period in classes of L_{in} of 20 Wm^{-2} width. The points are drawn at the center of each class, and the error bars represent the standard deviation of the surface temperature values within one class. The red and blue lines represent the average curves for situations with high and low wind speeds.

ues (Fig. 4.8). The influence of the wind speed is clearly less pronounced for large values of L_{in} and high surface temperatures. A possible explanation is that the gradient between the air and the snow surface temperature is generally small in these cases, which prevents a strong exchange of energy independent of the formation of turbulence.

Throughout the entire dark winter period, strong sensible fluxes around $-30\,\mathrm{Wm}^{-2}$ to $-70\,\mathrm{Wm}^{-2}$ are associated with high wind speeds, which cause neutral or only weakly stable atmospheric stratifications, with a stability parameter $\zeta = z/L_*$ close to zero. When wind speeds are low, a stable stratification and a strong near-surface temperature inversion can form, which significantly reduces the fluxes between surface and atmosphere. This is illustrated in Fig. 4.9, which shows surface temperature, wind speed, air temperature inversion between 9.3 m and 1.3 m height and the fluxes Q_h, Q_e and Q_g for a period with approximately constant L_{in} of around -180 Wm^{-2}. Initially, the wind speed is low and a stable atmospheric stratification exists, which prevents a significant sensible heat flux. Thus, the surface temperature cannot be sustained and starts to decrease to a minimum value of -18°C. This increases the temperature gradient across the snow pack and hence triggers a strong snow heat flux, which moderates the drop in surface temperature. Around 27 November, an increase in wind speed breaks up the stable stratification, and significant sensible heat fluxes of up to -50 Wm^{-2} stabilize the surface temperature around -15°C. Decreasing wind speeds around 29 November again lead to a stable atmospheric stratification, with an associated drop in surface temperature to about -23°C. Even during the polar night, considerable latent heat fluxes of up to 30 Wm^{-2} occur, mainly at high wind speeds and neutral atmospheric stratifications (see Fig. 4.9). These positive fluxes correspond to a cooling of the surface through sublimation of snow or, when present, evaporation of water. Particularly in

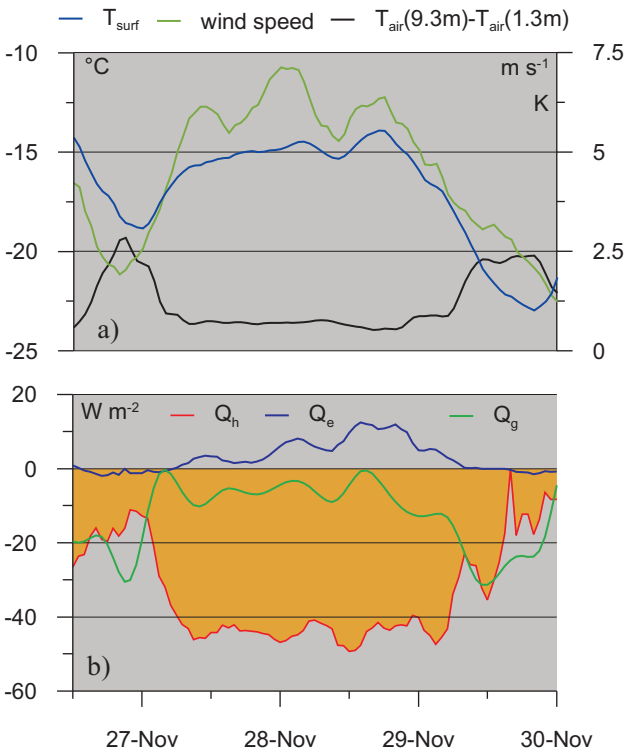

Figure 4.9: (a) Surface temperature (left axis), wind speed (right axis), and temperature difference at the gradient tower (right axis) for a period in November 2008. The snow depth is 0.7 m at this time. (b) Sensible heat flux Q_h, latent heat flux Q_e and snow heat flux Q_g (conductive method) for the same period.

case of stable stratifications, negative latent heat fluxes of up to -5 Wm^{-2} are detected (Fig. 4.9). Hence, a limited amount of condensation or resublimation occurs, but its contribution to the total energy budget is insignificant. The total net sublimation or evaporation during dark winter amounts to 30 $\mathrm{kg\,m}^{-2}$, which corresponds to a snow column of almost 0.1 m at the recorded snow densities (see Sect. 4.1.3).

The snow heat flux is of great importance, particularly when a stable atmospheric stratification limits the sensible heat flux. Then, the snow heat flux becomes the dominant energy supply. The refreezing active layer provides a weak, but constant flux of energy, which is reflected in a negative average heat flux through the snow surface. Nevertheless, the storage effect of the snow and strong fluctuations of the surface temperature result in both positive and negative snow heat fluxes at the snow surface.

A strongly stable atmospheric stratifications occurs frequently, but usually does not last longer than a few days. The stability parameter $\zeta = z/L_*$ exceeds values of 0.5 in about 15% of the time, while values greater than 5 have only been recorded in about 1% of the time (Fig. 4.3). During stable stratifications, the temperature inversion in the lowest 10 m of the atmosphere can be considerable,

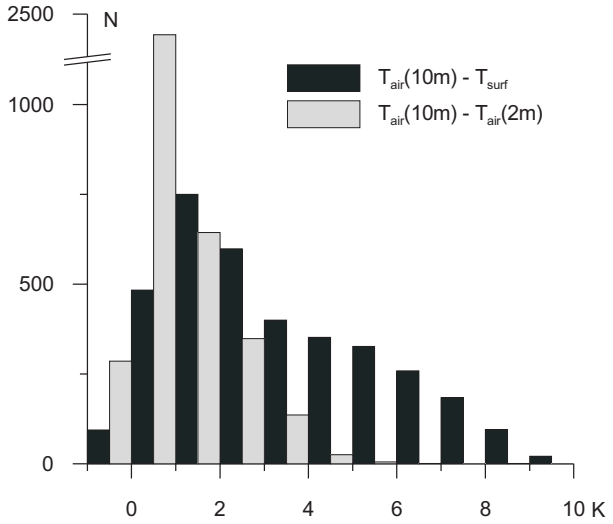

Figure 4.10: Number of hourly values during the dark winter period N vs. temperature difference (in classes of 1 K) between air temperature at 10 m height and air temperature at 2 m height, and air temperature at 10 m height and surface temperature, respectively. Due to the snow accumulation, the heights decrease from 10 m to 8.8 m and 2.0 m to 0.8 m during the considered period.

so that an average difference of +0.8 K occurs between the air temperatures at 10 m and 2 m height (Fig. 4.10). An even more pronounced temperature inversion is found between the surface temperature and the air temperature measured at different heights, i.e. $T_{\mathrm{air}}(2\,\mathrm{m})$ and $T_{\mathrm{air}}(10\,\mathrm{m})$, where temperature differences of more than 5 K are common (Fig. 4.10).

4.2.4 Light winter (15 March 2008–15 April 2008)

The net short-wave radiation is rapidly increasing in light winter, although its role is still limited due to the high snow albedo of about 0.8. Other than that, the surface energy budget very much resembles the dark winter period: the energy loss through the net long-wave radiation is compensated to equal parts by the sensible heat flux and the short-wave radiation (Fig. 4.11, Table 4.2). The snow heat flux still remains negative, corresponding to a further cooling of the underlying soil column. At the end of the light winter period, the lowest soil temperatures are reached, with about -8°C at the soil surface and -4°C at 1.5 m depth at the Bayelva station.

4.2.5 Pre-melt period (16 April 2008–31 May 2008)

From mid of April, the net short-wave radiation ΔS becomes the dominant energy supply, with an average of -41 Wm^{-2} (Fig. 4.12, Table 4.2). The sensible heat flux provides an additional energy of -8 Wm^{-2}, while the net long-wave

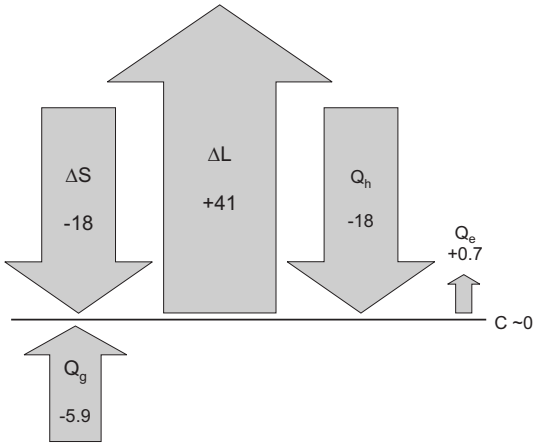

Figure 4.11: Schematic diagram of the contributions of the surface energy budget for the light winter period. Notation as in Fig. 4.2.

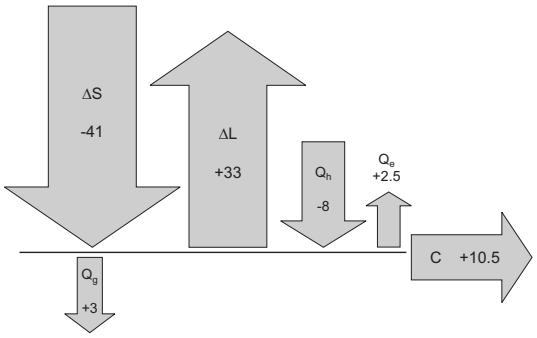

Figure 4.12: Schematic diagram of the contributions of the surface energy budget for the pre-melt period. Notation as in Fig. 4.2.

radiation ΔL is the main balancing factor, with an average of $33\,\mathrm{Wm}^{-2}$. The latent heat flux is positive, but remains insignificant with an average of $2.5\,\mathrm{Wm}^{-2}$. The snow and soil column start to gradually warm during the pre-melt period, which is reflected in a now positive average snow heat flux. A positive residual of around $10\,\mathrm{Wm}^{-2}$ remains, which largely builds up at the end of the pre-melt period. This indicates that melting of the snow already occurs, which is not accounted for in the surface energy budget during the pre-melt period. One snow melt event has indeed been observed on 30 May. Hereby, the temperature sensor at the snow-soil interface at P1 recorded a rapid temperature increase of 2 K within a few hours, which can only be explained by infiltrating melt water. In addition to this single strong melt event, it is possible that more snow melt occurs close to the surface without causing detectable melt water infiltration.

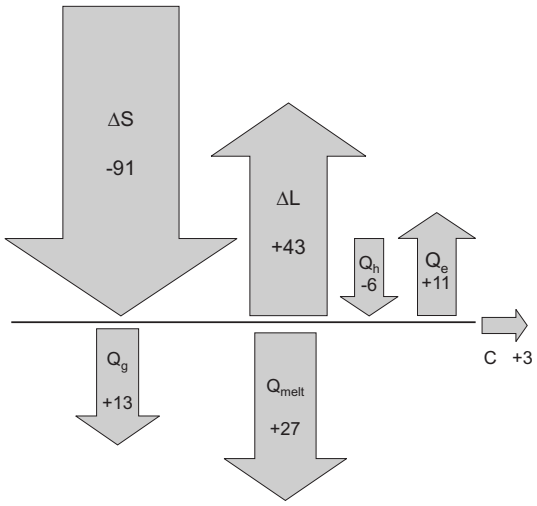

Figure 4.13: Schematic diagram of the contributions of the surface energy budget for the snow melt period. Notation as in Fig. 4.2.

4.2.6 Snow melt (1 June 2008–30 June 2008)

The warming of the snow pack towards 0°C at the end of the pre-melt period is followed by the period of snow melt. Hereby, the energy consumed by the phase change of the melting snow appears as a dominant component in the energy budget (Fig. 4.13, Table 4.2). The average snow density before snow melt in 2008 has been determined to $0.35\,\mathrm{g\,cm^{-3}}$, with an average snow depth of 0.6 m. Thus, the average latent heat stored in the snow pack amounts to $70\,\mathrm{MJ\,m^{-2}}$, which yields an average energy consumption of $27\,\mathrm{Wm^{-2}}$ for the time between 1 June and 30 June, during which most of the snow melt occurs in 2008.
The net short-wave radiation ΔS increases considerably (Fig. 4.13, Table 4.2) despite of the still high albedo of the snow. It is partly compensated by the net long-wave radiation ΔL, so that the average net radiation Q_{net} is around $-40\,\mathrm{Wm^{-2}}$. Until large snow-free patches appear, the air temperature is confined in a narrow range between -1°C and +5°C, while the snow surface temperature remains close to 0°C due to the melt processes, so that the resulting temperature gradient is necessarily small. This yields weak sensible heat fluxes, with peak values around $-20\,\mathrm{Wm^{-2}}$ and an average of $-6\,\mathrm{Wm^{-2}}$. The positive latent heat flux, which causes a cooling of the surface, becomes more and more significant during the snow melt period, with an average of $11\,\mathrm{Wm^{-2}}$. Most likely, it is stimulated by the presence of water due to the melting snow.
During the snow melt period, the net radiation Q_{net} is a much stronger energy supply compared to the sensible heat flux (Fig. 4.13, Table 4.2). The snow melt can therefore be considered as almost entirely controlled by radiation, which confirms earlier studies during snow melt by Harding and Lloyd (1998) and Boike et al. (2003a) at the same location. Our study can also confirm the order of magnitude and sign of the fluxes of these previous studies.
During snow melt, infiltrating melt water and subsequent refreezing processes dominate the snow pack, which is more or less isothermal close to 0°C. The

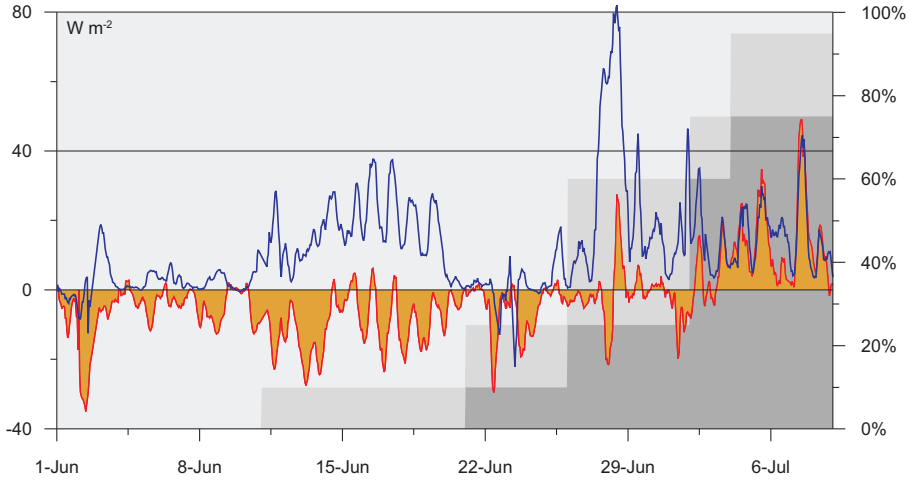

Figure 4.14: Sensible (red) and latent heat flux (blue) for the snow melt and the beginning of the summer period (left axis). The light gray area represents the snow-covered and the dark gray area the snow-free fraction of the surface area around the eddy covariance system (right axis), which is taken to be approx. equal to the 90% source limit shown in Fig. 4.1. The intermediate gray area indicates the uncertainty in area fraction between consecutive surveys.

underlying soil still shows colder temperatures, which results in a heat transport from the snow-soil interface into the soil. The energy consumed by this ground heat flux is provided by the cooling and refreezing of melt water at the snow-soil interface, but initially originates from the short-wave radiation. At $13\,\mathrm{Wm^{-2}}$ (estimated with the calorimetric method), this ground heat flux constitutes an important component of the surface energy budget. The large value can be explained by the fact that the temperatures in the upper soil column are within the freezing range of the soil (Roth and Boike, 2001), where a temperature change is associated with a change in latent heat content.

The sensible and latent heat fluxes during the snow melt period and the first eight days of the summer period, when snow patches are still present, are displayed in Fig. 4.14. As in winter, pronounced flux peaks such as the one around 15 June are associated with high wind speeds and neutral stratifications. Dewfall or white frost (negative latent heat flux), which has been found during snow melt in previous studies (Takeuchi et al., 1995; Boike et al., 2003b), occurs in few cases, but is insignificant as an energy source for snow melt. In 2008, the evolution of the snow-free areas around the eddy covariance system has been monitored in intervals of two to ten days using aerial photography and systematic GPS-surveys. The results show that a patchwork of snow-covered and snow-free surfaces exists for several weeks due to the large spread in snow depths throughout the study area. Snow-free areas feature a completely different energy turnover compared to the snow patches. Accordingly, the sensible and latent heat fluxes must be seen as a mixture of both surface properties and their relevant percentages of the total footprint area. An example is the pronounced latent heat flux peak of about $80\,\mathrm{Wm^{-2}}$ on 28 June (Fig. 4.14),

which is presumably triggered by a high percentage of wet snow-free patches with strong evaporation in the footprint at that time. Meanwhile, the sensible heat flux is still negative or only slightly positive with absolute values below $20\,\mathrm{Wm}^{-2}$, most likely because the remaining cold snow patches prevent a net exchange of sensible heat. The sensible heat flux keeps on alternating between negative and positive values for another couple of days, until it finally turns positive, after about three quarters of the area are free of snow (Fig. 4.14).

Table 4.2: Average values for air temperature T_{air}, precipitation P, relative humidity RH, cloud fraction cf (see Sect. 3.2.5) and for the various contributions of the surface energy budget for different segments of the study period. S_{in}, S_{out}, ΔS: incoming, outgoing and net short-wave radiation; L_{in}, L_{out}, ΔL: incoming, outgoing and net long-wave radiation; Q_h: sensible heat flux; Q_e: latent heat flux; $\mathrm{Q}_{g\,cal}$, $\mathrm{Q}_{g\,\mathrm{cond}}$: ground heat flux, determined by calorimetric and conductive method (see Sect. 2.3); Q_{melt}: heat flux consumed by melting snow; C: residual of the energy balance. Values in parentheses are estimates or based on data records with frequent data gaps. The value for $Q_{g\,\mathrm{cal}}$ during dark winter is composed of the flux due to the refreezing of the active layer, -5.0 Wm^{-2}, and a flux of -1.8 Wm^{-2} due to rain-on-snow events.

	Summer	Fall	Dark winter	Light winter	Pre-melt	Snow melt	Total
	01/07/08	01/09/08	01/10/08	15/03/08	16/04/08	01/06/08	15/03/08
	–31/08/08	–30/09/08	–15/03/09	–15/04/08	–31/05/08	–30/06/08	–15/03/09
$T_{\mathrm{air}}/\,^{\circ}\mathrm{C}$	5.0	2.7	−10.1	−16.0	−5.6	2.0	−5.4
$P/\,\mathrm{mm}$	32	99	278	12	11	8	440
RH	82%	81%	73%	59%	71%	73%	74%
cf	6.4/ 8	6.9/ 8	5.5/ 8	3.6/ 8	5.7/ 8	5.5/ 8	5.6/ 8
$S_{\mathrm{in}}/\,\mathrm{Wm}^{-2}$	−144	−33	−2.1	−73	−185	−261	−78
$S_{\mathrm{out}}/\,\mathrm{Wm}^{-2}$	22	9	1.7	55	144	(170)	42
$\Delta S/\,\mathrm{Wm}^{-2}$	−122	−24	−0.4	−18	−41	(−91)	−36
$L_{\mathrm{in}}/\,\mathrm{Wm}^{-2}$	−303	−299	−234	−196	−255	−276	−254
$L_{\mathrm{out}}/\,\mathrm{Wm}^{-2}$	346	318	262	237	288	319	286
$\Delta L/\,\mathrm{Wm}^{-2}$	43	19	28	41	33	43	32
$Q_h/\,\mathrm{Wm}^{-2}$	22.5	(−7)	−16	−18	−8	−6	−6.9
$Q_e/\,\mathrm{Wm}^{-2}$	22.5	(9)	2.5	0.7	2.5	11	6.8
$Q_{g\,\mathrm{cal}}/\,\mathrm{Wm}^{-2}$	(11)	–	(−5.0)−1.8	−3.1	3.0	13	∼0.5
$Q_{g\,\mathrm{cond}}/\,\mathrm{Wm}^{-2}$	12	(0.6)	−5.0	−5.9	–	–	
$Q_{\mathrm{melt}}/\,\mathrm{Wm}^{-2}$	?	?	0	0	?	(27)	2.3
$C/\,\mathrm{Wm}^{-2}$	22	2	−9	0	10.5	3	1

4.2.7 The annual budget

The presented data set allows an estimate for the annual net budget for each of the components of the energy budget (see Table 4.2). With an average value of -35 Wm^{-2}, the net short-wave radiation is the dominant source of energy. It is almost compensated by the net long-wave radiation, with an annual average of 32 Wm^{-2}. The latent heat flux is usually positive, and the annual average of 6.8 Wm^{-2} is almost exclusively a result of strong fluxes during snow melt, summer and fall. The value corresponds to a water loss of approximately 85 mm, so that about 20% of the precipitation of the study period evaporates or sublimates. While insignificant for the overall energy budget, positive average latent heat fluxes are detected during the polar night, which has not been observed at similar latitudes on arctic sea ice by the SHEBA study (Persson et al., 2002). The average sensible heat flux is negative with a value of -6.9 Wm^{-2}, but shows a strong seasonal dependence. While the study site is actually a strong heat source for the atmosphere during the two months of summer ($Q_h = 22.5\,\mathrm{Wm}^{-2}$), it is a heat sink for the rest of the year, with an average of $Q_h = -13\,\mathrm{Wm}^{-2}$. During winter, the nearby ice-free sea is most likely an important heat source for the near-surface atmosphere, which might increase the air temperatures at the study site and thus fuel the relatively strong sensible heat transfer to the snow surface. The average ground heat flux is close to zero, as should be the case for equilibrium or near-equilibrium conditions of the permafrost. A strong warming of the permafrost at the study site has not occurred over the course of the considered year.
During winter, the system is entirely forced by long-wave radiation, while a strong short-wave forcing dominates the system during summer. The timing of the albedo change induced by the snow melt is a key point for the annual surface energy budget, since the snow at the study site usually disappears between end of May and beginning of July (Winther et al., 2002), when the incoming short-wave radiation reaches its annual maximum with daily averages of about -200 Wm^{-2}. The correct representation of the snow melt must therefore be considered crucial to successful modeling of the annual surface energy budget and the permafrost dynamics. In contrast, the timing of the albedo change due to the formation of the snow cover in fall is of little importance, as the daily average for incoming short-wave radiation is already low during September, when the permanent snow cover usually forms (Winther et al., 2002).

4.2.8 Concluding remarks on the energy balance closure

For nearly all periods, a residual term of the surface energy budget remains, which is usually found in investigations of the surface energy budget (overview in Foken, 2008b). We can identify four levels of uncertainty in our study: (a) measurement errors; (b) uncertainties due to assumptions taken or parameters used; (c) inconsistencies due to different measurement locations and/or footprint areas; (d) systematic bias inherent in the measurement method.

(a) The BSRN radiation measurements are supposedly associated with an accuracy of better than 10 Wm^{-2} (Ohmura et al., 1998). Unsupervised measurements under arctic conditions bear an additional potential for measurement

errors due to e.g. snow-covered sensors or instrument malfunctions. The unmaintained radiation measurements are checked against the reference data set of the BSRN station, so that unreasonably large deviations are prevented. The soil temperature measurements from which the ground heat flux is inferred contain a few spikes and erroneous measurements, which are not considered in the evaluation. We conclude that random measurement errors and data gaps do not strongly influence the long-term averages presented in this study. Only in the fall period, data gaps of the turbulent fluxes occur frequently (see Sect. 4.2.2), so that a bias of the average fluxes is possible.

(b) To evaluate the thermal conductivity, the soil and snow are idealized as a domain with constant thermal properties (in space and time) and purely conductive heat transfer is assumed (see Sect. 2.3.2). In reality, the soil or snow properties can change, which is reflected in different values for the thermal diffusivity, if the fit is conducted for different periods (see Sect. 4.1.3). The range of obtained diffusivity values, in conjunction with the spread of soil or snow compositions determined in field measurements, is used to estimate the uncertainty of the thermal conductivity. Despite the resulting relative error of 25–30%, the absolute error of the ground or snow heat flux remains at least a factor of four smaller than the energy balance closure term due to the generally low magnitude of the fluxes. Another issue associated with the ground heat flux is the storage effect of the thin soil layer above the uppermost sensor, which is not accounted for in the calculation of Q_g. However, the day and night-time contributions of this effect cancel, so it is insignificant on the considered timescales.

(c) Point measurements from different locations are considered as well as eddy covariance measurements, which integrate over an extended footprint area (Amiro, 1998; Schmid, 2002) with considerable small-scale heterogeneity of the surface cover (Fig. 4.1). As the study focuses on average fluxes, only a sustained difference between the average flux of the eddy footprint area and the flux at the point measurement site is of importance. Firstly, this may be the case for the albedo, mainly for the snow melt, summer and fall period. From 40 point measurements (see Sect. 4.1.1), we estimate the spread in summer albedo throughout the study area and thus the albedo uncertainty to about 0.05. For the snow melt period, the albedo value is estimated from the BSRN station, where the albedo decreases from 0.8 to 0.5 during the course of the snow melt. An additional uncertainty arises, as a small fraction of snow-free surfaces with much lower albedo contributes to the eddy footprint area at the end of the snow melt period (Fig. 4.14), so that a maximum albedo uncertainty of 0.1 appears realistic during snow melt. The potential bias in net short-wave radiation may thus be as large as $8\,\mathrm{Wm^{-2}}$ for the summer and $25\,\mathrm{Wm^{-2}}$ for the snow melt period, while it is presumably negligible for the other periods. In addition to albedo variations, the average surface temperature could vary due to differences in soil moisture and surface properties, which would affect both L_{out} and Q_g. A sustained difference of 1 K would lead to a bias of L_{out} on the order of $5\,\mathrm{Wm^{-2}}$. In Sect. 4.3, the spatial variability of the surface temperature is investigated for a site located approximately 400 m from the eddy covariance system. Hereby, sustained differences in the surface temperature of more than 2 K

between wet and dry areas have been observed, so that a bias of L_{out} of 5 to 10 Wm^{-2} appears possible. An uncertainty in the ground heat flux is not only induced by variations of the surface temperature, but also by spatial variations of the soil properties, which most likely occur throughout the study area. However, the good agreement between the fluxes inferred with different methods from the locations P1 and P3 during the summer period gives us confidence in the accuracy of Q_g, within the liberal error estimates of about 25–30% (see above).

(d) A basal ice layer present in parts of the study area has not been included in the survey of the snow water equivalent prior to snow melt (see Sect. 4.1.4). An average ice layer thickness of 5 cm corresponds to an additional flux of 5 Wm^{-2} in the snow melt period, so the true value of Q_{melt} during the snow melt period is most likely higher than 27 Wm^{-2} (Table 4.2). Furthermore, there may be a contribution of Q_{melt} in the pre-melt period (see Sect. 4.2.5).

In eddy covariance studies on the surface energy budget, the failure to close the energy balance is commonplace (Inagaki et al., 1996). A bias of more than 25% on the obtained turbulent fluxes has been estimated in some studies (Wilson et al., 2002), which could largely explain the closure terms observed in this study. In Sect. 2.5.2, the principal problem to obtain covariances from time averaging at a single point in space for non-stationary conditions has been outlined. To further investigate the origin of the closure term in the surface energy budget at the study site, Large-Aperture-Scintillometers could be employed (Meijninger et al., 2006), which evaluate the turbulent fluxes from fluctuations of the refractive index of air along a beam path of several 100 m length and thus replace time averaging of turbulent fluctuations at a single point by a combination of time and line averaging (see Sect. 2.4.2). While Large-Aperture-Scintillometry is an evolving technique, it has demonstrated its potential by achieving a closed energy balance in several field experiments (Foken, 2008b).
Another conceivable reason for the energy balance closure are advective circulation patterns. In turbulence measurements, one generally requires spatial homogeneity of all relevant variables, so that the turbulent flux at the measurement height can be assumed equal to the turbulent flux at the surface, which is the relevant quantity for the surface energy budget. However, if horizontal gradients of temperature and water vapor content exist, advection between the surface and the measurement height can occur, so that the turbulent fluxes obtained with the eddy covariance system are different from the surface fluxes. An overview on the different landscape scales at which horizontal advection can play a significant role is given by Pielke and Avissar (1990) and Mahrt (2000). Advection may occur in the study area, as the surrounding is characterized by mountains, glaciers and the open water body of the Kongsfjorden, so that large temperature contrasts and extremely inhomogeneous surface heating exist over distances of a few kilometers. An independent estimate of the magnitude of the flux bias caused by such features could be given by Large Eddy Simulation (LES) studies of the entire boundary layer dynamics for the wider area around the study site (Beare et al., 2006).

We conclude that the magnitude of the observed closure terms is still in range of the closure terms found in a number of carefully designed field experiments (overview in Foken, 2008b), despite the considerable uncertainties inherent in measurements under under arctic conditions. Therefore, it seems reasonable that the true magnitude and relative importance of the terms of the surface energy budget do not differ substantially from the results presented above.

4.3 Spatial variability of the surface temperature

In the previous section, the annual surface energy budget of the study area has been evaluated. With the eddy covariance method, it is only feasible to evaluate the turbulent fluxes averaged over the footprint area, but not for a specific point in space. Furthermore, at the chosen location of the eddy covariance system, the footprint area features a relatively homogeneous surface cover compared to other locations of the study area, where during the snow-free period strong variations of particularly the surface soil moisture can occur over distances of a few meters.
However, the surface energy budget can be modeled on the point scale with the coupled land-atmosphere model presented in Sect. 2.4.7, if the parameters albedo, roughness length and surface resistance against evapotranspiration are adjusted to reproduce measured surface temperatures. Therefore, spatially resolved measurements of the surface temperature can be considered a tool to access the surface energy budget on the point scale. In addition, they allow to assess the impact of spatially different surface temperatures on the seasonal thawing of the ground, as the soil temperatures at deeper layers are directly linked to the surface temperatures (see Sect. 2.2.3).
In the following, time series of georeferenced and radiometrically corrected surface temperatures are evaluated, that have been obtained with a thermal imaging system (see Sects. 2.7, 3.2.6) for an area characterized by a considerable small-scale heterogeneity of the surface cover and the surface soil moisture conditions (Figs. 3.5, 4.15). The measurements have been conducted from 25 July to 14 September 2008 and from 3 July to 17 August 2009 at a monitoring interval of 10 min, so that the study is based on a total of approximately 14,000 thermal images. In the year 2009, the period directly after snow melt has been captured, while the study extends well into fall in 2008. The success rate exceeds 95% of the 10 min-intervals, and is only limited by the occurrence of strong precipitation or fog.

4.3.1 Spatial variability in single scenes

Three examples for the considerable variability of the surface temperatures under clear-sky conditions are displayed in Fig. 4.16. The scene on 11 July 2009 represents the maximum spatial variability of the surface temperature, that has been observed in this study. It occurs in case of maximum values of net radiation less than one week after the snow melt has terminated in most parts of the scene. The soil is mostly water-saturated in this scene, except for the already dry upper parts, which have melted out more than two weeks earlier. They feature temperatures of almost 30°C, while the low-lying areas close to the thermal imaging system are still covered by snow and are hence around 0°C. In the still water-saturated central areas, where the snow has just disappeared a few days earlier, the temperatures are in the range between 14 and 20°C. Apart from the different surface moisture conditions, the proximity of the thaw front to the surface is most likely an additional reason for the much lower temperatures compared to the dry areas, where the snow has disappeared much earlier

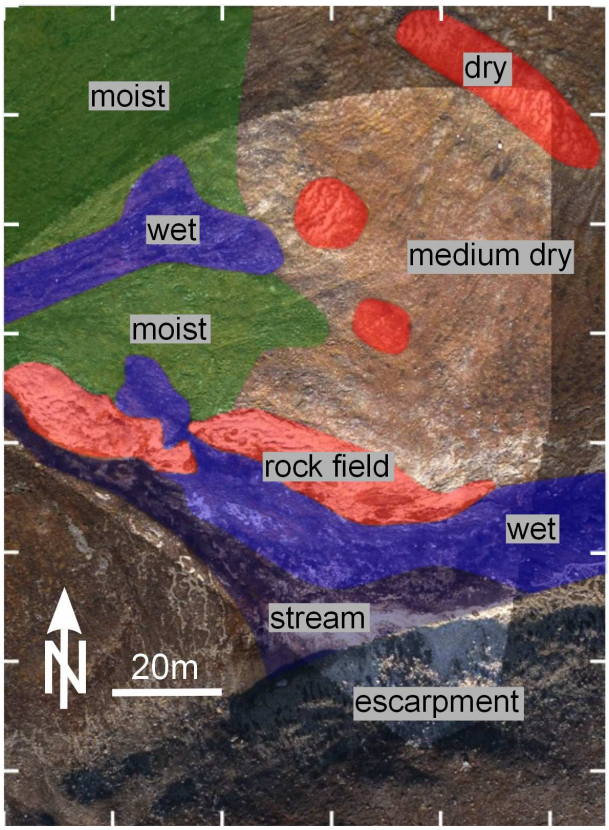

Figure 4.15: Coarse classification of the scene recorded by the thermal imaging system based on land cover and surface soil moisture conditions. The classification is compiled from field observations. The scene monitored in the study period of 2008 (as shown in Figs. 4.16, 4.19, 4.20) is indicated by shading.

and the thaw front has hence progressed further.

In the second scene taken on 30 July 2008, the snow has disappeared except for a small patch at the foot of the escarpment, from which the small stream with cold melt water originates. The wet and moist areas, that are not directly affected by the meltwater (see Fig. 4.15), are generally 4 to 8°C colder than the drier areas and the rock fields, although the net radiation with around 125 Wm^{-2} features intermediate values.

The scene on 1 September 2008 represents a clear-sky night after the end of the polar day season, with strongly negative values of the net radiation due to long-wave radiation losses. In this example, the temperatures are below 0°C throughout the entire scene. However, the dry areas and the rock fields cool out strongly to temperatures as low as -6°C, while the wet areas remain close to the freezing point, as the release of latent heat from the freezing water stabilizes the surface temperature.

The presented scenes represent examples of the spatial variability of the surface temperature under clear-sky conditions, but they are not characteristic for the

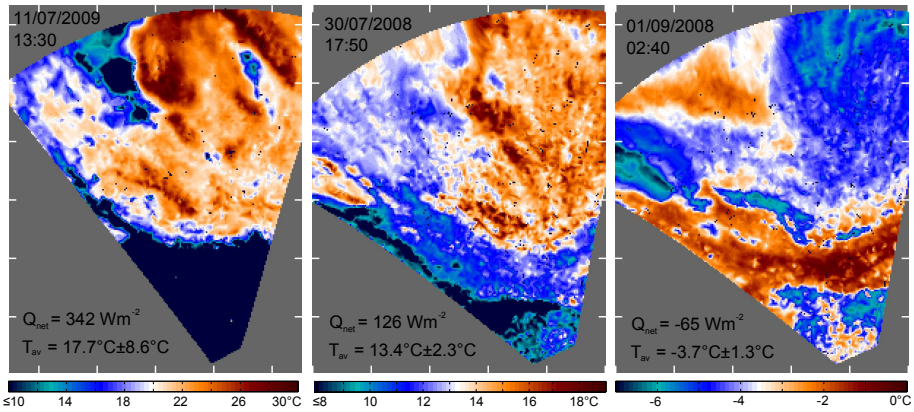

Figure 4.16: Example scenes with pronounced spatial variability of the surface temperature (note the difference in scale). The maximum uncertainty for a pixel is approximately 1.5 K. All scenes point North, the white bars are 20 m spaced from each other. The first scene stems from 2009 and is thus shifted by 10 m to the E (right) compared to the other two scenes, which are acquired in 2008. The average temperature of the scene T_{av} is provided with the spatial standard deviation as an indicator for the temperature spread present in the scene. The net radiation Q_{net} is recorded at the BSRN station. See text.

study period. As the most pronounced temperature differences occur between wet and dry areas, we evaluate the deviation of the surface temperatures of a dry and a wet area (see Fig. 3.5) from the average temperature of the scene in dependence of the net radiation Q_{net} (Fig. 4.17). For high positive values of the net radiation, the dry areas are 1 to 2 K warmer than the scene average, while the wet areas feature temperatures of several Kelvin below the scene average. For the case of 2009, the deviation of the wet areas from the scene average is more pronounced compared to the study period in 2008, probably because the wet areas have melted out later, so that the thaw front is closer to the surface compared to the dry areas, which leads to an additional cooling. When the net radiation becomes negative, the situation reverses and the dry areas are on average colder than the wet areas, where more energy per volume is stored due to the higher heat capacity (and in case of subzero temperatures a higher latent heat content) of the wet soil, so that a higher temperature is maintained. When the net radiation is low, which is typical for cloudy conditions, the differences between dry and wet areas vanish, and the entire scene features a more or less constant temperature.
The situations with low net radiation occur by far more often than situations with high negative or positive values of net radiation (Fig. 4.17) due to the frequent cloudiness, which is characteristic for the summer at the study site. Accordingly, the surface temperatures are relatively homogeneous in most of the recorded scenes, so that the spatial differences are within the uncertainty of about 0.5 to 1.0 K of the surface temperature measurements.

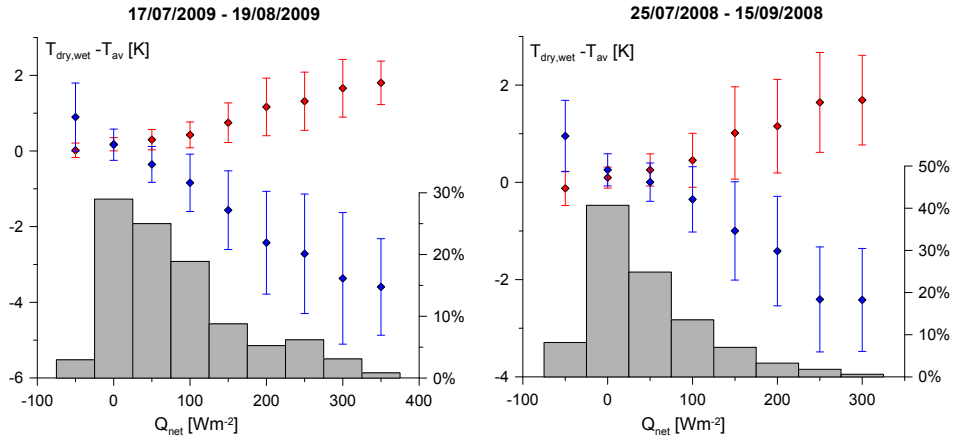

Figure 4.17: Difference from the scene average of the surface temperature for wet ($T_{\mathrm{wet}} - T_{\mathrm{av}}$, blue) and dry ($T_{\mathrm{dry}} - T_{\mathrm{av}}$, red) areas vs. net radiation in classes of 50 Wm^{-2} for the study period in 2009 and 2008. The selected reference areas for wet and dry conditions are depicted in Fig. 3.5. The net radiation is recorded at the BSRN station. The error bar indicates the standard deviation and thus the spread of the data points within a class of net radiation. The histograms show the distribution of the net radiation (in percentage of the total number of records) during the respective period.

4.3.2 Small-scale heterogeneity of the surface energy budget

The surface temperature forms as a result of the partitioning of energy at the surface, so that it is related to all components of the surface energy budget. As the exposition does not vary strongly within the study area, we do not expect considerable variations of the incoming short-wave radiation. An exception is the escarpment, which is also shaded during part of the time, so that we do not consider it any further in our analysis. The surface albedo is most likely lower in the wet areas compared to the dry areas (compare Fig. 3.5), so that they receive a higher net short-wave radiation, although they feature a colder surface temperature. The measurements of sensible and latent heat fluxes with the eddy covariance method reveal a dependence of the Bowen ratio on the surface soil moisture conditions (Fig. 4.5). Therefore, the differences in the surface temperature between wet and dry areas can most likely be explained by increased evapotranspiration over the wet areas, which cools the surface and efficiently reduces the difference between surface and air temperature. In contrast, the dry areas heat up and release energy via sensible heat fluxes and increased long-wave radiation. In the time directly after snow melt, when the thaw front is close to the surface, a significant ground heat flux cools the surface and constitutes an important term in the surface energy budget (Sect. 4.2, Fig. 4.4). As the the sum of sensible, latent and ground heat fluxes is equal to the net radiation, this interpretation is supported by the observed dependence of the spatial variability of the surface temperatures on Q_{net} (Fig. 4.17). In

case of high net radiation, strong sensible, latent and ground heat fluxes, which differ throughout the study area, lead to a large spatial variability of the surface temperature. In case of low net radiation, they necessarily feature low values, so that spatially different fluxes and thus differences of the surface temperature cannot develop.
We support this reasoning by applying the energy balance model described in Sect. 2.4.7 to model the spatial differences of the surface temperature with a common set of forcing data. The forcing data are

- soil temperature at 0.15 m depth measured in a dry and a wet area within the scene monitored by the thermal imaging system,
- air temperature, relative humidty and wind speed at 2 m height measured at the Bayelva station, approximately 400 m from the thermal imaging system,
- incoming short-wave and longwave radiation measured at the BSRN station, approximately 1.5 km from the thermal imaging system.

For simplicity, we use a constant albedo α=0.15 and emissivity ε=0.97. Furthermore, a constant soil thermal conductivity K_h=1.3 Wm^{-2} is assumed, which most certainly does not reflect the true soil conditions with spatially variable thermal conductivities. However, the impact on the surface temperature is rather limited, as the ground heat flux is a relatively small contribution to the surface energy budget (see Sect. 4.2). Therefore, the two parameters varied are the roughness length z_0 and the surface resistance r_s. Fig. 4.18 displays surface temperatures from a wet and a dry area (depicted in Fig. 3.5) measured by the thermal imaging system and model results for two different surface resistances for a period in summer 2009. A satisfactory agreement between measured and modeled surface temperatures can be achieved with a roughness length of z_0=1 mm common to both areas, but strongly different surface resistances r_s. Accordingly, the average Bowen ratio obtained from the surface energy budget equation is highly different between the two sites, which confirms the above interpretation: while the latent heat flux is dominant at the wet area with a Bowen ratio of less than 0.5, it is more than ten times smaller than the average sensible heat flux at the dry area. The Bowen ratio of the wet area is well in the range determined with eddy covariance in case of a high surface soil moisture (Sect. 4.2, Fig. 4.5), while the Bowen ratio determined for the dry area is much higher than all Bowen ratios in the eddy covariance measurements. However, the dry area recorded by the thermal imaging system most likely features a much smaller surface moisture content compared to the footprint of the eddy covariance system, which even under dry conditions maintains a volumetric soil water content of around 0.2 at the surface (Fig. 4.4). Particularly in case of the dry area, a few systematic deviations between measured and modeled surface temperature are obvious. On the first few days after 11 July and after 31 July, the modeled temperatures are too high, which is most likely explained by wetter soil conditions after snow melt and after precipitation events, respectively. Accordingly, a smaller surface resistance r_s would be appropriate during these times, which illustrates the difficulties when modeling surface temperatures in case of changing surface soil moisture. The selected roughness length z_0=1 mm

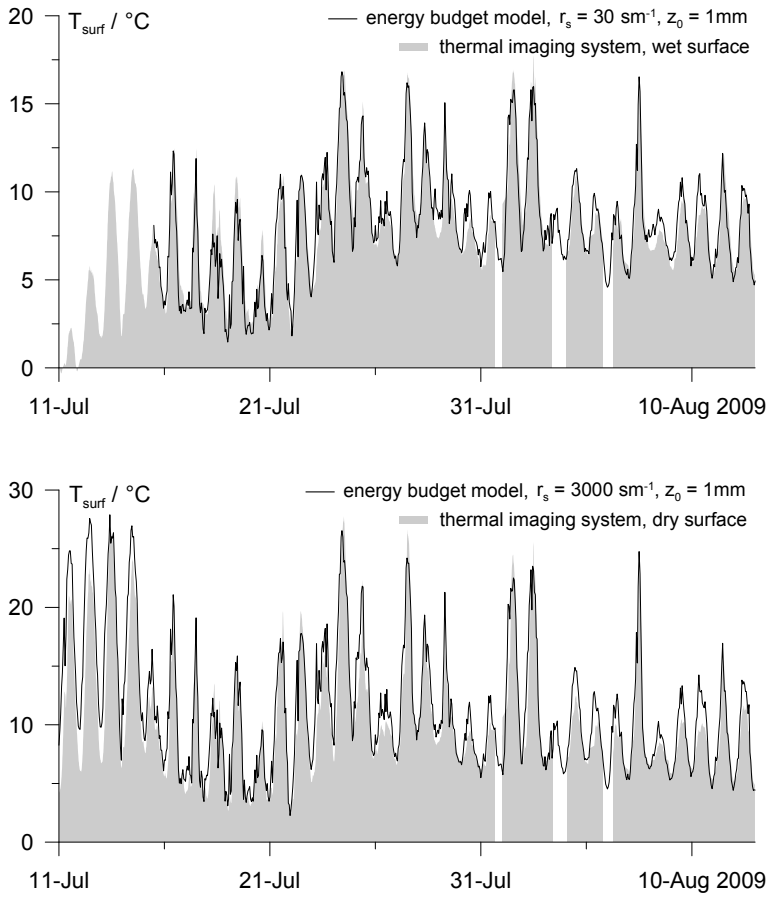

Figure 4.18: Surface temperature of a wet and a dry area (depicted in Fig. 3.5) measured by the thermal imaging system and modeled from atmospheric parameters by the surface energy budget equation. See text.

is smaller than the roughness length of 7 mm, that has been determined by measurements of the eddy covariance system (see Sect. 4.1.2). However, the wider area around the eddy covariance system (Fig. 4.1), that is characterized by mudboils and scattered rocks, may indeed feature a higher roughness length compared to the area recorded by the thermal imaging system.
The example illustrates the potential of process-oriented models based on the surface energy budget equation to model the spatial variability of the surface temperature. They basically allow to describe a large part of the recorded spatial variability by one parameter, the surface resistance r_s. Similarly, variations of the surface temperature due to different albedo or exposition can be naturally accounted for in terms of the surface energy budget equation.

Table 4.3: Maximum uncertainty associated with the weekly average temperature of each pixel according to the error calculation (see Sect. 2.7). High values indicate frequent clear-sky conditions, where the incoming thermal radiation is small.

max. error/ K	2008	2009
04/07-10/07		1.0
11/07-17/07		1.3
18/07-24/07		1.3
25/07-31/07	1.0	0.4
01/08-07/08	0.7	0.7
08/08-14/08	0.4	0.6
15/08-21/08	0.6	
22/08-28/08	0.4	
29/08-04/09	0.9	
08/09-14/09	0.3	

4.3.3 Weekly averages of surface temperature

Long-term averages (daily to weekly) of the surface temperature are relevant for the temperature distribution in the ground at depths below approximately 0.5 m, as the daily temperature fluctuations have decayed at this depth (see Sect. 2.2.3). For the understanding of spatial variability of the soil temperatures in the active layer, one hence needs to evaluate the spatial variability of such long-term averages of the surface temperature. The spatial variability in weekly averages of surface temperatures is presented in Fig. 4.19: it displays the deviation from the scene average for weekly averages of the surface temperature, which are evaluated from the time series of the thermal images acquired at 10 min intervals. The maximum uncertainties associated with the average surface temperature at each point are given in Tab. 4.3. In the following, only differences in the surface temperature, which are statistically significant, are considered.

In the study period in 2009, the first week is dominated by the remaining snow cover, which naturally leads to strong differences in the surface temperature between snow-free and snow-covered areas. The measured differences exceed 10 K in the weekly average, which is by far greater than the variability caused by different soil moisture conditions later in the summer. In the second week, the snow cover has largely disappeared, except for the snow drift at the foot of the escarpment and small patchy areas. The regions, which have already been snow-free in the first week and have dried up since then, are significantly warmer than the areas, where the snow melt has just terminated and which are hence water-saturated. In addition, the thaw front is much closer to the surface in these areas, which presumably leads to additional cooling of the surface. From the third week onwards, the coarse soil moisture classification displayed in Fig. 4.15 is valid, although the soil moisture particularly of the dry areas can vary due to rain events. We do not consider the shrinking snow field at the foot of the escarpment in the following, since it is the only remaining snow patch in a large area around the study site, so that it is immaterial in the context of surface

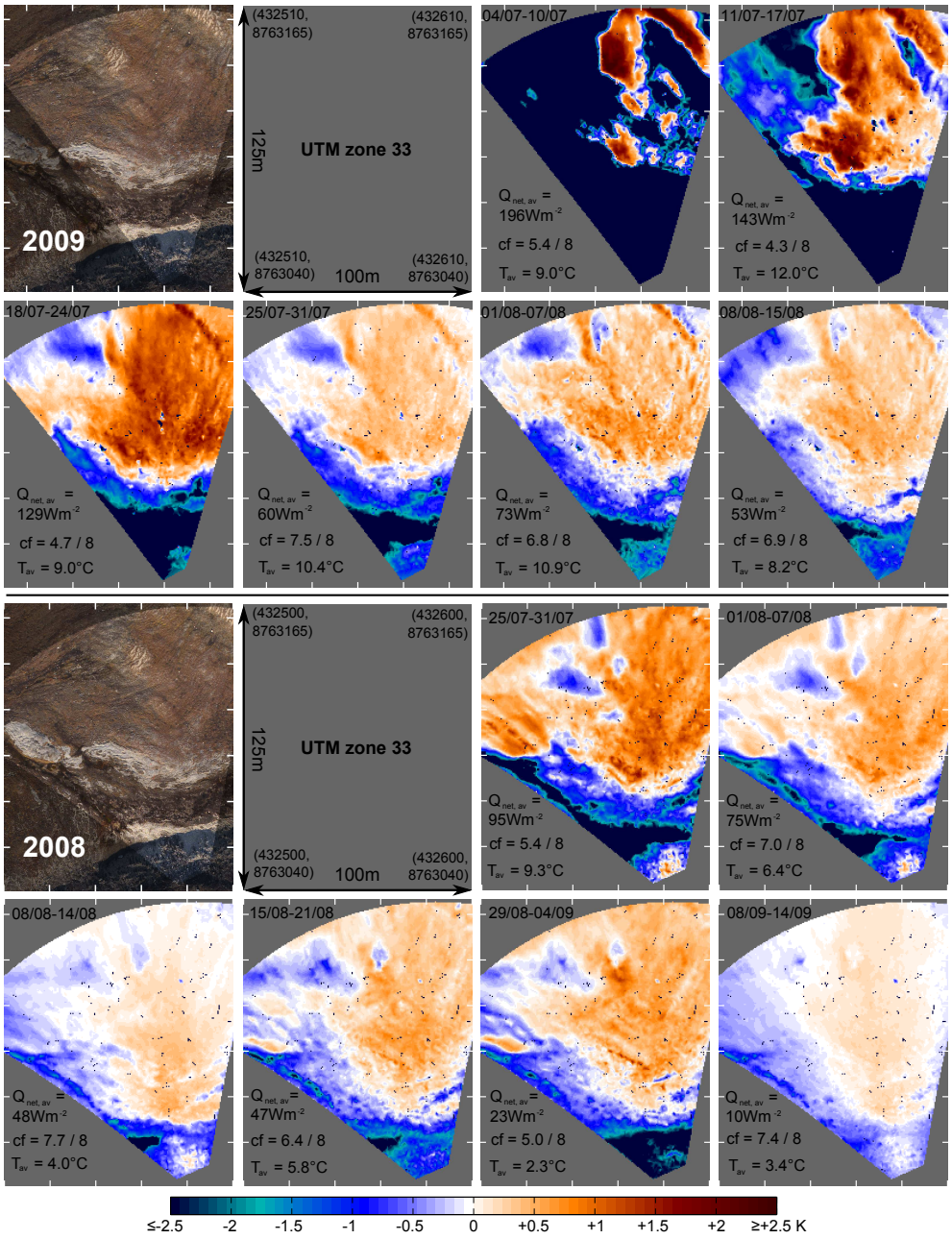

Figure 4.19: Weekly averages of surface temperatures based on the record of scenes in 10 min intervals. To facilitate an intercomparison between the weeks, the deviation from the spatial average T_{av} of the surface temperatures is shown (in the first three weeks, T_{av} is not the true spatial average, but is selected to facilitate a discrimination between the temperatures of the snow-free surfaces). The net radiation Q_{net} and the cloud fraction cf is derived from the respective records at the village of Ny-Ålesund. See text.

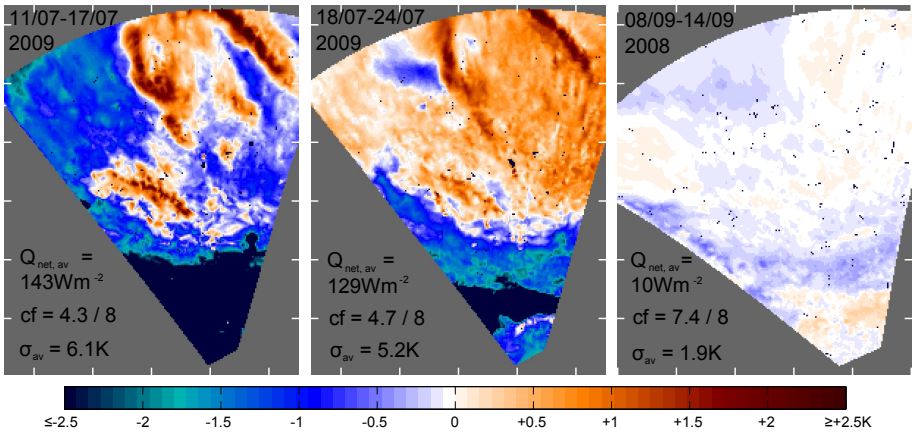

Figure 4.20: Standard deviations σ of the weekly time series of the surface temperature, which are a measure for the daily temperature amplitude, at each pixel for three example weeks. For better comparability, the deviation from the spatial average σ_{av} is shown. Ancillary data as in Fig. 4.19. See text.

temperature variability on larger scales. The maximum temperature differences between dry and wet areas of up to 4 K occur in the third week, where relatively frequent clear-sky conditions lead to a high average of the net radiation. With frequent cloudiness and reduced net radiation, the spatial differences reduce to about 2 to 3 K in the remaining three weeks of the study period in 2009.
In 2008, we again do not consider the snow field and also the meltwater stream, which is in the field of view of the thermal imaging system. Strong differences in surface temperature of up to 3 K are only observed in the first week at the end of July, where the net radiation features the highest values observed in the study period 2008. August and September 2008 are characterized by mostly cloudy conditions and declining net radiation according to the annual radiation cycle (Westermann et al., 2009), and the spatial differences of the surface temperature are generally small in the range below 2 K. We conclude that pronounced differences in the weekly averages of the surface temperature are only observed in July, when the net radiation reaches its annual maximum.
The standard deviation σ of the time series of surface temperatures for each pixel is a measure for the daily temperature amplitude. Fig. 4.20 displays the deviations from the average standard deviations for three example weeks in the study period. The first example week features frequent clear-sky conditions and thus high high values of net radiation, while the ground is water-saturated after the snow melt in most areas (the soil moisture classification of Fig. 4.15 is not valid). The dry areas, where the snow melt has terminated earlier (see Fig. 4.19), feature a considerably higher daily temperature amplitude than the wet areas, while the temperature amplitude of the snow patches is naturally close to zero. The second example week features similar cloud and radiation conditions and hence a similar average standard deviation. The considerable differences between the first and second image therefore rather reflect the change in soil moisture conditions, that has occurred due to the drying of the tundra

after snow melt. The wet areas (see Fig. 4.15) again feature standard deviations that are 3 to 4 K smaller than those of the dry areas, which corresponds to a difference in diurnal temperature spread of roughly 10 K. With declining values of net radiation and increased cloudiness later in summer, both the absolute values of the standard deviation and the differences between the dry and wet areas gradually decrease, until they almost completely vanish in mid of September (example week three).

4.3.4 The surface temperature during the summer season

To assess the potential impact of the spatial differences for the active layer evolution, we calculate the accumulated degree-day total (Lunardini, 1981), i.e. the average temperature (in °C) of a certain period multiplied by its duration in days, for the study period in 2009 and 2008 (Fig. 4.21). In the 2009 study period, pronounced differences of up to a factor of two occur, which mainly stem from the spatial differences in snow melt, but also from sustained deviations between wet and dry areas in case of high net radiation. A much smaller spatial variability is observed in the 2008 study period, which can be attributed to increased cloudiness and lower net radiation later in the season. Considering the uncertainties on the weekly averages of the surface temperatures given in Tab. 4.3, an uncertainty up to 100 degree-days in the difference between maximum and minimum value seems possible at least for 2009: as the uncertainty mainly stems from the potential spatial variability of the emissivity, which is approximately constant over time, the temperatures would be consistently biased in the same direction for each point. However, dry areas usually feature lower values ε than wet areas (e.g. Wan and Zhang, 1999), which would result in even lower surface temperatures of the wet and/or higher surface temperatures of the dry areas. Therefore, the sustained spatial variability of the surface temperature in 2009 are persistent in the light of the uncertainty considerations.

The degree-day total calculated from the beginning of the thaw period corresponds to the thawing index J_t, which has been introduced in the context of the Stefan model (see Sect. 2.2.3). In the Stefan model, the seasonal thaw depth is proportional to the square root of the thawing index. Hence, a difference of a factor of two (as in Fig. 4.21) would result in a difference of approximately 40% in the thaw depth, given the same soil properties. However, this simple picture is misleading in the presented case, as the soil properties, particularly the soil moisture, differ strongly throughout the study area. Furthermore, the Stefan model does not take into account crucial factors like the temperature distribution in the soil, so that a more realisticw soil model would have to be employed to estimate the net effect on the thaw depth and the ground thermal regime. Nevertheless, we conclude that the surface temperature, which is one of the key variables determining the annual thaw of the active layer, features a pronouced spatial variability in the study area, which may contribute to differences in the thermal regime the subjacent permafrost.

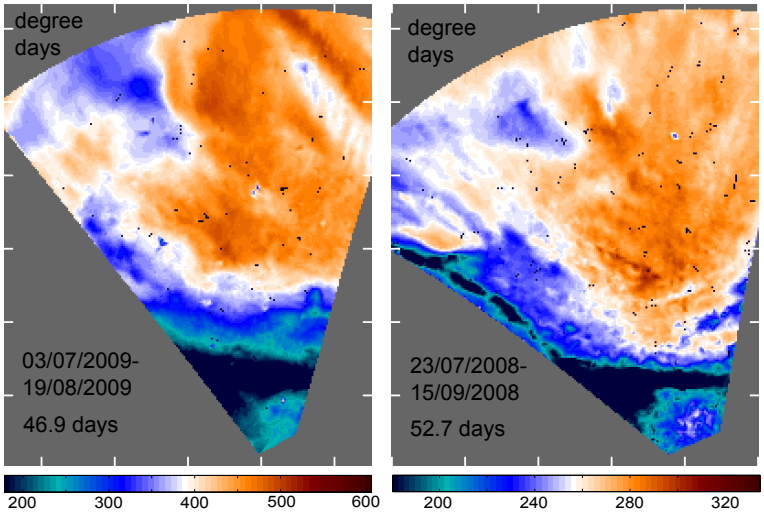

Figure 4.21: Accumulated degree-day totals during the study period in 2009 and 2008 from the 10 min records of the thermal imaging system. The pronounced differences in the 2009 study period stem from the spatial differences in snow melt and from differences in surface temperature between wet and dry areas in case of high net radiation.

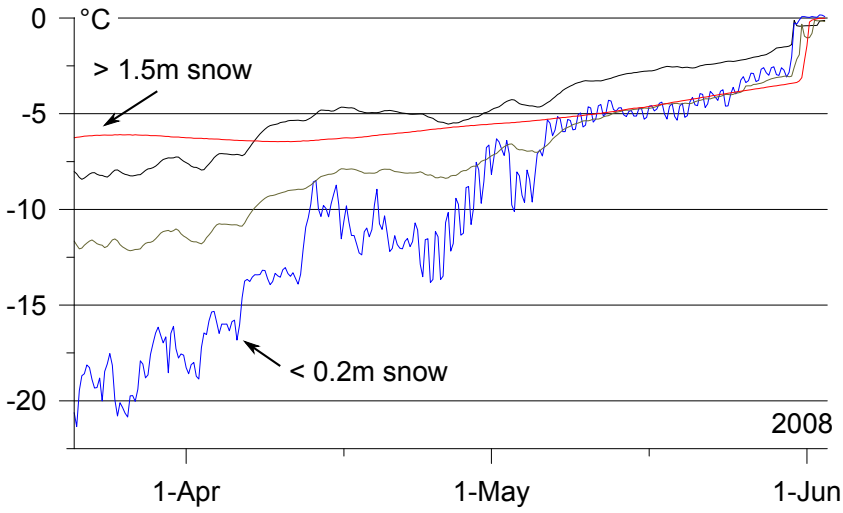

Figure 4.22: Temperature at the snow-soil interface measured in spring 2008 at four locations with significantly different snow depths within the study area. The snow depths are determined on 15 March 2008, when the temperature sensors were installed. The two unmarked lines feature intermediate snow depths of 0.8 m and 1.1 m, as they are characteristic for the study area.

4.4 Spatial and temporal variability of soil temperatures

The spatial variations of the average surface temperature during the snow-free time (see previous section) must be related to the spatial variability of the snow-soil interface temperature during the winter season. Here, spatial differences are almost entirely caused by differences in the thickness of the snow pack, and not by spatially different temperatures of the snow surface. As snow has a much lower thermal conductivity than soil, it effectively insulates the soil from the cold winter temperatures, so that the temperatures at the snow–soil interface are much higher than the snow surface temperatures. For the study area, the thermal conductivities have been determined to $K_h = 0.45\,\mathrm{Wm^{-1}K^{-1}}$ for snow and and $K_h = 1.3\,\mathrm{Wm^{-1}K^{-1}}$ for unfrozen soil (see Sect. 4.1.3). As the thermal conductivity of ice is considerably higher than that of water, this suggests a difference of at least a factor of three between the thermal conductivities of snow and the frozen soil during winter. Within the study area, a large spread in the snow depths exists, which is induced by the strong snow drift during periods with high wind speeds and the hilly topography. Low snow heights are typically found at wind-blown ridge tops, while snow accumulations occur in gullys and at hillsides. Fig. 4.22 displays snow-soil interface temperatures from March 2008 to the onset of the snow melt in June for four different snow depths, from less than 0.2 m to more than 1.5 m. With cold temperatures in the beginning of the considered period (compare Fig. 3.4), the snow-soil interface temperatures differ by more than 10 K between sites with small and large snow

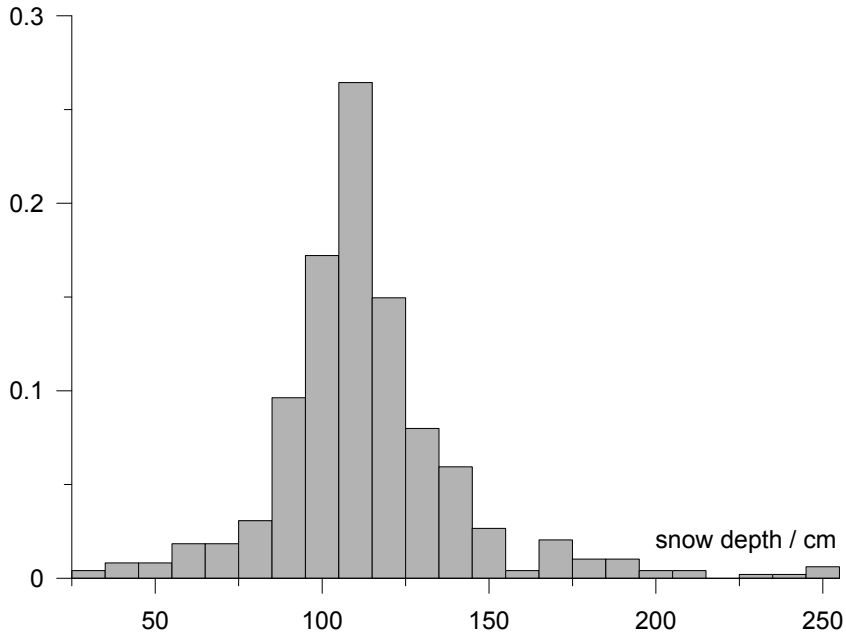

Figure 4.23: Distribution of snow depths in the study area measured between 24 March and 1 April 2009 on a $20 \times 20\,\mathrm{m}^2$ grid, in fractions of classes of 10 cm. The total number of snow depth measurements is 488.

depths, which is significant compared to the spatial variability of the surface temperatures during summer.

In March 2009, a systematic survey of the snow depths within the study area has been conducted (Fig. 4.23). While the range of detected snow depths is large with values between 0.3 and more than 2.0 m, the majority of the snow depths are concentrated between 0.9 and 1.3 m, so that it is indeed feasible to account for the largest part of the study area in terms of an average snow depth. However, it is important to keep in mind that areas with strongly different snow depths do exist, which can display a distinctly different thermal regime of the ground. In the winter season 1997/1998, a similar survey has been conducted by Bruland et al. (2001) using radar measurements to determine the snow depth of an area of $3\,\mathrm{km}^2$, in which the study area is fully contained. An average snow depth of 0.7 m with a standard deviation of 0.4 m is observed, which reflects the considerable spread in the snow depths. Compared to the winter 2008/2009, a significantly larger variability of the snow depths is recorded, which most likely can be explained by a different dynamics of snowfall and snow drift events.

Fig. 4.24 displays the annual course of active layer temperatures at two sites, that represent the two extremes of the snow depth distribution in the winter season 2008/2009: while the first temperature profile is located on top a wind-blown ridge (denoted ridge site), which only permits a low snow depth of less than 0.5 m, the second profile is buried under a snowdrift forming at the foot of a slope (denoted snowdrift site). As the distance between the two sites is less than 200 m, the external factors (radiation, air temperature, wind speed, etc.)

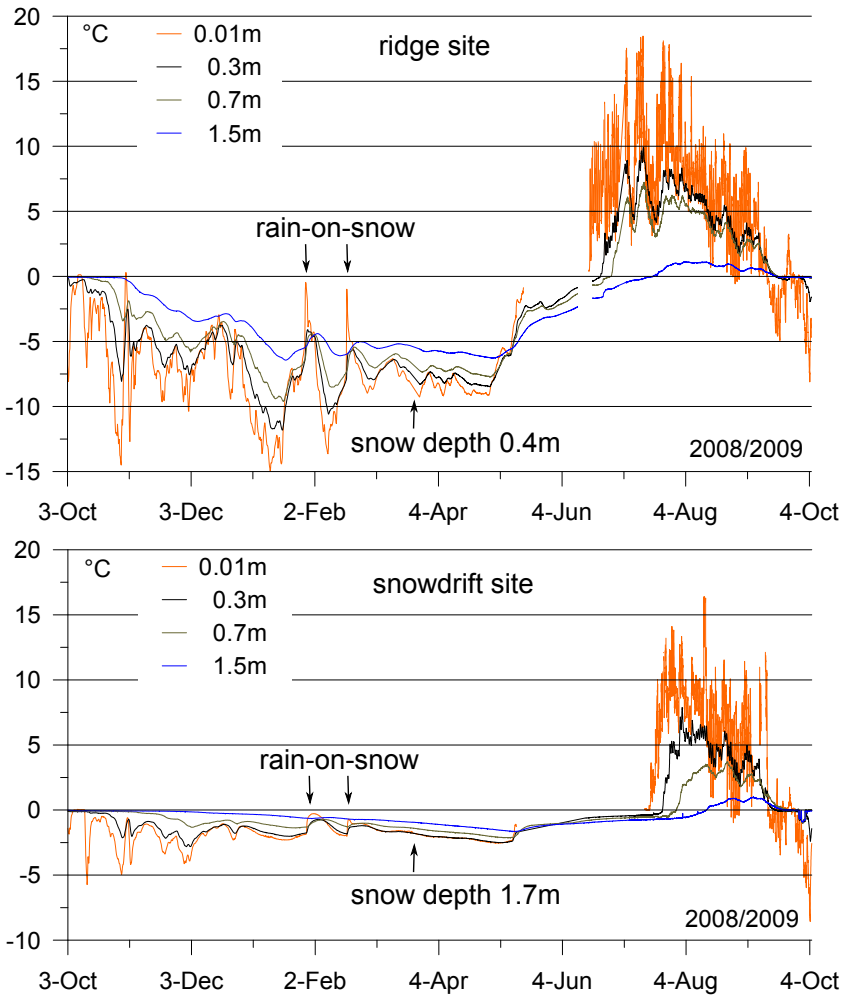

Figure 4.24: Soil temperatures in the active layer for two sites within the study area, denoted the ridge and the snowdrift site. The sites are located within a distance of less than 200 m, but feature distinctly different snow depths during winter. The snow depth has been measured on 25 March 2009 at both sites, while the effect of two rain-on-snow events around beginning of February 2009 is visible in the temperature data (all indicated by arrows).

can be assumed equal, so that the difference in soil temperatures during winter is caused by the snow cover and possibly also by differences of the soil properties. The ridge site features much colder soil temperatures than the snowdrift site during the period from October to May. The observed temperature difference on average is about 5 K at the snow-soil interface and about 3 K at a depth of 1.5 m. The impact of the snow cover on the soil temperature is severe at the snowdrift site, as the snow cover impedes the heat transfer towards the surface so strongly, that a sizable fraction of the soil water remains unfrozen during the entire winter, and the temperatures are confined within the freezing range of the soil (estimated from the freezing characteristic of the soil at the Bayelva station displayed by Roth and Boike (2001)). Accordingly, the soil temperature at 1.5 m depth does not decrease below -1.5°C at the ridge site. On the other hand, the snow cover persists one month longer at the snowdrift site, so that the thaw season is considerably shortened compared to the ridge site. At the study area, this effect is particularly strong, as the snow melt terminates around or even after the annual maximum of the solar radiation.

It must be emphasized that the ridge and the snowdrift site represent the extreme cases present within the study area. Most of the other 10 installed soil temperature profiles (see Sect. 3.2.3) feature similar active layer temperatures, corresponding to snow depths within the pronounced central peak of the snow depth distribution. However, if degradation of permafrost should commences, it will most likely occur at a few localized "weak points", such as the snowdrift site. This onset of permafrost degradation is hard to detect by temperature measurements in boreholes, which are typically placed at "representative" locations within an area. The same is true for coarse-grid models, that are operated with average values of input parameters.

Interannual differences in the height of the insulating snow cover are a determining factor for soil temperatures in winter (Fig. 4.25), as is evident from the time series of soil temperatures obtained from the Bayelva station for more than a decade (Boike et al., 2010). Winter temperatures that are strongly below the average, as in the winters 1999/2000 and 2002/2003, coincide with a low snow depth. A strong interannual variability of the snow surface temperature during winter (Fig. 4.28, Fig. 3.3 for air temperatures) is superimposed on the effect of the snow cover. However, the prominent influence of the snow cover becomes obvious, if two years with similar snow surface temperatures, but different snow heights are compared, e.g. the winters 2002/2003 and 2003/2004 (see Table 4.4 for surface temperatures).

The impact of rain-on-snow events on the soil temperatures is observed in both the time series of the Bayelva station and at the ridge and snowdrift sites (Fig. 4.24). When significant amounts of rain fall on the snow pack, the water can percolate towards the snow-soil interface, where it finally refreezes (Boike et al., 2003b; Putkonen and Roe, 2003). Due to the low thermal conductivity of the snow, the release of the latent heat from the refreezing rain water through the snow pack is impeded, with the consequence of a pronounced warming of the soil towards 0°C. As evident at the ridge site, the rain-on-snow events lead to a significant warming of the the uppermost 0.5 m of the soil, while a temperature increase is still visible at 1.5 m depth. The occurrence of strong rain-on-snow events can be suspected from the temperature record at the Bayelva station, particularly during the winter seasons 2005/2006 and 2006/2007, where frequent step-like increases of the temperature at 0.05 m depth towards 0°C are

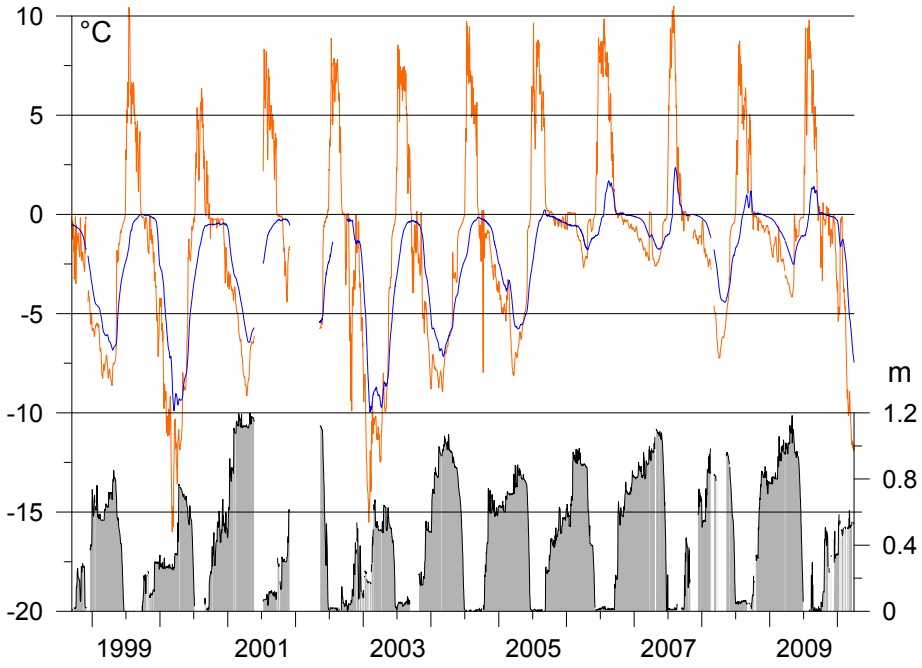

Figure 4.25: Soil temperatures (daily averages) at 0.05 m (orange, left axis) and 1.10 m depth (blue, left axis) and snow depths (gray, right axis) at the Bayelva station from fall 1998 until spring 2010. Data gaps due to instrument failure are indicated by missing gray shading.

observed. Presumably as a consequence of the rain-on-snow events, the soil temperatures remain warmer than -3°C for the entire winter in both years. The effect of rain-on-snow events is investigated further in Sect. 4.6.2 with a heat transfer model.

During the study period, the permafrost at the Bayelva station has been relatively warm, with a mean annual temperature around -2°C at 1.5 m depth and a maximum thaw depth exceeding 1.5 m (Boike et al., 2010). Since the installation of the station, the maximum thaw depth has increased by more than 0.5 m at Bayelva station (compare to Roth and Boike, 2001).

4.5 Performance of MODIS LST for the study area

For a permafrost monitoring scheme based on remotely sensed surface temperatures, it is critical that the employed remote sensing platform can provide accurate long-term averages of the surface temperature. To evaluate the performance of MODIS LST, we calculate weekly LST averages from the available satellite data and compare with the terrestrial observations. Two separate evaluations are performed, one for the snow-free season and one for the winter period when the ground is snow-covered. As the spatial heterogeneity of the surface cover and soil moisture conditions leads to spatially variable surface temperatures, the observations of the thermal imaging system (see Sect. 3.2.2) are used to file the MODIS LST measurements in the range of surface temperatures occurring within the footprint of the MODIS sensor. During the observation periods of the thermal imaging system in the summers 2008 and 2009, totals of 800 and 724 MODIS granules, respectively, are considered for the evaluation. When the ground is snow-covered, a much smaller variablity of the surface temperature is likely to occur, so that point measurements of outgoing long-wave radiation L_{out} from the Bayelva station (using Eq. 2.130, $\varepsilon = 0.99$ for snow and L_{in} from the BSRN station) seem appropriate as terrestrial ground truth. For the analysis, a total of more than 11,000 MODIS granules from the winter periods (defined as the time from 1 November until 15 April) from 2002/2003 to 2008/2009 are considered.
The frequent cloudy conditions lead to a strongly clustered times series of MODIS LST data, which is problematic for the calculation of weekly LST averages from the satellite: while there are up to ten measurements available for cloud-free days, only few data points exist for periods with frequent clouds. We therefore evaluate the performance of an incremental time averaging procedure, which successively calculates hourly, six-hourly, daily and finally weekly averages to moderate the overrepresentation of clear-sky conditions in weekly averages.

4.5.1 Summer surface temperatures

The scene recorded by the thermal imaging system (Fig. 3.5) features a wide range of surface covers that are typical for the wider area around the study area. However, it cannot necessarily be assumed representative for the much larger target area of the MODIS sensor (Fig. 3.7). A comparison of satellite and terrestrial measurements is still meaningful, particularly if weekly averages are considered, where spatial differences are strongly reduced. The available MODIS L2 LST data points and the almost continuous record of the average scene temperature from the thermal imaging system are displayed in Figs. 4.26 and 4.27. It is evident, that the average surface temperature in the footprint of MODIS depends on the fractions of wet and dry areas. For the comparison, the spatial average of the scene recorded by the thermal imaging system is used, while we keep the spatial variability of the weekly average surface temperatures (Fig. 4.19) in mind.
In the study period of 2009, the deviations of the weekly averages of satellite and

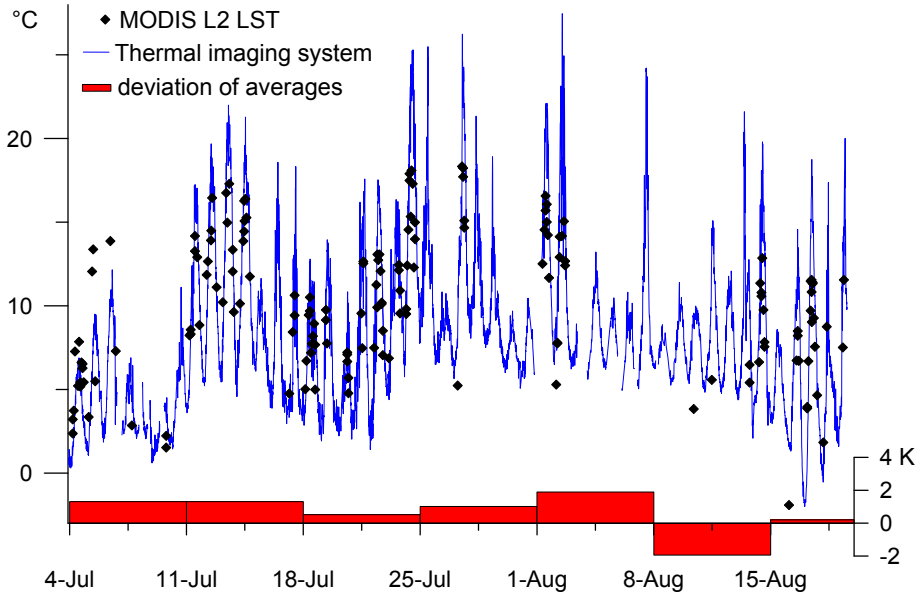

Figure 4.26: Land surface temperature measurements derived from the MODIS L2 LST product (black diamonds) and average scene temperature (blue line) obtained from the terrestrial thermal imaging system for the study period in 2009. The bar diagram displays the deviation between the weekly average temperatures inferred from the satellite record and the "true" value for the scene derived from the thermal imaging system.

terrestrial measurements are below 2 K. In the first three weeks, frequent clear-sky conditions lead to an excellent data density of MODIS LST measurements. In the first week, the deviation of 1.3 K of the weekly averages is largely caused by the three satellite measurements that are significantly warmer than the terrestrial measurements, which can most likely be explained by different fractions of snow in the scenes of the satellite and the thermal camera. In the following period from 11 to 18 July, five days feature medium to excellent data densities of MODIS LST, while two on average colder overcast days are not represented at all, resulting in a net positive bias of 1.3 K of the satellite record. With a relatively balanced data density, the third week from 18 to 24 July shows only an small offset of 0.5 K. The following three weeks are dominated by overcast conditions (see Fig. 4.19) causing prolonged periods without satellite measurements, so that the agreement within 2 K of the weekly averages of satellite data and terrestrial observations appears rather fortuitous.

Except for the first week, the study period in 2008 is characterized by more frequent cloudy conditions compared to 2009, which results in a smaller density of satellite measurements. More pronounced deviations between satellite and terrestrial measurements are observed, for which two reasons can be identified. Firstly, the overrepresentation of cloud-free periods with on average warmer surface temperatures can lead to a strong positive bias of the satellite averages, particularly if the averaging period is almost entirely dominated by clouds, while

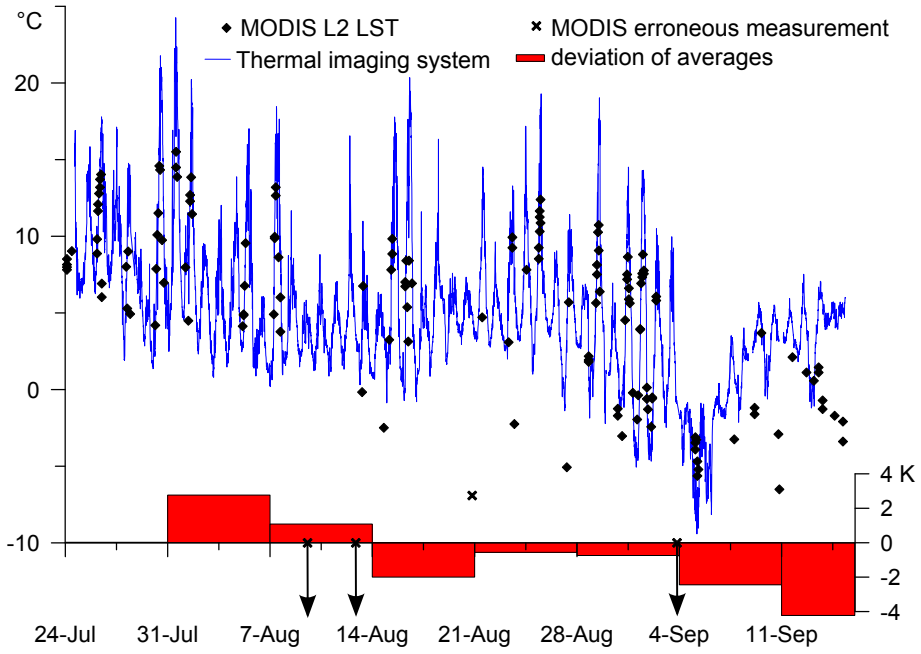

Figure 4.27: Land surface temperature measurements derived from the MODIS L2 LST product (black diamonds) and average scene temperature (blue line) obtained from the terrestrial thermal imaging system for the study period in 2008. Data points diagnosed as erroneous measurements (see text) are marked by crosses. The bar diagram displays the deviation between the weekly average temperatures inferred from the satellite record and the "true" value for the scene derived from the thermal imaging system.

the available satellite measurements stem from short cloud-free periods. Secondly, there exist measurement errors in the MODIS data set, some of which are obvious, such as a measurement of -20.5°C obtained on 9 August. At this day, terrestrial observations of the cloud fraction cf (www.eklima.no, 2010) indicate fully overcast skies, so that presumably cloud top temperatures are measured instead of land surface temperatures, which range around +5°C according to the record of the thermal imaging system. A significant number of satellite measurements is considerably colder than the terrestrial measurements, which indicates at least a partly contamination by cloud top temperatures. These measurement errors can invoke a serious bias of the weekly averages, as they are the only data points in prolonged cloud-covered periods and thus receive a strong weighting in the employed incremental averaging procedure. The erroneous measurement on 9 August would for example result in a negative bias of more than 9 K of the weekly average, which is clearly intolerable for the purpose of permafrost monitoring. The possible contamination by cloud top temperatures is supported by the quality flags provided in the MODIS L2 product, which indicate that more than 99% of the data set may be affected by nearby clouds. The calculation of meaningful weekly averages is obviously no longer feasible, if only few data

points are employed, so that we only discard cases with extreme deviations between the two data series. Therefore, we define a data point a measurement error if the satellite measurement is more than 10 K colder than the terrestrial measurement. These data points are excluded from our evaluation of the weekly averages, which in total concerns four measurements with temperatures between -7.0°C and -20.5°C. Particularly in the second half of the 2008 study period, many more satellite measurements exist, that are considerably colder than the terrestrial measurements, which suggests an admixing of cloud top temperatures. However, it does not seem appropriate to a priori exclude them as measurement errors due to the large scaling gap between the terrestrial and satellite footprints. In some cases, e.g. for the week between 21 and 28 August, these probably cloud-influenced, cold-biased data points are found to balance the warm-bias due to the overrepresentation of clear-sky periods to some extent. In September, with almost entirely overcast conditions, cold-biased data points dominate, so that the satellite average is more than 4 K colder than the average of the terrestrial observations. As the available MODIS LST observations are mainly below 0°C after 4 September, this would lead to a false estimation for the onset of freezing, which in reality occurs after the end of the study on 15 September.

4.5.2 The surface temperature during winter

When the ground is covered by snow, spatial differences in surface temperature are most certainly reduced, so that it becomes feasible to compare a point measurement of the surface temperature with the satellite record of MODIS LST. The procedure yet remains problematic due to of the large scaling gap between the point measurement and the satellite footprint of more than 1 km^2. As spatially distributed measurements of the surface temperature are not available, the long time series of measurements of L_{out} is employed to improve the statistical significance and to account for the wide range of synoptic conditions encountered during the winter season (see Sect. 4.2.3). The comparison is performed for the period from 1 November until 15 April for seven winter seasons from 2002/2003 to 2008/2009. During the chosen period, the ground is usually covered by snow and melt processes do not occur, except for sporadic rain-on-snow events (see Sect. 4.2.3). For each season, on the order of 2500 MODIS granules are available, which fulfill the overlap criterion of 60% with the target area depicted in Fig. 3.7. However, the frequent cloudiness results in a rather limited success rate of about 25% to 30%, which is nevertheless better than the success rates of less than 20% during the snow-free season.
The average surface temperatures for each of the years derived from MODIS L2 LST and the "true" surface temperature inferred from measurements of L_{out} (Eq. 2.130) at the Bayelva station (columns in bold face, T_1^M and T_2^B) is presented in Table 4.4. It is clear that the average surface temperature derived from the satellite records is systematically biased to colder temperatures by on average more than 3 K. Using the incremental averaging procedure (first hourly, then six-hourly, daily and weekly averages, see Sect. 3.3.1) for MODIS LST does not significantly improve the results (T_2^M, Table 4.4). Three reasons for the strong deviation are conceivable:

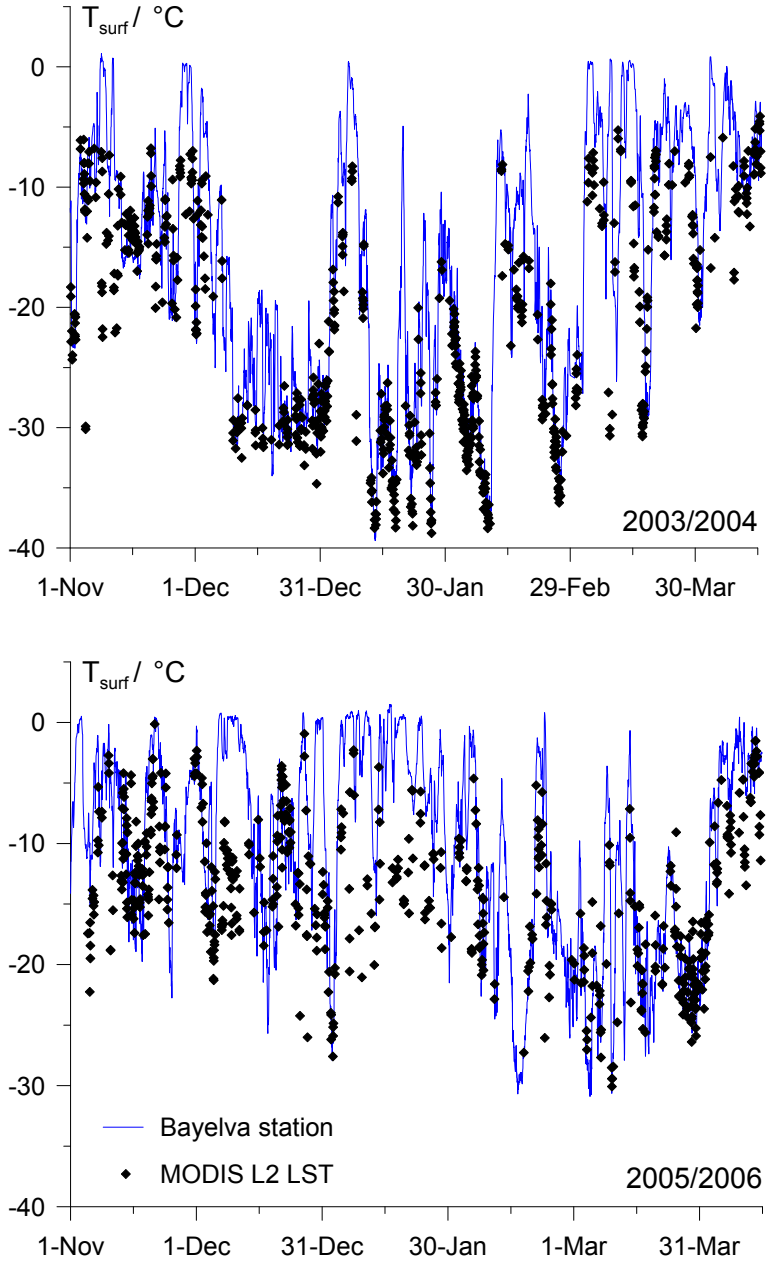

Figure 4.28: Comparison of surface temperature measurements from MODIS L2 and surface temperature measured at the Bayelva climate station for the periods between 1 November and 15 April of the winter seasons 2003/2004 and 2005/2006.

Table 4.4: Average surface temperatures for the winter seasons (defined as 1 November to 15 April) of seven years derived from hourly averages of the MODIS L2 LST product and the hourly record of the Bayelva station. T_1^M: average of MODIS L2 LST; T_2^M: average of MODIS L2 LST, incremental averaging procedure; T_1^B average of surface temperatures at the Bayelva station for times, when MODIS LST measurements are available; T_2^B average of surface temperatures at the Bayelva station.

winter season	MODIS		Bayelva station		bias
	T_1^M/°C	T_2^M/°C	T_1^B/°C	T_2^B/°C	(T_1^M-T_2^B)/°C
2002/2003	**-17.0**	-17.9	-14.4	**-15.1**	-2.6
2003/2004	**-22.9**	-20.1	-20.2	**-16.1**	-6.8
2004/2005	**-17.1**	-16.5	-15.8	**-14.0**	-3.1
2005/2006	**-14.0**	-14.0	-10.8	**-10.3**	-3.7
2006/2007	**-14.9**	-15.8	-13.3	**-12.7**	-2.2
2007/2008	**-15.8**	-16.2	-15.6	**-14.0**	-1.8
2008/2009	**-17.2**	-17.8	-15.2	**-14.2**	-3.0
average	**-17.0**	-16.9	-15.0	**-13.8**	-3.2

1. During polar night, clear-sky conditions feature systematically colder temperatures than overcast conditions (see Sect. 4.2.3). Therefore, the single satellite measurements can be accurate, but as satellite detection of LST is limited to clear-sky conditions, cold conditions are systematically overrepresented in averages.

2. Strongly erroneous measurements, as they have been observed for the summer season, exist in the MODIS data set during winter. The systematic contamination with colder cloud top temperatures could be responsible for the cold-bias in the MODIS-derived LST averages.

3. The point measurements at the Bayelva station are not representative for the satellite footprint, so that a strong spatial heterogeneity of the surface temperatures must exist within the satellite footprint.

The first point can be investigated by calculating the average of the surface temperature recorded at the Bayelva station at times, when a satellite LST measurement is available. The result is displayed in Table 4.4 (T_1^B): if the single MODIS LST measurements would conform to the surface temperature at the Bayelva station, T_1^B would have to be equal to T_1^M, the average derived from MODIS L2 LST. However, the temperature is considerably warmer than the average of MODIS LST, though still colder than the terrestrial average for most of the years. Fig. 4.28 displays the surface temperature at the Bayelva station and MODIS LST for the two example years. The winter 2003/2004 is the coldest in the record, and T_1^B is close to the T_1^M, the average of MODIS LST, so that the strong deviation between satellite and terrestrial average can be largely explained by reason 1. Indeed, the MODIS LST measurements are strongly concentrated in periods with cold surface temperatures, while measurements are almost completely missing during the regular events when the surface temperature is in the range of 0°C. The agreement between single MODIS LST

measurements and the terrestrial record is generally good. In the second example year 2005/2006, which features the warmest average surface temperatures in the record, the value of T_1^B is almost equal to the terrestrial average, so that systematic overrepresentation of cold periods can only play a minor role in explaining the cold bias of -3.7°C of MODIS LST. Instead, a large number of strongly cold-biased MODIS LST measurements are observed during prolonged periods of warm surface temperatures in the range from -5°C and 0°C. The cold-bias of single measurements regularly exceeds $10\,K$, which clearly classifies them as measurements errors with likely admixing of cloud top temperatures, as it has been reported in the previous section. The same is actually observed in the much colder winter 2003/2004, e.g. in beginning of November, beginning of January and beginning of March. However, as the warm periods are much shorter than in 2005/2006, these erroneous measurements play a much smaller role.
The systematic cold-bias of MODIS LST in case of warm surface temperatures, that predominantly occur in case of overcast conditions, is corroborated by Fig. 4.29. It displays the scatter plot between MODIS LST and the record of the Bayelva station (i.e. the hourly value closest in to the acquisition time of MODIS). Despite of a considerable spread, the agreement between terrestrial and satellite measurements is excellent for surface temperatures colder than -15°C, but the performance rapidly degrades towards $0°C$, where MODIS LST features a cold bias of on average more than 10 K.
Finally, the possibility, that spatially heterogeneous surface temperatures do exist during winter, must be critically elucidated. In this case, the systematic cold-bias of MODIS LST could only be explained by areas with significantly colder surface temperatures than those at the Bayelva station. Apart from the Kongsfjorden, which would be much warmer than the land areas, high-lying mountain slopes and glaciers characterize the immediate surrounding of the MODIS target area (Fig. 3.7). The surface temperature of these features is most likely on the order of the lowland area around the Bayelva station, or even higher due to the prevailing stable atmospheric stratifications (see Sect. 4.2.3). Therefore, the magnitude of the cold-bias of average MODIS LST measurements cannot be explained by spatial heterogeneity of the footprint area. However, it is well possible that the spread between single terrestrial and MODIS LST measurements (Fig. 4.29) is at least partly caused by areas in the satellite footprint featuring slightly different surface temperatures than those at the Bayelva station.

4.5.3 MODIS LST - a solution for permafrost monitoring?

The following limitations can be identified for the use of MODIS LST products in a permafrost monitoring scheme:

1. In some cases, the cloud detection algorithm for MODIS LST fails to prevent admixing of cloud top temperatures, which leads to strongly erroneous measurements and possibly a systematic negative bias of many more data points. The same effect has been observed by Langer et al. (2009) for a site in Siberia, so that the problem seems to occur under a wide range of conditions. For permafrost monitoring, the erroneous data points must be detected and excluded to prevent a considerable bias of the

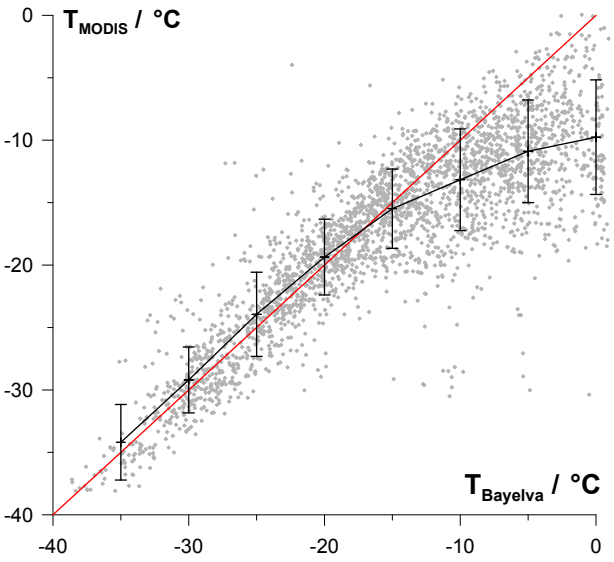

Figure 4.29: Comparison of surface temperature derived from the MODIS L2 product and surface temperature inferred from measurements of L_{out} at the Bayelva climate station. The data comprise the winter seasons, defined as 1 November until 15 April, from 2002/2003 until 2008/2009. The red line represents the angle bisector, while the black line represents the mean value of bins of 5 K width (point drawn in the center of a bin). The error bars indicated the standard deviation of the values in a bin.

calculated time averages. While an improvement of the cloud detection is highly desirable, a too rigorous approach, which would discard partly cloud-affected, but still reasonable measurements and thus reduce the data density, might actually be counter-productive for the calculation of temporal LST averages. If improvements of the cloud detection algorithm of MODIS LST are conducted, a balance between the accuracy of a single measurement and the density of the measurements should be sought.

2. When the sky is fully cloud-covered as typical for arctic conditions, it is not possible to measure LST from a satellite. This results in prolonged periods without satellite measurements and thus an overrepresentation of short clear-sky conditions in temporal LST averages. While the employed incremental averaging procedure can moderate a possible bias of the LST averages, only a reliable gap filling algorithm could resolve this issue in a satisfactory way. Hachem et al. (2009) employ a gap filling procedure based on a simple sinusoidal course of the annual temperature.

3. For permafrost monitoring, an adequate trade-off between the spatial resolution of the satellite pixels and the overpass frequency, which determines the upper bound of the temporal resolution of the time series, must be achieved. A strongly reduced measurement density compared to MODIS is hardly feasible for the calculation of long-term LST averages, so that

an LST-based permafrost monitoring scheme will have to cope with spatial resolutions around 1 km^2, which cannot resolve the scale of the heterogeneity of the surface cover and the soil moisture conditions in many permafrost areas. Fig. 4.16 represent examples of the spatial variability of the surface temperature under clear-sky conditions, which is a good estimate for the maximum temperature spread, that may be present in a single satellite scene. However, the calculation of weekly averages from the satellite data strongly moderates the observed spatial variability (see also Langer et al., 2009), so that the satellite-derived average is a much better representation of the terrestrial conditions than it is for a single satellite scene. Nevertheless, we have illustrated sustained differences of the surface temperature, which are relevant for the local thermal conditions of the active layer and possibly even the subjacent permafrost. A similar effect is reported for polygonal ponds in Siberia, which feature a lower average surface temperature compared to the surrounding land areas (Langer et al., 2009).

Some of the mentioned limitations are inherent in the measurement principle of remotely sensed land surface temperatures, so that a significant progress cannot be expected. Therefore, it is desirable to explore other schemes that can deliver the surface temperature. In the next section, a process-oriented model is presented, in which the surface temperature is evaluated according to the partitioning of energy at the surface.

4.6 A surface energy budget model for permafrost temperatures

In this section, an energy budget model is introduced, that is capable to reproduce the temperature distribution in the permafrost soil. In principle, the model is a stand-alone module of land-atmosphere exchange, as it is used in Soil-Vegetation-Atmosphere-Transfer Schemes (SVATS) implemented in General Circulation Models (GCMs). However, it includes a more realistic representation of the soil (finer discretization of the soil domain, soil freezing characteristic), which is generally not implemented in circulation models due to computational costs. In contrast to circulation models, which are designed to yield a realistic representation of the radiation budget and the turbulent fluxes, the focus of this model is clearly shifted towards reproducing soil temperatures. For the sake of brevity, the surface energy budget model is referred to as SEB model in the following.
The SEB model is designed to be forced by the long time series of ERA reanalysis data (see Sect. 3.3.2), which moderates one of the main problems in permafrost modeling: how to properly initialize the soil model for a point of time in the past, when the temperature distribution in the soil is generally not known? With ERA reanalysis data available since the 1950s, a spin-up period of a few decades is feasible for the model, so that the initialization can be accomplished with a coarse guess of soil temperatures. As measurements from the Bayelva soil station are available from 1998 to 2009, only the model results in this period are investigated here, while the period until 1998 is considered to be the spin-up phase.
The distinction is made between the operational data sets driving the model, that are derived from ERA reanalysis, and constant or at least slowly varying parameters which are denoted status parameters in the following. Examples of status parameters are the roughness length, the surface albedo or the soil properties. Thus, the success of the model not only depends on the accuracy of the operational data sets, but also on the choice of the status parameters. The asset of a SEB model is the possibility to downscale or deaggregate coarsely resolved operational data sets of quantities, that do not vary strongly in space, by using a set of status parameters at a much finer spatial resolution. For the model runs presented in this section, the status parameters are derived from the extensive data set on the surface energy budget and the soil temperatures at the study area. In Chapter 5, possible schemes to estimate status parameters over larger areas from remote sensing applications are outlined.

4.6.1 The SEB model

The model consists of two basic part: a numerical solver for the surface energy budget equations (Eqs. 2.107 to 2.114) and a soil model, that is based on conductive heat transfer with freezing of soil water (Eq. 2.12). On the one hand, the two parts are coupled through the surface temperature, which is the result of the surface energy budget equations, but also the upper boundary condition of the soil model. On the other hand, the temperature gradient at the surface must be delivered by the soil model to calculate the ground heat flux in the

surface energy budget equations.

Soil model

The soil model evaluates the heat transfer equation with freezing of soil water (Eq. 2.12) with the partial differential equation solver of MATLAB (Skeel and Berzins, 1990) to a depth of 100 m, where the temperature is fixed at 0°C. This value is chosen to reflect the approximate depth of the permafrost in coastal regions of Svalbard (Førland and Hanssen-Bauer, 2003). The model operates on a grid, that becomes finer towards the surface to account for the increasing temperature gradient, with a spacing of 10 m between 50 and 100 m depth, 5 m between 30 and 50 m, 1 m between 10 and 30 m, 0.5 m between 3 and 10 and 0.01 m spacing between 0 and 3 m. When a snow cover is present, its height is determined on a daily basis from the ERA reanalysis precipitation record (see below). The grid spacing of the snow layers is again 0.01 m. The heat capacity of the soil is determined from Eq. 2.8, while the thermal conductivity is calculated by the de Vries-approach described in Sect. 2.2.4. In the current model version, infiltration processes in the soil are not accounted for (see Sect. 2.2), so that the sum of the volumetric water and ice contents of the soil is constant over time.
The soil model is driven by daily averages of the surface temperature, as reproducing the large temperature gradients induced by the diurnal cycle in the uppermost soil layers is computationally expensive and unnecessary, when the temperatures of deeper soil layers are the main interest. For the calculation of the ground heat flux, the temperature gradient is linearly interpolated between the surface and the depth d, at which the temperature amplitude of the diurnal cycle is damped to about 10% of the value at the surface. For the diffusivities for unfrozen soil (see Sect. 4.1.3), this depth is approximately 0.3 m according to Eq. 2.35. As the temperature variations are largest during summer, a depth of 0.3 m is adequate for the entire year. Two exception are required:

- If the freeze or thaw front is located within 0.3 m from the surface, the temperature of the cell just above the freeze or thaw front is used.
- When the snow depth is less than 0.3 m, the temperature of the lowest snow cell is used.

Surface energy budget

The basic equations for the surface energy budget are given in Sect. 2.4.7. The driving input variables incoming short- and long-wave radiation, air temperature and relative humidity at 2 m height and wind speed at 10 m height are derived at a temporal resolution of six hours from ERA–40 and ERA–interim reanalysis (see Sect. 3.3.2), while the ground heat flux is determined from the soil model (see above). The main parameters determining the partitioning of energy at the surface are the roughness length z_0 and the surface resistance r_s (see Sect. 4.3.2). When the ground is snow-covered and the surface energy budget equation yields a surface temperature of more than 0°C, the snow will in reality start to melt. In this case, the surface energy budget equation must be complemented by a

melt term. The surface temperature is set to 0°C, so that the equations for L_*, u_*, Q_h and Q_e (Eqs. 2.109 to 2.112) again form a set of coupled equations with four unknowns, that can be solved. The melt term Q_{melt} is then evaluated as the residual of the surface energy budget

$$-Q_{\mathrm{melt}} = (1-\alpha)S_{\mathrm{in}} + \varepsilon L_{\mathrm{in}} + \varepsilon\sigma_{\mathrm{sb}}T_{\mathrm{surf}}^4 + Q_h + Q_e + Q_g \,, \tag{4.1}$$

from which the amount of melt water produced between two time steps and thus the accumulated amount of melt water $MELT$ can be calculated. Conversely, the surface temperature is sustained at 0°C in the model when melt water is present (i.e. $MELT > 0$), so a melt term with opposites sign can occur, until all melt water has refrozen and $MELT$ is zero. If large amounts of melt water are produced, it infiltrates the snow pack and create a more complex situation. However, except for the snow melt period, the amounts of produced melt water are small in most cases (less than 1 mm snow water equivalent) so that the chosen procedure appears to be an adequate representation. During the snow melt period, the surface temperature remains at 0°C and $MELT$ accumulates, until it reaches or exceeds the snow water equivalent SWE (see below).

Precipitation and snow

Precipitation is only accounted for when it contributes to the evolution of the seasonal snow pack, while the moisture content of the soil does not change in response to precipitation in the model. ERA reanalysis delivers the water equivalent of the total precipitation and the snowfall, from which the build-up dynamics of the snow cover is inferred assuming a constant snow density. As all precipitation falling during winter, whether it is snow or rain, eventually contributes to the snow water equivalent of the snow pack, the total precipitation is used to calculate the snow water equivalent SWE, once a snow cover has formed (see below).
A delicate, but important issue are the "rain-on-snow" events (Putkonen and Roe, 2003), which are included in the model in a phenomenological way, as a physically-based model representation of infiltration in the snow is not available at the moment. To assess the impact of rain-on-snow events on the ground thermal regime, two qualitative observations are important:

- Melt water refreezing at the bottom of the snow pack has a much larger impact on the ground thermal regime than melt water refreezing at the top. Latent heat released at the bottom is insulated from the surface by the snow pack and predominantly warms the soil. Latent heat released at the top of the snow pack is mainly released through the surface without significant warming of the ground (see Sect. 4.4).
- The higher the snow depth is, the more rain is required in a single rain-on-snow event, so that water can percolate to the bottom. Conversely, if this occurs, the fraction of the total amount of rain percolating to the bottom decreases with increasing snow depth.

These observations motivate the following implementation of rain-on-snow events in the SEB model:

1. Only if the amount of rain occurring within 48 hours exceeds a threshold ROS, rain during winter is considered a "rain-on-snow event".

2. Only the refreezing of a fraction P_{ROS} of the total amount of rain, that percolates to the bottom of the snow pack, is considered.

3. For a snow water equivalent of less than 0.05 m, any rain event is considered, and the entire amount refreezes at the bottom (see below), i.e. $ROS = 0$ and $P_{\mathrm{ROS}} = 1$.
   For a snow water equivalent of more than 0.3 m, ROS and P_{ROS} are set to predefined values, i.e. $ROS = ROS_{\mathrm{max}}$ and $P_{\mathrm{ROS}} = P_{\mathrm{ROS,min}}$.
   For a snow water equivalent between 0.05 m, and 0.3 m, a linear interpolation between the two regimes is implemented.

4. The amount of rain water refreezing at the bottom is determined from the ERA precipitation record and P_{ROS}. The refreezing is prescribed to occur in the lowest 0.1 m (or less, if the snow depth is lower) of the snow pack, which are subsequently set to 0°C. The heat fluxes through the upper and lower boundary of this domain, which are evaluated from the temperature gradients, are accumulated until all the rain water has refrozen. The rain-on-snow event is then terminated and normal heat conduction through the snow pack resumes.

This reasoning results in two free parameters, ROS_{max} and $P_{\mathrm{ROS,min}}$, which control the number and the strength of rain-on-snow events, respectively.

The annual dynamics

The SEB model distinguishes three periods with different properties in the annual cycle (Fig. 4.30), namely a summer, winter and a melt period. Table 4.5 gives an overview of the properties of the of the different periods. For the calculation of the saturation vapor pressure, the Magnus formula (Stull, 1988) is used, which distinguishes between saturation vapor pressure over water and ice surfaces according to the respective period. During the melt period, the surface energy budget equations are only solved to determine the amount of melt water, but the soil dynamics is computed with a constant temperature of 0°C at the snow-soil interface, as the snow pack is saturated with melt water at this time. Accordingly, it is unnecessary to consider the temperature dynamics of the snow pack at all during the melt period. Furthermore, different values for albedo, emissivity, roughness length and surface resistance are used for the different periods (Table 4.5). For the albedo during winter α_w, the parameterization employed in the ECHAM GCM is used (Roeckner et al., 2003), where the albedo is a function of the surface temperature. The albedo is linearly interpolated between $\alpha_{\mathrm{w\,min}}$ at T_{surf}=0°C and $\alpha_{\mathrm{w\,max}}$ at T_{surf}=-5°C, and $\alpha_{\mathrm{w\,max}}$ is used for surface temperatures colder than -5°C. This scheme has not been validated for the study area, and alternative formulations are conceivable.

The transition between the three periods is accomplished by a number of conditional statements, indicated by the numbers in Fig. 4.30:

1. SWE >0.01 m, start of winter period, $MELT$ starts accumulating,

Table 4.5: Settings and status parameters for the different periods. e^*(surface) denotes the vapor pressure at the surface (Eq. 2.107).

	surface	T_{surf}	e^*(surface)	α	ε	z_0	r_s
			Magnus formula				
summer	soil	SEB	water	α_s	0.97	$z_{0\,\text{s}}$	r_s
winter	snow	SEB	ice	α_w	0.99	$z_{0\,\text{w}}$	0
melt	soil	0°C	ice	α_w	0.99	$z_{0\,\text{w}}$	0

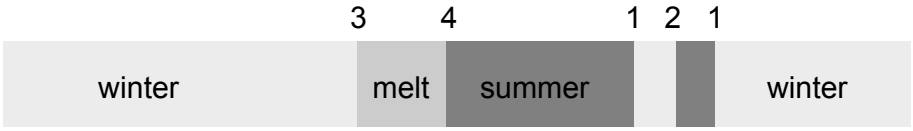

Figure 4.30: Schematic diagram of the different periods distinguished in the SEB model. See text for explanation of the numbers.

2. $MELT \geq SWE$, switches back to summer settings,
3. $MELT >$0.05 m, start of melt period, SWE stops accumulating,
4. $MELT \geq SWE$, start of summer period.

The conditions trigger the transitions between periods. Hereby, thresholds are chosen in case of conditions (1) and (3), that are to a certain extent arbitrary, but have negligible impact on the ground thermal regime, at least if reasonable values are chosen. Furthermore, the threshold values can be adjusted to reflect the start of the respective periods determined by field measurements, i.e the formation of the perennial snow cover, or the onset of strong snow melt leading to a temperature of 0°C at the snow-soil interface, respectively. The threshold in condition (1) is necessary, as the precipitation records from ERA reanalysis can feature unrealistically low snow amounts of a few micrometers of snow water equivalent, as the precipitation data are spatial averages for a large grid cell, while the snow fall in reality can occur locally at a few spots within the grid cell. To prevent such low snow amounts from triggering the start of the winter period in the model, a threshold corresponding to a snow depth of a few centimeters is set. Condition (2) is designed to account for strong melt events in fall, which cause the snow pack to melt and thus disappear entirely. It can only be triggered, when the snow water equivalent is less than 0.05 m, while otherwise condition (4) would switch to the snow melt period.

4.6.2 First model results

In this section, the performance of the SEB model is evaluated against the extensive data sets on the surface energy budget and the surface and soil temperatures, that have been presented in this thesis. The model runs are performed

for the period from 15 June 1958 to 31 December 2009, so that they cover almost the entire ERA reanalysis period. The model is initialized with the status parameters of the summer period (see Table 4.5), so that the soil initially starts to thaw (in the summer of 1958). The soil domain therefore is initialized with a "winter-like" temperature distribution, which for simplicity is a linear interpolation between -4°C at the surface and 0°C at a depth of 100 m. It must be emphasized that the chosen initial condition is a coarse guess, so that a spin-up period of at least ten years is required before the soil temperatures become reasonably independent of the initial condition. For the comparison with the measured surface energy budget and surface temperatures, the SEB model is run without including the phenomenological representation of the rain-on-snow events.

The employed set of status parameters (compare to Table 4.5) is:

- **Albedo**: $\alpha_s = 0.15$, $\alpha_{\mathrm{w\,max}} = 0.80$, $\alpha_{\mathrm{w\,min}} = 0.65$.
  The employed values are derived from radiation measurements at the study site and the BSRN station (see Sect. 4.1.1).

- **Roughness lengths**: $z_{0_s} = 10^{-3}$ m, $z_{0_w} = 10^{-4}$ m.
  The summer value z_{0_s} has been selected according to the results presented Sect. 4.3.2, where surface temperatures measured with the thermal imaging system have been reproduced with a surface energy budget model using a roughness length of 10^{-3} m. The winter value $z_{0_w} = 10^{-4}$ m is commonly employed for snow surfaces (e.g. Foken, 2008a) and has been confirmed by measurements in the vicinity of Ny-Ålesund (Lüers and Bareiss, 2009b).

- **Surface resistance against evapotranspiration during summer**: $r_s = 300\,\mathrm{sm^{-1}}$.
  In Sect. 4.3.2, surface resistances of $30\,\mathrm{sm^{-1}}$ for wet areas and $3000\,\mathrm{sm^{-1}}$ for dry areas are estimated. The selected value of $300\,\mathrm{sm^{-1}}$ lies between these two extremes, but has finally been fixed, so that the SEB model roughly reproduces the average summer surface temperatures measured at the Bayelva station (see below).

- **Snow properties**: $\rho_{\mathrm{snow}} = 370\,\mathrm{kg\,m^{-3}}$, $c_{h,\mathrm{snow}} = 0.75\,\mathrm{MJ\,m^{-3}K^{-1}}$, $K_{h,\mathrm{snow}} = 0.45\,\mathrm{Wm^{-1}K^{-1}}$.
  The values have been derived by measurements in the study area (see Sects. 4.1.3, 4.1.3). It must be emphasized that the snow properties are assumed to be constant in the SEB model, which is most certainly a coarse simplification (e.g. Sturm et al., 1997).

- **Volumetric fractions of soil constituents**: $\theta_w = 0.3$, $\theta_m = 0.6$, $\theta_o = 0.0$, $\theta_a = 0.1$.
  The volumetric fractions are in the range of the values determined from soil samples in the study area (see Sect. 4.1.3) and agree well with the soil composition determined by Roth and Boike (2001) for the soil at the Bayelva station. For unfrozen soil with this composition, the de Vries model (see Sect. 2.2.4) yields a thermal conductivity of $K_h = 1.4\,\mathrm{Wm^{-1}K^{-1}}$, which agrees well with the value of $1.3\,\mathrm{Wm^{-1}K^{-1}}$ determined by the conductive method (see Sect. 4.1.3). For freezing soil with an unfrozen soil water

content of less than 0.1, the de Vries model yields a thermal conductivity on the order of $2.4\,\mathrm{Wm^{-1}K^{-1}}$. Roth and Boike (2001) report a thermal diffusivity of $d_h = 8 \times 10^{-7}\,\mathrm{m^2 s^{-1}}$ for the soil at the Bayelva station during winter for soil temperatures between $-2°\mathrm{C}$ and $-9°\mathrm{C}$. Furthermore, Roth and Boike (2001) display the freezing characteristic and estimate a volumetric heat capacity of $2.0\,\mathrm{MJ\,m^{-3}}$ for fully frozen soil. From the slope of the displayed freezing characteristic, one can estimate effective heat capacities (Eq. 2.10) between $2.2\,\mathrm{MJ\,m^{-3}}$ and $3.5\,\mathrm{MJ\,m^{-3}}$, which yields thermal conductivities in the range from $1.8\,\mathrm{Wm^{-1}K^{-1}}$ to $2.8\,\mathrm{Wm^{-1}K^{-1}}$ (Eq. 2.13). Thus, the thermal conductivity of freezing soil of $2.4\,\mathrm{Wm^{-1}K^{-1}}$ obtained from the de Vries model agrees well with the observations of Roth and Boike (2001).

- **Freezing characteristic**: The freezing characteristic of the soil at the Bayelva station presented by Roth and Boike (2001) is fitted with a polynomial function. A residual content of unfrozen soil water of 0.05 is assumed for soil temperatures below -15°C, as observed in measurements at the Bayelva station by Roth and Boike (2001).

Performance of ERA reanalysis

The performance of the SEB model strongly depends on the quality of the operational data set, i.e. the ERA reanalysis product. The air temperature has been recorded in the village of Ny-Ålesund for more than 40 years (www.eklima.no, 2010), so that it is a particularly suited for validating ERA reanalysis. Fig. 4.31 displays a comparison of measured air temperatures and air temperatures obtained from ERA reanalysis. A generally good agreement is found for temperatures between -20°C and +3°C, while significant deviations occur for colder and warmer air temperatures. The latter is particularly critical during summer, when the air temperatures are underestimated by several Kelvin in ERA reanalysis. Most likely, this bias is explained by the large fractions of ocean contained in the relevant ERA reanalysis grid cells, which cause cooler summer and warmer winter temperatures in the reanalysis. However, it must be concluded that air temperatures obtained from ERA reanalysis are a good representation for more than 95% of the time, when the air temperature is in the intermediate range from -20°C to +3°C (Fig. 4.31).
A similarly long time series of measurements is available for precipitation, which on average show a good agreement with ERA reanalysis. However, as ERA reanalysis delivers the average precipitation for a large area, the reported interannual variability is much smaller than in the measurements (Fig. 3.3), so that large deviations between the two data sets occur regularly for single years. For the other operational data sets, i.e. incoming short- and longwave radiation, relative humidity, wind speed and snow fall, a comparably long time series of measurements does not exist for Ny-Ålesund.

The surface energy budget in the SEB model

Ideally, an SEB model would be validated with long time series of radiation, turbulent fluxes, etc., which is neither available for Ny-Ålesund nor for any other

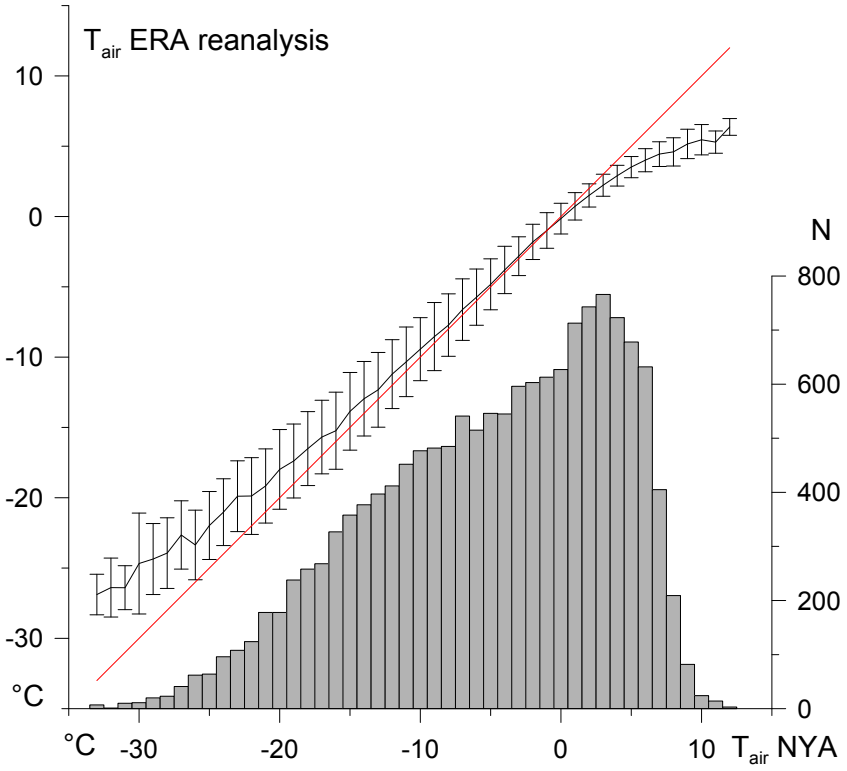

Figure 4.31: Daily averages of air temperatures measured in the village of Ny-Ålesund (www.eklima.no, 2010) vs. air temperatures derived from ERA reanalysis (see Sect. 3.3.2), in classes of 1 K width. The error bars indicate the standard deviation in each class. The considered period ranges from 1969 to 2009. The histogram gives the number of days N, at which average temperatures in the class have been measured in Ny-Ålesund.

location in the Arctic. However, the annual record of the surface energy budget, that has been compiled in this thesis, facilitates the validation of the modeled fluxes for the period of one year. It must be emphasized that a comparably comprehensive data set on the surface energy budget is currently not available for any other arctic land site, which illustrates the intricacy to validate results of coupled land-atmosphere models in these regions.
The allocation of the three periods "summer", "winter" and "snow melt" in the SEB model is in excellent agreement with observed events. The snow melt period begins on 31 May 2008, while a first melt event has been recorded on 30 May at the Bayelva station (see Sect. 4.2.5). The snow pack has disappeared on 28 June 2008 in the model, while field data indicate a snow-free fraction of the study area on the order of 50% at this time (compare Fig. 4.14). The winter period starts on 29 September 2008, which is exactly the day, when the perennial snow cover has formed in the study area (see Sect. 4.2.2). Although this exact agreement must be considered fortutious, it justifies the chosen threshold values, that trigger the beginning of the snow melt and the winter period (see Sect. 4.6.1).
Table 4.8 displays the measured and modeled components of the surface energy budget for the summer, fall, dark winter, light winter, pre-melt and snow melt periods, as introduced in Sect. 4.2. The incoming short- and longwave radiation are directly obtained from the ERA reanalysis data and generally agree with the measured values within less than $10\,\mathrm{Wm}^{-2}$, which is the measurement accuracy assigned to radiation measurements at the BSRN station (Ohmura et al., 1998). As measured albedo values have been employed in the SEB model, the outgoing shortwave radiation naturally matches the measured values, too.
More interesting is the excellent agreement of the outgoing longwave radiation, that adjusts according to the partitioning of the energy at the surface. It implies a good representation of the surface temperature in the SEB model, which is investigated further for a longer time series of measurements. Tables 4.6 and 4.7 display the average surface temperatures measured at the Bayelva station and obtained from the SEB model for seven winters (from 1 November to 15 April, when a snow cover is present in all considered years) and eight summers (from 1 July to 31 August), respectively. The agreement is excellent for almost all considered periods and by far superior to average surface temperatures obtained from MODIS LST, which are shown for comparison (see Sect. 4.5). Hereby, it is indeed remarkable, that the employed flux parameterizations can reproduce the observed strong near-surface inversions of the air temperature during winter (Fig. 4.10). In contrast, the good agreement between measured and modeled surface temperatures during summer is a direct consequence of the employed surface resistance against evapotranspiration, r_s, which has been adjusted to achieve a good agreement with measured surface temperature (see above). However, it must be emphasized, that a satisfactory agreement is realized in almost all summers by using a constant value for r_s.
As the air temperatures obtained from ERA reanalysis are significantly colder than the true air temperatures during summer (Table 4.8, Fig. 4.31), the correct representation of the average surface temperature comes at the expense of an incorrect partitioning of energy between the sensible and the latent heat flux. The latent heat flux is partly suppressed to yield an enhanced sensible heat flux and thus a larger gradient between surface and air temperature. Accordingly, the distribution of the turbulent fluxes differs strongly from the eddy covariance

Table 4.6: Average surface temperatures for the winter seasons (defined as 1 November to 15 April) of seven years derived from hourly averages of the MODIS L2 LST product (corresponding to T_1^M, Table 4.4), the six-hourly record of the SEB model and the hourly record of the Bayelva station.

winter season	MODIS LST [°C]	SEB model [°C]	Bayelva station [°C]
2002/2003	-17.0	-15.2	-15.1
2003/2004	-22.9	-16.0	-16.1
2004/2005	-17.1	-13.6	-14.0
2005/2006	-14.0	-10.3	-10.3
2006/2007	-14.9	-12.9	-12.7
2007/2008	-15.8	-14.0	-14.0
2008/2009	-17.2	-13.3	-14.2
average	-17.0	-13.6	-13.8

measurements during the summer period, with a Bowen ratio of 3.5 (Table 4.8). As it is not possible to obtain both a correct surface temperature and a correct Bowen ratio with the biased air temperatures from ERA reanalysis, the correct representation of the surface temperature, which determines the ground heat flux and the soil temperatures, is given priority by selecting an appropriate surface resistance r_s (see above).

During the other periods, the measured and modeled sensible heat fluxes agree reasonably well (Table 4.8), while the measured and modeled latent heat fluxes are of opposite sign during the dark and light winter period. In the SEB model, significant amounts of resublimation can occur in case of strong near-surface inversions, which have not been observed in eddy covariance measurements. However, the absolute values of both measured and modeled latent heat fluxes are small and thus associated with a considerable uncertainty, so that an interpretation of this result is difficult.

As a result of the well reproduced average surface temperatures, the modeled ground and snow heat fluxes are in good agreement with the measured fluxes, which are associated with relative uncertainties on the order of 20 to 30%. The amount of energy consumed by the melting of the snow pack Q_{melt} is considerably larger in the SEB model, since the snow water equivalent derived from the precipitation record of ERA reanalysis is larger than the measured snow water equivalent. However, the measurements are associated with a considerable uncertainty due to an unsurveyed basal ice layer, which could potentially increase the value of $27\,\mathrm{Wm}^{-2}$ (Table 4.8) by up to $20\,\mathrm{Wm}^{-2}$ (see Sect. 4.2.8) and thus lead to a much better agreement with the SEB model.

It is interesting to note which factors contribute to a closed surface energy budget in the model. During the summer period, the sum of sensible and latent heat flux is clearly increased compared to eddy covariance measurements, while all other modeled components are similar to the measurements. This may be an indication that the eddy covariance technique indeed underestimates the turbulent fluxes, as has been hypothesized in Sect. 4.2.8. In the other periods, it is not possible to attribute the energy balance closure to a single term.

Table 4.7: Average surface temperatures for the summers seasons (defined as 1 July to 31 August) of eight years derived from hourly averages of the MODIS L2 LST product, the six-hourly record of the SEB model and the hourly record of the Bayelva station.

summer season	MODIS LST [°C]	SEB model [°C]	Bayelva station [°C]
2002	10.3	7.8	7.5
2003	8.3	7.6	7.2
2004	9.0	7.8	7.3
2005	10.4	7.1	7.8
2006	8.5	7.2	7.1
2007	9.8	7.3	7.1
2008	9.1	7.1	6.3
2009	8.7	8.7	6.9
average	9.3	7.6	7.2

Table 4.8: Comparison of the measured surface energy budget (see Table 4.2) and the surface energy budget obtained from the SEB model for the study period. T_{air}: air temperature; P precipitation; S_{in}, S_{out}, ΔS: incoming, outgoing and net short-wave radiation; L_{in}, L_{out}, ΔL: incoming, outgoing and net long-wave radiation; Q_h: sensible heat flux; Q_e: latent heat flux; Q_g: ground or snow heat heat flux compiled from calorimetric and conductive method (see Table 4.2 for the original values of both methods); Q_{melt}: heat flux consumed by melting snow. Values in parentheses are estimates or based on data records with frequent data gaps. The model values for T_{air}, P, S_{in} and L_{in} are directly obtained from the ERA reanalysis data set.

	Summer		Fall		Dark winter		Light winter		Pre-melt		Snow melt	
	01/07/08 –31/08/08		01/09/08 –30/09/08		01/10/08 –15/03/09		15/03/08 –15/04/08		16/04/08 –31/05/08		01/06/08 –30/06/08	
	meas.	model	meas.	model	meas.	model	meas.	model	meas.	model	meas.	model
$T_{\mathrm{air}}/\,^{\circ}\mathrm{C}$	5.0	3.0	2.7	2.0	−10.1	−8.6	−16.0	−13.3	−5.6	−5.0	2.0	0.9
$P/\,\mathrm{mm}$	32	71	99	59	278	195	12	19	11	37	8	26
$S_{\mathrm{in}}/\,\mathrm{Wm}^{-2}$	−144	−147	−33	−32	−2.1	−1.0	−73	−77	−185	−195	−261	−266
$S_{\mathrm{out}}/\,\mathrm{Wm}^{-2}$	22	22	9	5	1.7	0.8	55	62	144	146	(170)	173
$\Delta S/\,\mathrm{Wm}^{-2}$	−122	−125	−24	−27	−0.4	−0.2	−18	−15	−41	−49	(−91)	−93
$L_{\mathrm{in}}/\,\mathrm{Wm}^{-2}$	−303	−309	−299	−303	−234	−229	−196	−191	−255	−247	−276	−276
$L_{\mathrm{out}}/\,\mathrm{Wm}^{-2}$	346	348	318	325	262	258	237	230	288	287	319	315
$\Delta L/\,\mathrm{Wm}^{-2}$	43	39	19	22	28	29	41	39	33	40	43	39
$Q_h/\,\mathrm{Wm}^{-2}$	22.5	56	(−7)	1.8	−16	−19	−18	−16	−8	−7	−6	−7
$Q_e/\,\mathrm{Wm}^{-2}$	22.5	16	(9)	4	2.5	−2.5	0.7	−2	2.5	6.3	11	9
$Q_g/\,\mathrm{Wm}^{-2}$	11.5	13.5	0.6	−0.6	−6	−7.5	−5	−6	3.0	1.3	13	10
$Q_{\mathrm{melt}}/\,\mathrm{Wm}^{-2}$	?	0	?	0	0	0	0	0	?	8	(27)	42

4.6.3 Soil temperatures

The SEB model is capable to reproduce the average surface temperature correctly, which is a prerequisite for modeling the ground thermal regime. However, particularly during winter, the soil temperatures critically depend on the build-up dynamics and properties of the perennial snow pack (see Sect. 4.4). Furthermore, rain-on-snow events can have a strong influence on the soil temperatures (Putkonen and Roe, 2003). In Fig. 4.32, the soil temperatures measured at the Bayelva station at 0.05 m and 1.1 m depth are contrasted to the corresponding soil temperatures obtained from the SEB model. If rain-on-snow events are not included (Fig. 4.32 b), the modeled soil temperatures are generally too cold during the winter. However, the agreement is good for some periods, most notably for the winter seasons 1998/1999, 2000/2001 and 2002/2003. In contrast, particularly the winter seasons 2005/2006 and 2006/2007 are characterized by much warmer soil temperatures as predicted by the SEB model, despite of well reproduced surface temperatures. If rain-on-snow events are included in the SEB model (see Sect. 4.6.1), the winter temperatures are increased significantly for the entire time series, so that the soil temperatures of e.g. the winter seasons 2005/2006 and 2006/2007 are now much better reproduced. Conversely, the SEB model predicts repeated rain-on-snow events during periods, when they have not been observed in reality, e.g. in the winter season 2002/2003, so that the obtained soil temperatures are much too warm in these cases. The reason for this misrepresentation is inherent in the precipitation record of ERA reanalysis, which features a relatively constant amount of rain of approximately 60 mm during the winter periods from 1998 to 2009, so that repeated rain-on-snow events necessarily occur in the model during all years. However, the distribution of soil temperatures measured at the Bayelva station is most likely explained by rain-on-snow events, that are concentrated in a few years. Therefore, one must conclude that the ERA reanalysis data set is not suitable to properly model the impact of rain-on-snow events on the ground thermal regime in the study area. While the maximum snow depths are at least partly well represented in the ERA reanalysis data (Fig. 4.32), it is evident that the build-up dynamics of the snow cover is not. A rather constant accumulation rate is inferred from the reanalysis data, in contrast to the irregular and highly dynamic build-up process recorded at the Bayelva station. As a consequence, misrepresentations of the soil temperatures occur in some years. An example is the winter season 2003/2004, for which the SEB model generates much colder soil temperatures than observed at the Bayelva station, as a high insulating snow pack in reality builds up much earlier than reported by the model. The effect of different snow depths on the soil temperatures, that has been observed in measurements (Fig. 4.24), can be simulated in the SEB model by scaling the snow water equivalent inferred from ERA reanalysis with a constant factor. Fig. 4.33 displays model runs conducted without including rain-on-snow events for two years and scaling factors of 1, 0.5 and 2. It is evident, that both effects of a greater snow depth - the warmer winter temperatures and the delayed snow melt (see Sect. 4.4) - are reproduced in the SEB model. Thus, it seems feasible to simulate the spread of the soil temperatures due to spatially variable snow depths with an SEB model, if the distribution of snow depths is known, e.g. from a snow distribution model (e.g. Luce et al., 1998).
Despite of the observed misrepresentations of the SEB model, Fig. 4.32 is also

clear evidence of the potential of surface energy budget schemes. In both model runs, the maximum thaw depth during summer increases by about 20 to 30 cm from 2003 to 2008 and can thus at least qualitatively reproduce the increase of more than 50 cm that has been observed at the Bayelva station (Boike et al., 2010). With a more realistic representation of rain-on-snow events, possibly based on remote sensing applications to determine their occurrence (see Sect. 5.2), it appears realistic that a convincing representation of the ground thermal regime can be achieved with surface energy budget models.
The presented model results must be understood as a first evaluation of the performance the SEB model. While an excellent agreement between measured and modeled surface temperature can be achieved, the representation of the snow cover and rain-on-snow events have been identified as the main challenges. It seems unlikely to the author of this thesis, that major improvements to the perfomance of the SEB model can be achieved with the employed ERA reanalysis data, so that the assimilation of new data sets, e.g. from remote sensing applications, would be a logical next step. Even more general, future studies must focus on techniques to estimate the status parameter sets without the need for extensive field measurements, so that a surface energy budget model could be applied over larger areas (see Sect. 5.3).

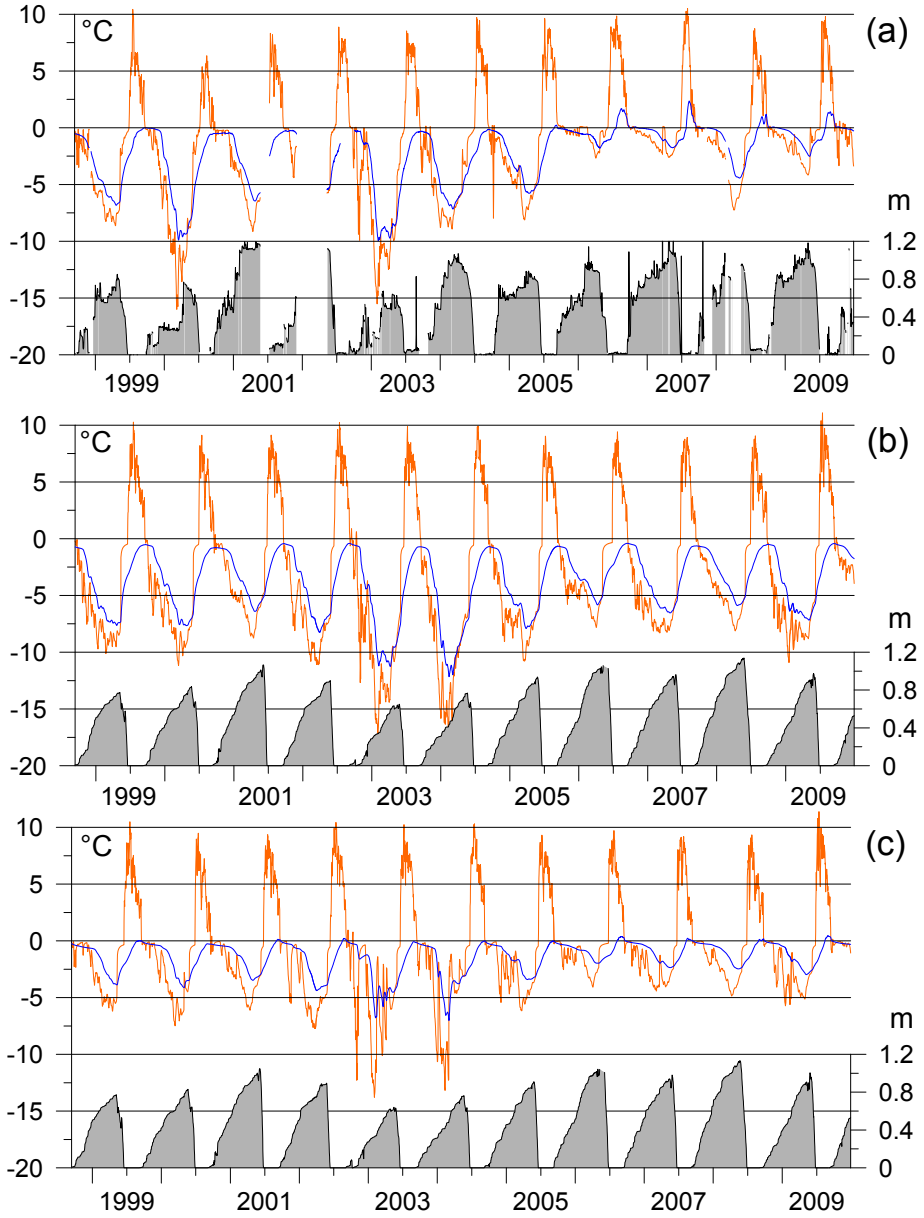

Figure 4.32: Soil temperatures at depths of 0.05 m (orange) and 1.1 m (blue): (a) measured at the Bayelva station (see Sect. 4.4); (b) SEB model without rain-on-snow events; (c) SEB model with rain-on-snow events (see text for the status parameter set of the model runs). The evolution of the perennial snow cover is depicted in gray for the measurements and the SEB model. The model run with rain-on-snow-events has been conducted using $ROS_{\max} = 5\,\mathrm{mm}$ and $P_{\mathrm{ROS,min}} = 0.1$.

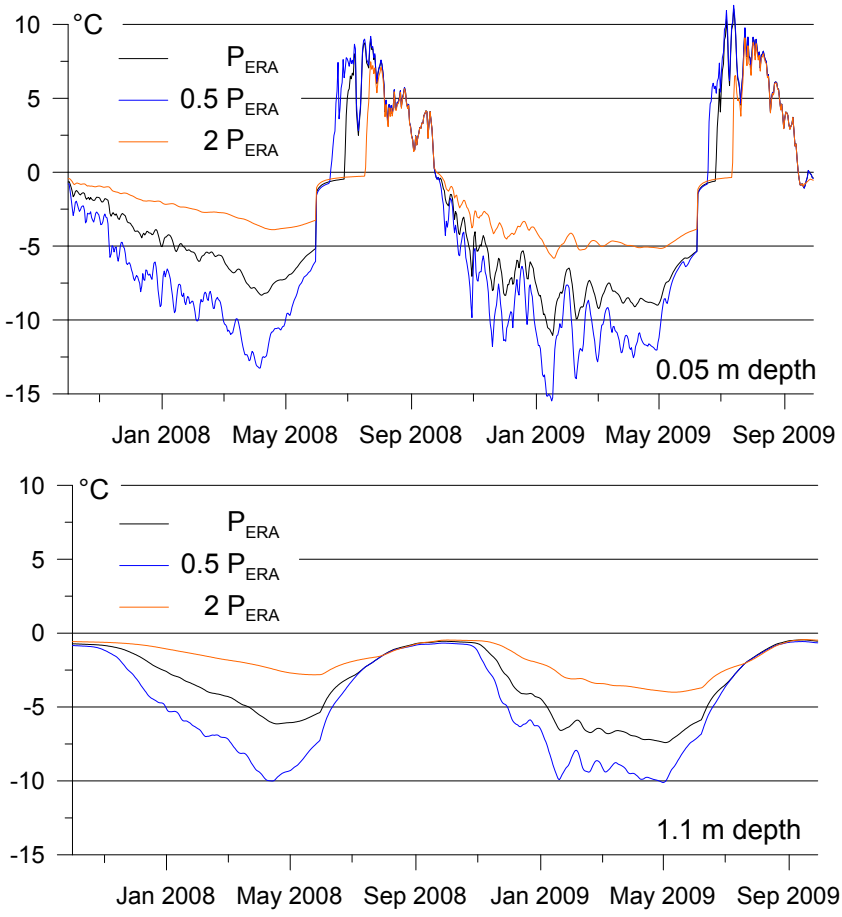

Figure 4.33: Soil temperatures at depths of 0.05 m and 1.1 m for the SEB model run without rain-on-snow events (Fig. 4.32 b), for snow depths inferred from the precipitation record of ERA reanalysis (P_{ERA}) and assuming half and double the winter precipitation of ERA reanalysis. Note that the soil properties and the other status parameters are equal for the three scenarios.

Chapter 5

Discussion

5.1 Monitoring of process variables under arctic conditions

In this thesis, a comprehensive set of field measurements has been compiled for a permafrost site on Svalbard, that contains not only the target variables of modeling efforts, but also many of the process variables, such as the turbulent land-atmosphere exchange fluxes. In the Arctic, similar data sets are extremely scarce, and comparable studies covering the entire annual cycle do not exist for arctic land areas so far. However, such studies can only constitute a sweeping support for modeling efforts, if long time series are available for a range of locations.
Due to the broadness of the employed methods and the considerable effort, it appears highly questionable to the author of this thesis, that similar concepts will be endorsed as long-term monitoring programs at a number of sites in the Arctic. Even with the relative proximity of the village of Ny-Ålesund, which greatly simplifies the access, logistical support and maintenance of field instrumentation, numerous problems with instrument failure have occurred in the course of this study, which can be expected to be even more severe in remote locations, where maintenance is not possible for long periods.
In this chapter, possibilities for robust monitoring approaches across climatic and ecological gradients are outlined. It must be emphasized that such conceptes should be adjusted to the requirements of modeling schemes.

5.1.1 Radiation

The short- and long-wave radiation components constitute the largest terms in the surface energy budget. The incoming short- and longwave radiation and the outgoing long-wave radiation are the only terms in the surface energy budget equation (Eq. 2.1), that do not have a direct functional dependence on the surface temperature (compare Eqs. 2.107 to 2.114). Thus, they determine the range within which the surface temperature can adjust according to land-atmosphere exchange processes and the heat flux in the ground. An example for the close

correlation between surface temperature and incoming long-wave radiation during winter is presented in Fig. 4.8. The importance of radiation measurements is reflected in the "Baseline Surface Radiation Network" (BSRN), which is an excellent example for a world-wide long-term monitoring program, that aims at providing an extensive data base in support of modeling efforts (Ohmura et al., 1998). Accurate radiation measurements under arctic conditions are challenging at best. During winter, considerable measurements errors can occur, particularly for the incoming long-wave radiation, if the sensors are not kept free of snow. Since such regular maintenance can only be provided close to settlements, only four BSRN sites (Barrow, USA; Alert, Canada; Summit, Greenland; Ny-Ålesund, Svalbard) exist north of the polar circle (www.bsrn.awi.de, 2010). While an extension of the BSRN network to other settlements in the Arctic is desirable, measurements of all four components of the radiation budget could also be conducted automatically at more remote sites, which would be a significant improvement of the radiation data set in the Arctic despite of a reduced measurement accuracy.
The albedo plays a central role in the surface energy budget, when the incoming short-wave radiation features high values. Over largely unpopulated areas, astonishing misrepresentations of this important parameter in circulation models have been revealed in the past: the winter albedo of boreal forest has been overestimated by as much 0.6 (!) in the ECMWF weather forecast model until late 1990s, which has led to a systematic underestimation of the near-surface air temperatures by as much as 10 K in the affected areas (Betts and Ball, 1997; Sellers et al., 1997). Therefore, further systematic studies on spatial and temporal albedo variations for different arctic landcover types would be desirable. This is particularly true for the snow melt period, where the albedo critically determines the timing of the snow melt in models.

5.1.2 Turbulent fluxes

The use of eddy covariance systems is limited by the power consumption and the need for regular maintenance and calibration. Furthermore, the failure to close the energy balance with eddy covariance measurements (Foken, 2008b) seriously questions the value of the method, if the long-term energy balance is targeted. At least, the question arises whether a similar performance can be achieved by using less sophisticated, less expensive and more robust instrumentation.
For flux monitoring at remote locations and over longer periods, gradient measurements of air temperature, relative humidity and wind speed are a substantial alternative. They rely on flux-gradient relationships analogous to Eqs. 2.109 to 2.112. If measurements of air temperature T, specific humidity q (from relative humidity and temperature) and wind speed u at two heights z_1 and z_2 above

the surface are available, the system of coupled equations

$$L_* = \frac{\rho_a c_p T(z_1)}{\kappa g} \frac{u_*^3}{Q_h + 0.61 c_p L_{lg}^{-1} T(z_1)\, Q_e} \tag{5.1}$$

$$u_* = \kappa \left(u(z_1) - u(z_2)\right) \left[\ln \frac{z_1}{z_2} - \psi_M \left(\frac{z_1}{L_*}, \frac{z_2}{L_*}\right)\right]^{-1} \tag{5.2}$$

$$Q_h = -\rho_a c_p \kappa u_* \left(T(z_1) - T(z_2)\right) \left[\ln \frac{z_1}{z_2} - \psi_H \left(\frac{z_1}{L_*}, \frac{z_2}{L_*}\right)\right]^{-1} \tag{5.3}$$

$$Q_e = -\rho_a L_{\mathrm{lg}} \kappa u_* \left(q(z_1) - q(z_2)\right) \left[\ln \frac{z_1}{z_2} - \psi_W \left(\frac{z_1}{L_*}, \frac{z_2}{L_*}\right)\right]^{-1} \tag{5.4}$$

can be solved to deliver the sensible and latent heat flux Q_h and Q_e, the friction velocity u_* and the Obukhov length L_*. The method implicitly assumes the correctness of the employed stability functions ψ_M, ψ_H and ψ_W, which is not guaranteed particularly during the arctic winter (Grachev et al., 2007). Therefore, it seems imperative to measure at several levels above ground to ensure the consistency of the obtained fluxes, which would also allow to directly assess the performance of the different parameterizations of the stability functions. As the accuracy of the obtained fluxes is largely determined by the accuracy of the measured gradients, a tower structure of at least 10 m height (preferably more) is required. While gradient measurements are classically performed at 2 and 10 m height, lower heights also seem promising in treeless arctic tundra, where well mixed conditions can be assumed close to the surface.

It is a considerable advantage of gradient measurements that the same framework, that is used in surface energy budget models (see Sect. 2.4.7), is employed to measure sensible and latent heat fluxes. With the fluxes and the height above ground of one of the sensors known, the gradient method facilitates to calculate the roughness length z_0 and also the roughness lengths z_{0_Θ} of temperature and z_{0_q} of humidity (see Sect. 2.4.6), for which almost no measurements exist in the Arctic (Andreas et al., 2010).

The perennial snow cover constitutes a serious challenge, as it alters the height of the measurements above the surface and possibly damages sensors, that are buried under the snow. Therefore, the snow height must be recorded, and measurements of wind speed and relative humidity, that are performed with rather fragile sensors, must be restricted to heights above the largest possible snow depth. With the use of more robust sonic anemometers, that are entirely waterproof and can be exposed to the mechanical stress by freezing and thawing processes, it may be feasible to measure wind speeds at lower heights.

The problems inherent in eddy-covariance measurements due to time averaging of turbulent fluctuations (see Sect. 2.5.2) can be at least partly circumvented by the use of Large-Aperture Scintillometry (e.g. Meijninger et al., 2002, 2006). This technique relates the turbulent fluctuations of air temperature and water vapor content within the path of a beam of electromagnetic radiation to intensity fluctuations ("scintillations") of the beam signal. The main advantage over eddy covariance systems is that time-averaging of turbulent fluctuations at a point is replaced by line-averaging across a beam path of several 100 m to a few kilometers. Therefore, large turbulence structures associated with low frequencies (see Sect. 2.5.2) can be captured by scintillometry. Furthermore, the technique can provide area averages of sensible and latent heat fluxes over large

areas with a much more defined footprint area compared to eddy covariance. Evidence has been gathered that turbulent fluxes obtained by Large Aperture Scintillometry using a combination of near-infrared and microwave radiation can indeed close the energy balance over heterogeneous terrain (overview in Foken, 2008b). However, it must be emphasized that the universal stability functions $\varphi_{M,H,W}$ proposed by the Monin-Obukhov similarity theory must be invoked (see Sect. 2.4.6) in order to calculate fluxes from intensity fluctuations of the beam. Therefore, the obtained fluxes depend on the functional form of the universal functions, that are based on few studies of atmospheric turbulence, such as the Kansas experiment (see Sect. 2.4.6).
While Large Aperture Scinitillometry is an evolving technique, it offers exciting prospects to improve the precision of the measurements of turbulent fluxes and thus explore land-atmosphere exchange processes in the Arctic with state-of-the-art techniques. However, the power requirements and maintenance needs of the instruments are a limiting factor for the use under arctic conditions, so that scintillometry will most likely be restricted to short campaigns in the near future, while long-term monitoring of turbulent fluxes must be accomplished by other techniques.

5.1.3 Ground heat flux and soil temperatures

The ground heat flux and the thermal regime of the soil constitute a considerable challenge for both measurements and models and significant uncertainties must be accepted (see Sect. 4.1.3). This may seem surprising in first place, considering the simple physical law of conductive heat transfer, that is largely applicable in permafrost soils (e.g. Kane et al., 2001). However, the uncertainty is much more caused by the small-scale heterogeneity of the soil parameters than by the actual description of the process of heat transfer into the soil.
In this thesis, two different approaches to determine the ground heat flux have been followed. The assets of the conductive method (see Sect. 2.3.2) are the excellent temporal resolution of the obtained fluxes and the relative simplicity of the installation: as a record of three temperatures between the surface and approximately 0.3 m depth is sufficient, it is feasible to apply the method at a large number of sites. However, the technique is limited to temperatures, where freezing or thawing of soil water does not occur, so that it is not possible to compile an annual budget based entirely on the conductive method. Furthermore, the method requires rapid temperature changes within the monitored soil domain, which may not occur during winter. A strong source of uncertainty is the determination of the volumetric heat capacity c_h from soil samples, which is required to calculate the thermal conductivity from the thermal diffusivity d_h. Taking the average from many soil samples collected in the vicinity of the temperature profile is not ideal, as the value may not be representative for the temperature profile due to the small-scale heterogeneity of the soil properties. Furthermore, the heat capacity can change over time, e.g. after rainfall events, which is difficult to capture with soil samples. A significant accuracy improvement could be achieved by in-situ measurements of the heat capacity by heated-needle probes, which have been successfully applied for unfrozen and fully frozen soil (Putkonen, 2003; Overduin et al., 2006; Ochsner et al., 2006). Ochsner and Baker (2008) optimize the technique to be applicable close to a freeze front and are

able to derive ground heat fluxes during the time of soil freezing and thawing. Thus, it seems possible to combine the conduction method with heated needle probes to facilitate monitoring of ground heat fluxes during the entire year.
In the calorimetric method (see Sect. 2.3.1), the volumetric heat capacity is a major source of uncertainty, too. The problem is even more severe, as it must be determined over a profile up to the depth, where the annual temperature cycle is negligible. As it is unpractical to install heated-needle probes deeply within the permanently frozen ground, a soil core must be obtained by drilling a borehole to determine the heat capacity in laboratory measurements. Despite of these limitations, the calorimetric method is more suitable than the conductive method to establish an annual budget of the internal energy content or long-term averages of the ground-heat flux, respectively.
In addition to the volumetric heat capacities, a record of temperature and volumetric soil water content is required up to the depth, where annual temperature cycle become insignificant. While it is feasible to drill a borehole, in which the temperature is recorded, the determination of the content of unfrozen water is more difficult. Time-Domain-Reflectometry (TDR) can be installed within the active layer (Boike et al., 2003b), where a hole can be dug to insert the TDR probes. However, the soil water content can also change below the depth of annual thaw due to the freezing characteristics of the soil. Instrumenting the permanently frozen ground with TDR would be an extremely arduous task, which would also involve a considerable destruction of the site.
Non-invasive radar techniques can provide averages of the soil water content over larger volumes with high accuracy, as they are required by the calorimetric method. Two schemes are conceivable:

1. Multi-channel ground penetrating radar (GPR) can determine the soil water content of the thawed zone by evaluating the travel times of multiple radar signals reflected from the freeze-thaw interface (Gerhards et al., 2008). Multi-channel GPR has been successfully applied at permafrost sites by Wollschläger et al. (2010) and Westermann et al. (2010), who determine both the thaw depth and the soil water content of the thawed zone over transects of several 100 m length. For permafrost sites that feature soils with a low content of unfrozen water at subzero temperatures, a combination of temperature records from one or multiple boreholes in conjunction with multi-channel GPR measurements could e.g. deliver the annual minimum and maximum content of internal energy of the soil column, which would be a near-ideal monitoring scheme for the soil thermal conditions: a radar survey conducted just before the onset of refreezing in fall could provide the soil water content and thus the latent heat content of the thawed zone at the end of the thaw season. The annual maximum content of internal energy is then calculated from the latent heat content and the temperature profile data (Westermann et al., 2010). The annual minimum of internal energy during winter can directly be derived from temperature measurements in the fully frozen soil. It must be emphasized that such a scheme could still produce meaningful results when the soil contains a non-negligible content of unfrozen water at subzero temperatures, but a reduced accuracy must be tolerated.

2. Cross-borehole radar can provide horizontal averages of the soil moisture

content by evaluating the travel time of a radar signal, that is emitted at depth d_1 in one borehole and received at depth d_2 in another borehole a few meters next to the first hole. Other than multi-channel GPR, it holds potential to measure the content of unfrozen soil water below the freeze-thaw interface. By recording travel times at a number of depths (d_1, d_2), a tomography of the soil water content between the two boreholes can be performed. While cross-borehole radar has not yet been employed in permafrost monitoring, its potential for hydrological applications and mapping the vertical distribution of the soil water content has become manifest in non-permafrost regions (e.g Binley et al., 2001; Olsson et al., 2006).

Finally, the potential of heat flux plates is briefly discussed, as they are widely applied to determine the ground heat fluxes in studies on the surface energy budget (Foken, 2008a). Heat flux plates consist of thin plate with known thermal conductivity, across which the temperature gradient is measured. The method is satisfactory, if the thermal conductivities of the heat flux plate and the surrounding soil material are equal. If not, the assumption of 1D-heat transfer is clearly violated, and the heat flux through the plate is not the same as in the surrounding soil. When the soil freezes, the thermal conductivity can change considerably, so that a number of heat flux plates with different thermal conductivities would be required to successfully determine the ground heat flux. While heat flux plates are appealing in their simplicity, significant and unacceptable errors in the determination of the ground heat flux have been documented (Sauer et al., 2003; Ochsner et al., 2006), so that great care must be warranted when applying the method.
In some permafrost areas, it might be feasible to determine ground heat fluxes by measuring temperature gradients across permanent layers of pure ice with known thermal conductivity, which would thus act as a natural in-situ heat flux plate. As these ice layers naturally occur below the depth of annual thaw, additional techniques, e.g. the calorimetric method, must be employed to obtain the ground heat flux at the surface.

5.1.4 Depth and properties of the snow pack

The perennial snow pack is of outstanding importance for the thermal regime in permafrost regions, as has been shown for the study area in Sect. 4.4. The insulating effect of the snow cover can essentially be described by three properties, the snow depth, the snow water equivalent and the thermal conductivity (note that the average snow density and thus the volumetric heat capacity can be calculated from snow depth and snow water equivalent). To record the snow depth over large regions, a georadar system mounted on a sled, that is towed from a snowmobile, can be employed (Holmgren et al., 1998; Sand and Bruland, 1998; Bruland et al., 2001). In addition to the average snow depth, the distribution of snow depths can be evaluated (Liston, 1999), from which the spatial variability of snow-soil interface temperatures can be estimated (see Sect. 4.4). In terrestrial measurements, the snow water equivalent and snow density are generally derived from snow samples. Determining the thermal conductivity of

snow is a difficult task, as it critically depends on the internal structure of the snow pack, that can be highly variable (Goodrich, 1982; Sturm et al., 1997). For modeling purposes, a bulk value representative for a larger snow volume, as it has been obtained with the conductive method in this thesis (see Sect. 4.1.3), is more appropriate than values obtained for small snow volumes e.g. using a heated-needle probe (compare Sturm et al., 2002). In case of a layered snow structure with frequent internal ice lenses, as it is typical for the study area, application of a heated-needle probe in the snow between the ice lenses could result in a considerable bias of the obtained thermal conductivities. The conductive method could potentially yield profiles of the thermal conductivity, if more temperatures in the snow pack are available. The technique could then be applied for a number of combinations of three sensors, or inversion schemes could be employed to derive a profile of the thermal conductivity in the snow pack. A near-ideal instrumentation would therefore include a profile of temperature sensors with a spacing of less than 0.1 m up to a height of 2 to 3 m. While the sensors above the snow pack yield the profile of the air temperature, that is required for determining the sensible heat fluxes and the near-surface stratification (see above), the sensors within the snow pack can deliver the thermal conductivity and the heat flux into the snow pack. Even the snow depth can be inferred with an accuracy of less than 0.1 m by determining the highest temperature sensor buried under snow, as its temperature record must features a phase shift relative to the sensors in the air (Lewkowicz, 2008).

5.2 Remote sensing techniques for large-scale monitoring

In contrast to terrestrial measurements, satellite-based sensors can cover large areas, which makes them ideally suited for monitoring the remote and largely unpopulated permafrost areas in the Arctic. Since the launch of the first weather satellites in the 1960s, the capabilities of earth observation satellites have expanded rapidly. In 2009, the European Space Agency initiated the "DUE Permafrost" project (www.ipf.tuwien.ac.at, 2010), which is dedicated to providing a range of new remote sensing products for permafrost research. Despite of the manifest potential in this approach, many remote sensing products are still in the validation stage in arctic regions, so that terrestrial measurements are even more required to achieve a satisfactory performance of satellite-based earth system monitoring in permafrost areas. In the following, a short synopsis of remote sensing applications in permafrost research is given, with a particular focus on the surface energy budget and the requirements of a large-scale permafrost monitoring scheme.

Radiation: In case of cloud-free conditions, the outgoing short- and long-wave radiation are accessible through various remote sensing platforms, that operate at different temporal and spatial resolutions. As the radiation is modified by scattering, absorption and emission in the atmosphere of the earth, a radiometric correction similar to the scheme applied for the thermal imaging system (see Sect. 2.7) is required. However, as satellite sensors perform spectrally resolved

measurements, e.g. 36 spectral bands between 400 nm and 15 μm for MODIS (King et al., 1992), a coincident characterization of the atmosphere and clouds is possible by combining the information from spectral bands, that are modified differently in the atmosphere. With Terra and Aqua MODIS, atmospheric profiles of temperature and water vapor as well as information on aerosols and ozone can be retrieved with a spatial resolution of 5 km for clear-sky conditions (Seemann et al., 2003; Gao and Kaufman, 2003). With a radiation transfer code (see Sect. 2.6), both incoming short- and long-wave radiation could thus be evaluated. The outgoing long-wave radiation is derived in the context of LST evaluation from satellite sensors. The albedo and even Bidirectional Reflectance Distribution Functions (BRDF) are available from several satellite sensors, e.g. from MODIS at a resolution of 500 m (Schaaf et al., 2002), so that the outgoing short-wave radiation can be evaluated. Therefore, the radiation budget under clear-sky conditions can in principle be evaluated from satellite measurement.
Prolonged periods with cloudy conditions, where measurements from satellites are not available, are a strong limitation for determining the radiation budget through remote sensing in the Arctic. In this thesis, the implications of the frequent cloud cover for the accuracy of remotely sensed land surface temperatures have been demonstrated (see Sect. 4.5). Despite of the great potential of remote sensing, terrestrial radiation measurements should be routinely conducted at many more sites in the Arctic to support both the improvement of satellite retrieval algorithms and modeling schemes.

Turbulent fluxes: A number of studies have evaluated possibilities to derive sensible and latent heat fluxes from remote sensing applications (e.g. Hall et al., 1992; Bastiaanssen et al., 1998; Friedl, 2002). However, as direct measurements of turbulent fluxes are not possible from satellites, the approaches are based on the surface energy budget equation or even make use of empirically derived relations in terms of e.g. surface temperature and soil moisture. Therefore, direct measurements of turbulent fluxes on the ground cannot be replaced by remote sensing at the moment.

Soil properties: Similarly, direct measurements of the ground heat flux or the soil composition from satellites are not possible. However, a few promising approaches have been made to characterize some of the soil parameters that are required for modeling the thermal dynamics of the soil:

- The surface soil moisture can be assessed from passive or active microwave sensors, e.g. AMSR–E (Njoku et al., 2003) or Envisat/ASAR (Baghdadi et al., 2006). However, the result is not independent of the surface cover, so that it is problematic to derive absolute values for the volumetric soil water content, which would be required to determine soil thermal properties. The penetration depth of the signal varies depending on the surface cover and the soil water content, so that the measured volume cannot be determined properly. Furthermore, typical penetration depths are on the order of a few centimeters, so that the by far largest part of the relevant soil region is not covered. Despite of these limitations, space-borne microwave sensors can offer an extremely valuable assessment of the soil moisture

regime in arctic regions, that may become of fundamental importance to improve modeling of the soil thermal regime.

- A highly practical approach is to assign representative soil properties to certain land cover elements, e.g. vegetation communities (e.g Walker et al., 2003). In many cases, land cover classes can be distinguished by their spectral characteristics in high-resolution multispectral images or the backscatter signature in Synthetic Aperture Radar images (e.g. Haack and Bechdol, 2000). This procedure inherently assumes that land cover classes determined from surface characteristics are good indicators for subsurface properties, which is not necessarily true. Furthermore, rather labor-intensive field campaigns are indispensable, which on the one hand must provide suitable training data sets for classifying the satellite images, while the representative thermal properties of the land cover classes must be evaluated on the other hand. Due to the wide range of ecosystems and climatic conditions found in permafrost areas, a pan-arctic classification scheme appears questionable. Therefore, regional landcover classes must be successively developed in a series of field campaigns in order to claim a convincing benefit for modeling. For Svalbard, a landcover map compiled from multispectral images of the Landsat Thematic Mapper is available (www.npolar.no, 2010). With 27 land cover classes, the map can be considered an excellent starting point for modeling efforts, although the study does not assign thermal properties of the soil to the land cover classes. Considering the relative homogeneity of the surface cover on Svalbard compared to other permafrost areas, a supreme long-term effort would be required in order to accomplish such detailed work on a pan-arctic scale.

Snow: The snow cover of the earth has been the target of remote sensing missions since the 1970s. Four different applications have a great potential for permafrost studies.

1. The presence of a snow cover can be determined with a high spatial resolution by multispectral images in the visible and near-infrared range of the electromagnetic spectrum (Hall et al., 1995). The formation and the disappearance of the perennial snow cover can therefore be determined with high temporal precision from satellite sensors such as MODIS (Hall et al., 2002). As with measurements of the land surface temperature, the cloud cover is the limiting factor for the temporal resolution. As the termination of the snow melt period with the associated change of the surface albedo is a crucial event in the annual cycle of the surface energy budget and the thermal dynamics of the permafrost, snow cover products may be critical for the success of permafrost monitoring schemes (see Sect. 5.3.1).

2. The snow water equivalent is accessible through space-borne passive microwave sensors, such as SMMR (1978–1987, Nimbus–7 satellite), SSM/I (1987–2002, DMSP satellites) and AMSR–E (2002–2010, Aqua satellite). These satellites record microwave emission from the ground due to blackbody radiation in frequency bands, that experience a different amount of attenuation from a snow cover (Foster et al., 1984), e.g. frequency bands centered around 19 and 39 GHz for the AMSR–E algorithm (Kelly et al.,

2003). Due to the weak signal of the emitted microwave radiation, passive microwave sensors must integrate over large areas, which leads to limited spatial resolutions of 25 km or more. For the study area, meaningful results for the snow water equivalent cannot be obtained, as sizable fractions of ocean and glaciers contribute to the footprint area of the satellite sensor. However, in less heterogeneous regions, the capabilities of passive microwave sensors to evaluate the snow water equivalent have been demonstrated in a number of studies (e.g. Derksen et al., 2003, 2005; Pulliainen, 2006).

3. The onset of the snow melt period can be obtained from active microwave sensors, such as QuickScat/SeaWinds (Long and Hicks, 2000), with which dry and wet snow can be distinguished. By exploiting the high temporal resolution of several measurements per day, Bartsch et al. (2007) developed a method to determine the first snow melt events as well as the end of daily freeze-thaw cycles on the snow surface. As with (1), such data may play an important role in permafrost monitoring schemes.

4. Bartsch et al. (2010) and Bartsch (2010) report the detection of rain-on-snow events in the backscatter signal of QuickScat/SeaWinds, which has great potential in permafrost modeling and monitoring, as rain-on-snow events can have a drastic impact on the winter soil temperatures (see Sect. 4.4). The representation of rain-on-snow events has been identified as the main limitation in the SEB model, as the employed precipitation record obtained from ERA reanalysis cannot properly resolve their occurrence (see Sect. 4.6.3). Therefore, data on rain-on-snow events from active microwave sensors may contribute to progress in modeling the ground thermal regime in permafrost regions, that are affected by rain-on-snow events.

5.3 Permafrost monitoring and modeling

In this section, we return to the initial question, how a permafrost monitoring scheme could be realized for large areas. While this thesis has touched many aspects relevant for permafrost models, it is evident that a large-scale scheme cannot evolve from a study restricted to one area alone. However, few studies in permafrost areas have operated with both field measurements, remote sensing and modeling, so this thesis wants to contribute to the discussion about the best monitoring concept. This is especially true in the wake of large-scale efforts, such as the DUE permafrost project from the "European Space agency" (www.ipf.tuwien.ac.at, 2010), which will make a wealth of new data sets available for permafrost monitoring.
While monitoring schemes based on MODIS-LST (Marchenko et al., 2009) can be successful on pan-arctic scale, the underrepresentation of predominantly cloud-covered periods in long-term LST averages and problems with cloud cover detection have been revealed (Liu et al., 2004; Langer et al., 2009, this study). Furthermore, MODIS-LST does not circumvent the problem to find an adequate representation of the snow cover, which requires the use of other satellite products, such as snow water equivalents from passive microwave sensors. Finally,

the maximum spatial resolution of a monitoring scheme based on MODIS-LST is fixed by the spatial resolution of the used satellite sensors, so that subgrid variability of permafrost temperatures may become an issue at some sites (see Sects. 4.3, 4.4). Therefore, it is worthwhile to evaluate alternative schemes, that may facilitate operational permafrost monitoring on a pan-arctic scale.
We formulate the following constraints to be met by such a permafrost monitoring scheme:

1. For all points, the performance of a new monitoring scheme must match or exceed the performance of MODIS LST-based permafrost monitoring. Only then, a scheme could claim to be a scientific advance.

2. As significant technological progress of remote sensing platforms and senors can be expected in the future, the monitoring scheme should be sufficiently flexible to incorporate new remote sensing products. The same should be true for improved reanalysis products.

3. A quality assessment for the obtained ground temperatures should be possible at least in a qualitative way.

4. As the initialization of the soil model is a critical issue, the scheme should incorporate a long spin-up period to moderate the impact of the initial condition.

5. The scheme should be capable to account for small-scale spatial heterogeneity of different processes. A scale-independent formulation would thus be desirable.

6. The approach should be directly linkable to models targeting the future permafrost conditions.

In the following, a monitoring scheme based on the SEB model presented in Sect. 4.6 is sketched, which has the potential to exploit the information content of a variety of remotely sensed data and field observations in addition to MODIS LST. The challenge is to integrate data sets at highly different spatial and temporal resolutions in a flexible scheme, that is on the other hand sufficiently robust to handle the inherently variable data quality of many data sets.

5.3.1 Data fusion to incorporate satellite data and ground observations

Data fusion is a technology to integrate information from a number of sources to form a unified picture (Hall and Llinas, 1997). The basic idea is to regard surface energy budget models as a tool for data fusion of various remote sensing applications, but also modeling results and ground observations. In such a scheme, they would be employed as training data to determine, optimize or confine the status parameters, that are required in a surface energy budget model. This reduces the importance of spatial and temporal resolution of the training data sets, as long as the contained information suffices to estimate the model parameters. The data fusion strategy can only be successful if enough training data

sets with orthogonal information content are available to constrain the status parameters in the SEB model (see Sect. 4.6). If long time series of the training data sets are available, it may be feasible to compile statistical relationships for the status parameters, that can be applied to improve the model results for periods, when the training data are not available. This is of particular importance, as most remote sensing products are available for less than a decade, while the time series of the operational ERA reanalysis data set encomprises more than fifty years. In principle, it is possible to apply such a procedure in near real-time, so that newly obtained training data contribute to improvements of the entire time series of results.
Similar concepts are widely used in remote sensing applications: an example is the operational MODIS BRDF/albedo algorithm, which has been started with an initial guess for the BRDF kernel for each pixel at the launch of the Terra satellite, but could gradually refine the functional form with the amount of available data to even yield the seasonal characteristics (Schaaf et al., 2002). The significance of such spatially resolved statistics of parameters sets in global models has been realized for the example of the MODIS BRDF/albedo algorithm: "This global archetypal database of entirely MODIS-derived representations of seasonal BRDFs may well prove to be one of the most valuable byproducts of this effort and be of particular interest to global modelers interested in using realistic land surface parameterizations of the surface anisotropy" (Schaaf et al., 2002). The same would be true for a permafrost monitoring scheme that could eventually compile an extensive data base of surface parameters. Similar strategies have been followed in the past (Sellers et al., 1996), but substantial improvements could be achieved for the so far poorly represented arctic land areas.
In the following, a data fusion strategy is exemplified that integrate different data sets to facilitate the application of an SEB model over larger areas, where ground information is generally unavailable.

Albedo

As stated above, the albedo can be determined at spatial resolutions of 500 m from the MODIS sensor. As the albedo changes rather slowly over time, the MODIS-derived values from cloud-free periods can be assigned to cloud-covered periods without problems. In a refined model simulation, it would be feasible to distinguish between black-sky and white-sky albedo provided by MODIS (Schaaf et al., 2002) to account for different aspects and expositions of the ground by splitting the short-wave radiation in a diffuse and a direct part. The albedo information is also crucial to determine the termination of the snow melt period, the development of the albedo during snow melt as well as the evolution of the fraction of snow-free surfaces over time (by assuming a mixing between a "summer" value for snow-free and a "winter" value for still snow-covered surface). While all three points crucially contribute to determining the true snow water equivalent before snow melt (see below), the two latter could even help to develop or validate a model for the snow depth distribution during winter. As stated before, it is not necessary to continuously monitor the albedo during the snow melt period, as the scheme would simply use the existing data to evaluate the above parameters and relationships. Therefore, cloud-covered

periods are not a principal problem, although they can lead to an increased error if only few data points are available.

Land surface temperature

Due to its central role in the surface energy budget, the surface temperature is ideally suited for validating surface energy budget models of permafrost (see Sect. 4.6). The free parameters that determine the surface temperature for fixed operational data sets are the surface albedo α, the surface resistance against evapotranspiration r_s and the roughness length z_0. When the albedo is fixed from independent satellite observations (see above), the roughness length and the surface resistance can be adjusted to fit the remote sensing observations. To a certain extent, the roles of the roughness length and the surface resistance are interchangeable in the latent heat flux equation 2.112. However, the roughness length is usually constrained within reasonable boundaries, that may be obtained from ground measurements or existing literature values for different land cover types (Hasager et al., 2003). Furthermore, the roughness length can be assumed constant in time (during summer) and over larger areas with similar surface cover, while the surface resistance can vary in space and time according to the surface soil moisture content. In addition, remotely sensed surface soil moisture products can constrain the surface resistance, while a number of concepts to determine the roughness length have been discussed (e.g. Schaudt and Dickinson, 2000; Prigent et al., 2005).
It must be emphasized that the clustered times series typical for remotely sensed LST is not constrictive to this approach. Furthermore, infrequent measurement errors due to inaccurate cloud detection (see Sect. 4.5) become apparent as misfits with the surface temperature obtained from a surface energy budget model and could thus be discarded. In this sense, an SEB scheme, in which MODIS LST are included as training data, must be considered superior to a purely MODIS LST-based scheme.

Snow

On a coarse grid, the snow water equivalent is provided by passive microwave sensors (see above), such as AMSR–E. However, the snow water equivalent can change on much smaller scales, as has been observed in the study area, so that remotely sensed snow water equivalents can only be used to constrain the average over larger areas. Therefore, the termination of the snow melt (see above) could be used to determine the snow water equivalent before the ablation, as areas with a higher snow water equivalent will take longer to melt out. This is exemplified by simulations with the SEB model for different snow water equivalents (Fig. 4.33), which would facilitate to "fit" the correct snow water equivalent if the termination of the snow melt is determined from remote sensing. Crucial to this approach is a correct representation of the albedo during the snow melt period (see above) and correct forcing data from the reanalysis products. However, there is great potential in such a joint strategy to do justice to the outstanding importance of the snow cover.
Nevertheless, two critical parameters for the thermal regime of the ground, the

snow density and the thermal conductivity are hardly accessible through remote sensing, so that one must resort to empirical parameterizations obtained from field measurements (e.g Sturm et al., 1997).

Land cover

Land cover classifications can be considered the most simple concept to upscale ground measurements to larger areas. Surface or subsurface properties determined in field measurements are assigned to a land cover class that can be identified by remote sensing. The advantage of this concept is its simplicity and easy applicability, while it is also prone to serious misrepresentations, if too few ground measurements are considered to be representative for too large areas. As field measurements are generally rare in the Arctic, the latter is indeed problematic. Nevertheless, a permafrost monitoring scheme will have to intensively rely on land cover classifications particularly for subsurface properties, which are generally inaccessible to remote sensing. It must be emphasized that an adequate land cover classification scheme must be developed, that is specifically designed to deliver surface and subsurface properties, that cannot be accessed in another way.

Terrestrial observations

Terrestrial observations, as they have been presented in this thesis, must be conducted at a number of designated sites to validate all employed parameterizations and procedures. Firstly, the long-term monitoring of a number of physical properties, as it has been highlighted in the previous section for radiation, turbulent fluxes, snow properties and the ground thermal regime, is crucial to the success of any permafrost monitoring scheme, as it is the only way to directly evaluate the performance and thus motivate improvements to the scheme. As such, the monitoring of borehole temperatures and thaw depths within the TSP and CALM programs are direct ground truth data to be reproduced by a pan-arctic scheme, and it is indispensable to add further localities, especially in underrepresented areas. Secondly, field campaigns and laboratory experiments must be designed to develop, validate and improve employed parameterizations. Among the most urgent and rewarding are improved parameterizations of the thermal conductivities of frozen and freezing organic and mineral soil as well as of snow under different climatic conditions.

Reanalysis products

Finally, the operational data sets of incoming radiation, air temperature, relative humidity, wind speed and precipitation derived from ERA-reanalysis must be critically evaluated. While these quantities can be assumed to vary on much greater distances compared to the surface and the subsurface temperatures, they are obtained from model runs constrained by only few ground data in the Arctic (Uppala et al., 2006), so that the employed data may be erroneous. An example is the summer air temperature at the study site, which is systematically too low, probably since the region around the study area is predominantly represented

as ocean in the reanalysis model. It is the hope that such misrepresentations can be largely detected by an insufficient fit with training data sets, or produce parameters that strongly deviate from expected values. If e.g. the surface energy budget model predicts the turbulent land-atmosphere exchange of an area to be dominated by sensible heat fluxes, but remotely sensed data suggest wet surface soil moisture conditions, this may pinpoint to wrong input data, such as air temperature or radiation and thus a reduced reliability. Such problems may suggest a reduced reliability of the obtained soil temperatures and should be documented in terms of a quality assessment scheme.
With the NCEP/NCAR reanalysis (Kalnay et al., 1996) and the JRA-25 reanalysis (Onogi et al., 2005), alternatives to the employed ERA product are available that could be tested for sites where such quality issues arise. Bromwich et al. (2007), who evaluate the differences between the three reanalysis products for polar regions, observe differences in the representation of clouds and the associated radiation impacts, so that it may indeed be worthwhile to evaluate different reanalyses in permafrost monitoring.

5.3.2 Spatial variability

Due to the essentially scale-independent formulation of a surface energy budget formulation, it is in principle possible to model on sufficiently small grids to account for the spatial heterogeneity typical for permafrost regions. However, the spatial resolution is in practice determined by the training data sets, so that the resolution of e.g. a MODIS-LST based scheme cannot be improved.
However, there exist possibilities to deaggregate spatially variability on the subgrid scale by probability density functions or, even more simple, in terms of different scenarios, that span the range of truly existing conditions. Two examples for such strategies are given:

- The spatial variability of the summer surface temperatures due to different surface soil moisture conditions has been documented in this thesis (see Sect. 4.3). The land surface temperature is also accessible by sensor such as Landsat Thematic Mapper at a much better spatial resolution of 60 m (Wukelic et al., 1989; Sobrino et al., 2004), but only few, if any measurements can be provided for a summer season. However, this may be sufficient to at least estimate the surface resistance at a much finer resolution compared to MODIS-LST, particularly since data from different years could be combined. Then, the SEB model could be run on the refined scale, while the operational consistency check with MODIS-LST training data would be accomplished for spatially averaged surface temperatures from the refined scale. Nevertheless, spatial differences in the surface temperature on scales of a few meters, as they have been observed for the study area, can still not be represented in this way. A different approach could be to compile a distribution function for a specific land cover class in field measurements, which may be feasible for certain land cover types with regular subgrid features, such as polygonal tundra.
  Other sources of subgrid variability may be different aspects and expositions, which could be derived from high-resolution digital elevation models. Within a surface energy budget model, they could be accounted for with

relative ease in terms of a modified short-wave radiation budget.

- The spatial variability of the snow cover is the largest source of spatial variability of the ground thermal regime in the study area, which is most likely conferrable to other regions with a pronounced topography. The variability of snow depths could e.g. be inferred from snow distribution models (Liston and Sturm, 1998) and incorporated in the model in terms of different scenario runs. This way, both counterbalancing effects of e.g. above-average snow depths, namely the stronger insulation from the cold winter temperatures and the shortening of the summer thaw season (see Sect. 4.4), would be represented in a surface energy budget scheme. As outlined above, such a snow depth distribution could be compiled from albedo measurements by assuming a functional dependence on the snow fraction, or by observing the snow melt pattern with high-resolution satellite images (König and Sturm, 1998; Liston, 1999). Other than that, the topographical information obtained from a high-resolution digital elevation model could be used to obtain a snow depth distribution which has been realized in a number of studies (e.g. Evans et al., 1989; Luce et al., 1998).

Care must be taken when probability density functions for more than one parameter are used, as these are generally not independent of each other. An example observed at the study area is an indirect correlation between the winter snow depth and the surface soil moisture conditions. Low snow heights are usually restricted to windblown ridge tops, which on the other hand are well-drained and thus feature a low soil water content. Conversely, snowdrifts with above-average snow depths form in concave structures, such as gullys and hillsides, which are generally characterized by wet soil conditions. Such dependencies between different parameters add additional complexity to modeling. Nevertheless, techniques to access subgrid information should be explored further, as the observed spatial variability of the determining factors for the ground thermal regime may also imply a spatially different susceptibility and vulnerability of the permafrost to a warming climate, which would be obscured in coarse-resolution schemes. For monitoring and modeling the present and future state of the permafrost, this aspect deserves more attention, as most approaches are designed to use average quantities for large grid cells. Such average quantities may indeed be inappropriate for some monitoring tasks: while a spatial average of the active layer thickness is adequate for e.g. the projection of methane emissions from thawing permafrost, the monitoring of erosion or natural hazards due to permafrost degradation, which would initially occur at few localized "weak points" within a grid cell, is only feasible if subgrid information is available.

5.3.3 Final assessment

Based on the constraints on a permafrost modeling scheme formulated above, a final assessment of the prospects of a surface energy budget scheme is given:

1. The performance of a MODIS-LST based scheme is matched by a surface energy budget model, if the satellite measurements are adequately reproduced in such schemes. This is accomplished by using MODIS-LST and

surface temperature measurements from other remote sensing platforms as training data to adjust parameters like the surface resistance to evapotranspiration or the roughness length. The performance of a MODIS-LST based scheme is exceeded, as surface energy budget models deliver surface temperatures during cloud-covered periods. Furthermore, measurements errors in satellite-based LST measurements can be deduced. All other satellite data sets employed for LST-based schemes, such as data on the snow cover, are accounted for in surface energy budget schemes as training data.

2. If new or improved remote sensing products become available, they can be incorporated in a surface energy budget scheme as additional training data. To exploit the full performance, it may become necessary to at least partly adapt or refine the calculations performed for the entire time series. An example would be an LST-product with improved spatial resolution: if the new product identifies a significant spatial variability within one of the old, coarsely resolved grid cells, this new information can be used to calculate e.g. spatially resolved surface resistances. If the surface temperature on the new, better resolved grid conforms with the time series of the coarse-resolution product, the grid could be refined for the entire time series, resulting in an improved spatial resolution.

3. The quality and reliability of the obtained soil temperatures can be assessed from the degree of agreement with training data. Furthermore, as many preliminary results and physically meaningful properties are available a in surface energy budget scheme, inconsistencies can be detected more easily. Such quality assessment will eventually result in improved parameter and input data sets, as it signposts remaining deficits and thus prospects for future research.

4. As surface energy budget schemes can exploit the long time series provided by reanalysis products, they can be initialized in the mid of the 20th century, which allows for a significantly improved spin-up of the soil model, compared to the decade-long record of LST provided by remote sensing platforms. The spin-up period could be extended to several hundreds or even thousands of years by using control runs of GCMs, that have been validated with paleoclimatic data (e.g Jones et al., 1998; Crowley, 2000; Kitoh et al., 2001).

5. A priori, a surface energy budget model is a point formulation. If applied over larger spatial domains, all input parameters are assumed to be constant for this domain. When spatially resolved input parameter sets are not available, distribution functions for parameters like the snow depth, that have a large impact on the ground thermal regime, could be incorporated to estimate subgrid variability.

6. Surface energy budget schemes share the common framework of the surface energy budget equation with GCMs, although their focus is clearly different. Nevertheless, the extensive statistics in space and time of surface and subsurface parameters, that would be obtained within the framework of an operational surface energy budget scheme, could be exploited to improve the performance of GCMs in the Arctic. Conversely, the output of

GCMs could seamlessly drive a surface energy budget scheme to deliver predictions of the future state of permafrost. It must be emphasized that the thorough initialization of the soil model with present-day conditions, as it could be accomplished by a permafrost monitoring scheme, may be key to greatly improving the accuracy and credibility of modeling results on future permafrost conditions.

Chapter 6

Summary and concluding remarks

In this thesis, the sensitivity of the ground thermal regime towards a variety of environmental factors has been elucidated for a high-arctic permafrost site on Svalbard. Specifically, the annual surface energy budget, the spatial and temporal variability of surface temperatures and the impact of the snow cover on the ground thermal regime have been investigated. The results of the field measurements are subsequently conceptualized in a process-based permafrost model.

Annual surface energy budget: In extensive field measurements, the surface energy budget has been evaluated for an entire year with independent measurements of all components. The most important aspects of the annual surface energy budget of the study area can be summarized as follows:

- During polar night conditions in winter, the long-wave radiation, the sensible heat flux and the heat released from the refreezing active layer have been identified as the main components of the surface energy budget. The incoming long-wave radiation is the determining factor for the surface temperature of the snow, but a significant influence particularly of the sensible heat flux remains.

- During the snow-free period of the polar day season, the system is governed by the short-wave radiation, while turbulent fluxes and the long-wave radiation are the main balancing factors in the surface energy budget.

- A more "winter-like" surface energy budget is found during the first half of the polar day season due to the the long-lasting snow cover with its high albedo, which effectively limits the role of the short-wave radiation. The albedo change induced by the snow melt is therefore of critical importance for the annual surface energy budget, as it marks the transition point between two fundamentally different regimes. Therefore, the correct representation of the snow melt must be considered crucial for both monitoring and modeling schemes in permafrost areas.

Impact of the snow cover: When the ground is snow-covered, the soil temperatures critically depend on two factors: the snow depth and the occurrence of rain-on snow events. If rain water percolates to the bottom of the snow pack and refreezes, the snow-soil interface temperature is sustained close to the freezing point for prolonged periods. The soil temperature records established for this thesis and the decadal record from the Bayelva station within the study area give ample evidence for the significant impact of rain-on-snow events on the soil temperatures.
In the study area, the snow depths during winter are observed to differ by more than a factor of four due to strong snow drift. In measurements of soil temperatures at sites with different snow depths, two partly counterbalancing effects on the soil temperatures have been observed:

- During winter, a higher snow pack insulates the ground from the cold surface temperatures, so that the soil temperatures remain much warmer compared to sites with lower snow depths.
- A larger snow depth results in a delayed snow melt. Accordingly, the termination of the snow melt varies by more than four weeks within the study area, so that the length of the summer thaw season can differ by up to a factor of two.

Surface temperature: The impact of a delayed snow melt on the average summer surface temperature has been observed in spatially resolved measurements of the surface temperature using a thermal imaging system, that have been conducted over the course of two summer seasons. The monitored area features a pronounced spatial variability of the snow cover, the soil moisture conditions and the surface cover, so that an assessment on the long-term impact on the surface temperature can be given.

- The differences in the termination of the snow melt result in differences of more than 10 K in weekly averages of the surface temperature.
- The weekly averages of the surface temperature feature maximum differences of 3 to 4 K between dry and wet areas, which diminish towards fall.
- In the study area, the spatial differences caused by the snow melt and by different soil moisture conditions add up, as wet areas on average feature greater snow depths and thus melt out later compared to dry areas. Therefore, the degree-day totals of the snow-free period can differ by more than 60% throughout the study area.
- The differences in the surface temperature between wet and dry areas are a result of a different surface energy budget. In a model of the surface energy budget, that can reproduce the surface temperatures of both wet and dry sites, the turbulent fluxes at dry sites are dominated by the sensible heat flux, while latent heat fluxes outweigh the sensible heat flux over wet areas.
- The sum of the turbulent fluxes depends on the net radiation, which turns out to be a good control parameter for the occurrence and magnitude of spatial variability between wet and dry areas: the maximum differences

of the surface temperatures exist under clear-sky conditions with high positive or negative values of net radiation, while the spatial variability largely vanishes with declining net radiation towards fall and in case of overcast conditions, respectively.

Ground thermal regime: From the extensive set of measurements, three determining factors for the ground thermal regime can be condensed, that vary both in space and time in the study area:

- The average surface temperature
- The snow depth
- The occurrence of rain-on-snow events

The impact on the soil temperatures is particularly pronounced, if sustained variations of these factors occur on annual and multiannual timescales, i.e. a pronounced increase in snow depth during an entire winter season or the cumulative occurrence of rain-on-snow events in certain winters. For permafrost monitoring and modeling schemes, an adequate representation of the three factors is indispensable.

Permafrost monitoring using MODIS LST: Remotely sensed land surface temperatures (LST) from the Moderate Resolution Imaging Spectroradiometer (MODIS) appear to be well suited as input for a permafrost monitoring scheme. To evaluate the performance of MODIS LST for the study area, terrestrial observations of surface temperatures are compared to remotely sensed land surface temperatures from MODIS. The following conclusions for LST-based permafrost monitoring can be drawn:

- LST measurements from a satellite require clear-sky conditions, which leads to strongly clustered time series of MODIS LST measurements. To avoid an overrepresentation of fair-weather periods in temporal averages and thus a potential bias, a robust gap filling algorithm is required for prolonged periods with overcast skies, when satellite-derived LST measurements are not available.
- The current version of the MODIS L2 LST data set contains strongly erroneous measurements, which are presumably caused by incorrect cloud detection. As the erroneous data points can give rise to a considerable bias of temporal averages of the surface temperature, they must be detected and discarded prior to application of a permafrost monitoring scheme.
- During winter, the combined effects of systematic overrepresentation of clear-sky conditions and erroneous cloud detection cause a negative bias of the average of MODIS LST of around 3 K, which has been verified for a time series of seven winter seasons.
- During summer, sustained differences in the average surface temperature on the order of a few Kelvin occur on distances of less than 100 m, which are not resolved in satellite-based LST measurements. This clearly causes

a bias of the summer surface temperature for some areas within a satellite pixel.

Surface energy budget schemes: While the above statements in a strict sense are only valid for the study area, they suggest principal deficiencies when obtaining average surface temperatures for permafrost monitoring from MODIS LST. Therefore, it is desirable to develop and validate alternative schemes, that could facilitate monitoring of the ground thermal regime over larger areas.
In this thesis, a surface energy budget model has been developed, that conceptualizes the findings on the annual surface energy budget and the determining factors for the ground thermal regime. Hence, it is designed to account for the surface temperature, the dynamics of the snow cover and rain-on-snow events using the 50-year record of globally available ERA reanalysis products. While modeled surface temperatures are in excellent agreement with measurements and clearly superior to the record of MODIS LST, the build-up dynamics of the snow cover and the detection of rain-on-snow events from the precipitation record of the reanalysis product have been identified as major shortcomings. However, there is great potential in using remote sensing applications to overcome these limitations.
To facilitate permafrost monitoring with a surface energy budget scheme on large scales, one must find ways to estimate the required model parameters, e.g. the albedo or the roughness length, with an adequate spatial resolution. However, with an increasing number of remote sensing products available, data fusion concept may allow great progress in this question, as they would allow to integrate a variety of remotely sensed data sets, including MODIS LST, in a surface energy budget scheme. While such ideas may evolve to a pan-arctic permafrost monitoring scheme, they also contribute to improving model predictions on the future thermal state of the permafrost.

Final notes: As a concluding remark to this thesis, the author wishes to emphasize the importance of extensive data sets on the surface energy budget, or even more general, the importance of field observations in the Arctic. The field measurements for this thesis have been performed at a site on Svalbard where a significant warming trend is expected in the near future, so they can be considered a baseline study to assess future shifts in the surface energy budget and other variables. It must be emphasized that an ongoing monitoring of radiation, land-atmosphere exchange processes and ground heat fluxes is indispensable to gain a better understanding of climate changes and its impact on permafrost. This should include the winter season, where the most pronounced future warming is projected to occur in most arctic regions (e.g. Chapman and Walsh, 2007), but for which few studies exist.
The correct representation of the surface energy budget is crucial in all coupled land-atmosphere models. As stressed in the most recent Implementation Plan of the "World Climate Research Programme" (wcrp.wmo.int, 2010), data sets on the surface energy budget are fundamental in order to validate and potentially improve such modeling schemes. In strong contrast to their recognized importance, comprehensive observations of soil, snow and atmospheric quantities are extremely sparse in the Arctic. This study exemplifies the need to initiate similar efforts at various locations across the climatic and ecological gradients in

permafrost areas to eventually establish a pan-arctic data base. Such a compilation would be of outstanding importance to improve the understanding of the sensitivity of permafrost and high-latitude ecosystems and their susceptibility to climate change.

Bibliography

ACIA, 2005. Arctic Climate Impact Assessment. Cambridge University Press. URL `http://www.acia.uaf.edu`

Amiro, B., 1998. Footprint climatologies for evapotranspiration in a boreal catchment. Agricultural and Forest Meteorology 90, 195–201.

Andreas, E., Horst, T., Grachev, A., Persson, P., Fairall, C., Guest, P., Jordan, R., 2010. Parametrizing turbulent exchange over summer sea ice and the marginal ice zone. Quarterly Journal of the Royal Meteorological Society.

Baghdadi, N., Holah, N., Zribi, M., 2006. Soil moisture estimation using multi-incidence and multi-polarization ASAR data. International Journal of Remote Sensing 27 (10), 1907–1920.

Bartsch, A., 2010. Ten Years of SeaWinds on QuikSCAT for Snow Applications. Remote Sensing 2 (4), 1142–1156.

Bartsch, A., Kidd, R., Wagner, W., Bartalis, Z., 2007. Temporal and spatial variability of the beginning and end of daily spring freeze/thaw cycles derived from scatterometer data. Remote Sensing of Environment 106 (3), 360–374.

Bartsch, A., Kumpula, T., Forbes, B., Stammler, F., 2010. Detection of snow surface thawing and refreezing in the Eurasian Arctic using QuikSCAT: implications for reindeer herding. Ecological Applications.

Bastiaanssen, W., Menenti, M., Feddes, R., Holtslag, A., 1998. A remote sensing surface energy balance algorithm for land (SEBAL). 1. Formulation. Journal of Hydrology 212, 198–212.

Beare, R., MacVean, M., Holtslag, A., Cuxart, J., Esau, I., Golaz, J., Jimenez, M., Khairoutdinov, M., Kosovic, B., Lewellen, D., et al., 2006. An intercomparison of large-eddy simulations of the stable boundary layer. Boundary-Layer Meteorology 118 (2), 247–272.

Becker, F., Ramanantsizehena, P., Stoll, M., 1985. Angular variation of the bidirectional reflectance of bare soils in the thermal infrared band. Applied optics 24 (3), 365–375.

Beine, H., Argentini, S., Maurizi, A., Mastrantonio, G., Viola, A., 2001. The local wind field at Ny-Ålesund and the Zeppelin mountain at Svalbard. Meteorology and Atmospheric Physics 78 (1), 107–113.

Betts, A., Ball, J., 1997. Albedo over the boreal forest. Journal of Geophysical Research-Atmospheres 102 (D24), 28901–28909.

Binley, A., Winship, P., Middleton, R., Pokar, M., West, J., 2001. High-resolution characterization of vadose zone dynamics using cross-borehole radar. Water Resources Research 37 (11), 2639–2652.

Boike, J., Hinzman, L., Overduin, P., Romanovsky, V., Ippisch, O., Roth, K., 2003a. A comparison of snow melt at three circumpolar sites: Spitsbergen, Siberia, Alaska. In: Proceedings of the 8th International Conference on Permafrost, Zürich, Switzerland. pp. 21–25.

Boike, J., Ippisch, O., Overduin, P., Hagedorn, B., Roth, K., 2008. Water, heat and solute dynamics of a mud boil, Spitsbergen. Geomorphology 95 (1-2), 61–73.

Boike, J., Roth, K., Ippisch, O., 2003b. Seasonal snow cover on frozen ground: Energy balance calculations of a permafrost site near Ny-Ålesund, Spitsbergen. Journal of Geophysical Research-Atmospheres 108 (D2), 8163–8173.

Boike, J., Westermann, S., Piel, K., Overduin, P., 2010. Warming of Permafrost Temperatures on Svalbard - What Is the Effect of the Snow Cover? European Conference on Permafrost, Longyearbyen, Norway.

Brandt, R., Warren, S., 1993. Solar-heating rates and temperature profiles in Antarctic snow and ice. Journal of Glaciology 39 (131), 99–110.

Bromwich, D., Fogt, R., Hodges, K., Walsh, J., 2007. A tropospheric assessment of the ERA-40, NCEP, and JRA-25 global reanalyses in the polar regions. Journal of Geophysical Research 112 (D10), 10111.

Brown, J., Ferrians Jr, O., Heginbottom, J., Melnikov, E., 1997. Circum-Arctic map of permafrost and ground-ice conditions. US Geological Survey Circum-Pacific Map.

Bruland, O., Sand, K., Killingtveit, A., 2001. Snow distribution at a high arctic site at Svalbard. Nordic Hydrology 32 (1), 1–12.

Burgess, M., Smith, S., Brown, J., Romanovsky, V., Hinkel, K., 2000. The Global Terrestrial Network for Permafrost (GTNet-P): permafrost monitoring contributing to global climate observations. Current Research 2000-E, Geological Survey of Canada.

Businger, J., 1982. Equations and concepts, in: Atmospheric Turbulence and Air Pollution Modelling. Reidel, Dordrecht, pp. 1–36.

Bussières, N., 2002. Thermal features of the Mackenzie Basin from NOAA AVHRR observations for summer 1994. Atmosphere-Ocean 40 (2), 233–244.

Campbell, G., Jungbauer Jr, J., Bidlake, W., Hungerford, R., 1994. Predicting the effect of temperature on soil thermal conductivity. Soil Science 158 (5), 307–313.

Carlson, H., 1952. Calculation of depth of thaw in frozen ground. Frost Action in Soils: A Symposium, 192–223.

Chandrasekhar, S., 1960. Radiative transfer. Dover Publications.

Chapin, F., Sturm, M., Serreze, M., McFadden, J., Key, J., Lloyd, A., McGuire, A., Rupp, T., Lynch, A., Schimel, J., et al., 2005. Role of land-surface changes in Arctic summer warming. Science 310 (5748), 657–660.

Chapman, W., Walsh, J., 2007. Simulations of Arctic temperature and pressure by global coupled models. Journal of Climate 20 (4), 609–632.

Chernykh, I., Eskridge, R., 1996. Determination of cloud amount and level from radiosonde soundings. Journal of applied meteorology 35 (8), 1362–1369.

Comiso, J., 2006. Arctic warming signals from satellite observations. Weather 61 (3).

Comiso, J., Parkinson, C., 2004. Satellite-observed changes in the Arctic. Physics Today 57 (8), 38–44.

Comiso, J., Parkinson, C., Gersten, R., Stock, L., 2008. Accelerated decline in the Arctic sea ice cover. Geophysical Research Letters 35 (1), L01703.

Cottier, F., Nilsen, F., Inall, M., Gerland, S., Tverberg, V., Svendsen, H., 2007. Wintertime warming of an Arctic shelf in response to large-scale atmospheric circulation. Geophysical Research Letters 34 (10).

Crowley, T., 2000. Causes of climate change over the past 1000 years. Science 289 (5477), 270.

Curry, J., Rossow, W., Randall, D., Schramm, J., 1996. Overview of Arctic cloud and radiation characteristics. Journal of Climate 9 (8), 1731–1764.

de Vries, D., 1952. The thermal conductivity of soil. Mededelingen van de Landbouwhogeschool te Wageningen 52 (1), 1–73.

Delisle, G., 2007. Near-surface permafrost degradation: How severe during the 21st century? Geophysical Research Letters 34 (9), 9503.

Dereniak, E., Boreman, G., 1996. Infrared detectors and systems. Wiley-Interscience.

Derksen, C., Walker, A., Goodison, B., 2005. Evaluation of passive microwave snow water equivalent retrievals across the boreal forest/tundra transition of western Canada. Remote sensing of environment 96 (3-4), 315–327.

Derksen, C., Walker, A., LeDrew, E., Goodison, B., 2003. Combining SMMR and SSM/I data for time series analysis of central North American snow water equivalent. Journal of Hydrometeorology 4 (2).

Douville, H., Royer, J., Mahfouf, J., 1995. A new snow parameterization for the Meteo-France climate model. Climate Dynamics 12 (1), 21–35.

Durre, I., Vose, R., Wuertz, D., 2006. Overview of the integrated global radiosonde archive. Journal of Climate 19 (1), 53–68.

Eugster, W., Rouse, W., Pielke Sr, R., McFadden, J., Baldocchi, D., Kittel, T., Chapin, F., Liston, G., Vidale, P., Vaganov, E., Chambers, S., 2000. Land–atmosphere energy exchange in Arctic tundra and boreal forest: available data and feedbacks to climate. Global Change Biology 6 (1), 84–115.

Evans, B., Walker, D., Benson, C., Nordstrand, E., Petersen, G., 1989. Spatial interrelationships between terrain, snow distribution and vegetation patterns at an arctic foothills site in Alaska. Holarctic Ecology 12 (3), 270–278.

Farouki, O., 1981. The thermal properties of soils in cold regions. Cold Regions Science and Technology 5 (1), 67–75.

Foken, T., 2008a. Micrometeorology. Springer.

Foken, T., 2008b. The energy balance closure problem – An overview. Ecological Applications 18, 1351–1367.

Foken, T., Göckede, M., Mauder, M., Mahrt, L., Amiro, B., Munger, J., 2004. Post-field data quality control, in: Handbook of Micrometeorology: A guide for surface flux measurement and analysis. Kluwer.

Foken, T., Wichura, B., 1996. Tools for quality assessment of surface-based flux measurements. Agricultural and Forest Meteorology 78 (1-2), 83–105.

Førland, E., Hanssen-Bauer, I., 2003. Past and future climate variations in the Norwegian Arctic: overview and novel analyses. Polar Research 22 (2), 113–124.

Førland, E., Hanssen-Bauer, I., Nordli, P., 1997. Climate statistics and longterm series of temperatures and precipitation at Svalbard and Jan Mayen. Det Norske Meteorologiske Institutt Klima Report 21/97.

Foster, J., Hall, D., Chang, A., Rango, A., 1984. An overview of passive microwave snow research and results. Reviews of Geophysics 22 (2).

Friedl, M., 2002. Forward and inverse modeling of land surface energy balance using surface temperature measurements. Remote Sensing of Environment 79 (2), 344–354.

Gao, B., Kaufman, Y., 2003. Water vapor retrievals using Moderate Resolution Imaging Spectroradiometer (MODIS) near-infrared channels. Journal Geophysical Research 108 (D13), 4389.

gcos.wmo.int, 2010. Gcos: Global climate observing system.
URL `http://gcos.wmo.int`

Gerhards, H., Wollschläger, U., Yu, Q., Schiwek, P., Pan, X., Roth, K., 2008. Continuous and simultaneous measurement of reflector depth and average soil-water content with multichannel ground-penetrating radar. Geophysics 73, J15–J23.

Gerland, S., Renner, A., 2007. Sea-ice mass-balance monitoring in an Arctic fjord. Annals of Glaciology 46 (1), 435–442.

Goodrich, L., 1982. The influence of snow cover on the ground thermal regime. Canadian Geotechnical Journal 19 (4), 421–432.

Grachev, A., Andreas, E., Fairall, C., Guest, P., Persson, P., 2007. SHEBA flux–profile relationships in the stable atmospheric boundary layer. Boundary-Layer Meteorology 124 (3), 315–333.

Haack, B., Bechdol, M., 2000. Integrating multisensor data and RADAR texture measures for land cover mapping. Computers & Geosciences 26 (4), 411–421.

Hachem, S., Allard, M., Duguay, C., 2009. Using the MODIS land surface temperature product for mapping permafrost: an application to northern Québec and Labrador, Canada. Permafrost and Periglacial Processes 20 (4), 407–416.

Hall, D., Llinas, J., 1997. An introduction to multisensor data fusion. Proceedings of the IEEE 85 (1), 6–23.

Hall, D., Riggs, G., Salomonson, V., 1995. Development of methods for mapping global snow cover using moderate resolution imaging spectroradiometer data. Remote Sensing of Environment 54 (2), 127–140.

Hall, D., Riggs, G., Salomonson, V., DiGirolamo, N., Bayr, K., 2002. MODIS snow-cover products. Remote Sensing of Environment 83 (1-2), 181–194.

Hall, F., Huemmrich, K., Goetz, S., Sellers, P., Nickeson, J., 1992. Satellite remote sensing of surface energy balance: success, failures, and unresolved issues in FIFE. Journal of geophysical research 97 (D 17), 19061–19089.

Handorf, D., Foken, T., Kottmeier, C., 1999. The stable atmospheric boundary layer over an Antarctic ice sheet. Boundary-layer meteorology 91 (2), 165–189.

Hansen, J., Ruedy, R., Sato, M., Imhoff, M., Lawrence, W., Easterling, D., Peterson, T., Karl, T., 2001. A closer look at United States and global surface temperature change. Journal of Geophysical Research-Atmospheres 106 (D20), 23947–23963.

Hanssen-Bauer, I., Førland, E., 1998. Long-term trends in precipitation and temperature in the Norwegian Arctic: can they be explained by changes in atmospheric circulation patterns? Climate Research 10, 143–153.

Harding, R., Lloyd, C., 1998. Fluxes of water and energy from three high latitude tundra sites in Svalbard. Nordic Hydrology 29 (4), 267–284.

Harris, S., French, H., Heginbottom, J., Johnston, G., Ladanyi, B., Sego, D., van Everdingen, R., 1988. Glossary of permafrost and related ground ice terms. Permafrost Subcommittee, Associate Committee on Geotechnical Research, National Research Council of Canada, Ottawa.

Hasager, C., Nielsen, N., Jensen, N., Boegh, E., Christensen, J., Dellwik, E., Soegaard, H., 2003. Effective roughness calculated from satellite-derived land cover maps and hedge-information used in a weather forecasting model. Boundary-Layer Meteorology 109 (3), 227–254.

Hillel, D., 1982. Introduction to soil physics. San Diego, USA, 58–63.

Hinzman, L., Bettez, N., Bolton, W., Chapin, F., Dyurgerov, M., Fastie, C., Griffith, B., Hollister, R., Hope, A., Huntington, H., et al., 2005. Evidence and implications of recent climate change in northern Alaska and other arctic regions. Climatic Change 72 (3), 251–298.

Hinzman, L., Goering, D., Kane, D., 1995. A distributed thermal model for calculating soil temperature profiles and depth of thaw in permafrost regions. Journal of Geophysical Research-Atmospheres 103 (D22), 28975–28991.

Hoelzle, M., Mittaz, C., Etzelmueller, B., Haeberli, W., 2001. Surface energy fluxes and distribution models of permafrost in European mountain areas: an overview of current developments. Permafrost and Periglacial Processes 12 (1), 53–68.

Høgstrøm, U., 1988. Non-dimensional wind and temperature profiles in the atmospheric surface layer: A re-evaluation. Boundary-Layer Meteorology 42 (1), 55–78.

Holmgren, J., Sturm, M., Yankielun, N., Koh, G., 1998. Extensive measurements of snow depth using FM-CW radar. Cold Regions Science and Technology 27 (1), 17–30.

Inagaki, A., Letzel, M., Raasch, S., Kanda, M., 1996. Impact of surface heterogeneity on energy balance: A study using LES. Journal of the Meteorological Society of Japan 84, 187–198.

Isaksen, K., Holmlund, P., Sollid, J., Harris, C., 2001. Three deep alpine-permafrost boreholes in Svalbard and Scandinavia. Permafrost and Periglacial Processes 12 (1), 13–25.

Isaksen, K., Sollid, J., Holmlund, P., Harris, C., 2007. Recent warming of mountain permafrost in Svalbard and Scandinavia. Journal of Geophysical Research-Earth Surface 112 (F2), F02S04.

Jones, P., Briffa, K., Barnett, T., Tett, S., 1998. High-resolution palaeoclimatic records for the last millennium: interpretation, integration and comparison with General Circulation Model control-run temperatures. The Holocene 8 (4), 455.

Jorgenson, M., Racine, C., Walters, J., Osterkamp, T., 2001. Permafrost degradation and ecological changes associated with a warming climate in Central Alaska. Climatic Change 48 (4), 551–579.

Jury, W., Horton, R., 2004. Soil physics. Wiley.

Kaimal, J., Wyngaard, J., 1990. The Kansas and Minnesota experiments. Boundary-Layer Meteorology 50 (1), 31–47.

Kalnay, E., Kanamitsu, M., Kistler, R., Collins, W., Deaven, D., Gandin, L., Iredell, M., Saha, S., White, G., Woollen, J., et al., 1996. The NCEP/NCAR 40-year reanalysis project. Bulletin of the American Meteorological Society 77 (3), 437–472.

Kane, D., Hinkel, K., Goering, D., Hinzman, L., Outcalt, S., 2001. Non-conductive heat transfer associated with frozen soils. Global and Planetary Change 29 (3–4), 275–292.

Kelly, R., Chang, A., Tsang, L., Foster, J., 2003. A prototype AMSR-E global snow area and snow depth algorithm. IEEE Transactions on Geoscience and Remote Sensing 41 (2), 230–242.

King, M., Kaufman, Y., Menzel, W., Tanre, D., 1992. Remote sensing of cloud, aerosol, and water vapor properties fromthe moderate resolution imaging spectrometer (MODIS). IEEE Transactions on Geoscience and Remote Sensing 30 (1), 2–27.

Kitoh, A., Murakami, S., Koide, H., 2001. A simulation of the Last Glacial Maximum with a coupled atmosphere-ocean GCM. Geophys. Res. Lett 28 (11), 2221–2224.

König, M., Sturm, M., 1998. Mapping snow distribution in the Alaskan Arctic using aerial photography and topographic relationships. Water Resources Research 34 (12), 3471–3483.

Kraus, H., 2008. Grundlagen der Grenzschicht-Meteorologie. Springer-Verlag Berlin Heidelberg.

Kudryavtsev, V., Garagulya, L., Kondratyeva, K., Melamed, V., 1974. Fundamentals of frost forecasting in geological engineering investigations. US Army Cold Regions Research snd Engineering Laboratory, Hanover, USA.

Labed, J., Stoll, M., 1991. Angular variation of land surface spectral emissivity in the thermal infrared: laboratory investigations on bare soils. International Journal of Remote Sensing 12 (11), 2299–2310.

Langer, M., Westermann, S., Boike, J., 2009. Spatial and temporal variations of summer surface temperatures of wet polygonal tundra in Siberia - implications for MODIS LST based permafrost monitoring. subm. to Remote Sensing of Environment.

Lawrence, D., Slater, A., Romanovsky, V., Nicolsky, D., 2008. Sensitivity of a model projection of near-surface permafrost degradation to soil column depth and representation of soil organic matter. Journal of Geophysical Research 113, F02011.

Lewkowicz, A., 2008. Evaluation of miniature temperature-loggers to monitor snowpack evolution at mountain permafrost sites, northwestern Canada. Permafrost and Periglacial Processes 19 (3), 323–331.

Ling, F., Zhang, T., 2004. A numerical model for surface energy balance and thermal regime of the active layer and permafrost containing unfrozen water. Cold Regions Science and Technology 38 (1), 1–15.

Liston, G., 1999. Interrelationships among snow distribution, snowmelt, and snow cover depletion: Implications for atmospheric, hydrologic, and ecologic modeling. Journal of Applied Meteorology 38 (10).

Liston, G., Sturm, M., 1998. A snow-transport model for complex terrain. Journal of Glaciology 44 (148), 498–516.

Liu, Y., Key, J., Frey, R., Ackerman, S., Menzel, W., 2004. Nighttime polar cloud detection with MODIS. Remote sensing of environment 92 (2), 181–194.

Long, D., Hicks, B., 2000. Standard BYU QuikScat/SeaWinds land/ice image products. Brigham Young Univ., Provo, UT, QuikScat Image Product documentation.

Luce, C., Tarboton, D., Cooley, K., 1998. Subgrid parameterization of snow distribution for an energy and mass balance snow cover model. In: Paper presented at the International Conference on Snow Hydrology. Vol. 6. Citeseer, p. 9.

Lüers, J., Bareiss, J., 2009a. Direct near surface measurements of sensible heat fluxes in the arctic tundra applying eddy-covariance and laser scintillometry - The Arctic Turbulence Experiment 2006 on Svalbard (ARCTEX-2006). submitted to Theoretical and Applied Climatology.

Lüers, J., Bareiss, J., 2009b. The effect of misleading surface temperature estimations on the sensible heat flux at a high Arctic site - The Arctic Turbulence Experiment 2006 on Svalbard (ARCTEX-2006). Atmospheric Chemistry and Physics Discussions 9, 16913–16939.

Lunardini, V., 1981. Heat Transfer in Cold Climates. Van Nostrand Reinhold, New York.

Mahrt, L., 2000. Surface heterogeneity and vertical structure of the boundary layer. Boundary-Layer Meteorology 96 (1), 33–62.

Marchenko, S., Hachem, S., Romanovsky, V., Duguay, C., 2009. Permafrost and Active Layer Modeling in the Northern Eurasia using MODIS Land Surface Temperature as an input data. Geophysical Research Abstracts 11, EGU2009–11077.

Mauder, M., Foken, T., 2004. Documentation and instruction manual of the eddy covariance software package TK2. Univ. of Bayreuth, Dept. of Mikrometeorology.

Mauder, M., Foken, T., Clement, R., Elbers, J., Eugster, W., Grünwald, T., Heusinkveld, B., Kolle, O., 2007. Quality control of CarboEurope flux data? Part II: Inter-comparison of eddy-covariance software. Biogeosciences Discussions 4 (6), 4067–4099.

Mauder, M., Foken, T., Clement, R., Elbers, J., Eugster, W., Grünwald, T., Heusinkveld, B., Kolle, O., 2008. Quality control of CarboEurope flux data–Part II: Inter-comparison of eddy-covariance software. Biogeosciences 5, 451–462.

Mauder, M., Liebthal, C., Göckede, M., Leps, J., Beyrich, F., Foken, T., 2006. Processing and quality control of flux data during LITFASS-2003. Boundary-Layer Meteorology 123, 67–88.

Mayer, B., Kylling, A., 2005. Technical note: The libRadtran software package for radiative transfer calculations–description and examples of use. Atmos. Chem. Phys 5, 1855–1877.

Meijninger, W. M. L., Green, A. E., Hartogensis, O. K., Kohsiek, W., Hoedjes, J. C. B., Zuurbier, R. M., R., D. H. A., 2002. Determination of area-averaged water vapour fluxes with large aperture and radio wave scintillometers over a heterogeneous surface: Flevoland field experiment. Boundary-Layer Meteorology 105, 63–83.

Meijninger, W. M. L., Lüdi, A., Beyrich, F., Kohsiek, W., DeBruin, H. A. R., 2006. Scintillometer-based turbulent surface fluxes of sensible and latent heat over a heterogeneous land surface: a contribution to LITFASS-2003. Boundary-Layer Meteorology 121, 89–110.

Monin, A., Obukhov, A., 1954. Basic laws of turbulent mixing in the ground layer of the atmosphere. Tr. Geofiz. Inst. Akad. Nauk SSSR 151, 163–187.

Moore, C., 1986. Frequency response corrections for eddy correlation systems. Boundary-Layer Meteorology 37 (1), 17–35.

Nelson, F., Shiklomanov, N., Hinkel, K., Brown, J., 2008. Decadal results from the Circumpolar Active Layer Monitoring (CALM) Program. In: Proceedings of the Ninth International Conference on Permafrost. Edited by DL Kane and KM Hinkel. Fairbanks, Alaska. Vol. 2. pp. 1273–1280.

Nicolsky, D., Romanovsky, V., Panteleev, G., 2009. Estimation of soil thermal properties using in-situ temperature measurements in the active layer and permafrost. Cold Regions Science and Technology 55 (1), 120–129.

Nicolsky, D., Romanovsky, V., Tipenko, G., 2007. Using in-situ temperature measurements to estimate saturated soil thermal properties by solving a sequence of optimization problems. The Cryosphere 1 (1), 41–58.

Nishihama, M., Wolfe, R., Solomon, D., Patt, F., Blanchette, J., Fleig, A., Masuoka, E., 1997. MODIS level 1A Earth location: Algorithm theoretical basis document version 3.0. SDST-092, MODIS Science Data Support Team.

Njoku, E., Jackson, T., Lakshmi, V., Chan, T., Nghiem, S., 2003. Soil moisture retrieval from AMSR-E. IEEE Transactions on Geoscience and Remote Sensing 41 (2), 215–229.

Norman, J., Becker, F., 1995. Terminology in thermal infrared remote sensing of natural surfaces. Agricultural and Forest Meteorology 77 (3-4), 153–166.

Ochsner, T., Baker, J., 2008. In situ monitoring of soil thermal properties and heat flux during freezing and thawing. Soil Science Society of America Journal 72 (4), 1025.

Ochsner, T., Sauer, T., Horton, R., 2006. Field tests of the soil heat flux plate method and some alternatives. Agronomy Journal 98 (4), 1005.

Ohmura, A., Gilgen, H., Hegner, H., Müller, G., Wild, M., Dutton, E., Forgan, B., Fröhlich, C., Philipona, R., Heimo, A., et al., 1998. Baseline Surface Radiation Network (BSRN/WCRP): New precision radiometry for climate research. Bulletin of the American Meteorological Society 79 (10), 2115–2136.

Olsson, O., Falk, L., Forslund, O., Lundmark, L., Sandberg, E., 2006. Borehole Radar Applied to the Characterization of Hydraulically Conductive Fracture Zones in Crystalline Rock. Geophysical Prospecting 40 (2), 109–142.

Onogi, K., Koide, H., Sakamoto, M., Kobayashi, S., Tsutsui, J., Hatsushika, H., Matsumoto, T., Yamazaki, N., Kamahori, H., Takahashi, K., et al., 2005. JRA-25: Japanese 25-year re-analysis project-progress and status. Quarterly Journal of the Royal Meteorological Society 131 (613), 3259–3268.

Osterkamp, T., 2005. The recent warming of permafrost in Alaska. Global and Planetary Change 49 (3-4), 187–202.

Osterkamp, T., 2007. Characteristics of the recent warming of permafrost in Alaska. Journal of Geophysical Research-Earth Surface 112 (F2), F02S02.

Overduin, P., Kane, D., van Loon, W., 2006. Measuring thermal conductivity in freezing and thawing soil using the soil temperature response to heating. Cold Regions Science and Technology 45 (1), 8–22.

Overland, J., Wang, M., Salo, S., 2008. The recent Arctic warm period. Tellus A 60 (4), 589–597.

Parker, W., 2001. Effect of permafrost changes on economic development, environmental security and natural resource potential in Alaska, in: Permafrost response on economic development, environmental security and natural resources. Kluver Academic Publishers, Dordrecht, The Netherlands, pp. 293–296.

Persson, P., Fairall, C., Andreas, E., Guest, P., Perovich, D., 2002. Measurements near the Atmospheric Surface Flux Group tower at SHEBA: Near-surface conditions and surface energy budget. Journal of Geophysical Research-Oceans 107 (C10).

Pielke, R., Avissar, R., 1990. Influence of landscape structure on local and regional climate. Landscape Ecology 4 (2), 133–155.

Prandtl, L., 1925. Bericht über Untersuchungen zur ausgebildeten Turbulenz. Zeitschrift für angewandte Mathematik und Mechanik 5, 136–139.

Prigent, C., Tegen, I., Aires, F., Marticorena, B., Zribi, M., 2005. Estimation of the aerodynamic roughness length in arid and semi-arid regions over the globe with the ERS scatterometer. J. Geophys. Res 110 (D9).

Prowse, T., Furgal, C., Chouinard, R., Melling, H., Milburn, D., Smith, S., 2009. Implications of climate change for economic development in Northern Canada: energy, resource, and transportation sectors. AMBIO: A Journal of the Human Environment 38 (5), 272–281.

Pulliainen, J., 2006. Mapping of snow water equivalent and snow depth in boreal and sub-arctic zones by assimilating space-borne microwave radiometer data and ground-based observations. Remote sensing of Environment 101 (2), 257–269.

Putkonen, J., 1998. Soil thermal properties and heat transfer processes near Ny-Ålesund, northwestern Spitsbergen, Svalbard. Polar Research 17 (2), 165–179.

Putkonen, J., 2003. Determination of frozen soil thermal properties by heated needle probe. Permafrost and Periglacial Processes 14 (4), 343–347.

Putkonen, J., Roe, G., 2003. Rain-on-snow events impact soil temperatures and affect ungulate survival. Geophysical Research Letters 30 (4), 1188.

Rees, W., 1993. Infrared emissivities of arctic land cover types. International Journal of Remote Sensing 14 (5), 1013–1017.

Reynolds, O., 1895. On the dynamical theory of incompressible viscous fluids and the determination of the criterion. Philosophical Transactions of the Royal Society of London. A 186, 123–164.

Ricchiazzi, P., Yang, S., Gautier, C., Sowle, D., 1998. Bulletin American Meteorological Society 79, 2101–2114.

Roeckner, E., Bäuml, G., Bonaventura, L., Brokopf, R., Esch, M., Giorgetta, M., Hagemann, S., Kirchner, I., Kornblueh, L., Manzini, E., et al., 2003. The atmospheric general circulation model ECHAM5: part 1: model description.

Romanovsky, V., Osterkamp, T., 1997. Thawing of the active layer on the coastal plain of the Alaskan Arctic. Permafrost and Periglacial Processes 8 (1), 1–22.

Roth, K., Boike, J., 2001. Quantifying the thermal dynamics of a permafrost site near Ny-Ålesund, Svalbard. Water Resources Research 37 (12), 2901–2914.

Rothman, L., Gordon, I., Barbe, A., Benner, D., Bernath, P., Birk, M., Boudon, V., Brown, L., Campargue, A., Champion, J., et al., 2009. The HITRAN 2008 molecular spectroscopic database. Journal of Quantitative Spectroscopy and Radiative Transfer 110 (9-10), 533–572.

Salisbury, J., D'Aria, D., 1992. Emissivity of terrestrial materials in the 8-14 microns atmospheric window. Remote Sensing of Environment 42 (2), 83–106.

Sand, K., Bruland, O., 1998. Application of georadar for snow cover surveying. Nordic Hydrology 29 (4), 361–370.

Sauer, T., Meek, D., Ochsner, T., Harris, A., Horton, R., 2003. Errors in heat flux measurement by flux plates of contrasting design and thermal conductivity. Vadose Zone Journal 2 (4), 580.

Sazonova, T., Romanovsky, V., 2003. A model for regional-scale estimation of temporal and spatial variability of active layer thickness and mean annual ground temperatures. Permafrost and Periglacial Processes 14 (2), 125–139.

Schaaf, C., Gao, F., Strahler, A., Lucht, W., Li, X., Tsang, T., Strugnell, N., Zhang, X., Jin, Y., Muller, J., et al., 2002. First operational BRDF, albedo nadir reflectance products from MODIS. Remote Sensing of Environment 83 (1-2), 135–148.

Schaudt, K., Dickinson, R., 2000. An approach to deriving roughness length and zero-plane displacement height from satellite data, prototyped with BOREAS data. Agricultural and Forest Meteorology 104 (2), 143–155.

Schmid, H., 1994. Source areas for scalars and scalar fluxes. Boundary-Layer Meteorology 67 (3), 293–318.

Schmid, H., 2002. Footprint modeling for vegetation atmosphere exchange studies: A review and perspective. Agricultural and Forest Meteorology 113, 159–183.

Schotanus, P., Nieuwstadt, F., Bruin, H., 1983. Temperature measurement with a sonic anemometer and its application to heat and moisture fluxes. Boundary-Layer Meteorology 26 (1), 81–93.

Schuur, E., Bockheim, J., Canadell, J., Euskirchen, E., Field, C., Goryachkin, S., Hagemann, S., Kuhry, P., Lafleur, P., Lee, H., et al., 2008. Vulnerability of permafrost carbon to climate change: Implications for the global carbon cycle. BioScience 58 (8), 701–714.

Seemann, S., Li, J., Menzel, W., Gumley, L., 2003. Operational retrieval of atmospheric temperature, moisture, and ozone from MODIS infrared radiances. Journal of applied meteorology 42 (8), 1072–1091.

Sellers, P., Hall, F., Kelly, R., Black, A., Baldocchi, D., Berry, J., Ryan, M., Ranson, K., Crill, P., Lettenmaier, D., et al., 1997. BOREAS in 1997: Experiment overview, scientific results, and future directions. Journal of Geophysical Research 102 (D24), 28731.

Sellers, P., Los, S., Tucker, C., Justice, C., Dazlich, D., Collatz, G., Randall, D., 1996. A revised land surface parameterization (SiB2) for atmospheric GCMs. Part II: The generation of global fields of terrestrial biophysical parameters from satellite data. Journal of Climate 9 (4), 706–737.

Serreze, M., Walsh, J., Chapin, F., Osterkamp, T., Dyurgerov, M., Romanovsky, V., Oechel, W., Morison, J., Zhang, T., Barry, R., 2000. Observational evidence of recent change in the northern high-latitude environment. Climatic Change 46 (1), 159–207.

Shiklomanov, N., Nelson, F., Streletskiy, D., Hinkel, K., Brown, J., 2008. The Circumpolar Active Layer Monitoring (CALM) program: Data collection, management, and dissemination strategies. In: Proceedings of the Ninth International Conference on Permafrost. Edited by DL Kane and KM Hinkel. Fairbanks, Alaska. Vol. 2. pp. 1647–1652.

Simmons, A., Uppala, S., Dee, D., Kobayashi, S., 2007. ERA-Interim: New ECMWF reanalysis products from 1989 onwards. ECMWF Newsletter 110, 25–35.

Skeel, R., Berzins, M., 1990. A method for the spatial discretization of parabolic equations in one space variable. SIAM Journal on Scientific and Statistical Computing 11, 1.

Slama, C., Theurer, C., Henriksen, S., 1980. Manual of photogrammetry. American Society of Photogrammetry Falls Church, Virginia.

Slater, A., Pitman, A., Desborough, C., 1998. The validation of a snow parameterization designed for use in general circulation models. International Journal of Climatology 18 (6), 595–617.

Smith, L., Sheng, Y., MacDonald, G., Hinzman, L., 2005. Disappearing arctic lakes. Science 308 (5727), 1429.

Snyder, W., Wan, Z., 1998. BRDF models to predict spectral reflectance and emissivity in the thermal infrared. IEEE Transactions on Geoscience and remote Sensing 36 (1), 214–225.

Snyder, W., Wan, Z., Zhang, Y., Feng, Y., 1997. Thermal infrared (3-14 micron) bidirectional reflectance measurements of sands and soils. Remote Sensing of Environment 60 (1), 101–109.

Sobrino, J., Jimenez-Munoz, J., Paolini, L., 2004. Land surface temperature retrieval from LANDSAT TM 5. Remote Sensing of Environment 90 (4), 434–440.

Sonntag, D., 1990. Important new values of the physical constants of 1986, vapour pressure formulations based on the ITS-90, and psychrometer formulae. Zeitschrift für Meteorologie 40 (5), 340–344.

Stow, D., Hope, A., McGuire, D., Verbyla, D., Gamon, J., Huemmrich, F., Houston, S., Racine, C., Sturm, M., Tape, K., et al., 2004. Remote sensing of vegetation and land-cover change in Arctic Tundra Ecosystems. Remote Sensing of Environment 89 (3), 281–308.

Stull, R., 1988. An introduction to boundary layer meteorology. Springer.

Sturm, M., Holmgren, J., König, M., Morris, K., 1997. The thermal conductivity of seasonal snow. Journal of Glaciology 43 (143), 26–41.

Sturm, M., Perovich, D., Holmgren, J., 2002. Thermal conductivity and heat transfer through the snow on the ice of the Beaufort Sea. Journal of Geophysical Research-Oceans 107 (C10), 8043.

Takeuchi, Y., Kodoma, Y., Nakabayashi, H., 1995. Characteristics of evaporation from snow and tundra surface in Spitsbergen in the snowmelt season 1993. In: Proceedings of the NIPR Symposium on Polar Meteorology and Glaciology. Vol. 9. pp. 54–65.

Thamm, H., Judex, M., 2006. The “low cost drone”–an interesting tool for process monitoring in a high spatial and temporal resolution. In: ISPRS Mid-term Symposium. pp. 8–11.

Turner, J., Overland, J., Walsh, J., 2007. An Arctic and Antarctic perspective on recent climate change. International Journal of Climatology 27 (3), 277–293.

UNEP/GRID-Arendal, 2010. Projected changes in the arctic climate, 2090, unep/grid-arendal maps and graphics library.
URL http://maps.grida.no/go/graphic/

Uppala, S., Kållberg, P., Simmons, A., Andrae, U., Bechtold, V., Fiorino, M., Gibson, J., Haseler, J., Hernandez, A., Kelly, G., et al., 2006. The ERA-40 re-analysis. Quarterly Journal of the Royal Meteorological Society 131 (612), 2961–3012.

Uttal, T., Curry, J., Mcphee, M., Perovich, D., Moritz, R., Maslanik, J., Guest, P., Stern, H., Moore, J., Turenne, R., et al., 2002. Surface heat budget of the Arctic Ocean. Bulletin of the American Meteorological Society 83 (2), 255–275.

Viterbo, P., Beljaars, A., 1995. An improved land surface parameterization scheme in the ECMWF model and its validation. Journal of Climate 8 (11), 2716–2748.

Viterbo, P., Beljaars, A., Mahfouf, J., Teixeira, J., 1999. The representation of soil moisture freezing and its impact on the stable boundary layer. Quarterly Journal of the Royal Meteorological Society 125 (559), 2401–2426.

Walker, D., Jia, G., Epstein, H., Raynolds, M., Chapin Iii, F., Copass, C., Hinzman, L., Knudson, J., Maier, H., Michaelson, G., et al., 2003. Vegetation-soil-thaw-depth relationships along a low-arctic bioclimate gradient, Alaska: synthesis of information from the ATLAS studies. Permafrost and Periglacial Processes 14 (2), 103–123.

Walter, K., Zimov, S., Chanton, J., Verbyla, D., Chapin III, F., 2006. Methane bubbling from Siberian thaw lakes as a positive feedback to climate warming. Nature 443 (7107), 71–75.

Wan, Z., 2008. New refinements and validation of the MODIS land-surface temperature/emissivity products. Remote Sensing of Environment 112 (1), 59–74.

Wan, Z., Dozier, J., 1996. A generalized split-window algorithm for retrieving land-surfacetemperature from space. IEEE Transactions on geoscience and remote sensing 34 (4), 892–905.

Wan, Z., Zhang, T., 1999. MODIS UCSB Emissivity Library: http://www.icess.ucsb.edu/modis/EMIS/html/em.html.

wcrp.wmo.int, 2010. World Climate Research Programme Implementation Plan 2010–2015.
URL http://www.wmo.ch/pages/prog/wcrp/documents/WCRP_IP_2010_2015.pdf

Westermann, S., Lüers, J., Langer, M., Piel, K., Boike, J., 2009. The annual surface energy budget of a high-arctic permafrost site on Svalbard, Norway. The Cryosphere 3 (2), 245–263.
URL http://www.the-cryosphere.net/3/245/2009/

Westermann, S., Wollschläger, U., Boike, J., 2010. Monitoring of active layer dynamics at a permafrost site on Svalbard using multi-channel ground-penetrating radar. The Cryosphere Discussions 4, 287–319.

Wilson, K., Goldstein, A., Falge, E., Aubinet, M., Baldocchi, D., Berbigier, P., Bernhofer, C., Ceulemans, R., Dolman, H., Field, C., et al., 2002. Energy balance closure at FLUXNET sites. Agricultural and Forest Meteorology 113 (1-4), 223–243.

Winther, J., Godtliebsen, F., Gerland, S., Isachsen, P., 2002. Surface albedo in Ny-Ålesund, Svalbard: variability and trends during 1981–1997. Global and Planetary Change 32 (2-3), 127–139.

Wolfe, R., Nishihama, M., Fleig, A., Kuyper, J., Roy, D., Storey, J., Patt, F., 2002. Achieving sub-pixel geolocation accuracy in support of MODIS land science. Remote Sensing of Environment 83 (1), 31–49.

Wollschläger, U., Gerhards, H., Yu, Q., Roth, K., 2010. Multi-channel ground-penetrating radar to explore spatial variations in thaw depth and moisture content in the active layer of a permafrost site. The Cryosphere 4, 269–283.
URL http://www.the-cryosphere.net/4/269/2010/tc-4-269-2010.pdf

Wukelic, G., Gibbons, D., Martucci, L., Foote, H., 1989. Radiometric calibration of Landsat Thematic Mapper thermal band. Remote Sensing of Environment 28, 339–347.

www.bsrn.awi.de, 2010. WRMC-BSRN: World Radiation Monitoring Center - Baseline Surface Radiation Network.
URL http://www.bsrn.awi.de

www.eklima.no, 2010. Free access to weather- and climate data from norwegian meteorological institute from historical data to real time observations.
URL http://www.eklima.no

www.gtnp.org, 2010. Global terrestrial network for permafrost.
URL http://www.gtnp.org

www.ipf.tuwien.ac.at, 2010. Website of the project Due Permafrost.
URL http://www.ipf.tuwien.ac.at/permafrost/

www.licor.com, 2010. LiCor LI–7500 CO_2 and H_2O open-path gas analyzer.
URL http://www.licor.com

www.npolar.no, 2010. Land cover classification of svalbard.
URL http://www.npolar.no/svalbardkartet/

Yamanouchi, T., Ørbaek, J., 1995. Comparative study of the surface radiation budget at Ny-Ålesund, Svalbard and Syowa Station, Antarctica, 1987. In: Proceedings of the NIPR Symposium on Polar Meteorolgy and Glacialogy. National Institute of Polar Research, Japan, pp. 118–132.

Zilitinkevich, S., Perov, V., King, J., 2002. Near-surface turbulent fluxes in stable stratification: Calculation techniques for use in general-circulation models. Quarterly Journal of the Royal Meteorological Society 128 (583), 1571–1587.

Zimov, S., Schuur, E., Chapin III, F., 2006. Permafrost and the global carbon budget. Science 312 (5780), 1612–1613.

Acknowledgments

This dissertation has been accomplished in the Helmholtz-University Young Investigator Research group on "Sensitivity of the permafrost system's water and energy balance under changing climate: A multiscale perspective" (SPARC). During the past years, a great number of people have contributed to the success of this work.

First and foremost, I want to thank my supervisor Julia Boike who provided me with any possible support and encouragement and fueled my curiosity in many discussions. I would especially like to thank her for giving me the freedom to develop and realize my own ideas during the project. In addition, Julia has managed to create a great working environment in the SPARC group which has been both productive and fun for me.

I am sincerely grateful to Kurt Roth, my supervisor at the University of Heidelberg. His advice has always been a guidance for my work, and he has inspired me in intellectually challenging discussions. The scientific exchange with his soil physics group, where I was always welcomed warmly, has contributed to my work in many ways.

I am thankful to Ulrich Platt for his willingness to act as second referee for my dissertation.

Moritz Langer, with who I was fortunate enough to shape the reputation of an office over the past years, has not only become a valued colleague, but also a great friend. This work certainly would have not been possible without our endless after-hour discussions about the utility and futility of our ideas and our work. Although we certainly took a few detours along this way, I am left with great memories of this time.
In addition, it was reassuring to know that there was another person in the endless plains around Potsdam who started to flutter when confronted with the news of fresh snow in the mountains.

Konstanze Piel, engineer in our work group, has been an enormous help during the past years. I knew I could always rely on her work, from the design of measurement campaigns over the actual installation of the equipment in Ny-Ålesund to the processing and management of the obtained data.

With Bob Bolton I worked in Ny-Ålesund for the arctic summer of 2007 and therefore the first "field season" of my life. I have lots of great memories of this time. Muchas gracias, Bob!

A great thanks also goes to Emilie Guegan for helping me with the field work in summer of 2008.

The station personnel of the AWIPEV base in Ny-Ålesund has been crucial for the success of the field measurements on Svalbard. I would like to express my sincere gratitude to the station leaders Rainer Vockenroth and Marcus Schumacher, who continuously took care of our installations during the long arctic winter. Thanks a lot for the patience when spending hours in the cold troubleshooting for us. Whenever there was a problem, we could also rely on the station engineers Mareike Peterson, Cédric Couret, Eric Larmanou, Alan le Tréssoler and Moritz Sieber as well as the trainee Jonathan Plössl. Thanks to

all of you for helping us and for making my stays in Ny-Ålesund incredible fun.

I am indebted to Marion Maturilli and Roland Neuber who provided me with the long-term data set of the BSRN station in Ny-Ålesund, which in many ways proved valuable for this work.

In Potsdam, I have enjoyed to work with the members of the SPARC group. Sina Muster, Torsten Sachs, Molo Stoof, Niko Bornemann, Katrin Fröb, Anna Abnizova and Jenny Sobiech all had their share to give our group a productive and comfortable atmosphere. Thanks for that!

Johannes Lüers from the Department of Micrometeorology at the University of Bayreuth was an invaluable help in planning, analyzing and interpreting our eddy covariance measurements. He dedicated a lot of his time to give us "newcomers" in the field a smooth start.

Wolfgang Dorn provided me with a valuable introduction into large-scale climate modeling, from which this research benefited a lot. I would also like to thank him for proofreading parts of this dissertation.

With Ute Wollschläger I had a great collaboration and many interesting and fruitful discussions about geophysical techniques and other aspects of my work.

A special thanks goes to Thomas Amthor who always knew the answer whenever I had a question about designing electronics for the field measurements.

The stimulating discussions with Hugues Lantuit, Paul Overduin and Birgit Heim have been very helpful for defining and shaping the topic of this thesis, for which am I grateful to all of them.

Finally, I would like to thank all my friends and colleagues for the various ways of support and encouragement in the past years. You all had your great share in making my time in Potsdam both enjoyable and rewarding. A special thought is devoted to my parents for their never-ending support.

Potsdam in August 2010
Sebastian Westermann